

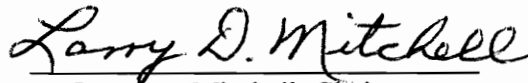
**CHARACTERIZATION OF LASER NOISE IN FREE-FREE BEAM  
STRUCTURES USING A SCANNING LASER DOPPLER  
VIBROMETER**

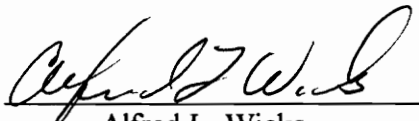
by

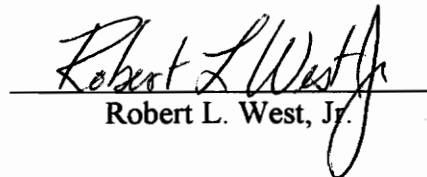
R. Flynt Streat

Thesis submitted to the Faculty of the  
Virginia Polytechnic Institute and State University  
in partial fulfillment of the requirements for the degree of  
MASTER OF SCIENCE  
in  
Mechanical Engineering

APPROVED:

  
Larry D. Mitchell, Chairman

  
Alfred L. Wicks

  
Robert L. West, Jr.

September, 1995

Blacksburg, VA

LD  
5655  
V855  
1995  
S774  
c.2

**CHARACTERIZATION OF LASER NOISE IN FREE-FREE BEAM  
STRUCTURES USING A SCANNING LASER DOPPLER VIBROMETER**

by

R. Flynt Streat

Committee Chairman: L.D. Mitchell

Mechanical Engineering

**(ABSTRACT)**

The advent of the laser has yielded many applications in modern science. One which has recently gained popularity in the area of structural dynamics is the use of a Scanning Laser Doppler Vibrometer (SLDV) to measure the dynamic response of vibrating structures. Essential in the optimal use of such a device is an understanding of the idiosyncrasies and operating parameters which may affect the quality of the experimental data. Specifically, the quality of the data taken with an SLDV system may contain noise which, for the purpose of this investigation, will be defined as "laser noise". It is the purpose of this thesis to characterize the laser noise, and investigate its potential sources.

Characterization of laser noise as a function of the range of velocities is presented. An investigation of the speckle pattern motions which correspond to the areas prone to the laser noise and the effect of increased retroreflective surface treatments are explored.

Additionally, the effect of three user defined parameters of the SLDV system are examined. In order to quantify the effect of the above on the experimental data, a statistical representation of the quality of the scan data is introduced.

The work presented in this thesis provides insight into the physical mechanisms and phenomenon which contribute to the occurrence of laser noise. Additionally, some guidelines which will help the experimentalist use the SLDV system more optimally are presented. Also, some recommendations on future improvements of the SLDV are made, along with proposals for future research.



To my parents,  
Richard and Beverly Streaan

## **ACKNOWLEDGEMENTS**

I would like to express my appreciation to the members of my graduate committee, Dr. Larry Mitchell, Dr. Alfred Wicks, and Dr. Robert West, for their significant and continued suggestions, contributions, and tutelage. I have enjoyed the opportunity to work with and learn from them throughout my graduate and undergraduate studies at Virginia Tech.

I would further like to express my deepest gratitude to Dr. Mitchell for his devoted instruction and guidance. His unselfish support and respect for the student is a personality trait which transcends academia. I sincerely appreciate the opportunity of having worked with him.

I would also like to thank Ometron, Inc., and especially Andy Barker for his advice, assistance, and insight concerning this research.

Finally, I would like to thank my family and friends for their support and understanding during the many ups and downs of my graduate experience.

# TABLE OF CONTENTS

|  |           |
|--|-----------|
| ABSTRACT.....                            | ii        |
| DEDICATION.....                          | iii       |
| ACKNOWLEDGMENTS.....                     | iv        |
| LIST OF FIGURES.....                     | x         |
| LIST OF TABLES.....                      | xiii      |
| NOMENCLATURE.....                        | xiv       |
| <i>CHAPTER 1: INTRODUCTION.....</i>      | <i>1</i>  |
| 1.1 BACKGROUND AND MOTIVATION.....       | 2         |
| 1.2 PROBLEM STATEMENT AND DOMAIN.....    | 7         |
| 1.2.1 Problem Domain.....                | 7         |
| 1.2.1.1 Laser Speckle.....               | 8         |
| 1.2.1.2 Working Distance.....            | 8         |
| 1.2.1.3 Measuring Beam Focus.....        | 9         |
| 1.2.1.4 Test Surface Preparation.....    | 9         |
| 1.2.2 Problem Statement.....             | 10        |
| 1.3 OBJECTIVE.....                       | 11        |
| 1.4 APPROACH.....                        | 12        |
| 1.5 ORGANIZATION OF THESIS.....          | 14        |
| <i>CHAPTER 2: LITERATURE REVIEW.....</i> | <i>16</i> |
| 2.1 LASER DOPPLER VIBROMETRY.....        | 16        |
| 2.1.1 Development.....                   | 17        |
| 2.1.2 Example Applications.....          | 20        |

|   |           |
|---|-----------|
| 2.1.3 Measurement Data Quality .....                            | 21        |
| 2.2 LASER SPECKLE PATTERN PHENOMENON .....                      | 28        |
| 2.2.1 Definitions .....   | 28        |
| 2.2.2 Example Applications .....                                | 30        |
| 2.3 SUMMARY .....   | 32        |
| <i>CHAPTER 3: EXPERIMENTAL METHODS</i> .....                    | <i>34</i> |
| 3.1 SCANNING LASER DOPPLER VIBROMETER.....                      | 35        |
| 3.1.1 Measurement Theory.....                                   | 35        |
| 3.1.2 Scan Control/Data Acquisition.....                        | 41        |
| 3.2 SETUP .....   | 45        |
| 3.3 DATA ANALYSIS .....   | 52        |
| 3.3.1 Calibration.....  | 53        |
| 3.3.2 Row Median.....   | 54        |
| 3.3.3 Fitted-Curve.....   | 56        |
| 3.3.4 'Deviation Factor' .....                                  | 60        |
| 3.3.5 Confidence Intervals.....                                 | 63        |
| 3.5 EXAMPLE.....  | 68        |
| 3.6 ASSUMPTIONS AND REMARKS.....                                | 79        |
| 3.6.1 Setup and Data Acquisition .....                          | 80        |
| 3.6.2 Data Analysis .....                                       | 82        |
| 3.7 SUMMARY .....   | 88        |
| <i>CHAPTER 4: EXPERIMENTAL DESCRIPTIONS AND RESULTS</i> .....   | <i>89</i> |
| 4.1 RANGE OF VELOCITY RESPONSES AS A PERCENTAGE OF FULL-SCALE . | 90        |
| 4.1.1 Experimental Description.....                             | 90        |
| 4.1.2 Experimental Observations .....                           | 95        |

|  |            |
|--|------------|
| 4.1.3 Experimental Results .....                   | 96         |
| 4.1.4 Discussion of Results .....                  | 105        |
| 4.2 SPECKLE PATTERN MOTION EXPERIMENT .....        | 121        |
| 4.2.1 Experimental Description .....               | 121        |
| 4.2.2 Experimental Observations .....              | 124        |
| 4.2.3 Experimental Results .....                   | 125        |
| 4.2.4 Discussion of Results .....                  | 127        |
| 4.3 SURFACE PREPARATION .....                      | 130        |
| 4.3.1 Experimental Description .....               | 130        |
| 4.3.2 Experimental Observations .....              | 132        |
| 4.3.3 Experimental Results .....                   | 133        |
| 4.3.4 Discussion of Results .....                  | 136        |
| 4.4 SUMMARY .....                                  | 137        |
| <i>CHAPTER 5: SUPPLEMENTAL EXPERIMENTS</i> .....   | <i>140</i> |
| 5.1 OUTPUT LENS SELECTION .....                    | 141        |
| 5.1.1 Experimental Description .....               | 141        |
| 5.1.2 Experimental Results .....                   | 142        |
| 5.1.3 Discussion of Results .....                  | 143        |
| 5.2 COHERENCE REPEAT DISTANCE .....                | 144        |
| 5.2.1 Experimental Description .....               | 144        |
| 5.2.2 Experimental Results .....                   | 145        |
| 5.2.3 Discussion of Results .....                  | 146        |
| 5.3 "SLIGHT DEFOCUS" OF LASER MEASURING BEAM ..... | 147        |
| 5.3.1 Experimental Description .....               | 148        |
| 5.3.2 Experimental Results .....                   | 150        |
| 5.3.3 Discussion of Results .....                  | 151        |

|  |            |
|--|------------|
| 5.4 SUMMARY .....  | 153        |
| <i>CHAPTER 6: CONCLUSIONS AND RECOMMENDATIONS</i> .....                                | <i>155</i> |
| 6.1 SUMMARY .....  | 155        |
| 6.2 CONCLUSIONS .....  | 156        |
| 6.3 RECOMMENDATIONS .....  | 158        |
| 6.3.1 Recommended Changes to the SLDV System.....                                      | 159        |
| 6.3.2 Recommended Guidelines for SLDV Optimal Use .....                                | 159        |
| 6.3.3 Recommendations for Future Work .....  | 160        |
| REFERENCES.....  | 162        |
| APPENDIX A.1: FIGURES FOR RANGE OF VELOCITIES EXPERIMENT .....                         | 167        |
| APPENDIX A.2: FIGURES FOR SURFACE PREPARATION EXPERIMENT .....                         | 182        |
| APPENDIX A.3: FIGURES FOR OUTPUT LENS SELECTION EXPERIMENT ....                        | 190        |
| APPENDIX A.4: FIGURES FOR COHERENCE REPEAT DISTANCE<br>EXPERIMENT .....                | 193        |
| APPENDIX A.5: FIGURES FOR “SLIGHT DEFOCUS” EXPERIMENT .....                            | 196        |
| APPENDIX B: MATLAB DATA ANALYSIS ALGORITHMS.....                                       | 200        |
| APPENDIX C: FREQUENCY RESPONSE FUNCTION (FRF) DIAGRAMS.....                            | 206        |
| APPENDIX D: EXAMPLES OF LASER NOISE OCCURRING AT OTHER<br>EXCITATION FREQUENCIES ..... | 213        |
| APPENDIX E: STANFORD SR640 FILTER PHASE RESPONSE CURVE .....                           | 216        |
| APPENDIX F: ANTICLASTIC CURVATURE CALCULATION.....                                     | 218        |
| APPENDIX G: LASER DOPPLER VIBROMETER CALIBRATION CHECK.....                            | 221        |
| VITA.....  | 224        |

# LIST OF FIGURES

|  |    |
|--|----|
| Figure 1.1: SLDV System, Data Acquisition and Scan Control via the HP .....                            | 4  |
| Figure 1.2: SLDV System, Data Acquisition and Scan Control via the Mac.....                            | 4  |
| Figure 1.3(a): Velocity scan data showing noise at maximum amplitudes.....                             | 6  |
| Figure 1.3(b): Velocity scan data showing noise at maximum amplitudes .....                            | 6  |
| Figure 2.1: Velocity and Doppler signals suffering from drop-out.....                                  | 24 |
| Figure 2.2: Example of a laser speckle pattern.....  | 29 |
| Figure 3.1: Schematic of the VPI Sensor unit.....  | 38 |
| Figure 3.2: VPI Sensor Optical Unit .....  | 39 |
| Figure 3.3: Oscilloscope plot showing Force, Velocity, Doppler, and Correlator<br>Output signals ..... | 44 |
| Figure 3.4: General experimental setup .....   | 46 |
| Figure 3.5(a): Overall experimental setup.....   | 48 |
| Figure 3.5(b): Experimental setup .....  | 49 |
| Figure 3.5(c): Experimental setup .....  | 50 |
| Figure 3.6: Example surface velocity plot.....   | 69 |
| Figure 3.7: Example two-dimensional representation of velocity .....                                   | 70 |
| Figure 3.8: Example DFT-IDFT fitted-curve.....   | 71 |
| Figure 3.9: Example ‘scan-fit plot’.....   | 72 |
| Figure 3.10: Example B surface velocity plot .....   | 75 |
| Figure 3.11: Example B two-dimensional representation of velocity.....                                 | 76 |
| Figure 3.12: Example B DFT-IDFT fitted-curve .....   | 77 |
| Figure 3.13: Example B ‘scan-fit plot’ .....   | 78 |
| Figure 3.14: Typical ‘scan-fit plot’ with scaled Euler-Bernoulli curve-fit .....                       | 83 |
| Figure 3.15: Typical ‘scan-fit plot’ with Forsythe polynomial curve-fit .....                          | 84 |

|  |     |
|--|-----|
| Figure 3.16: Typical ‘scan-fit plot’ with DFT-IDFT curve-fit .....   | 85  |
| Figure 4.1: ‘Deviation Factor’ vs. Maximum Velocity Response (LOW Range) .....                                   | 98  |
| Figure 4.2: ‘Deviation Factor’ vs. Maximum Velocity Response (MEDIUM Range).....                                 | 99  |
| Figure 4.3: Oscilloscope plot showing relatively stable velocity and Doppler signals.....                        | 100 |
| Figure 4.4: Oscilloscope plot showing velocity drop-out .....  | 102 |
| Figure 4.5: Oscilloscope plot showing velocity drop-out .....  | 103 |
| Figure 4.6: Oscilloscope plot showing velocity drop-out .....  | 104 |
| Figure 4.7: Example scan-fit plot .....  | 107 |
| Figure 4.8: Example scan-fit plot .....  | 108 |
| Figure 4.9: Residuals vs. Fraction of Maximum Velocity Response .....  | 110 |
| Figure 4.9(a): Normalized Residuals vs. Fraction of Maximum Velocity Response .....                              | 111 |
| Figure 4.10: Residuals vs. Gradient of Velocity Response Shape .....   | 112 |
| Figure 4.11: Residuals vs. Fraction of Maximum Velocity Response and Gradient<br>of Velocity Response Shape..... | 113 |
| Figure 4.12: Points of interest for speckle pattern motion experiment.....                                       | 122 |
| Figure 4.13: Speckle Motion Gain vs. Position Along Beam.....  | 126 |
| Figure 4.14: ‘Deviation Factor’ vs. Range of Velocities .....  | 134 |
| Figure 4.15: Oscilloscope plot showing Force, Velocity, Doppler, and Correlator<br>Output signals.....           | 135 |
| Figure A.1.1: Representative ‘scan-fit plot’ for scan group L1 .....   | 168 |
| Figure A.1.2: Representative ‘scan-fit plot’ for scan group L2 .....   | 169 |
| Figure A.1.3: Representative ‘scan-fit plot’ for scan group L3 .....   | 170 |
| Figure A.1.4: Representative ‘scan-fit plot’ for scan group L4 .....   | 171 |
| Figure A.1.5: Representative ‘scan-fit plot’ for scan group L5 .....   | 172 |
| Figure A.1.6: Representative ‘scan-fit plot’ for scan group L6 .....   | 173 |
| Figure A.1.7: Representative ‘scan-fit plot’ for scan group M1 .....   | 174 |
| Figure A.1.8: Representative ‘scan-fit plot’ for scan group M2 .....   | 175 |
| Figure A.1.9: Representative ‘scan-fit plot’ for scan group M3 .....   | 176 |



|   |     |
|---|-----|
| Figure A.1.10: Representative 'scan-fit plot' for scan group M4 .....               | 177 |
| Figure A.1.11: Representative 'scan-fit plot' for scan group M5 .....               | 178 |
| Figure A.1.12: Representative 'scan-fit plot' for scan group M6 .....               | 179 |
| Figure A.1.13: Representative 'scan-fit plot' for scan group M7 .....               | 180 |
| Figure A.1.14: Representative 'scan-fit plot' for scan group M8 .....               | 181 |
| Figure A.2.1: Representative 'scan-fit plot' for scan group P1.....                 | 183 |
| Figure A.2.2: Representative 'scan-fit plot' for scan group P2.....                 | 184 |
| Figure A.2.3: Representative 'scan-fit plot' for scan group P3.....                 | 185 |
| Figure A.2.4: Representative 'scan-fit plot' for scan group P4.....                 | 186 |
| Figure A.2.5: Representative 'scan-fit plot' for scan group P5.....                 | 187 |
| Figure A.2.6: Representative 'scan-fit plot' for scan group P6.....                 | 188 |
| Figure A.2.7: Representative 'scan-fit plot' for scan group P7.....                 | 189 |
| Figure A.3.1: Representative 'scan-fit plot' for scan group L.R. Lens.....          | 191 |
| Figure A.3.2: Representative 'scan-fit plot' for scan group S.R. Lens.....          | 192 |
| Figure A.4.1: Representative 'scan-fit plot' for scan group D1 .....                | 194 |
| Figure A.4.2: Representative 'scan-fit plot' for scan group D2.....                 | 195 |
| Figure A.5.1: Representative 'scan-fit plot' for scan group REF.....                | 197 |
| Figure A.5.2: Representative 'scan-fit plot' for scan group DFL.....                | 198 |
| Figure A.5.3: Representative 'scan-fit plot' for scan group DFR .....               | 199 |
| Figure C.1: Typical baseband FRF and coherence diagram.....                         | 207 |
| Figure C.2: Typical baseband FRF and coherence diagram.....                         | 208 |
| Figure C.3: Typical zoom FRF and coherence diagram.....                             | 209 |
| Figure C.4: Typical zoom FRF and coherence diagram.....                             | 210 |
| Figure C.5: Typical baseband FRF and coherence diagram.....                         | 211 |
| Figure C.6: Typical zoom FRF and coherence diagram.....                             | 212 |
| Figure D.1: Example of laser noise occurring at alternate excitation frequency..... | 214 |
| Figure D.2: Example of laser noise occurring at alternate excitation frequency..... | 215 |
| Figure E.1: Stanford SR640 phase response curve .....                               | 217 |

## LIST OF TABLES

|  |     |
|--|-----|
| Table 4.1: Scan groups and corresponding maximum velocity responses for the<br>LOW velocity range.....                               | 92  |
| Table 4.2: Scan groups and corresponding maximum velocity responses for the<br>MEDIUM velocity range .....                           | 93  |
| Table 4.3: Statistical summary of the ‘Deviation Factors’ for range of velocities<br>experiment (LOW velocity range setting) .....   | 97  |
| Table 4.4: Statistical summary of the ‘Deviation Factors’ for range of velocities<br>experiment (MEDIUM velocity range setting)..... | 97  |
| Table 4.5: Summary of the speckle pattern motion measurements and speckle gains.....   | 125 |
| Table 4.6: Statistical summary of the ‘Deviation Factors’ for surface preparation<br>experiment.....                                 | 133 |
| Table 5.1: Statistical summary of the ‘Deviation Factors’ for output lens selection<br>experiment.....                               | 143 |
| Table 5.2: Statistical summary of the ‘Deviation Factors’ for operating distance<br>experiment.....                                  | 146 |
| Table 5.3: Statistical summary of the ‘Deviation Factors’ for slight defocus<br>experiment.....                                      | 151 |

## NOMENCLATURE

|                 |   |
|-----------------|---|
| $A$             | - Theoretical beam curve-fit scaling factor   |
| $C_V$           | - Laser calibration factor                    |
| $D$             | - A/D converter digital range                 |
| $DF$            | - 'Deviation Factor'                          |
| $\overline{DF}$ | - Scan group Mean Deviation Factor            |
| DFL             | - Scan group for counter-clockwise defocus    |
| DFR             | - Scan group for clockwise defocus            |
| D1              | - Scan group for coherence distance           |
| D2              | - Scan group for intermediate distance        |
| $d$             | - Coherence repeat distance                   |
| $d_s$           | - Typical speckle diameter                    |
| $d^*$           | - Intermediate repeat distance                |
| $F_c$           | - Carrier frequency                           |
| $F_d$           | - Doppler frequency                           |
| $F_{out}$       | - Output frequency                            |
| $f$             | - Operating frequency                         |
| $f_c$           | - Filter cut-off frequency                    |
| $G$             | - Laser optical unit demodulation filter gain |

|           |   |
|-----------|---|
| $g(x)$    | - Free-free theoretical beam equation                 |
| $h_c$     | - Harmonic amplitude calibration                      |
| $i$       | - Row number  |
| $j$       | - Column number                                       |
| $k$       | - Scan group number                                   |
| $l$       | - Total number of scan rows                           |
| L.R. Lens | - Scan groups for Long Range lens                     |
| L1..L6    | - Scan groups for the LOW velocity range setting      |
| $m$       | - Total number of scan columns                        |
| M1..M8    | - Scan groups for the MEDIUM velocity range setting   |
| $n$       | - Total number of scans                               |
| $\bar{N}$ | - Noise basis mean                                    |
| P1..P7    | - Scan groups for Surface Preparation experiment      |
| $p_i$     | - Orthogonal polynomials                              |
| $R$       | - Laser range scaling factor                          |
| REF       | - Scan group for reference focus setting              |
| $S$       | - Lock-in amplifier sensitivity setting               |
| $SG$      | - 'Speckle motion gain'                               |
| $SL$      | - Number of spectral lines used in DFT-IDFT algorithm |
| $SSE$     | - Sum of squared error                                |
| S.R. Lens | - Scan groups for Short Range lens                    |

|                |   |
|----------------|---|
| $s_d$          | - Speckle motion span                         |
| $s_i$          | - Orthogonal polynomial equation coefficients |
| $U$            | - Units conversion                            |
| $W$            | - Weighting factor                            |
| $X$            | - Percentage of high frequency content        |
| $x_{ij}$       | - Observed experimental velocity value        |
| $\hat{x}_{ij}$ | - DFT-IDFT fitted velocity values             |
| $Y$            | - Number of standard deviations above mean    |
| $\lambda$      | - Wavelength of Helium-Neon laser light       |
| $v$            | - Surface velocity                            |
| $\Phi$         | - DFT-IDFT fitted curve data                  |
| $\sigma_N$     | - Noise basis standard deviation              |

# CHAPTER 1

## INTRODUCTION

In the design and redesign of structures, it often becomes necessary for the design engineer to accumulate as much data on the dynamic characteristics of a structure as possible. Such significant characteristics may be the identification of the natural frequencies and the operating shapes. Velocities or deflections that occur when exciting the structure near those natural frequencies are also of critical importance. Experimental modal analysis (EMA) has historically provided methods to obtain such data. This information is then very helpful in a new design or in the modification of a current structure.

The ability to gather the velocity or mobility data from a vibrating structure has recently become more advanced and simplified by the use of laser technology. The laser Doppler technique as described by Drain [1] has been adapted and applied into such commercially available instruments as a laser Doppler vibrometer (LDV) and a scanning laser Doppler vibrometer (SLDV). The use of an SLDV system can yield data that contains a spatially dense velocity matrix in a short time period, in some cases allowing in excess of 65,000 measurement points in less than 20 minutes [2].

Without the use of such an instrument, the alternative method of data gathering would require the experimentalist to attach a piezoelectric accelerometer to the structure on as many points as are considered adequate to prevent spatial aliasing of the data. Of course, one is never sure of the structural complexity of the experimental responses so retrospective analysis of the measured responses allow the experimentalist to determine whether more data needs to be taken. Additionally, the use of an accelerometer to gather EMA response data would add an undesired mass to the structure. In this manner, the SLDV system can be considered a non-contacting and non-destructive method of obtaining such data. The SLDV also lends itself to portability and to ease of use in the field. Data from the instrument can also be processed in conjunction with graphical output giving the experimentalist a visual feel for the response of the structure. When one considers the preceding, some of the advantages of the SLDV system become obvious.

As the use of such an instrument gains popularity, the ability to optimize the results obtained from the SLDV become an ever growing concern.

## **1.1 BACKGROUND AND MOTIVATION**

In broad terms, an SLDV system can essentially be broken into two major components: the laser optical unit, and the scan control/data acquisition system. The laser optical unit contains the actual laser, the optical elements, and electrical components needed to spatially position the laser beam. The scan control/data acquisition system

consists of the equipment and software needed to manipulate the scan mirrors and to acquire the velocity data.

The Structural Imaging and Modal Analysis Laboratory at Virginia Polytechnic Institute and State University (Virginia Tech) in Blacksburg, VA is currently involved in the use, analysis, and optimization of such an SLDV system. In 1991 the laboratory received the second of two versions of an SLDV system from OMETRON, Ltd., London, England. Specifically, the Vibration Pattern Imager (VPI) system allows for the measurement of velocity or mobility data from a vibrating structure. The VPI system measures velocity data in the line-of-sight of the laser beam. Additionally, the VPI system also allows for the rapid repositioning of the point of measurement in order to gather a spatially dense matrix of data in a relatively short-time period. As mentioned above, the VPI system allows for the graphical observation the data. Several real-time signal outputs are also available from the SLDV system.

There are two SLDV systems currently in use at Virginia Tech, both sharing the same laser optical (VPI Sensor) unit. The difference between the two systems lies in the scan control/data acquisition system. In one configuration, the VPI Sensor unit is controlled with an Hewlett Packard (HP) 380 workstation utilizing the Ometron 9000 Series software. Figure 1.1 shows the layout of the VPI system with this configuration.

The second configuration consists of the VPI Sensor with scan control/data acquisition via an Apple Macintosh (Mac) personal computer running LabView™



software with an internally developed program (GCI 3.2). Figure 1.2 shows the layout of the VPI system when scan control/data acquisition are obtained using the Mac.

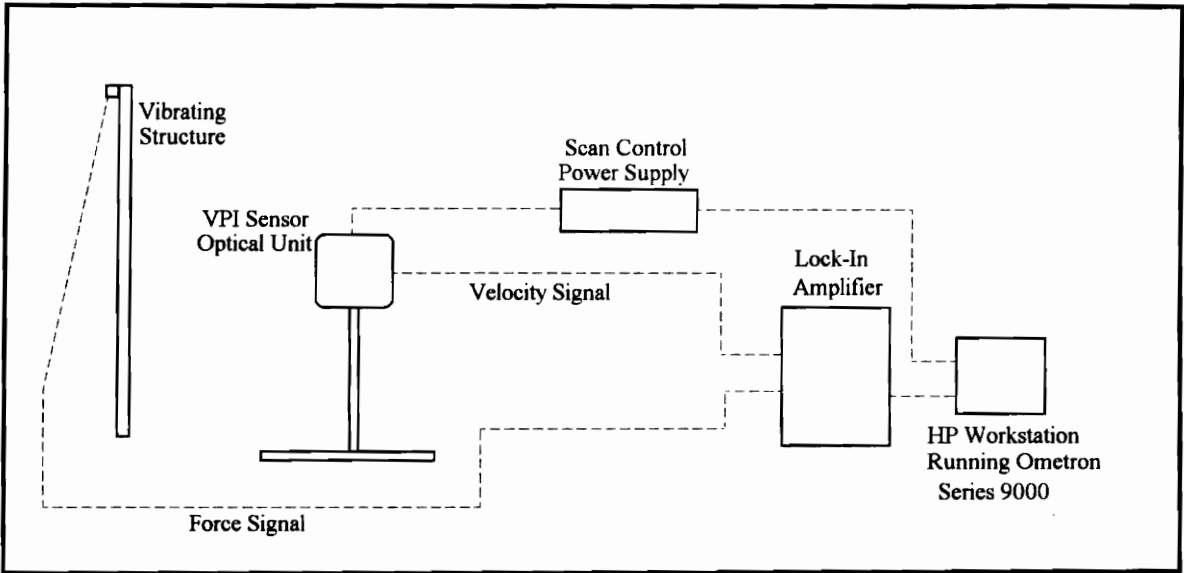


**Figure 1.1:** SLDV System, Data Acquisition and Scan Control via the HP.

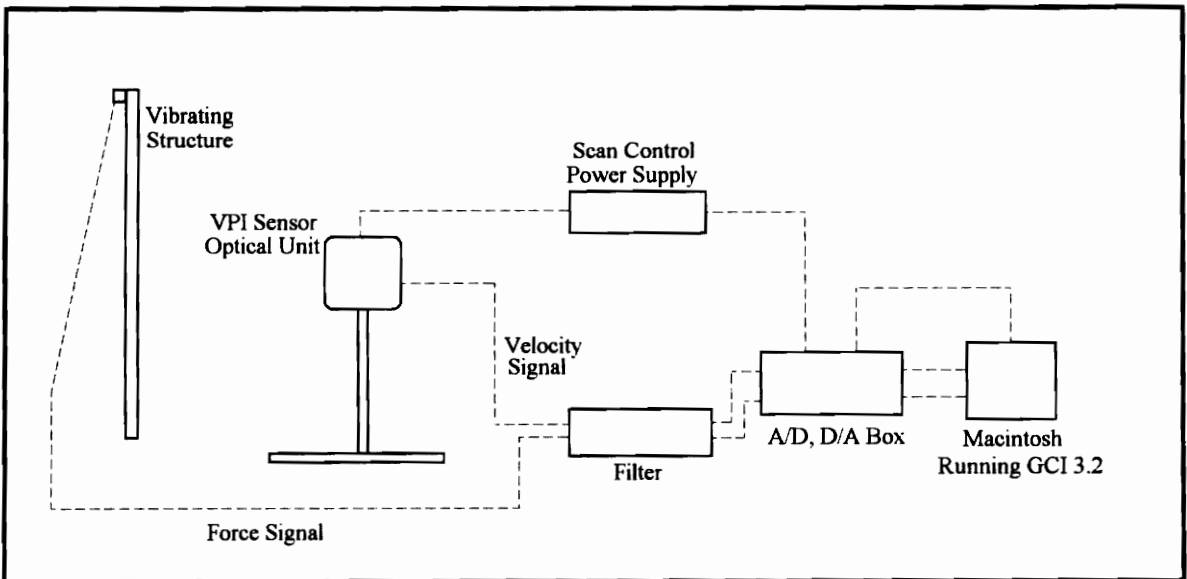


**Figure 1.2:** SLDV System, Data Acquisition and Scan Control via the Mac.

The reader should note that the experiments contained in this thesis were performed with Data Acquisition and Scan Control via the HP 380 utilizing the Ometron Series 9000 software configuration.

In the process of the employing the VPI Sensor, several users have noticed that the raw data gathered with the instrument contains some areas of seemingly erroneous data which did not seem consistent with the rest of the scan matrix. Specifically, the authors noted that the areas of noise seem to occur more predominately at areas of maximum velocity response. For the purpose of this thesis this noise will be referred to as *laser noise*. Two examples of laser noise are shown in Figures 1.3(a) and 1.3(b). Figure 1.3(a) shows the response shape, velocity data points, and corresponding residuals for a vibrating steel beam. Figure 1.3(b) shows raw velocity data versus beam position for a similar beam.

In these cases, the noise problem was “fixed” by either averaging, median filtering, or otherwise statistically smoothing the scan data. This may have provided smoother plots and clear graphical representations, but may not have correctly addressed the apparent noise problem. A concern also arises regarding the fact that any biased nature of the noise may result in a smoothed curve which may not accurately model the surface velocities. More specifically, a better understanding of the source of this noise and the possible factors which may affect its occurrence are necessary in order for optimal use of the SLDV system.

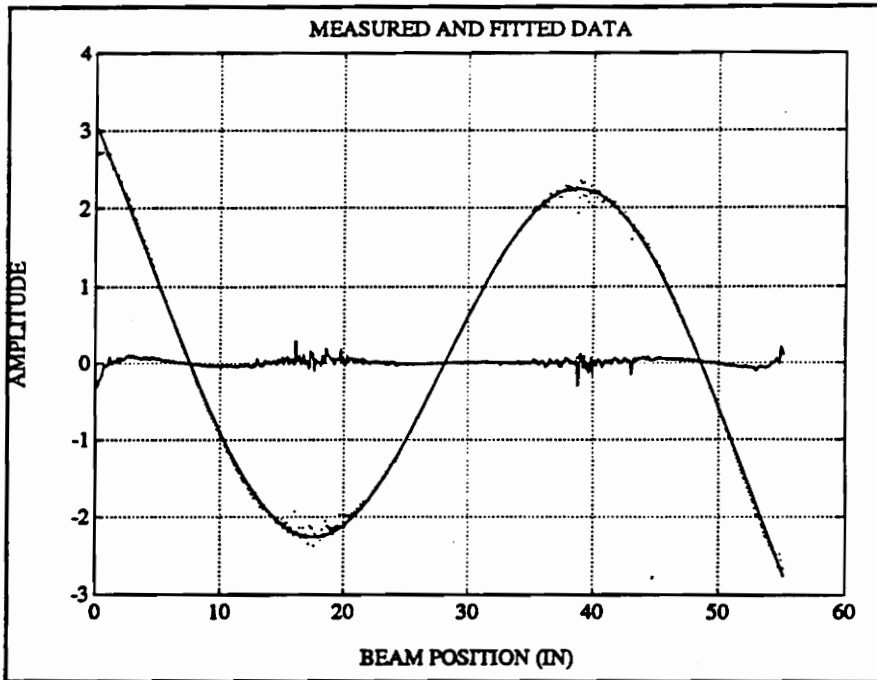


**Figure 1.3(a):** Velocity scan data showing noise occurring in areas of maximum absolute velocity (after Archibald [3]).

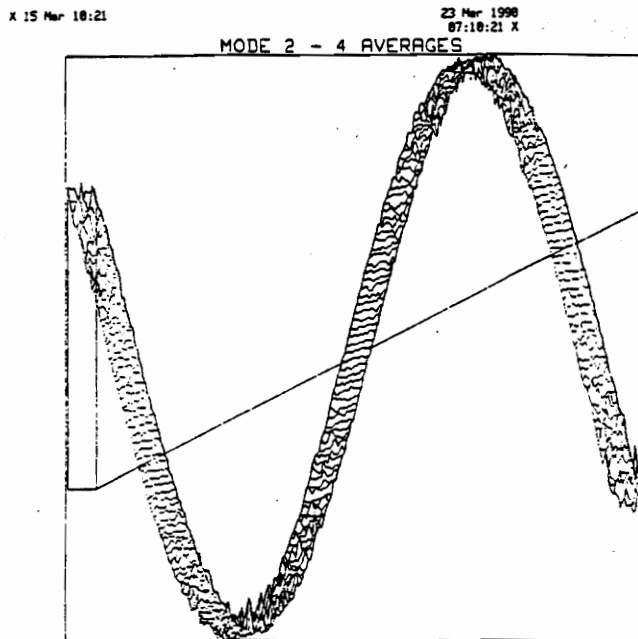


**Figure 1.3(b):** Velocity scan data showing noise occurring in areas of maximum velocity response (after Wicks *et. al* [4]).

## ***1.2 PROBLEM STATEMENT AND DOMAIN***

In its most basic form, the SLDV is simply a tool. And as with any other tool, it is imperative that the user know how to use it. More specifically, the user must have a basic understanding of the controlling parameters, idiosyncrasies, and limitations of that tool. Optimal use of the SLDV system would require the user to have knowledge concerning the source of any potential laser noise problems. In addition, the user should have knowledge concerning any parameters which may have a bearing on the quality of scan data taken with the SLDV system. The user may also desire to know how to adjust each parameter, the extent to which each parameter affects the limitations of the tool, and the relative sensitivity of the system to those parameters.

### ***1.2.1 PROBLEM DOMAIN***

The VPI Sensor operator's manual, supplied to Virginia Tech by Ometron Ltd., indicates that there are four variables which can affect the quality of velocity measurements taken with an SLDV system [5]. These variables are:

- Laser Speckle Noise
- Working Distance
- Measuring Beam Focus
- Test Surface Preparation

### **1.2.1.1 LASER SPECKLE**

Laser speckle, which will be covered in more detail in Chapter 2, refers to the interference of the scattered light from a surface that is rough as compared to the wavelength of the illuminating light source. This pattern resembles a combination of light and dark specks and has a distinctly granular appearance. Speckle is inherent to a diffusely reflective surface illuminated by coherent light, and in the case of the highly coherent He-Ne laser source used in the VPI Sensor, speckle-pattern is an inevitable occurrence.

### **1.2.1.2 WORKING DISTANCE**

The working distance indicates the distance from the laser optical to the structure of interest. There is a 'coherent length' inherent to all light sources. Because the SLDV is based on the utilization of light interference, more specifically laser light interference, coherence plays an important role in the operation of an SLDV system. The VPI Sensor utilizes a 2 mW (nominal, output  $\leq 1$  mW) Helium-Neon (He-Ne) laser source, and its properties require that a set of coherence repeat distances be specified. These coherent repeat distances result from the multi-mode characteristic of the particular He-Ne laser used in the VPI Sensor. The particular numerical values are derived from the geometric characteristics of the laser cavity [6]. The VPI Sensor Operator's Manual theorizes that

these distances should result in increased Doppler signal stability and increased quality in data measurements. Equation (1.1) indicates that this relation for the VPI Sensor [5] is:

$$d = 66.9 \pm n \times 8.3 \text{ in } (1700 \pm n \times 210 \text{ mm}), n = 1, 2, 3, \dots \quad (1.1)$$

Equation (1.2) indicates the resulting intermediate distances [5]. Operation at these distances is said to result in less optimal and less stable Doppler signal amplitudes.

$$d^* = 71.1 \pm n \times 8.3 \text{ in } (1805 \pm n \times 210 \text{ mm}), n = 1, 2, 3, \dots \quad (1.2)$$

### **1.2.1.3 MEASURING BEAM FOCUS**

The measuring beam focus is an indirect measure of the size of the measurement point on the structure. Transient focus level readings can be obtained by viewing a LED monitor displayed on the side on the VPI Sensor optical unit. This monitor reads full scale at 100 units. These readings are an indication of the corresponding Doppler signal amplitude (the reader should note that this signal will be discussed in more detail in Chapter 3). The VPI Sensor Operator's Manual reports that a focus reading of 30 units or greater will result in satisfactory operation of the SLDV system.

### **1.2.1.4 TEST SURFACE PREPARATION**

Test surface preparation indicates the texture, color, and/or other condition of the surface of the structure under investigation. As mentioned before, the SLDV system

operation is based on the interference of laser light. Because of this, laser light back scattered from the structure is the source of the vibrating information. According to [5] the VPI Sensor is designed to tolerate a wide range of test structure surfaces. Use of ARDROX 9D6F<sup>1</sup>, or similar developer spray that covers the structure surface with a fine layer of white particles, is recommended by Ometron. If better reflection is required, Ometron suggests the use of a retroreflective tape or paint such as 3M's Scotchlite™ Reflective Liquid.

Of these parameters, all but one can be controlled by the user. Working distance, measuring beam focus, and test surface preparation are all left to the user's discretion in the initial experimental setup using an SLDV system.

### ***1.2.2 PROBLEM STATEMENT***

As mentioned above, several experimentalists have noticed areas of noise in raw velocity data acquired using the SLDV system. Although the extent of the effects of the parameters listed above have not been determined, speckle-pattern motion is most commonly considered the culprit. An attempt is made in this research to examine the common claims made concerning the effects of these parameters.

The problem addressed by this thesis centers on the characterization of the areas of noise noted above. An attempt is also made to “zero-in” on the source of the laser noise.

---

<sup>1</sup> ARDROX 9D6F is manufactured by ADROX PYRENE Ltd., Ridgeway, Iver, Buckinghamshire SLO 9JJ, England.

It should be mentioned that the parameters above could all constitute an immense set of experiments each in and of themselves. The author has attempted to examine the parameters within the context of practical operation of the SLDV. That is to say, the extent of the experiments, with respect to each parameter, has been determined based on typical “scan” experiments of a vibrating structure.

### **1.3 OBJECTIVE**

The overall objective of this research is perform a preliminary investigation regarding the characterization and potential sources of the laser noise. Areas in which the noise tends to occur and any discernible patterns are also noted and/or confirmed. In addition, an investigation of the corresponding speckle pattern motions are investigated. Subsequent theories concerning the potential sources of this noise are also presented. The information presented in this thesis is designed to aid the laser Doppler vibrometer industry in determining which factor(s) have a major bearing on the quality of scan data taken with the SLDV system. Subsequently, supplementary experiments suggested by Ometron, Ltd. investigating some of the user-controlled setup parameters previously theorized as potential sources of the laser noise may shed some light concerning their relative importance and give the novice user a set of guidelines that will help him or her to use the SLDV system more optimally than previously possible. Also, some recommendations on future improvements of the VPI Sensor will be made, along with



proposals for future research. The results and conclusions of this thesis should open doors and provide direction for future investigation concerning the determination and minimization of the source(s) of the laser noise.

## **1.4 APPROACH**

As mentioned above, previous use of the SLDV system identified areas of noise which seemed to occur predominately in the areas of maximum velocity response. In addition, the most common explanation concerning the source of this noise is speckle pattern motion. Because this is a preliminary study and the source of the laser noise is previously unknown and unstudied, the experiments presented in this thesis are exploratory and, thus, progressive in nature. That is to say that the results from one experiment lead to investigation and theories concerning the next set of experiments.

In general, the progression of the experiments presented in this thesis are as follows. First, an investigation designed to confirm the spatial distribution of the laser noise is performed. This experiment is also designed to study any velocity response dependencies or characterizations intrinsic to the SLDV system. The results from the above experiment lead to the investigation of the spatial distribution of the corresponding speckle pattern motions. This experiment then leads to the investigation of the effect of surface preparation of the experimental structure.

In the midst of the above investigations, and per the request of Ometron, Ltd. [7], a set of supplementary experiments were performed to determine the effects of a set of user-controlled parameters on the observed laser noise. Those parameters are:

- Coherence Repeat Distance
- Slight Defocus of Laser Measuring Beam
- Output Lens Selection

A typical structure is desired which, among other reasons, would allow the author to duplicate previously observed occurrences of the laser noise. A long slender steel beam is chosen as the experimental structure (the reader should note that the specific reasons for the experimental structure choice are presented in Chapter 3). The following is a general description of experimental approaches which apply to most of the experiments utilized in this study. It should be stressed that a more specific description of the experimental methods and experimental setups are discussed in Chapters 3, 4, and 5:

- Velocity data is taken via the SLDV near a resonance frequency using the resonance-dwell technique.
- A curve-fitting algorithm is employed in order to obtain a functionalized velocity profile.
- Plots showing the residuals of the full-scan matrix from the functionalized velocity profile curve are also presented.

- An author-defined statistical representation of the total error of the scan matrix from this profile is calculated.

Following this procedure, comparisons can then be made concerning the relative effects of the parameters with respect to the statistical representation (which will be an indication of the overall quality of the scan data).

## **1.5 ORGANIZATION OF THESIS**

In order to gain proper perspective with regard to the use of the SLDV system, it is necessary to explore the development of the SLDV and the current applications of this system. Chapter 2 provides a examination of the current literature pertaining to these areas. In addition, a section of the chapter is devoted to the speckle-pattern phenomenon mentioned above.

The experimental methods and techniques employed by the author are described in detail within Chapter 3. Also included is a discussion on the data analysis methodologies and any applicable assumptions made in the experimental and analysis processes. These procedures are then illustrated using a typical example.

Chapter 4 represents a breakdown of the progression of experiments. For each experiment a description of the experimental setup and the succeeding results are presented.

Chapter 5 contains experimental descriptions and results for the supplemental experiments presented in this thesis.

Chapter 6 contains a summary of the research, along with conclusions and recommendations. Recommended changes to the SLDV system, as well as recommendations for future work are then presented. Recommendations are then given concerning a set of optimal-use guidelines for the SLDV.

## **CHAPTER 2**

### **LITERATURE REVIEW**

This chapter presents some of the work that has been completed in areas that are pertinent to the topics covered in this thesis. A review of the literature demonstrates that although there has been extensive research utilizing LDV and SLDV systems in a practical sense, there has been less work done concerning the effects of the parameters mentioned above on data gathered with these systems. Hence, this chapter offers a review of some of the literature regarding the development and usage of SLDV systems. Special attention is given to the development and applications of the SLDV system in use at Virginia Tech. Additionally, because the speckle effect is most commonly cited for inconsistencies in LDV and SLDV data, a section of this chapter is an introduction to the speckle pattern and speckle pattern motion phenomenon.

#### **2.1 LASER DOPPLER VIBROMETRY**

The advent of the laser (*Light Amplification by the Stimulated Emission of Radiation*) in the 1960's [8] has uncovered many avenues of research and technology. Specifically, the advantages of a low-power laser lend itself to many commercial and

industrial uses. Hecht [8] describes some of the practical advantages of a low-power laser, including the following:

- Lasers produce well-controlled light that can be focused precisely onto a small spot
- Laser light travels in a straight line
- Lasers generate coherent light
- Helium-Neon and Diode lasers produce steady powers for tens of thousands of hours or more
- Laser light covers only a narrow wavelength range

It was these advantages that lend to the initial development of Laser Doppler Anemometry (LDA) and later Laser Doppler Vibrometry (LDV).

### ***2.1.1 DEVELOPMENT***

The physical premise on which both LDA and LDV are based is the Doppler shift effect. This effect, common in acoustics, explains the phenomenon that occurs when either the source or the receiver of sound (or light) waves is moving relative to the other. A simple example of the Doppler effect is the different frequencies that occur when a car approaches and then passes a listener.

By realizing some of the advantages of a light source such as the laser, experimentalists have envisioned utilizing the Doppler effect to measure the velocity of fluids or the surface velocity of a vibrating structure. The optical configuration would require simply aiming a laser at the moving target and then measuring the Doppler shift resulting from the motion. Unfortunately, in practice it is not quite this simple. The velocities that are usually desired are relatively small compared to the speed of the laser source (the speed of light). For this reason, some sort of optical beating or heterodyning of the Doppler is required. This is usually accomplished by combining the Doppler shifted light with a reference beam of known frequency. Additionally, in order to determine the sign (or direction) of the motion, a constant shift of the frequency of the reference beam is needed. In practice this is accomplished in several ways. Diffraction gratings, Bragg cells, rotating scattering discs, and electronic shifting of the reference beam are common methods employed to remove this ambiguity concerning the direction of motion. L. E. Drain [9] lays out the theory behind many configurations utilizing laser light to measure the motion of fluid flow and vibrating structures. Of particular interest in the case of this research is the section pertaining to the measurement of the velocity of solid surfaces.

Halliwell [10] describes a laser Doppler vibrometer developed using a rotating scattering disc in order to frequency-shift the reference beam. Laboratory tests utilizing a 15 mW He-Ne laser are presented and a more portable system using a 2mW laser source is theorized. Comparisons to systems using Bragg cells and rotating diffraction gratings are presented and the resulting advantages of the rotating scattering disc are given. These

advantages are described including that the rotating scattering disc results in a self-aligning system and that when rigidly secured, the system is insensitive to external vibrations. Pickering *et al.* [11] further develops this same system and presents a more specific explanation of the underlying theory. Additionally, example applications of the vibrometer are presented. These include vibration measurements of a circular saw cutting granite and the “tweeter” from a loudspeaker system.

An example of frequency-shifting by the use of Bragg cells is presented by D’Emilia [12]. A single-point laser Doppler vibrometer prototype is developed and compared to an unnamed commercially available vibrometer. This prototype was developed by the author in order to achieve an inexpensive architecture for the optical and electronic components of an LDV system. The results indicate good agreement with the commercially available system resulting in amplitude differences in the range of  $\pm 3\%$ .

The development and use of a scanning LDV is discussed by Barker [13]. The author explains the theory and operation behind the initial version of the Vibration Pattern Imager (VPI) 9000 system, a commercially available SLDV from Ometron, Ltd., London, England. Three discrete measuring ranges are incorporated in the VPI system: 0-8, 0-80 and 0-800 mm/s. Furthermore, the author explains the incorporation of raw or smoothed data graphical display allowing for filled grid, open or filled contour, and isometric plot data presentation options. A later version of this SLDV system is currently employed by the researchers in the Structuring Imaging and Modal Analysis Laboratory at Virginia



Tech. For this reason, the specific theory behind the use of this SLDV will be covered in more detail in Chapter 3.

### **2.1.2 EXAMPLE APPLICATIONS**

As the advantages of LDV and SLDV systems become more evident, their applications have become broad-based. Examples of some of the recent applications of these systems include determining global estimates of natural frequency and modal damping coefficients [14], obtaining a non-contacting “full-field” determination of bending strains [15], utilizing a dual-beam laser vibrometer to extract three degrees of freedom (one dynamic translational and two dynamic rotational) from a vibrating structure [16], and using three lasers to extract six degrees of freedom from a vibrating structure [17,18].

Of particular interest in the scope of this research are applications utilizing the SLDV system used by the Structural Imaging and Modal Analysis Laboratory at Virginia Tech:

Yienger *et al.* [19] used the SLDV system in a resonance-dwell modal test experiment. The experiment was performed on the door of a Cadillac automobile in both the open and closed positions. Scans were taken at two separate frequencies and results show that the location of the peak vibration responses shifted with respect to the boundary conditions (i.e. open vs. closed door position). This proved to be an important step in order to determine the placement of localized damping for vibration and noise control.

The SLDV system has also been used to extract three degrees of freedom (3 DOF) from a vibrating structure [20]. In this case the 3 DOF obtained were translation in the x, y, and z directions. The extraction of these translations were accomplished by positioning the SLDV in three separate positions and extracting the velocity information resulting from the geometric configuration.

An extension of the research by Abel [20] is contained in a combined effort involving several researchers from Virginia Tech. These researches have developed a method utilizing the SLDV to extract 6 DOF from a vibrating structure.

Experimental spatial dynamics modeling (ESDM) is another avenue of research paralleling that listed above. ESDM [21] utilizes SLDV data in the finite element formulation of a continuous 3-D velocity response field. Additionally, the author has developed advanced visual software in order to animate the spatial dynamics model. Subsequent research has yielded the development of experimental spatial energy modeling (ESEM) which uses the results from ESDM to solve for the power flow through a structure [22].

### ***2.1.3 MEASUREMENT DATA QUALITY***

Most of the literature concerning the development and applications of LDV and SLDV systems contain little information on the quality of the data acquired with these systems and the factors that may affect those measurements. Some of the literature that does address these issues are presented below.

Realization of the importance of a vibrating surface's ability to generate enough back scattered light can be discovered in the work of some researchers. These papers present studies of the relative reflectivity of different working surfaces. Bruce and Fitzpatrick [23], whose primary area of expertise is mining geophysics, present an early development of a single-point laser Doppler vibrometer. The interferometric technique is described and demonstrated using a 4 mW He-Ne laser. Because earlier versions of similar interferometers required the use of mirror-like finishes normal to the direction of the sensing beam, the authors investigate the ability of their system to measure the motion of various rough unprepared surfaces. A table of signal-to-noise ratios is presented for six different surfaces at two operating distances, 5 meters and 100 meters. The authors conclude that the signal-to-noise ratios for all surfaces are better at 5 meters. Additionally, the surface rank in decreasing signal-to-noise ratio are Scotchlite™, sandstone, oil shale, granite, coal, and soot. Lewin and Siegmund [24], researchers at Polytec<sup>2</sup>, include the carrier signal strengths created when measuring various surfaces with their LDV system. The surface rank in decreasing order presented by the authors is Scotchtape, insulating tape at 90°, blank aluminum, white paper, and insulating tape at 60°. Another point of investigation included in this paper is the determination of an optimum laser output beam power split ratio, which is the percentage of power used in the output beam (with the remainder of the power contained in the reference beam). The authors report an optimum split ratio of 93% going to the output beam, for a surface reflectivity of 1%.

---

<sup>2</sup> Polytec GmbH, Polytec-Platz 5-7, 76337 Waldbronn

Drain [9] in his theoretical discussion concerning laser interferometry for solid surface vibration measurement explains that in order to obtain the best Doppler signals the illuminating measuring spot should be as small as possible so that coherence is maintained over a larger detector aperture. An optimal Doppler signal would be obtained if the detector were to receive just one bright speckle. He goes on to remark that if the surface were to move sideways illuminating a new area (giving rise to a different speckle pattern), the amplitude and phase may become randomized and thus producing errors. This, the author continues, may become a problem in the study of vibrations that contain appreciable sideways components. Increasing the measuring spot size, according to the author, can lessen these effects. Albeit he notes that this may increase the sensitivity to surface tilt.

According to the VPI Sensor Operator's Manual [5] the FM-demodulation circuits used to derive an analog velocity waveform from the Doppler signal in this SLDV require a certain amplitude threshold. This value has been approximated as 300 to 400 mV pk-pk [25]. Below this value, the resulting velocity will suffer from what is referred to as "drop-out". Drop-out is said to result from insufficient Doppler signal amplitude which, in turn, is said to result from unfavorable operating conditions. These include operating in between optimum distances, using a test surface with poor reflectivity, misfocus of the measuring beam, or operation at an incorrect operating range. A typical representation of drop-out and the corresponding Doppler signal are shown in Figure 2.1.

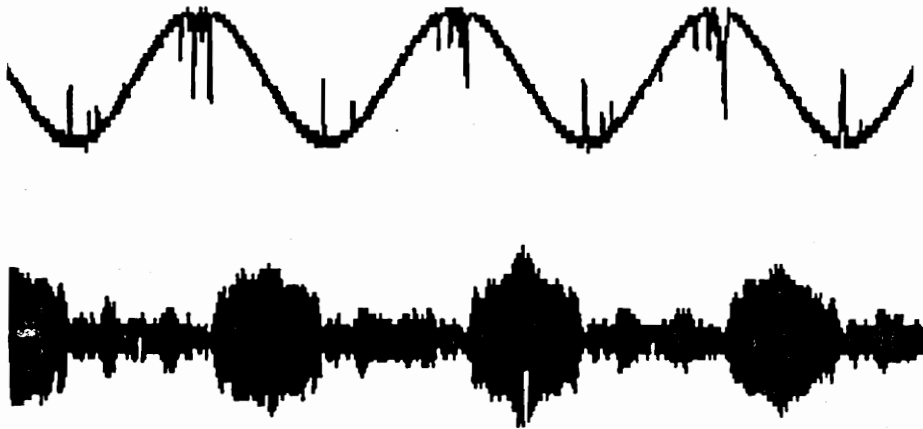


**Figure 2.1:** Velocity signal versus time (top) suffering from drop-out and the corresponding Doppler signal amplitude versus time (bottom).

Bream *et al.* [26] reiterate that optimum performance of the SLDV system used in their research is dependent on sufficient Doppler Signal amplitude. The factors indicated by the authors affecting this amplitude include working distance, field of view, measuring beam focus, surface preparation, and laser speckle noise.

Wicks *et al.* [4], in an early application of their SLDV system, present several scans of a slender steel beam vibrating with simulated free-free end conditions. Of particular note is the noise noticed by the authors at large amplitude responses (see Figure 1.4 in Chapter 1). Later, Kochersberger *et al.* [27] speculate that these data inconsistencies are due to laser speckle, low reflectivity, and/or uncorrelated noise in the measurement system. Mitchell *et. al* [28] further addresses this situation by explaining the speckle phenomenon produced by the laser, and its dynamic effects on the optical

detectors. In line with Drain's earlier contention, the authors explain that during vibration the point illuminated by the laser is not identical through the entire period of motion. This results in the detector "seeing" the motion of the speckle pattern over the course of the periodic motion of the structure. The authors speculate that this speckle pattern motion will induce noise into the velocity measurements.

Other authors seem to dispute the ability of some LDV and SLDV systems to make any velocity measurements in the presence of speckle. Wagner [29] contends that when a random (speckle) pattern is interfered with a plane (reference) wave, the optical detector would not be able to distinguish enough variation in (Doppler) intensity corresponding to the surface displacement. This seemingly calls into question the ability of a Michelson interferometer to derive a signal from a vibrating structure if the detector aperture is averaging over a large number of speckles.

This same theme is repeated by Nagy and Blaho [30] in their study of ultrasonic acoustical waves. They describe that ideally one hopes that when data is taken on a diffusely reflecting surface, the speckle pattern would produce instances where the photodiode is covered by a single bright speckle. Unfortunately, this is not always the case. In some instances, the diode is said to be covered by a completely dark speckle. When this occurs, the threshold sensitivity inherently fluctuates and the detector's signal-to-noise level greatly decreases. Because this phenomenon is unavoidable with the use of lasers, the authors present a method of using speckle to "enhance the process". A 'random speckle modulation' technique is theorized and applied whereby to assure that a

bright speckle falls on the photodiode, the speckle pattern is intentionally modulated. This technique is applied using a double-lens focusing system. The first, smaller, lens is used to expand the Helium-Neon laser source beam, and the second, larger, lens is used to focus the expanded beam to a diffraction limited spot on the object's surface. The method involves mounting the first lens on a spring cantilever which is vibrated at its resonance frequency. This motion, which is dominantly normal to the surface with some lateral wobbling, will in effect move the measurement point around the reference point on the specimen's surface. The theory is that this modulation will transfer the highly uneven spatial distribution of bright speckles (inherent in the speckle pattern) into a similarly uneven time distribution of bright speckles. The interferometer will then "see" these bright speckle 'flashes' long enough to trigger the transmitter. The authors note that although this technique can not increase the peak sensitivity of the interferometer, it can maintain this peak sensitivity everywhere on a diffusely reflecting surface. Accordingly, the authors found as much as 5-10 times improvement of optical sensitivity using this method.

The term "pseudo-vibration" is introduced by Rothberg *et al.* [31] in their investigation on the effects of speckle motion caused by non-normal to the surface motions (tilt, in-plane motion, and rotation) using a rotating diffraction grating LDV. Three separate motions of the surface, which theoretically contained no nominal out-of-plane vibrations, were measured with the LDV configured for normal-to-surface vibrations. It is found that spurious information may be introduced into the output

spectrum which is indistinguishable from normal-to-surface vibrations. This information manifests itself in pseudo-vibration peaks at the fundamental frequencies and subsequent harmonics for all three non-normal motions. This means that care must be taken in low-level vibrations, where the true out-of-plane vibrations may not be separable from the so called pseudo-vibrations. Additionally, the authors conclude that noise floors for systems like this one can not be determined without reference to the target surface dynamics.

Use of the LDV configuration that utilizes the rotating scattering disc introduces an additional noise problem that has been associated with the additional speckle motion formed by the scattering-disc. Wilmshurst and Halliwell [32] report that the noise floor of such an LDV is determined by speckle-noise caused by the rotating scattering disc. The method they term “speckle-noise cancellation” requires recording the response without vibration present, and then subtracting this “noise” from the vibration output. Limitations of this method include its intolerance to any changes in measuring beam position, which would introduce a different illumination area (and hence different speckle pattern) on the test surface, and its requirement for ability to record the response in the absence of vibration. The latter may be a problem in some industrial applications where it is not possible to cease the vibration.



## **2.2 LASER SPECKLE PATTERN PHENOMENON**

As demonstrated in some of the literature review discussed above, speckle is a common term in LDV and SLDV discussions concerning data quality. Speckle, or more appropriately speckle patterns, seem to be a misunderstood or otherwise unclear topic. It is the purpose of this section to help define and explain the speckle pattern phenomenon within the realm of laser vibrometry. Additionally examples of some positive applications of speckle being used to measure and to visualize surface displacements and vibrations are presented.

### **2.2.1 DEFINITIONS**

In the case of solid surfaces a *speckle pattern* can be defined as the random intensity distribution that is formed when coherent light illuminates an object with an optically rough surface. Figure 2.2 shows the appearance of a laser speckle pattern. The granular appearance apparent in the figure is created by the constructive and destructive interference of the coherent light scattered by the optically rough surface within the illuminated area of the structure. The term “optically rough surface” refers to the size of the surface roughness microtopology as compared with the wavelength of the illuminating source. The constructive and destructive interferences are created by the different path lengths and angles of reflection traveled by the scattered light due to the “optically rough” surface.

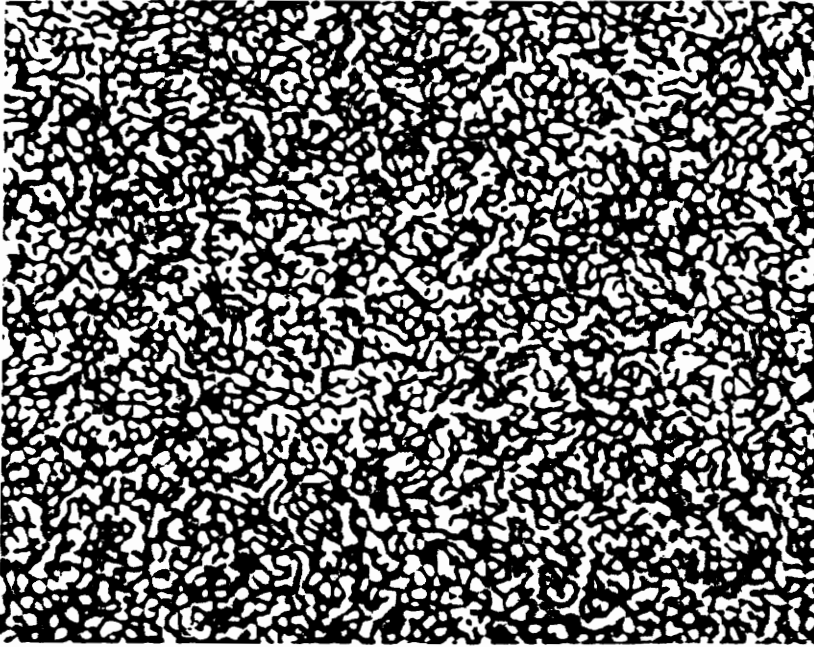


**Figure 2.2:** Example of a laser speckle pattern (after Dainty [33]).

For the purpose of this thesis, laser *speckle pattern motion* or *speckle motion* will be defined as the smearing, streaking, or otherwise blurring of a speckle pattern caused by structure or laser motion. This can be caused by the relative rotation or in-plane translation of the illuminated area. In the study of vibrating structures it can be demonstrated that laser speckle pattern motion can occur when the vibration of the structure results in a different area of illumination through the structure's periodic motion. Rothberg *et al.* [31] define three types of target motion which result in speckle pattern motion: tilt, in-plane motion, and rotation. Tilting of the target surface is claimed to produce an in-plane displacement on the detector plane. Small in-plane motions are said

to amplitude and phase modulate the detector output. Larger in-plane motions, which involve significant changes in the illuminated speckle population, are said to result in what is termed as speckle “boiling”. Speckle boiling results in speckles varying in an independent fashion at each point in the receiving plane.

Most, if not all, surfaces encountered in the practical operation of an LDV or SLDV are optically rough surfaces and will diffuse a speckle pattern when illuminated by the laser source. Therefore, speckle is presumably unavoidable and in cases requiring surface velocity measurements, speckle is necessary for operation of the laser vibrometer system.

### ***2.2.2 EXAMPLE APPLICATIONS***

The laser speckle effect has been used in a positive sense in the measurement of displacement and vibration. Researchers have found that the capturing of the full spatial representation of the laser speckle pattern effect resulting from a vibrating structure presents several opportunities for structural dynamics evaluation. Some examples of the use of speckle to extract information from vibrating structures are given below.

Hopkins and Tidbury [34] present the use of laser speckle to view the operating shape of a vibrating van panel in real-time. In this application, the laser beam is focused such that it illuminates the large area under investigation on the panel. Subsequent viewing, at an intermediate plane, of the speckle pattern produced by the measuring beam

on the panel will display a series of streaks and stationary speckle points. A camera can be used to capture the pattern. These patterns will represent the ridges, peaks, and saddle-points of the operating shape. Peaks and saddle points are shown as stationary speckle, whereas the ridges are shown as speckle streaks. Although the authors concede that this method does not yield quantitative amplitudes directly, one can visually identify the points of maximum amplitude in real-time.

Quantitative structural dynamics information can be obtained from a vibrating structure by employing Electronic Speckle Pattern Interferometry (ESPI). Generally speaking, this interferometric configuration splits the laser source beam into a measuring beam, which is expanded to illuminate the entire structure under investigation, and a reference beam. These two beams are then combined into an interferogram which is referred to as a *specklegram*. This specklegram can be observed using a vidicon and a T.V. camera and/or processed electronically. Shellabear and Tyrer [35] use a similar configuration with three different illumination geometry's to extract the orthogonal components of a vibration amplitude. Case studies are presented examining bending vibrations in a beam, and cylinder volume, turbine blade, and flat plate vibrations. Limitations of the ESPI system observed by the authors include a requirement for stability between the object and the recording system; an upper limit on observable amplitudes; and surface illumination limitations.

Digital Speckle Pattern Interferometry (DSPI) differs from ESPI in that the specklegram is recorded with a CCD camera and digitally processed as opposed to being

recorded by an electronic camera and processed by analogic filters. Slangen *et al.* [36] present an example of the use of DSPI to visualize the mode shape of a vibrating object. In the case of their investigation only the amplitude of vibration is obtainable using this technique. Several mode shapes of an aluminum cantilever plate are presented. Conclusions include good agreement with finite element results.

For further information on laser speckle and some its uses the reader is directed to the books of Dainty [33] and Fraçon [37]. This literature gives more detailed explanations of laser speckle, including extended discussions concerning applications and statistical properties.

## **2.3 SUMMARY**

The invention of the laser has produced several opportunities in the study of structural dynamics. By employing interferometric techniques, the laser can be used to measure the velocity of vibrating structures by analyzing the signals resulting from the Doppler effect. This type of instrument has been applied to a broad range of industrial- and research-based vibration situations. Recent applications of LDV and SLDV systems include extracting 3 to 6 degrees of freedom, measuring the strain and power flow, and experimental spatial dynamics modeling of a vibrating structure. Some researchers have noted, demonstrated, or theorized the cause of inconsistencies that result in data taken with these systems. Laser detected pseudo-vibrations, velocity drop-out, and speckle

pattern motion have been mentioned as potential sources of these inconsistencies. Surface reflectivity, focus, and working distance have also been discussed as important parameters that may affect the quality of vibration data. The aforementioned speckle is a circumstance that is seemingly unavoidable when using a coherent light source such as a laser to illuminate a diffusely reflecting surface. Speckle, in fact, has been desired in some applications, such as speckle pattern interferometry, to measure and visualize the mode shapes of a vibrating structure.

The work presented in this thesis will attempt to examine the relative effects of some of the factors and phenomenon mentioned above on the quality of data gathered using an SLDV. It is hoped that some guidelines for more optimal use of the SLDV can be derived from the conclusions given in this research. In particular these guidelines should help to improve data gathered using the SLDV at Virginia Tech, and thus improve the data used in the specific applications described above.

## **CHAPTER 3**

### **EXPERIMENTAL METHODS**

In order to examine the effects of the parameters mentioned in Chapter 1, it is necessary to lay out the procedures and methods used to gather and analyze the data. As mentioned previously, the experiments presented in this thesis can be divided into a progression of exploratory experiments presented in Chapter 4 and the supplemental experiments presented in Chapter 5. A general experimental setup and data analysis procedure, which applies to most of the experiments, will be presented in this chapter so as to illustrate the overall methods and procedures used to analyze data taken with the SLDV. The specific experimental descriptions will be broken down and discussed in greater detail in Chapter 4.

This chapter is intended to explain the experimental methods and procedures used in the analysis presented in this research. The theory behind the SLDV system used in the research is presented in the first section. In the third section, the procedures used in the data analysis process are presented. The fourth section illustrates a typical example and the corresponding results are given. Finally, some underlying assumptions and remarks are given in the sixth section.

## **3.1 SCANNING LASER DOPPLER VIBROMETER**

As discussed in Chapter 1, there are two methods in use at Virginia Tech of acquiring data taken with the VPI Sensor optical unit. Because the research presented in this thesis was performed with constant communication and suggestions from Ometron, Ltd., the experiments presented here were performed using the HP Workstation/Ometron 9000 Series software configuration. (All subsequent references to the ‘SLDV system’ will refer to the VPI Sensor optical unit with the HP Workstation/Ometron 9000 Series software scan control/data acquisition configuration).

### **3.1.1 MEASUREMENT THEORY**

The operating principle upon which the optical unit is based is the Michelson interferometer technique. The He-Ne laser source is divided into two beams: a reference beam which remains within the optical unit and a measurement output beam which is directed onto the vibrating structure. The back-reflected light from the vibrating structure is then recombined with the reference beam. The difference in frequencies of the reference and measuring beams will result in an intensity modulation due to the constructive or destructive interference between the beams. The frequency of intensity modulation which is called the Doppler frequency is given by:

$$F_d = \frac{2v}{\lambda} \quad (3.1)$$



where  $v$  is the surface velocity of the vibrating structure, and  $\lambda$  is the wavelength of the light source, and the units of  $F_d$  are Hertz. Specifically, for the He-Ne laser,  $\lambda = 24.91 \times 10^{-6}$  in (632.8 nm).

As mentioned in Chapter 2, the Michelson interferometer is incapable of resolving the direction of motion without some type of frequency-shifting of the Doppler signal. In the case of the VPI Sensor, the frequency-shifting is accomplished by electronic mixing of the detector output response with the recombined beam. This is achieved by splitting the recombined beam into two detection channels. These channels are configured so that one channel receives a signal that is effectively shifted by one-quarter wavelength (achieved by the use of a 1/4 wavelength plate in the optical circuit) than the signal received by the other channel. This results in a 90° phase shift between the channels, which are denoted 'sin' and 'cos'. The direction of motion is then determined by which signal leads the other in phase. The sin and cos signals are then sent into a dual-channel balanced modulator where they are modulated by internally generated sin and cos signals at a carrier frequency,  $F_c$ . The carrier frequencies for the LOW, MEDIUM, and HIGH ranges are 50 kHz, 500kHz, and 5.0 MHz respectively. Summation of the two modulated outputs yields a frequency-shifted output at:

$$F_{OUT} = F_c + F_d \quad (3.2a)$$

or

$$F_{OUT} = F_c - F_d \quad (3.2b)$$

A positive velocity corresponds to a summed output signal which is above the carrier frequency, Equation (3.2a). A negative velocity corresponds to a summed output signal which is below the carrier frequency, Equation (3.2b). Consistent with the above, a 0.03937 in/s (1mm/s) surface velocity will translate into a 3.16 kHz Doppler frequency.

This combined signal is the frequency-coded velocity signal, and is called the Single Side Band Suppressed Carrier (SSBSC). In order to obtain the instantaneous analog velocity, a frequency-tracking FM-demodulation circuit is employed. Figure 3.1 shows a schematic for the VPI Sensor laser optical unit. Doppler 1, Doppler 2, Analog Velocity, and the SSBSC correspond to instantaneous signals that are available to the user via BNC connections on the side of the optical unit.

Figure 3.2 shows the two side views of the VPI Sensor optical unit. Note the output BNC connections which correspond to the output signals shown in the schematic given in Figure 3.1.

The SLDV system is capable of velocity measurements up to 39.37 in/s (1000 mm/s) at working distances up to 7874 in (200 m) [5]. There are three different velocity ranges that can be chosen on the side of the optical unit. These settings are also shown in Figure 3.2. The settings are LOW, MEDIUM, and HIGH, and the corresponding velocity ranges are 0-0.3937 in/s (0-10 mm/s), 0-3.937 in/s (0-100 mm/s), and 0-39.37 in/s (0-1000 mm/s) respectively.

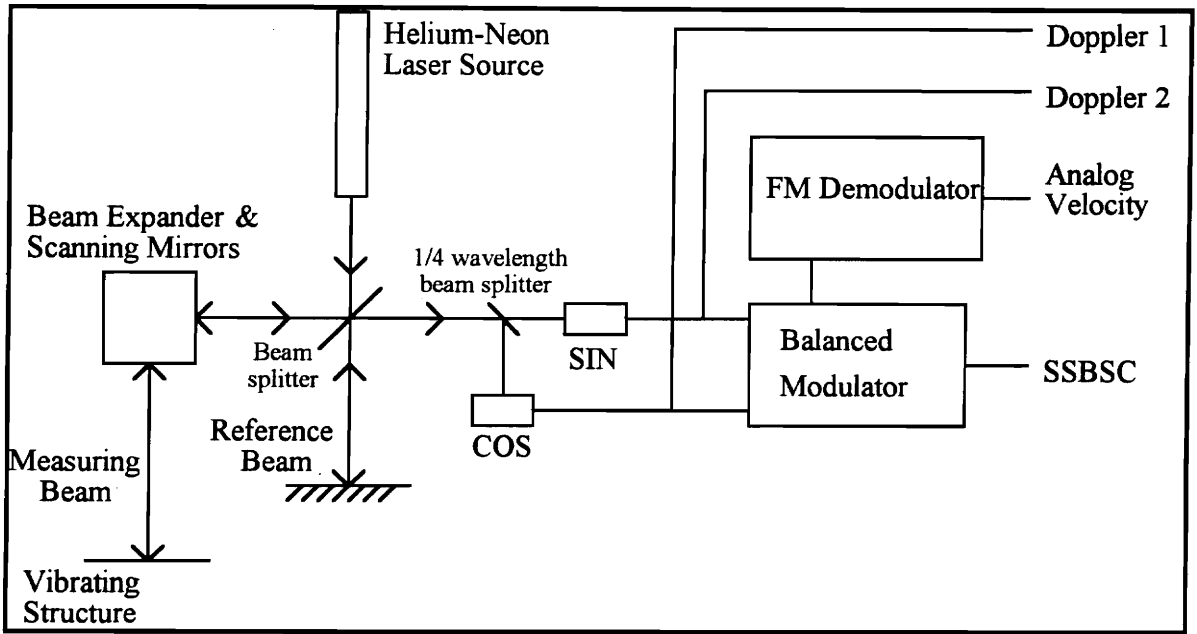


**Figure 3.1:** Schematic of the VPI Sensor unit (adapted from the VPI Sensor Operator's Manual [5]).

Focus is another important characteristic in the use of the SLDV system. Theoretically, maximum focus will occur when the laser measuring beam spot is minimized. Maximum focus will also theoretically result in the largest speckle grains within the speckle pattern. Note the focus knob on the side of the optical unit shown in Figure 3.2. This knob is used to control the size of the measuring laser 'spot' on the vibrating surface. Also shown in Figure 3.2 is the Signal Monitor level indicator. This LED indicator displays levels between 0 and 100, and toggles between a velocity signal level indicator and a focus level indicator. The levels denoted by the Signal Monitor Indicator when measuring focus level are proportional to a smoothed sum-of-squares of

VPI SENSOR OPTICAL UNIT - SIDE VIEWS

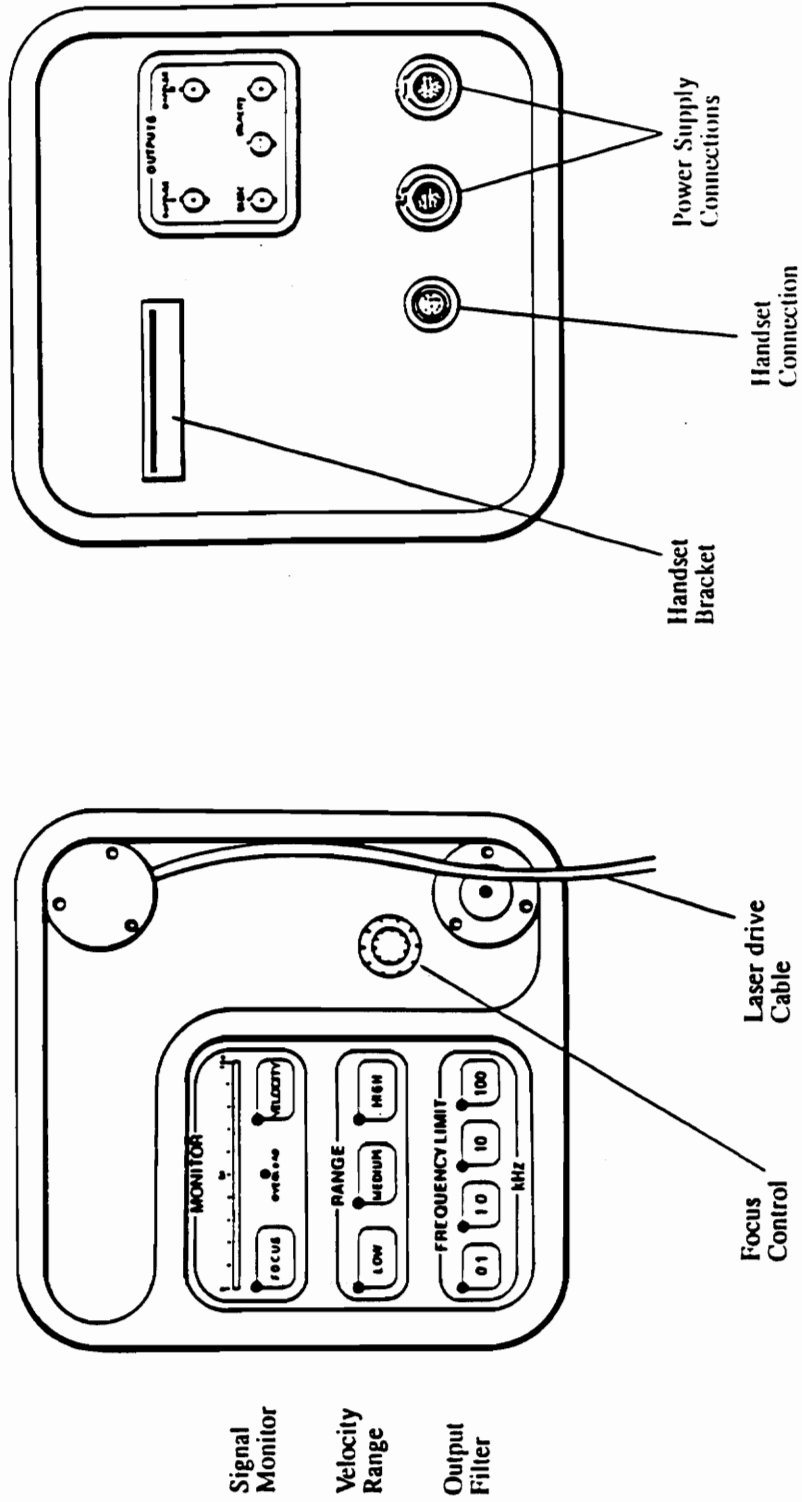


Figure 3.2: VPI Sensor Optical Unit (adapted from VPI Sensor Operator's Manual [5], Ometron, Ltd. London, England).

the Doppler signal amplitudes [38] and thus are proportional to the amount of light backscattered from the structure. Focus is an important parameter when one realizes an assumption upon which the SLDV system is based. Chapter 2 of this thesis described literature in which some concerns were raised referring to the ability of a Michelson interferometer based SLDV to generate any velocity signals at all. This concern is overcome by assuming that the laser optical unit detector only receives one bright speckle when acquiring data [39]. That is to say that a major assumption of this SLDV system is that the active area of the photodetector is covered with a single bright speckle during data acquisition. The size of the active area of the photodetector is given as approximately 0.04 in (1 mm) by 0.04 in (1mm) [40]. It should be stressed that this is an important assumption and will play a significant role in the discussion of results presented in the subsequent chapters of this thesis.

As mentioned above, the Signal Monitor can also be set so that it indicates the velocity level. The level displayed on the indicator in the velocity mode denotes a velocity level proportional to the velocity of a particular measurement point, and represents velocity readings from 0 to 100 for each individual velocity setting (i.e. LOW, MEDIUM, and HIGH) depending on which setting is chosen.

Another option available when using the SLDV system is the choice of two different output lenses: a 'short-range' lens and a 'long-range' lens. The long-range lens provides a lens diameter of 0.787 in (20 mm), whereas the short-range lens provides a diameter of 0.197 in (5 mm). The VPI Sensor Operator's Manual recommends that the

short-range lens be used from 0 - 197 in (0 - 5 m), and the long-range lens be used beyond 197 in (5 m). It should be noted that the long-range lens can be used within 197 in (5 m). The shortest working distance for the long-range lens is given as 43.3 in (1100 mm) [5]. It has also been reported that the long-range lens affords 16 times the light gathering capability than that of the short-range lens [41,42].

The preceding should leave the reader with a general understanding of the operating theory behind the SLDV system. Additionally, the reader should also have some insight into some of the particular options and functions of the SLDV system used in this research. The specifics of the scan control and data acquisition processes are discussed in the following section.

### ***3.1.2 SCAN CONTROL/DATA ACQUISITION***

The Ometron 9000 Series software was used for the scan control/data acquisition for the SLDV system. In order to acquire amplitude and phase data from the optical unit an EG&G lock-in amplifier (sometimes referred to as the correlator) is used. The lock-in amplifier uses a reference signal which is taken from the force transducer waveform of the vibrating structure to correlate with the analog velocity signal taken from the optical unit. The output from the lock-in amplifier is then converted into a DC voltage value that is proportional to the velocity at the measurement point of the vibrating structure.

The SLDV system provides for several scan geometries. These are area, line, or point scans. Repositioning of the laser beam is accomplished by two galvanometer driven mirrors within the optical unit. The Ometron 9000 Series software controls the positioning of the laser beam by generating the necessary voltages to each of these mirrors. The full range of motion for the mirrors results in an full-field scan area of 25° x 25°. Within this area, the SLDV system can obtain as many as 256 x 256 or 65,536 measurement points.

As the SLDV system scans, it pauses for several milliseconds at each measurement point, gathers signals proportional to the real and imaginary velocity components of the particular measurement point, and averages these signals over  $1.0 + n(0.5)$ ;  $n=0,1,2 \dots$  waveforms. The galvanometer-driven mirrors are then repositioned in approximately 7.8 ms by the Ometron 9000 Series software and data for the next measurement point is taken. In the area scan geometry mode, the SLDV will scan in this manner and acquire data from left to right until reaching the area boundary and then from right to left within the predetermined scan area geometry. The SLDV system will repeat this process until data for the full scan area has been taken. The result will be a bit-map of the velocity data for the entire scan area with a resolution that is determined by the user (resolution maximum of 256 x 256 measurement points). This data may then be saved into an ASCII matrix format for subsequent analysis.

It is important to include the specific method by which the data contained in the ASCII matrix are obtained in order to fully understand the effect of laser noise on the

resultant scan matrix. The EG&G lock-in amplifier translates the velocity information contained in the combined Doppler frequency signals into a corresponding voltage. This voltage is obtained by full-wave rectifying the demodulated velocity signal. An average DC voltage corresponding to the surface velocity is then determined by sampling the correlator output signal 45 times and generating an average for that signal. Figure 3.3 shows an oscilloscope plot showing force, analog velocity, Doppler, and the real component of the rectified output signal from the correlator (referred to as 'Correlator Output'). Note that this plot shows the drop-out effect referred to in Chapter 2. This drop-out will occur when the Doppler signal amplitude falls below the FM-demodulator threshold voltage value. One can theorize that in the areas of drop-out, the modulator-demodulator is attempting to drive towards zero output with some superimposed random noise, but some short time later again "locks in" on the velocity signal. This is apparent in the analog velocity signal shown second from the top. The effects of this drop-out on the correlator output can also be seen in the figure. Based on the method in which the correlator determines a voltage corresponding the surface velocity described above, one can see that any drop-out effects will result in a "pinching" of the correlator output signal. Because this is a full-wave rectified signal, these "pinched" down areas will result in lower average voltage magnitudes than that of a signal which does not contain "pinched" down areas. Therefore, one can see that these areas of drop-out will translate into data points which are closer to the zero axis for both positive and negative velocities. These affects can be seen in Figures 1.3(a) and 1.3(b) presented in Chapter 1. It should be stressed



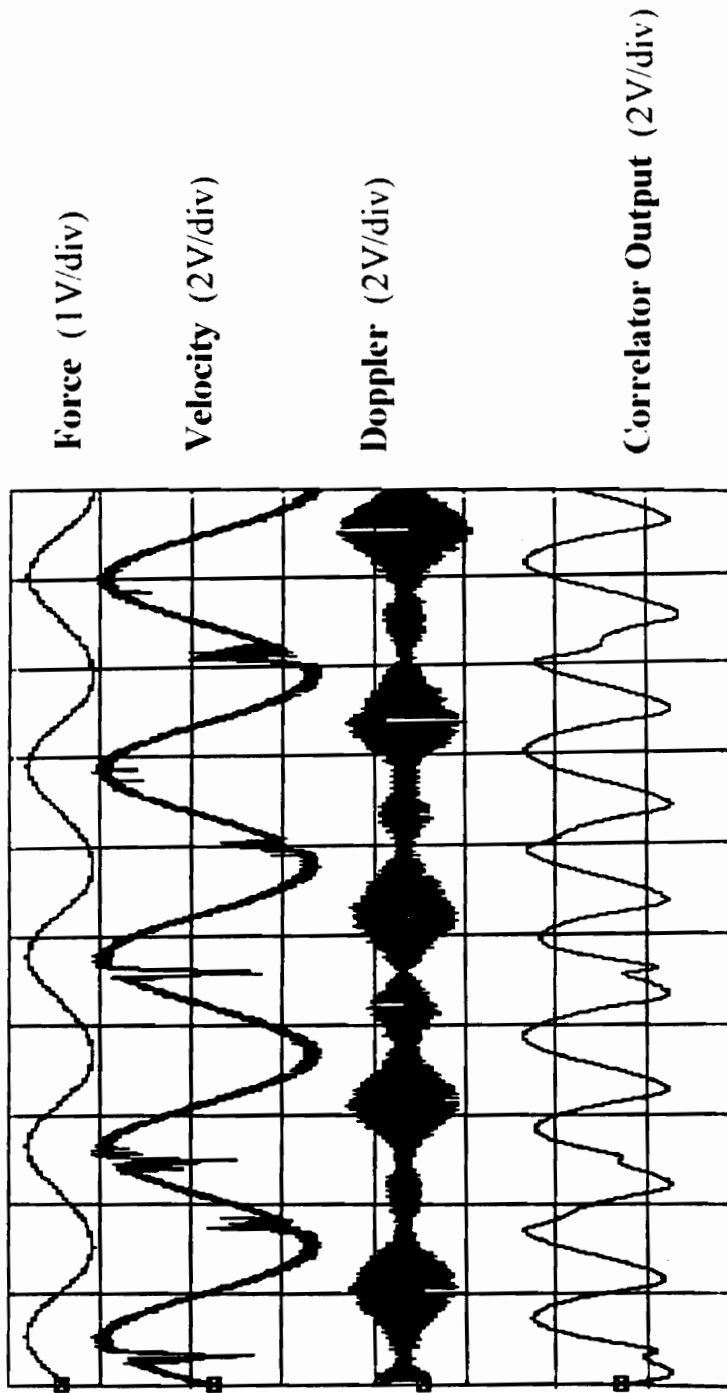


**Figure 3.3:** Oscilloscope plot showing Force, Velocity, Doppler, and Correlator Output Signals. Note the areas of velocity drop-out, the corresponding Doppler Signal and the effective “pinching” the Correlator Output Signal.

based on this description that the author will, henceforth, define the laser noise as “biased-low” due to the fact that drop-out effects in the velocity signal produce absolute velocity data which are lower than similar velocity signals which do not contain drop-out.

### **3.2 SETUP**

Figure 3.4 shows a general schematic indicating the major components used in the experimental setup. The experimental setup for the majority of the experiments required that velocity scan data be taken on a structure so that any data inconsistencies could be noted and subsequently analyzed. Previous experience had shown that a long slender steel beam presented several advantages that were desired in the case of this thesis. The reasons for the choice of a long slender beam included:

- Ability to compare to previous literature in order to duplicate laser noise phenomenon
- Provides simple operating shapes
- Operating shapes provide several differing speckle pattern motions resulting from angular rotations and linear displacements
- Large surface area consisting of speckle pattern variations

Thus, the structure that was chosen for use in these experiments was a steel beam measuring 54.75 in (1.39065 m) long, 3.0 in (0.0762 m) wide, and 0.26 in (0.006604m) thick.

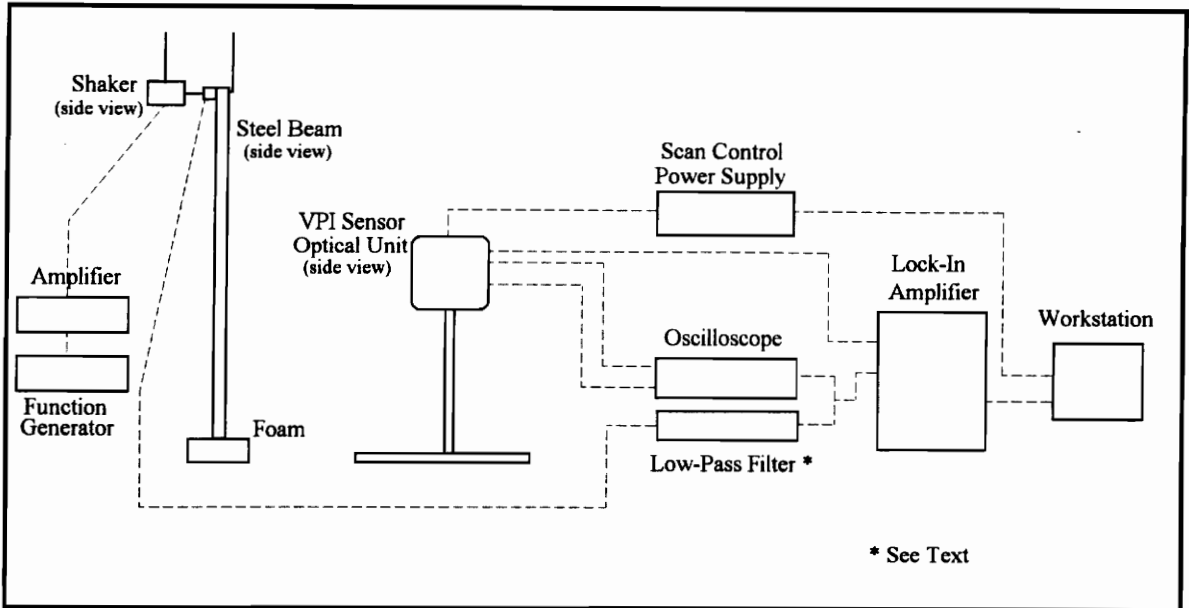


**Figure 3.4:** General experimental setup schematic showing major experimental components.

A free-free boundary condition was simulated by suspending the steel beam. An aluminum truss attached to the ceiling was used to hang a series of rope and bungee (elastic) cord. Approximately 9 in (228.6 mm) of rope was attached to a loop of 0.25 in (6.35 mm) diameter bungee cord. This created a length measuring 43 in (1092.2 mm) from the rope attachment to a small pulley. The pulley was then used to join the bungee cord with approximately 8 loops of 8 lb. test monofilament line which created a length of approximately 7.75 in (196.9 mm). The line was then used to attach to the beam. This was accomplished by looping the monofilament line around a steel stud which protruded from the front of the beam. The stud was located 0.25 in (6.4 mm) from the top and in the center (1.5 in [38.1 mm] from the edge) of the beam. For stability purposes, a piece of foam was placed lightly underneath the hanging beam to minimize any pendulum or

rotational motions. A piezoelectric force transducer, PCB Model 208B, was mounted on the back of the beam with a small beryllium copper threaded stud. The stud was placed approximately 0.25 in. from the top and in the center (1.5 in. from the edge) of the steel beam. Coupling wax was also used to ensure that complete contact was made between the transducer and the beam.

In order to excite the structure, an electrodynamic shaker was used. The shaker was separately suspended with rope and bungee cord. A stinger measuring approximately 2.125 in (54 mm) long and 3/64 in (1.19 mm) in diameter was then used to couple the shaker to the beam through the force transducer. Figure 3.5(a) shows the overall experimental setup, including the laser optical unit<sup>3</sup>. Figure 3.5(b) shows the suspended steel beam and shaker setup. Figure 3.5(c) shows a close-up view of the shaker connection. The shaker was driven by an Hewlett Packard 3324A Function Generator running through a Harmon Kardon HK770 power amplifier. The Function Generator is capable of generating a variety of signals with user defined amplitudes and frequencies. A signal was taken from the force transducer for display on an Tektronix 2214 Digital Storage Oscilloscope. This same force signal was also sent into the reference channel of the EG&G lock-in amplifier. Occasionally, in the presence of high frequency noise components in the force signal which could not be separated by the EG&G lock-in amplifier, a Stanford SR640 low-pass filter was used to filter the force signal. Note that

---

<sup>3</sup> Pictures imported via PhotoWorks Plus™ Release 1.0, Seattle FilmWorks, Seattle, WA.

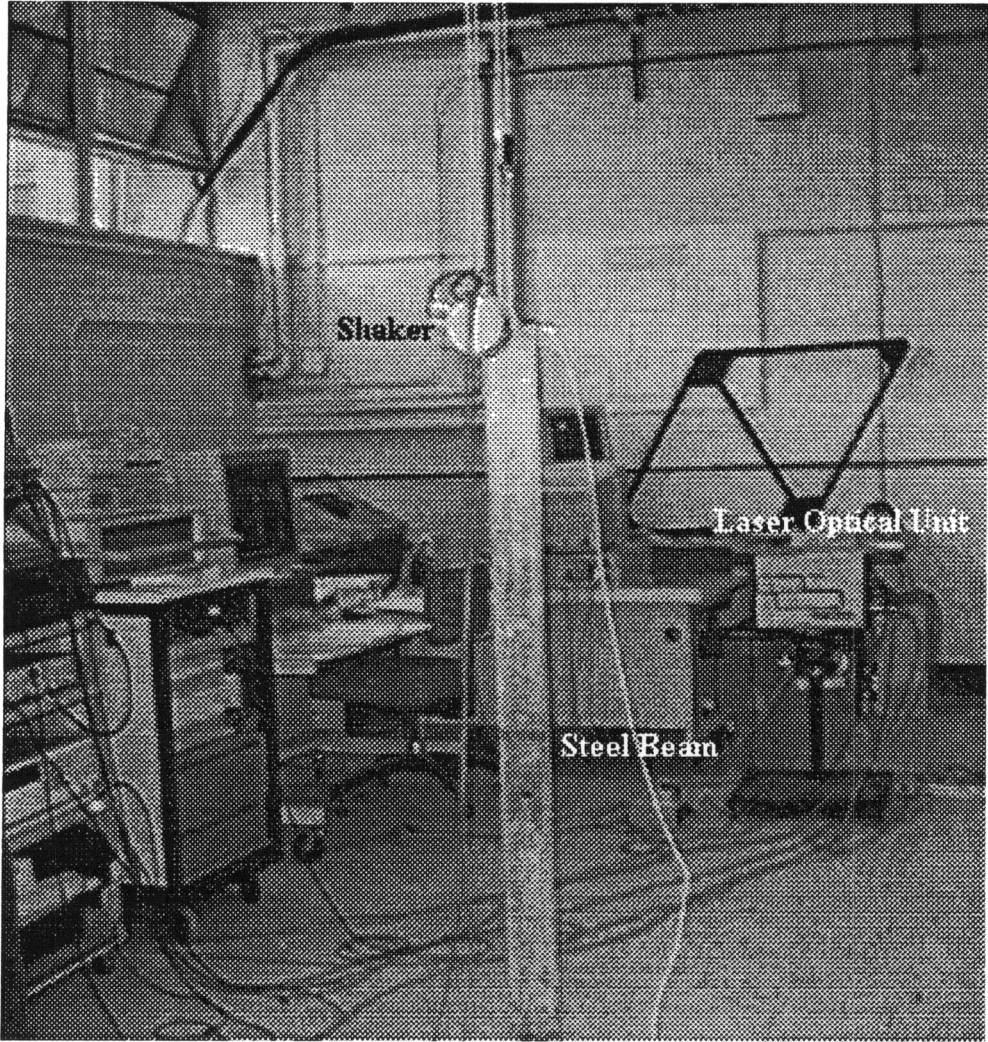


**Figure 3.5(a):** Overall experimental setup showing shaker, steel beam, and laser optical unit.

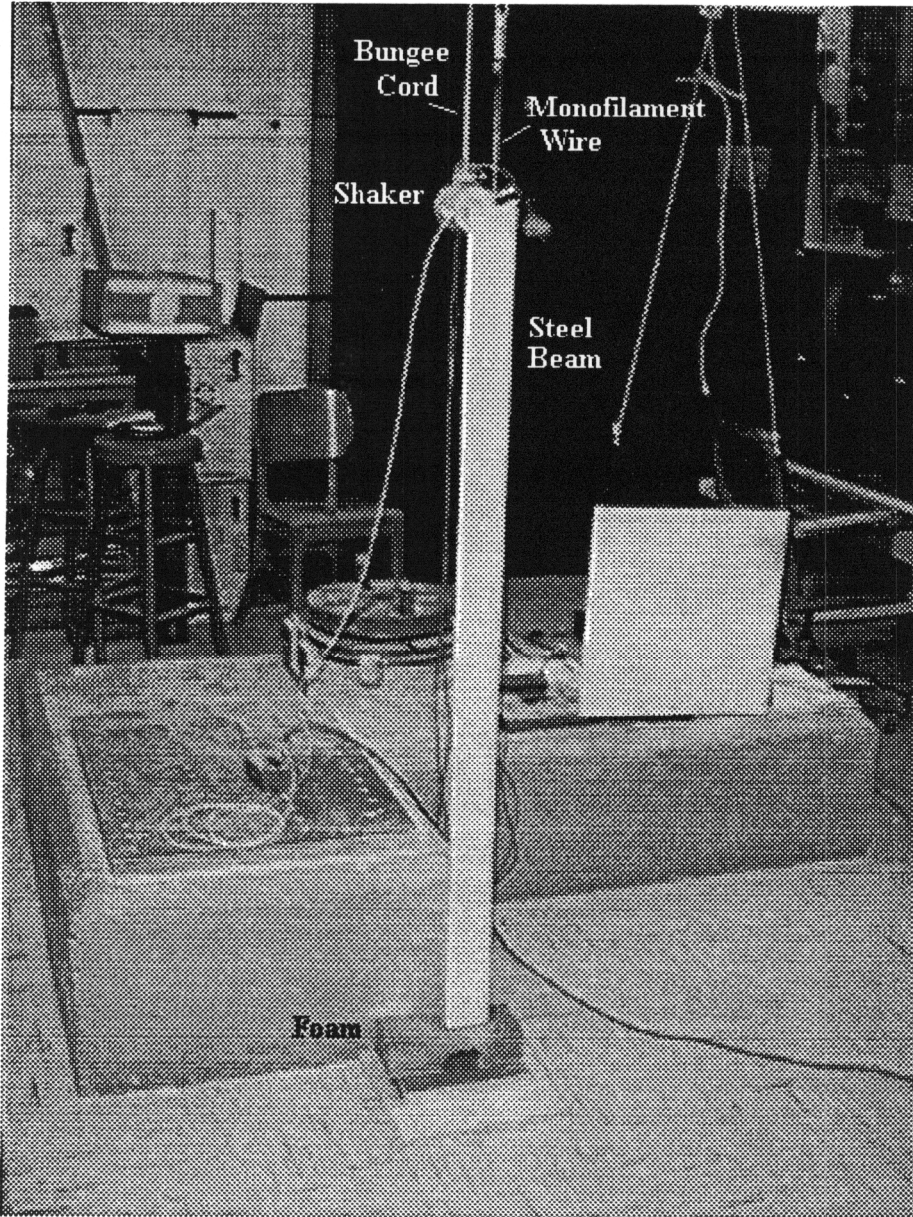


**Figure 3.5(b):** Experimental setup showing shaker, steel beam, and foam.



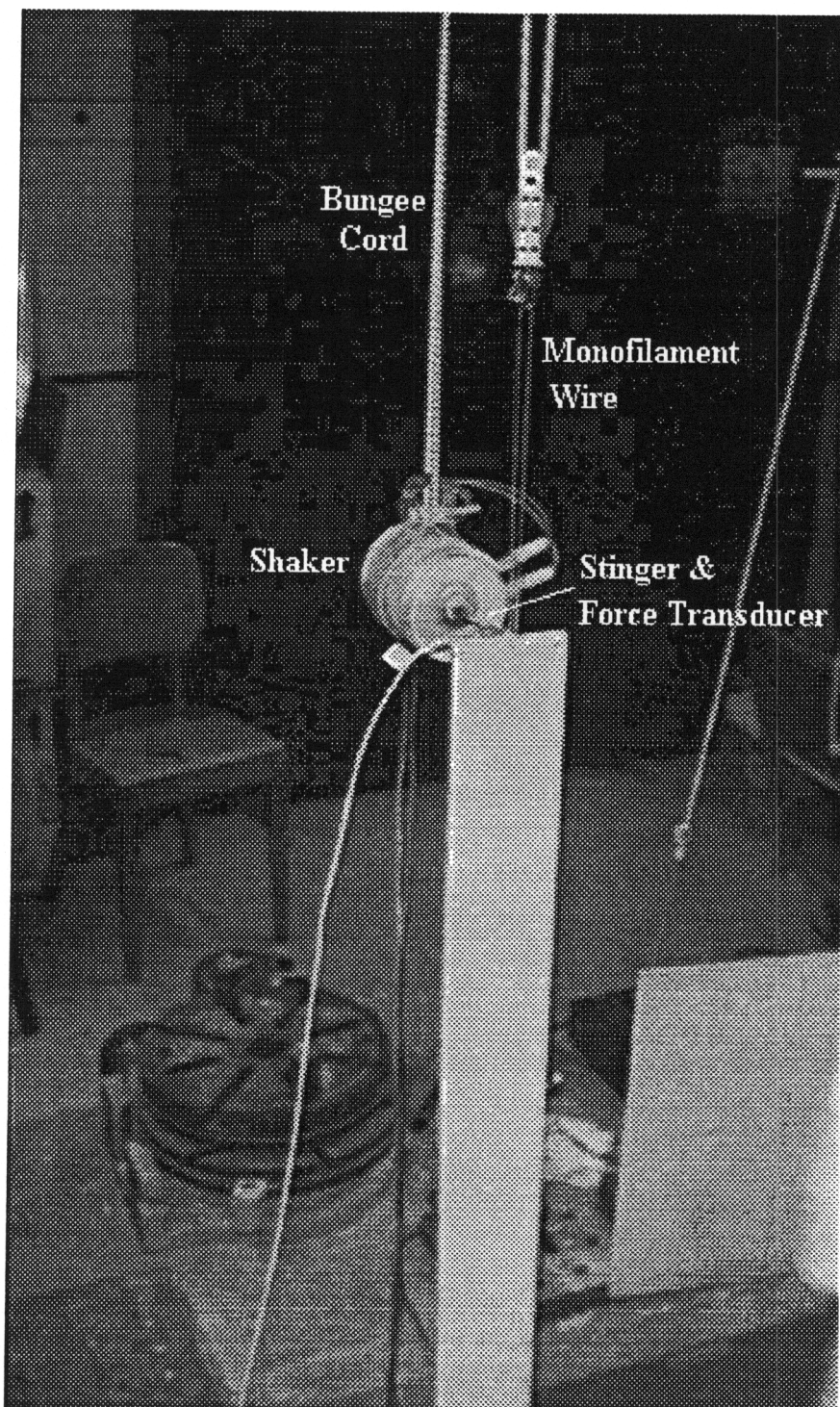


**Figure 3.5(c):** Experimental setup, close-up of shaker and stinger/force transducer attachment.

this filter will cause a phase distortion given by the Phase Response curve in Appendix E. In order to compensate for this phase distortion, the operating frequency to cut-off frequency ratio ( $f/f_c$ ) was set as close to 1.0 as possible. One can see from the SR640 Phase Response curve that this will result in a phase shift of approximately  $360^\circ$ . Therefore the filter will have a negligible effect on the force signal phase. The analog velocity and Doppler 1 signals taken from the side of the optical unit were also connected to the oscilloscope for display.

The experiments utilized the resonance-dwell technique. This technique involves excitation of a structure at a resonance frequency which can be found by a local peak amplitude on a frequency response function (FRF) plot due to the contribution of a dominant mode and neighboring modes. In many cases, the effect of the neighboring modes can be assumed negligible, and the response information can be assumed due to the dominant mode. As a prelude to choosing an excitation frequency, a frequency response test was performed on the structure in order to determine the frequency response function (FRF). This FRF diagram is shown in Appendix C. (Note that the reasons for the choice for the particular excitation frequency will be discussed in Section 3.6.1.) Accordingly, the shaker was driven at a frequency near resonance, and subsequently adjusted (or 'tuned') so that the velocity and force were either in phase or  $180^\circ$  out of phase with each other. This was determined by visually inspecting the force and velocity signals on the oscilloscope, utilizing the Lissajous x-y display option on the oscilloscope, and by reading the phase difference which is available via a readout on the EG&G lock-in amplifier.



The VPI Sensor laser optical unit was setup at working distance of 133.1 in (3380.7 mm) which corresponded to a coherence repeat distance which was most appropriate given the dimensions of the laboratory. The SLDV system was setup so that an area scan geometry could be used. This ensured that a dense spatial matrix representation of the velocity data would be obtainable. A scan matrix consisting of 13 columns and 238 rows, resulting in 3094 distinct velocity measurements, was used for data taking on the beam. Scan data was then taken using the HP Workstation/Ometron 9000 Series software. The resulting raw scan data consisted of the real and imaginary components of the velocity matrix. The Ometron software permits for visual representations of the resulting scan area and also allows for the saving of the data in ASCII matrix format. The latter was used in this case so that separate graphical representations and statistical analyses could be performed on the data.

### **3.3 DATA ANALYSIS**

The following sections explain the theory behind the data analysis methods used in this thesis. It should be noted that for the practical experimental data presented in Chapter 4, the procedures contained below were combined into a short code that was written in MATLAB™. This code was used to calibrate the full velocity scan matrix, separate the real and imaginary components, and perform the data analyses listed below for each velocity scan matrix. A copy of this code can be found in Appendix B.

### 3.3.1 CALIBRATION

Data that is taken with the SLDV system must be calibrated in order to represent the surface velocities in the proper dimensions. The calibration for velocity measurements acquired from the laser system involves the lock-in amplifier sensitivity, the laser optical unit signal processing gains, and any desired units conversions [26]. The overall calibration equation is shown in Equation (3.3):

$$C_v = \frac{SW}{D} \quad (3.3)$$

where  $S$  is the sensitivity setting of the lock-in amplifier (in  $\text{mV}_{\text{RMS}}$ ),  $D$  is the digital range of the A/D converter (in the case of a 12 bit converter  $D = 2048$  0-pk) and  $W$  is the weighting factor. The equation for this weighting factor is shown in Equation (3.4):

$$W = \frac{Rh_c U}{G} \quad (3.4)$$

where  $R$  is the laser range scaling factor (in  $\text{mm}_{\text{RMS}} \text{s}^{-1} / \text{mV}_{\text{RMS}}$  as found in [5]),  $h_c$  is the harmonic amplitude calibration (0-pk/RMS),  $U$  is a units conversion factor (if converting from millimeters to inches is 0.03937 in/mm), and  $G$  is the laser optical unit demodulation filter gain (as determined from Figures 12, 13, and 14 of the VPI Sensor Operator's Manual [5]). Calibration of the velocity scan matrix can then be accomplished by multiplying each term in the ASCII scan matrix by the calibration factor,  $C_v$ .

At this point, a full (real and imaginary components of the velocity data) matrix of calibrated velocity data can be obtained. Because the resonance-dwell technique is utilized, it can be assumed for the purpose of this thesis that the imaginary portion of the scan matrix is negligible and that the velocity information under investigation is contained in the real portion of the scan matrix. For this reason, the discussions contained in the remaining sections of this chapter (and all subsequent data analyses discussions including references to the “full” velocity matrix) will apply only to the real portion of the scan matrix.

### ***3.3.2 ROW MEDIAN***

It was assumed for the purpose of this experiment that the excited steel beam examined in this thesis followed classical beam theory. That is, in theory the velocities across a row of the beam could be assumed to be near constant (with the possible exception of the anticlastic effect which will be discussed later). It could also be assumed that this constant velocity could be represented as the mid-line velocity of the beam. Following along these assumptions, the velocities of such a beam could then be viewed in a two-dimensional sense. Also, a single ‘column matrix’ of velocities (which would represent a single velocity measurements for each vertical position on the beam) could then be used to model (or ‘curve-fit’) the mid-line velocity response of the beam. Further discussions of these assumptions can be found in Section 3.6.

Accordingly, once the real portion of the calibrated velocity data was available, a method could be chosen in order to model the mid-line response of the beam. Before this could be completed though, a single column velocity matrix of experimental data was needed for the fitted curve. While some previous experimentalists have proceeded to average across the rows of the beam in order to obtain a column matrix representation of the beam velocity response, this method did not lend itself for the purpose of this investigation since in the presence of “noisy” data the average would be biased low. As discussed above, several previous users of the SLDV system have noted that inconsistencies in scan data seem to occur at the areas of maximum response. More importantly though, it has also been noted that these inconsistencies were always in the absolute negative direction. In other words, as discussed these data inconsistencies tended to bias the velocity data on the low side. Because one of the objectives of this thesis is to note the areas and patterns in which these inconsistencies occur, averaging across the beam would mask any biased nature of the laser noise.

Correspondingly, another method of representing a column matrix of velocity data was pursued. After discussing the overall purpose of the investigation and more specifically the problem mentioned previously with the Virginia Tech Statistics Consulting Center, it was decided upon their recommendation that the row median value of the scan data would be used as the representative velocity column matrix [43]. This column matrix then represented a single value of velocity at each vertical beam position. By using the row median, the effects by any biased data on the fitted-curve would be minimized.

### 3.3.3 FITTED-CURVE

Once the row median velocity column matrix was calculated, a fitted-curve was needed to “smooth” the velocity response shape resulting from the experimental data. This smoothing is a common step in reproducing the deterministic velocities that correspond to the operating shape of a vibrating structure. For this reason, a smoothing algorithm was chosen to represent the velocities corresponding to the particular operating shape.

Three previously utilized curve fitting algorithms were investigated to fit the experimental scan data. These algorithms included a scaled Euler-Bernoulli algorithm and a Forsythe polynomial algorithm both written by Dr. R. L. West and used in [44], and a Discrete Fourier Transform - Inverse Discrete Fourier Transform (DFT-IDFT) algorithm which is a modified version of that used in [45].

The scaled Euler-Bernoulli algorithm calculates a fit for the observed velocity scan data based on the theoretical mode shape equations for a free-free beam [46] given by:

$$g(x) = [\sin \beta_n x + \sinh \beta_n x + \alpha (\cos \beta_n x + \cosh \beta_n x)] \quad (3.5)$$

where  $\alpha$  is given by:

$$\alpha = \frac{\sinh \beta_n l - \sin \beta_n l}{\cos \beta_n l - \cosh \beta_n l} \quad (3.6)$$

and  $n$  is the theoretical mode number and the  $\beta l$  values used in the algorithm are those which can be found in [46]. The final fitted curve  $y(x)$  is then given by:

$$y(x) = Ag(x) \quad (3.7)$$

where  $A$  is the scaling factor which is calculated based on the minimization of the squared sum of the error between the observed scan data points and the theoretical mode shape data points.

The Forsythe polynomial curve-fitting algorithm performs a recursive fit determined by the generation of a set of orthogonal polynomials based on the following equation:

$$y(x) = s_0p_0 + \dots + s_kp_k(x) \quad (3.8)$$

where  $y(x)$  is the fitted data,  $s_i$  are the coefficients,  $p_i$  are the orthogonal polynomials ( $s_0p_0$  is a constant), and  $k$  is the order of the polynomial. The coefficients of Equation (3.8) are calculated by minimizing the squared sum of the error between the fitted and the observed data points. A more specific description of the theory behind the Forsythe orthogonal polynomial data-fitting algorithm can be found in [47].

The DFT-IDFT curve fitting algorithm (which will be discussed in more detail below) performs a DFT of the data (which has been sheared, mirrored, and flipped), selectively discards the upper band of spectral components, and then inverse transforms the fit back into the spatial domain by the IDFT algorithm. Kochersberger, *et al.* [27]

present this method of extracting structural angular velocities utilizing the one-dimensional DFT-IDFT process. This method is further developed by Sun and Mitchell [48] for both velocity data smoothing and structural angular velocity extraction. It was this curve-fitting algorithm which was chosen for use in this thesis. Note that the reasons for this choice are discussed in Section 3.6 .

For the purpose of totality, the following describes the general method in which the DFT-IDFT performs a fit of the velocity data, it should be noted though that if the reader requires a more explicit explanation of the DFT-IDFT technique it is suggested that he/she refer to the references given above, namely [27] and [48]. First, a Discrete Fourier Transform (DFT) of the column velocity matrix is performed in order to represent the velocity data in the spatial-frequency domain. In order to properly apply the DFT method, the data set must meet two requirements. That is, the data must be evenly spaced, and the data must be periodic. The fact that the SLDV acquires data in equal scan angle increments is noted in [48] and it is determined that this occurrence meets the first requirement.

The second requirement (periodicity) is accomplished in the following manner. A “shear line” is generated by connecting the first and last data points in the data set. The data is then “sheared” so that the end points line on the x-axis. A “mirror” of the data set is then performed about the x-axis. The next step is then to “flip” the data about its right-hand endpoint. The resultant data set, although almost twice the size, has then been periodized.

At this point a spatial frequency-domain filtering is performed on the data set by utilizing only those spectral components that are necessary to represent the deterministic velocities that correspond to the operating shape of the structure. The spectral components that are not utilized are said to be high-frequency components that can be attributed to noise which are superimposed on the fundamental waveform of the spatial signal. The Inverse Discrete Fourier Transform (IDFT) is then performed, and the “shearing”, “mirroring”, and “flipping” of the data are performed in reverse order such that the result is a smoothed fit of the original data.

A particular area of the DFT-IDFT technique that should be discussed is the method by which the spatial cutoff frequency is determined. This process is developed at length by Neumann [45] and will be summarized here. Neumann presents a method in which the low-pass filter cutoff frequency is determined by the application of two parameters. The first of which is an arbitrarily determined percentage of frequency content which is used to determine the high frequency noise basis population. From this, the mean and standard deviation of the magnitude of spectral lines in the high frequency noise basis population can be calculated. The second parameter is a number of standard deviations above that mean level. The noise floor for the spatial signal is then set at this point. For example, if the first parameter (percentage of high frequency content) is set at  $X\%$  then the noise basis is set as the upper  $X\%$  of the spatial frequency components. The mean and standard deviation values of the noise basis ( $\bar{N}$  and  $\sigma_N$  respectively) is then determined from the magnitudes of the upper  $X\%$  of the spectral components. If the



number of standard deviations above the mean noise level is called  $Y$ , the noise floor would be set at a level equal to  $\bar{N} + Y\sigma_N$ . At this point, all spectral components are discarded which are above the spatial frequency of the last spectral component than can be classified as belonging to the non-noise population of the spectral term. In other words, only those spectral components whose magnitudes are above the noise floor ( $\bar{N} + Y\sigma_N$ ) are used to describe the DFT-IDFT curve.

Application of the theory presented above will ideally result in a representation of the velocity profile resulting from the excited beam. This curve can then be compared to the full scan matrix of the experimental velocity data. A method to statistically represent such a comparison is presented in the following section.

### **3.3.4 'DEVIATION FACTOR'**

It was desired in the case of this thesis to generate a statistical value that would represent the overall quality of the laser scan data which would in effect determine the extent by which an entire surface velocity matrix deviated from the fitted-curve determined by the DFT-IDT technique discussed above. This single statistical value was preferred so that simplified comparisons among individual scans could be made. In other words, if the extent by which the surface velocity matrix deviated from the fitted-curve could be represented by a single statistical value, then graphical depiction's of any trends that may occur could be made.

In order to generate such a statistical value a modification of a standard statistical term must first be made. Walpole and Meyers [49] define the error mean square as:

$$s^2 = \frac{SSE}{n(k-1)} \quad (3.9)$$

where  $n$  is the number of populations and  $k$  is the sample size, and where  $SSE$  is the sum of squared error and is defined as:

$$SSE = \sum_{i=1}^k \sum_{j=1}^n (y_{ij} - \bar{y}_i.)^2 \quad (3.10)$$

where  $y_{ij}$  is the  $j^{\text{th}}$  observation from the  $i^{\text{th}}$  treatment, and  $\bar{y}_i.$  is the mean of all observations in the sample from the  $i^{\text{th}}$  treatment.

For the purpose of the data analysis presented in this thesis, a modification of Equation (3.10) is made to satisfy the specific scan data structure. Equation (3.10) is then redefined as:

$$SSE = \sum_{i=1}^l \sum_{j=1}^m (x_{ij} - \hat{x}_i)^2 \quad (3.11)$$

where  $l$  represents of the number of rows and  $m$  represents the number of columns contained in the velocity data scan matrix. The term  $x_{ij}$  is defined as the observed experimental velocity pertaining to the  $i^{\text{th}}$  row and the  $j^{\text{th}}$  column. The term  $\hat{x}_i$  represents the DFT-IDFT fitted median velocity value corresponding to the  $i^{\text{th}}$  row. Therefore, for each row the squared sum of the difference between each column of surface velocity data

and the corresponding DFT-IDFT fitted value is calculated. Subsequently, the squared sum of these values is then calculated resulting in the expression described in Equation (3.11). This can then be used in Equation (3.9) to obtain a modified mean square error.

In order to generate a statistical value that can be used to compare different velocity scans, a normalized expression has to be developed. Bendat and Piersol [50] define normalized error in terms of a fractional portion of the quantity being estimated. For the specific data presented in this thesis, this corresponds to the DFT-IDFT fit of the velocity data. This value will be represented by  $\Phi^2$ , the mean square of the DFT-IDFT median fitted curve, and can be defined as:

$$\Phi^2 = \frac{\sum_{i=1}^l \hat{x}_i^2}{l} \quad (3.12)$$

Therefore, a modified normalized standard error mean square expression will be defined, for the purpose of this thesis, will be defined as the ‘Deviation Factor’ ( $DF$ ) and is represented by:

$$DF = \frac{s^2}{\Phi^2} = \frac{\frac{SSE}{m(l-2(SL))}}{\frac{\sum_{i=1}^l \hat{x}_i^2}{l}} \quad (3.13a)$$

This expression can be expanded into its full form, yielding:

$$DF = \frac{\sum_{i=1}^l \sum_{j=1}^m (x_{ij} - \hat{x}_i)^2}{\frac{m(l - 2(SL))}{\frac{\sum_{i=1}^l \hat{x}_i^2}{l}}} \quad (3.13b)$$

Where  $SL$  represents the number of spectral lines used by the DFT-IDFT algorithm. The product  $2(SL)$  represents the number of degrees of freedom used by the algorithm.

The result is a single statistical value that can be used to determine the overall quality of a scan matrix by measuring the relative extent by which all the velocity values in a scan matrix deviate from the DFT-IDT fitted-curve. (Assumptions and concerns resulting from this expression will be discussed in Section 3.6).

### 3.3.5 CONFIDENCE INTERVALS

In the results sections in Chapter 4, a confidence interval is calculated for a set of SLDV scans. This confidence interval is spread about the mean  $DF$  ( $\overline{DF}$ ) for the set of scans. Determination of the confidence intervals follows:

The mean  $DF$  value for  $n$  number of scans can be calculated as:

$$\overline{DF} = \frac{1}{n} \sum_{k=1}^n DF_k \quad (3.14)$$

In terms of Equation (3.13b) we have:

$$\overline{DF} = \frac{1}{n} \sum_{k=1}^n \left( \frac{\sum_{i=1}^l \sum_{j=1}^m (x_{ij,k} - \hat{x}_{i,k})^2}{m(l-2(SL_k))} \right) \frac{\sum_{i=1}^l \hat{x}_{i,k}^2}{l} \quad (3.15)$$

From this form, one can take the denominator (sum of the square of the fit curve amplitudes over  $l$  rows) as a constant. Thus, an average common factor can be defined as:

$$\frac{\sum_{k=1}^n \sum_{i=1}^l \hat{x}_{i,k}^2}{nl} \cong \frac{\sum_{i=1}^l \hat{x}_{i,k}^2}{l} = \text{constant} \quad (3.16)$$

Thus,

$$\frac{n \sum_{i=1}^l \hat{x}_{i,k}^2}{l} (\overline{DF}) = \sum_{k=1}^n \left( \frac{\sum_{i=1}^l \sum_{j=1}^m (x_{ij,k} - \hat{x}_{i,k})^2}{m(l-2(SL_k))} \right) \quad (3.17)$$

But, the term  $m(l-2(SL_k))$  can not be factored out because it changes with  $k$ . Now, realizing that  $\hat{x}_{i,k}$  is not the mean of this skewed biased distribution, take  $x_{i,k}$  as normally distributed with a mean equal to the median. Then:

$$y_k = (x_{ij,k} - \hat{x}_{i,k}) \quad (3.18)$$

is normally distributed with zero mean and  $\sigma_k$  is the square root of the variance of  $x_{ij,k}$  for the  $k^{\text{th}}$  set.

$$z_k = \frac{x_{ij,k} - \hat{x}_{i,k}}{\sigma_k} \quad (3.19)$$

is then normally distributed with zero mean and unit variance. (It should be pointed out at this time that the distribution is biased-low (not normal) and has its median value closer to theoretical expectations. Thus, the normal distribution and its mean suppression are questionable but are about all that can be used to establish confidence intervals within the scope of this thesis.) Now,

$$\sum z_k^2 \text{ is a } \chi^2 \text{ distribution} \quad (3.20)$$

where

$$\sigma_k = \sigma_{ij,k} \quad (3.21)$$

Using the additivity characteristic of a  $\chi^2$  distribution with the number of degrees of freedom equal to the sum of degrees of freedom, Equation (3.17) can be viewed as a sum of  $\chi_k^2$ :

$$\frac{\sum_{k=1}^n \sum_{i=1}^l \hat{x}_{i,k}^2}{l} (\overline{DF}) = \frac{\sum_{i=1}^l \sum_{j=1}^m (x_{ij,1} - \hat{x}_{i,1})^2}{m(l - 2(SL_1))} + \dots + \frac{\sum_{i=1}^l \sum_{j=1}^m (x_{ij,n} - \hat{x}_{i,n})^2}{m(l - 2(SL_n))} \quad (3.22)$$

Realizing that each denominator of the right hand side is approximately:

$$\frac{\sum_{k=1}^n (m(l - 2SL_k))}{n} \quad (3.23)$$

Substituting Equation (3.23) yields:

$$\frac{\sum_{k=1}^n \sum_{i=1}^l \hat{x}_{i,k}^2}{nl} \left[ \sum_{k=1}^n (m(l - 2SL_k)) \right] \overline{DF} = \sum_{i=1}^l \sum_{j=1}^m (x_{ij,1} - \hat{x}_{i,1})^2 + \dots + \sum_{i=1}^l \sum_{j=1}^m (x_{ij,n} - \hat{x}_{i,n})^2 \quad (3.24)$$

Each of the sums on the right hand side has a variance of  $\sigma_{xij,k}^2$ , each very slightly different from one another. Thus, if one assumes all have equal variances described by:

$$\sigma_{xij,k}^2 \cong \frac{\sum_{k=1}^n \left[ \sum_{i=1}^l \sum_{j=1}^m (x_{ij,k} - \hat{x}_{i,k})^2 \right]}{\sum_{k=1}^n (m(l - 2SL_k))} \quad (3.25)$$

Dividing both sides of Equation (3.24) with Equation (3.25) yields:

$$\frac{\sum_{k=1}^n \sum_{i=1}^l \hat{x}_{i,k}^2 \left[ \sum_{k=1}^n (m(l - 2SL_k)) \right] \overline{DF}}{nl \sigma_{xij,k}^2} = \frac{\sum_{i=1}^l \sum_{j=1}^m (x_{ij,1} - \hat{x}_{i,1})^2}{\sigma_{xij,1}^2} + \dots + \frac{\sum_{i=1}^l \sum_{j=1}^m (x_{ij,n} - \hat{x}_{i,n})^2}{\sigma_{xij,n}^2} \quad (3.26)$$

The right hand side approximately is a  $\chi^2$  distribution with the number of degrees of freedom,  $\nu$ , equal to:

$$\nu = \sum_{k=1}^n (m(l - 2SL_k)) \quad (3.27)$$

Noting that  $\nu$  is very large, and following Bowker and Lieberman's [51] discussion, it is sufficiently accurate to compute  $\sqrt{2\chi^2}$ , whose distribution is approximately normal about a mean of  $\sqrt{2\nu-1}$  with a standard deviation of 1. Thus:

$$z = \frac{\sqrt{2\chi^2} - \sqrt{2\nu-1}}{1} \quad (3.28)$$

which is normally distributed with a mean of zero and unit standard deviation. So for a 95% confidence interval on  $z$ :

$$P(-1.96 < z < 1.96) = 0.95 \quad (3.29a)$$

$$P(-1.96 < \sqrt{2\chi^2} - \sqrt{2\nu-1} < 1.96) = 0.95 \quad (3.29b)$$

$$P(\sqrt{2\nu-1} - 1.96 < \sqrt{2\chi^2} < \sqrt{2\nu-1} + 1.96) = 0.95 \quad (3.29c)$$

Squaring and dividing:

$$P\left(\frac{(\sqrt{2\nu-1} - 1.96)^2}{2} < \chi^2 < \frac{(\sqrt{2\nu-1} + 1.96)^2}{2}\right) = 0.95 \quad (3.30)$$

Now using Equation (3.26) for the  $\chi^2$  random variable:



$$P \left( \frac{(\sqrt{2\nu-1}-1.96)^2}{2} < \frac{\sum_{k=1}^n \sum_{i=1}^l \hat{x}_{i,k}^2 \left[ \sum_{k=1}^n (m(l-2SL_k)) \right] \overline{DF}}{nl\sigma_{xij,k}^2} < \frac{(\sqrt{2\nu-1}+1.96)^2}{2} \right) = 0.95 \quad (3.31a)$$

Rearranging:

$$P \left( \frac{(\sqrt{2\nu-1}-1.96)^2}{2} \frac{nl\sigma_{xij,k}^2}{\sum_{k=1}^n \sum_{i=1}^l \hat{x}_{i,k}^2 \left[ \sum_{k=1}^n (m(l-2SL_k)) \right]} < \overline{DF} < \frac{(\sqrt{2\nu-1}+1.96)^2}{2} \frac{nl\sigma_{xij,k}^2}{\sum_{k=1}^n \sum_{i=1}^l \hat{x}_{i,k}^2 \left[ \sum_{k=1}^n (m(l-2SL_k)) \right]} \right) = 0.95 \quad (3.31b)$$

where  $\nu = \sum_{k=1}^n (m(l-2SL_k))$ . Thus, Equation (3.31b) provides the confidence bounds for the mean  $DF$  value for each scan set consisting of  $n$  scans.

### 3.5 EXAMPLE

In order to fully illustrate the data analysis procedure used in this thesis, a typical example scan and the corresponding results as dictated by the data analysis procedure mentioned above are presented in this section. The following descriptions refer to Figures 3.6, 3.7, 3.8, and 3.9.

Example Scan, Real Velocity Components

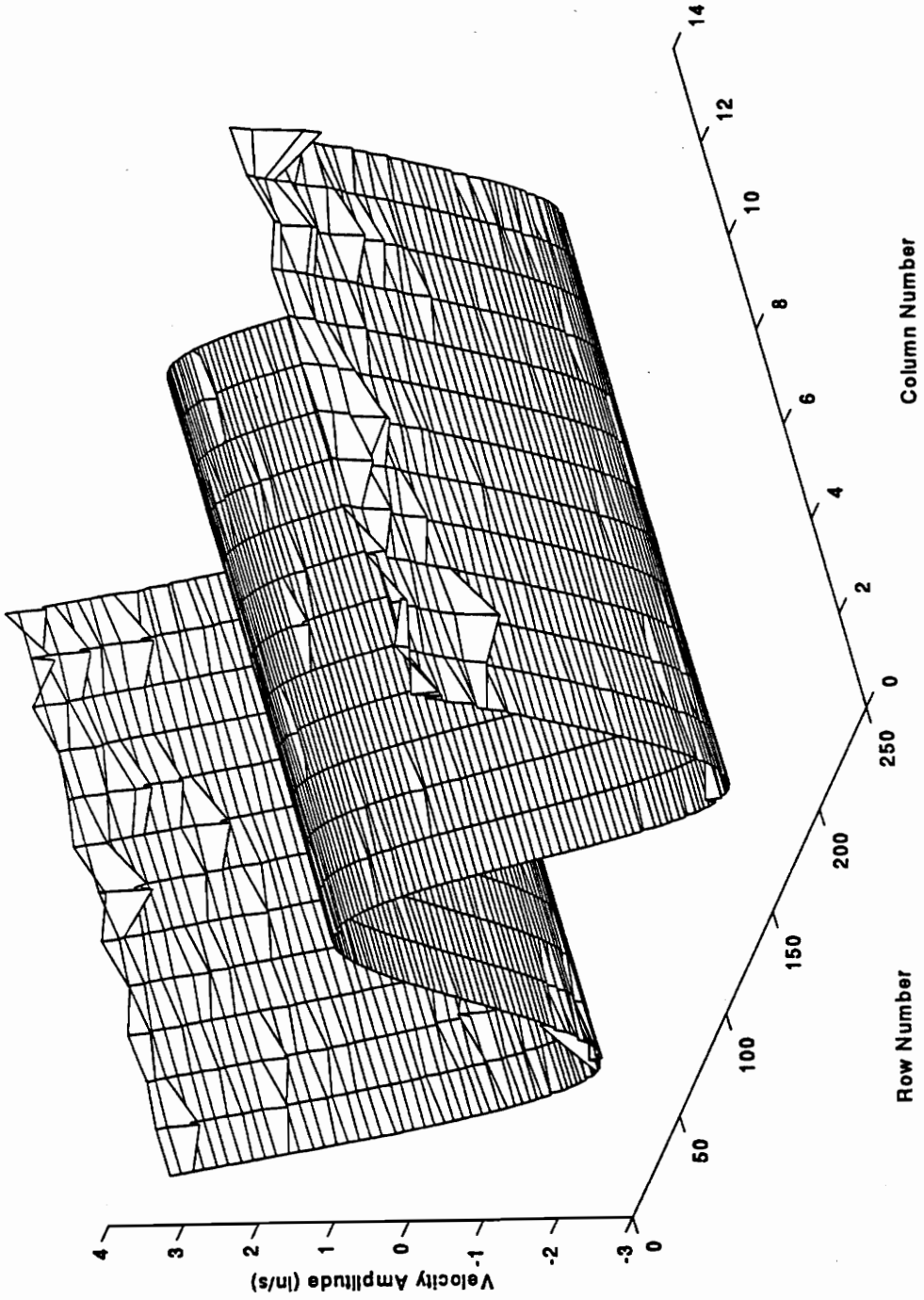


Figure 3.6: Example surface velocity plot showing the full velocity matrix (real components; 13 columns by 238 rows).

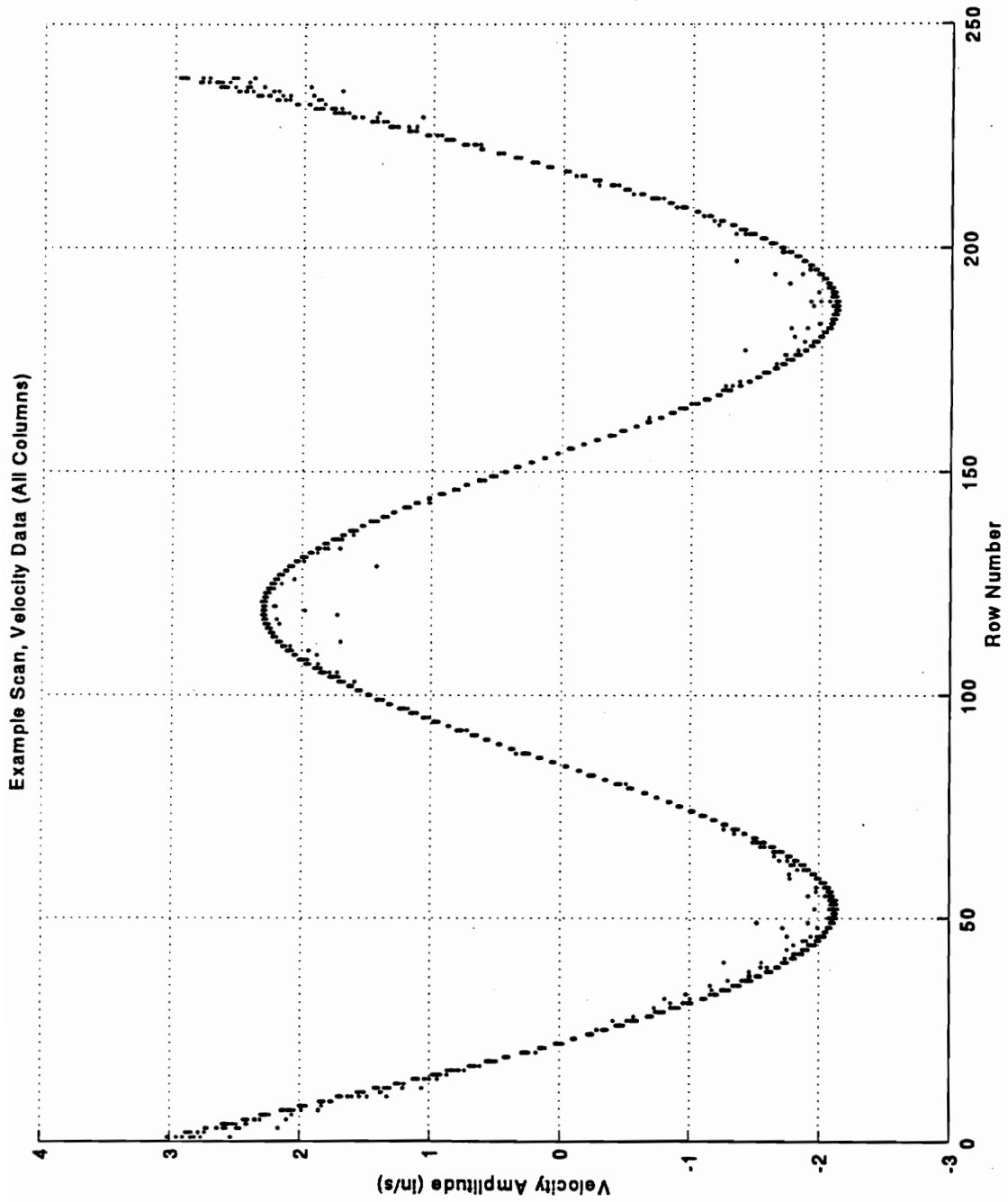


Figure 3.7: Example two-dimensional representation of the full surface velocity matrix.

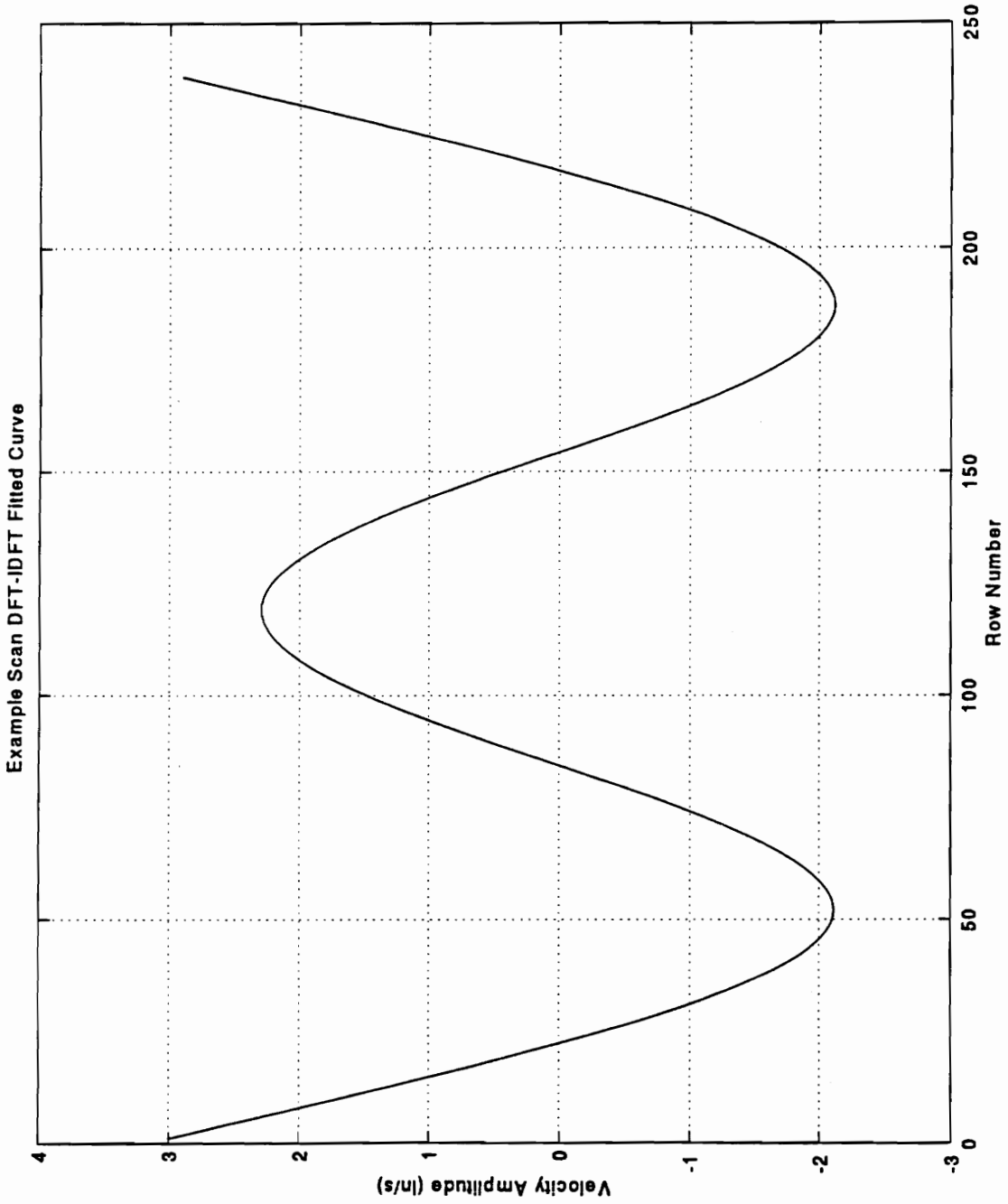
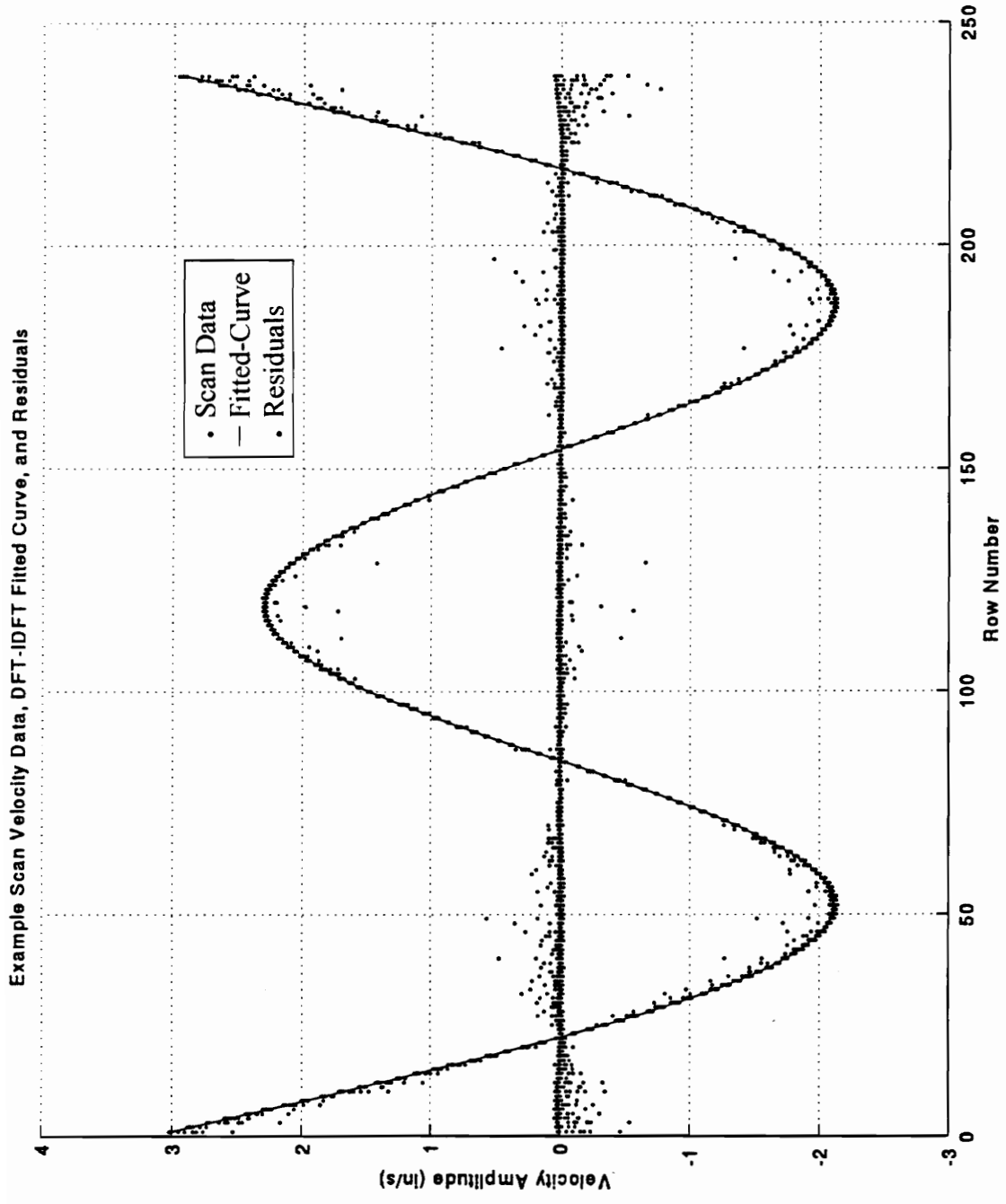


Figure 3.8: Example DFT-IDFT fitted-curve generated from row median surface velocities.



**Figure 3.9:** Example 'scan-fit plot' showing two-dimensional representation of full velocity matrix, DFT-IDFT fitted-curve, and resulting residuals.

Figure 3.6 shows the real velocity components of a typical scan matrix acquired from the steel beam. This matrix represents scan data taken at the third operating mode of the beam which was found to be approximately 94.5 Hz by tuning the excitation frequency via the resonance-dwell technique. The matrix consists of 13 columns and 238 rows of surface velocity data.

The resulting two-dimensional representation of the scan matrix is shown in Figure 3.7. Note that the x-axis corresponds to the row number of the scan matrix. With this configuration Row 1 coincides with the top of the beam, and the x-axis represents position along the length of the beam. The advantages of representing the data in this way can now be realized by noting the data inconsistencies within the scan matrix. As noted earlier, these inconsistencies occur primarily at the areas of maximum absolute velocity amplitude.

The velocity information contained in this matrix can now be utilized so as to generate a DFT-IDFT fitted-curve by means of a single column median velocity matrix. The resulting DFT-IDFT curve is presented in Figure 3.8. It should be noted that a discussion concerning the values chosen for the two DFT-IDFT parameters which determine the spatial cutoff frequency will also be discussed in Section 3.6.

A graphical representation of the biased nature of the data inconsistencies can be noted by combining the information contained in Figures 3.7 and 3.8. In addition, the residuals between the full velocity matrix and the corresponding DFT-IDFT curve can be

helpful in noting the relative extent of the inconsistencies and the spatial areas in which they occur. Such a plot is presented in Figure 3.9. Note that the solid line represents the DFT-IDFT fitted curve which portrays the operating shape. The circular dots along the shape represent the data points for the full velocity matrix (13 columns by 238 rows or 3094 individual data points). The circular dots along the zero axis represent the residuals between the measured data points and fitted-curve.

It should be noted for the remaining chapters of this thesis and for ease of communication plots similar to Figure 3.9 will be referred to as “scan-fit plots”. These plots will include scatter plots indicating the data points for the full scan matrix, the resulting fitted-curve, and the corresponding residuals between the observed data and the fitted-curve.

The data contained in the velocity matrix as well as the data contained in the DFT-IDFT curve can now be used in conjunction with Equation (3.13b) to generate a ‘Deviation Factor’ ( $DF$ ). This final analysis results in a  $DF$  value of  $1.314E-03$ .

As an illustration of contrast, a similar set of figures are presented in Figures 3.10, 3.11, 3.12, and 3.13 for a scan matrix consisting of relatively little laser noise. Note that the final analysis results in a  $DF$  value of  $2.934E-05$ .

Example Scan B, Real Velocity Components

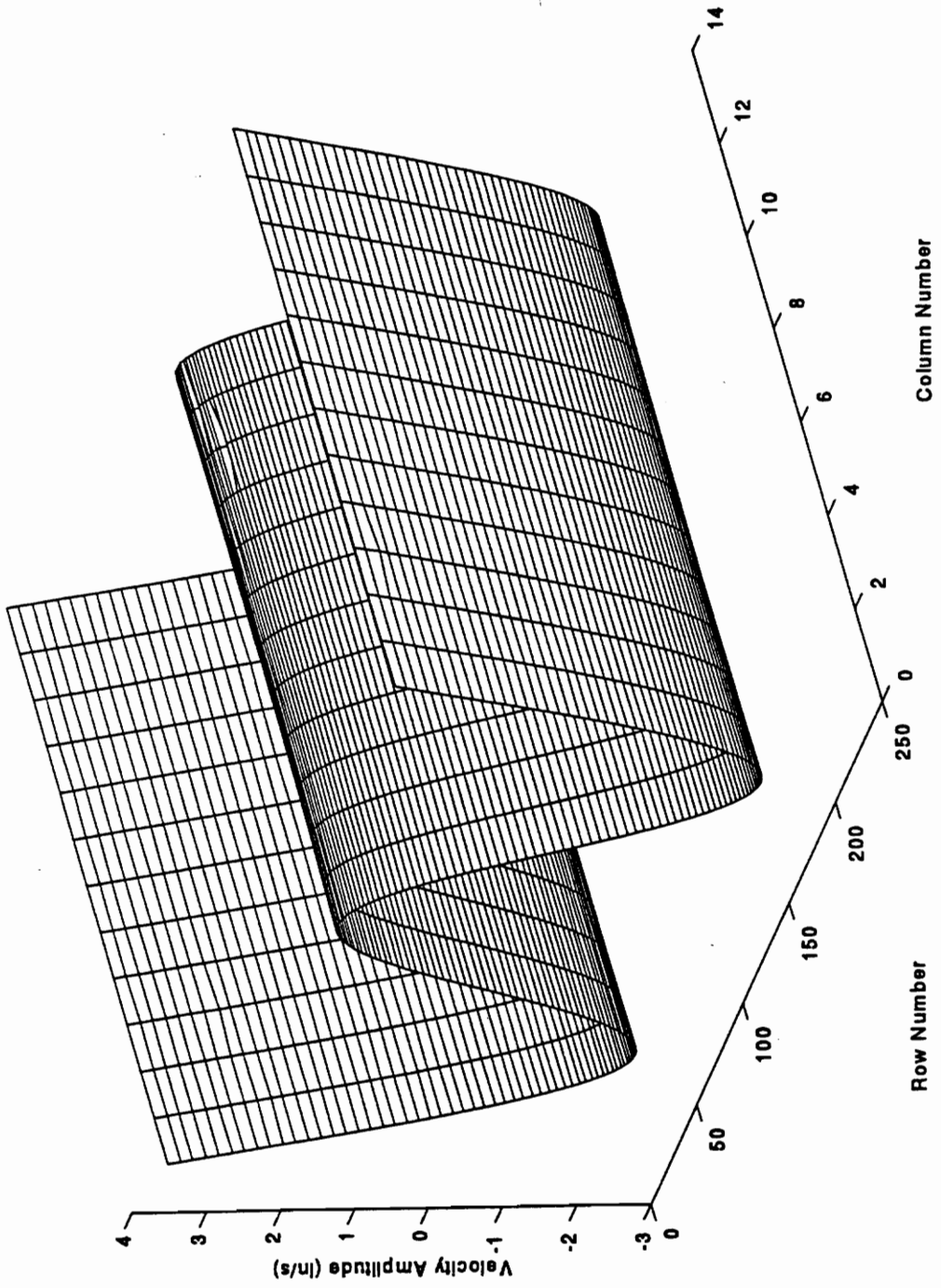
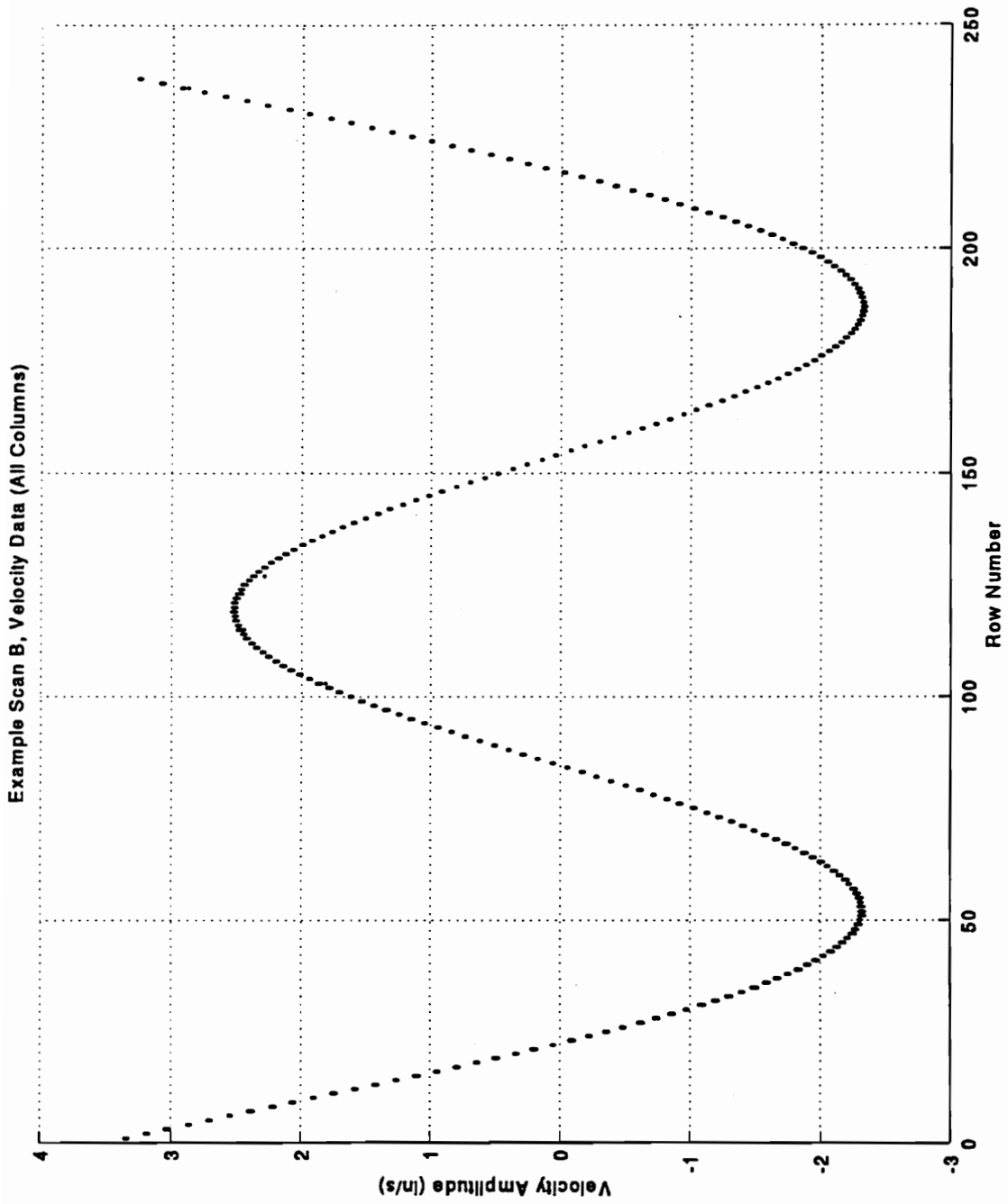


Figure 3.10: Example B surface velocity plot showing the full velocity matrix (real components; 13 columns by 238 rows).





**Figure 3.11:** Example B two-dimensional representation of the full surface velocity matrix.

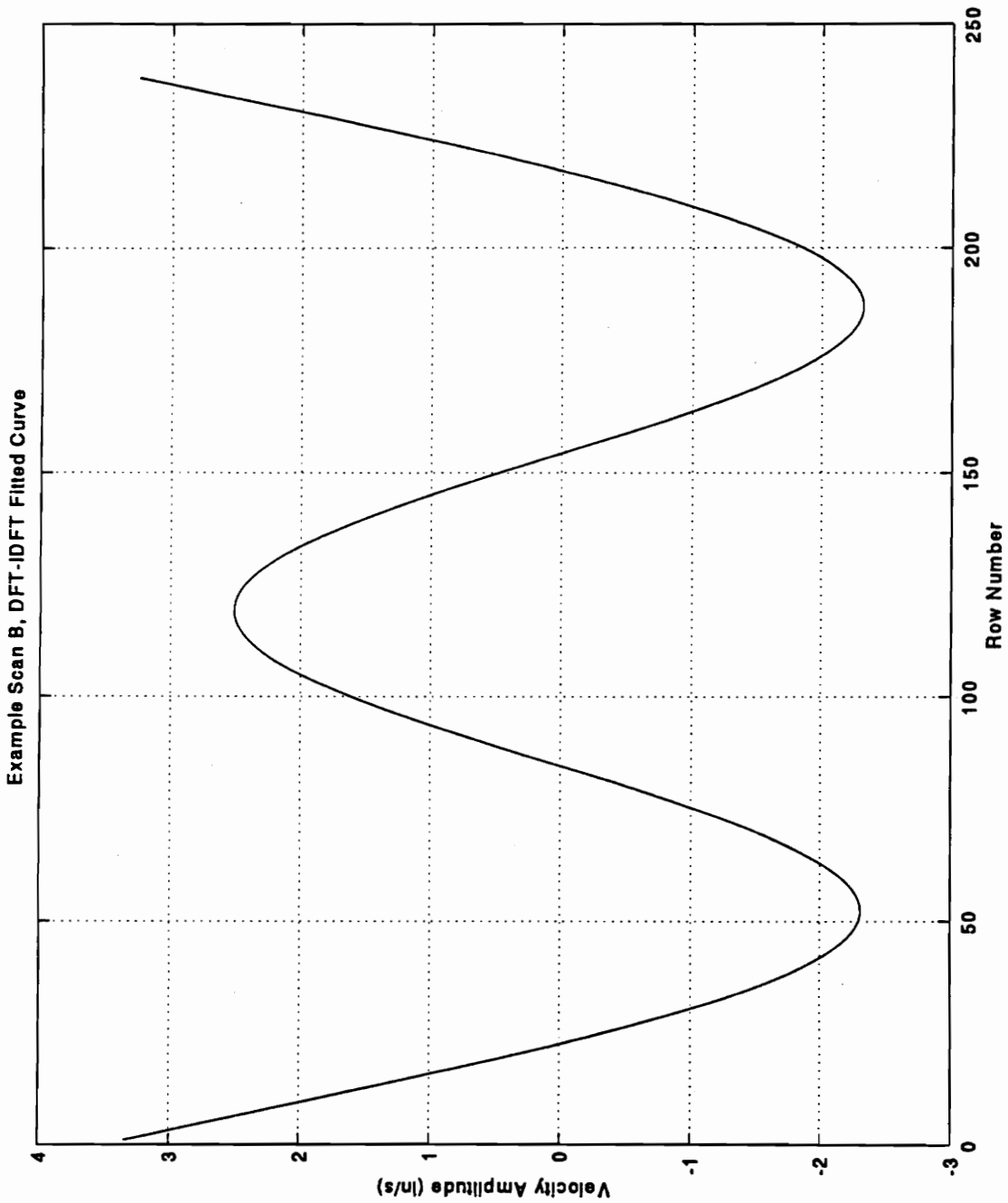
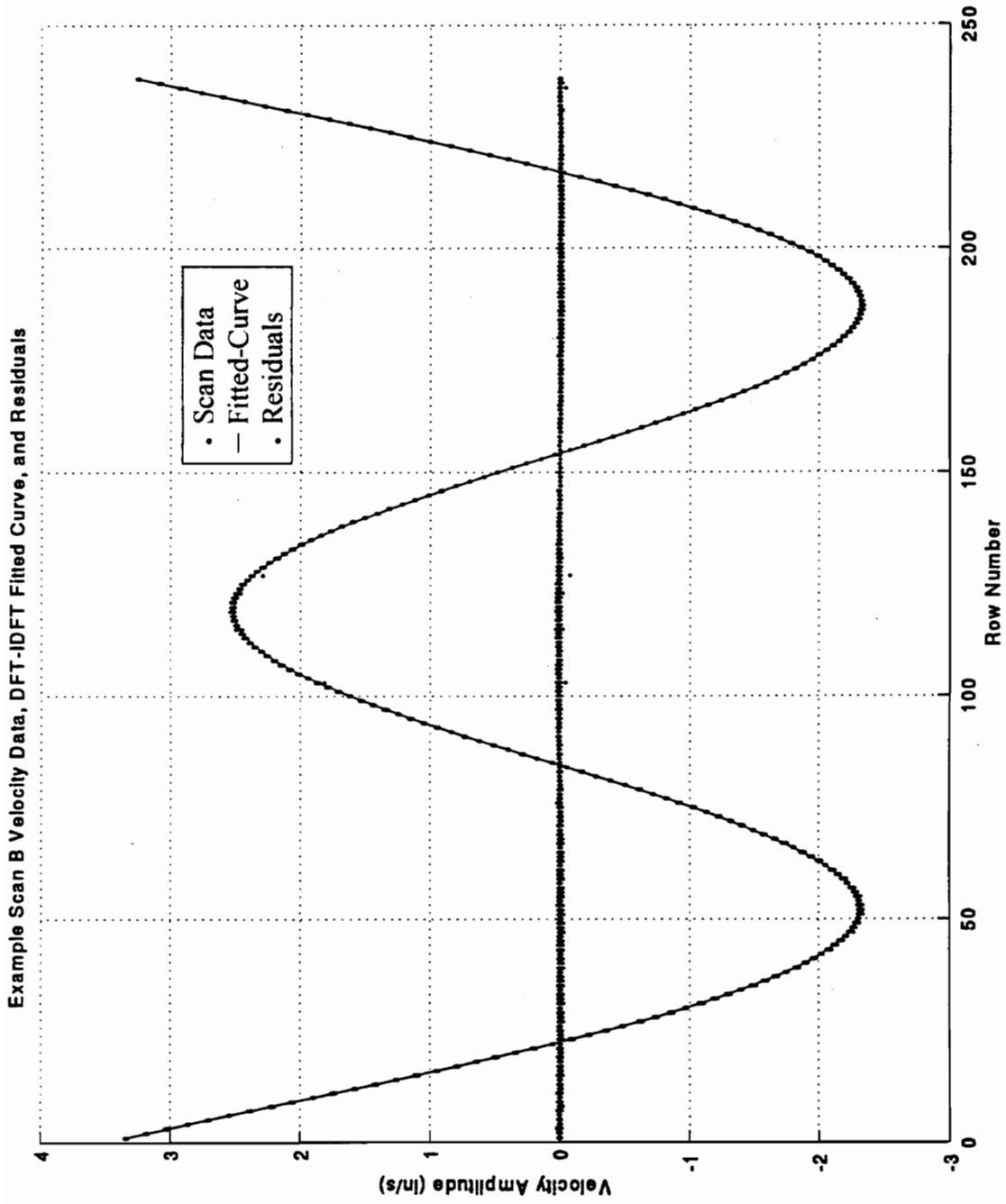


Figure 3.12: Example B DFT-IDFT fitted-curve generated from row median surface velocities.



**Figure 3.13:** Example B 'scan-fit plot' showing two-dimensional representation of full velocity matrix, DFT-IDFT fitted-curve, and resulting residuals.

The preceding illustrations should give the reader a good understanding of the methods used to generate a fitted-curve model from a typical scan velocity matrix, graphically represent the areas of biased noise, and determine a statistical value corresponding to the extent of variation of the full matrix from this curve. As mentioned above, there are some assumptions and remarks that are involved in these processes. These will be discussed in the following section.

### **3.6 ASSUMPTIONS AND REMARKS**

There are some assumptions and points that should be brought out concerning the setup and data acquisition, and the data analysis components of this investigation. These are important in understanding the extent to which conclusions can be made and any limitations that may arise from the experiments.

A major assumption addressed in this thesis concerns the occurrence of the velocity drop-outs. Before addressing this assumption, the reader should remember two points, one based on the assumption which the VPI Sensor operates, (i.e. the assumption that the photodetector is covered by a single speckle) and another based on the random intensity distribution of the speckle defined in Chapter 2. It can be argued from this that velocity drop-outs may be caused by a dark speckle (or insufficient intensity from a “bright” speckle or combination of speckles) covering the detector. Because the speckle pattern, although random, does not change with time, and because it can be argued that a

dark speckle (or insufficient intensity resulting from a speckle) will cause the drop-out effect, it can further be argued that the occurrence of drop-out is spatial and not temporal in nature. It should be noted that this assumption will be revisited during the discussion of results.

### ***3.6.1 SETUP AND DATA ACQUISITION***

A remark should be noted concerning the excitation frequency choice used for the experiments presented in the next chapter. The excitation frequency was chosen in order to excite the beam at its 3rd bending mode. This mode choice corresponds to an excitation frequency of approximately 94.5 Hz. Investigation of the FRF diagram for the structure shows that this is a well separated mode and contributions from other modes should be minimal. Additionally, due to the fact that the electrodynamic shaker is placed on the longitudinal center-line of the beam, and inspection of the response shape shows horizontal lines of zero response, it can be assumed that the velocity response is dominated by the *bending* mode. Thus, it can be assumed that any torsional modes were not excited. It can also be shown that the biased noise phenomenon under investigation in this research is evident in excitation frequencies near other bending modes of the slender steel beam (see Appendix D for examples).

It was also assumed for the purpose of these experiments that any temperature/humidity induced frequency response changes did not occur during each

individual scan. The author does acknowledge that such changes may occur as are discussed by Neumann [45]. For this reason, before each scan, the phase difference between the force and velocity signals were checked to ensure proper application of the resonance-dwell technique and any required 're-tuning' of the excitation frequency was performed.

Another note worthy of mention concerns the coherence and intermediate repeat distances mentioned in Chapter 1. The maximum length of measurement laser beam corresponds to the top or bottom of the beam. Given the dimensions of the steel beam, and the distance from the beam to the laser optical unit, it can be shown that this distance approaches but does not enter an intermediate distance. It is assumed, therefore, that any noise characteristics evident in such scans are not due to this lengthening of the measurement beam. Moreover, in light of this assumption comparisons between separate scans are assumed to be valid because this lengthening is equally involved in all scans.

Another assumption that was made concerns the stability of the free-free experimental setup used in this thesis. In light of time and equipment demand constraints, it was not feasible for the author to maintain the experimental setup for the duration of all the experiments. Although most of the experimental data was taken without disturbance of the setup, extra attempts were made to recreate the experimental setup when necessary. Appendix C also contains FRF diagrams taken during the span of the experiments. It was assumed that any changes in the response diagrams were minimal for the purpose of this thesis and did not affect the noise phenomenon under investigation.

### 3.6.2 DATA ANALYSIS

The DFT-IDFT method was chosen to generate a median fitted-curve from the experimental data. The reader should note further reasons for this choice. A typical velocity scan was arbitrarily chosen in order to choose the curve-fitting algorithm. Figures 3.14, 3.15, and 3.16 show the corresponding velocity scan data, fitted-curve, and resulting residuals (scan-fit plots) for the Euler-Bernoulli, Forsythe, and DFT-IDFT curve-fitting algorithms respectively. It can be seen that the Euler-Bernoulli fit does not fit the data as well as the DFT-IDFT and Forsythe algorithms. The author notes that although the Euler-Bernoulli fit does not account for the laser view angle, it has been previously found that these view angle errors are on the order of 3.5% [52]. The differences between the Forsythe and DFT-IDFT curves are not apparent to the naked eye. It can be shown, though, that the number of spectral lines used for the DFT-IDFT fitted-curve in the example case is 9. This corresponds to  $2 \times 9$  or 18 degrees of freedom used by the algorithm. The Forsythe polynomial algorithm uses 16 degrees of freedom. Given the number of available degrees of freedom (238), the author notes that the difference in these numbers is small. The author does concede that although a “goodness of fit” analysis could be performed as described by Walpole and Myers [49], the differences between the Forsythe and DFT-IDFT fitted-curves would most likely be minimal. The DFT-IDFT algorithm was then chosen as the curve-fitting algorithm for the velocity data presented in this thesis due to the fact that the author had increased accessibility to the authors of the algorithm for consultation. As mentioned above, visual inspection of the DFT-IDFT fit

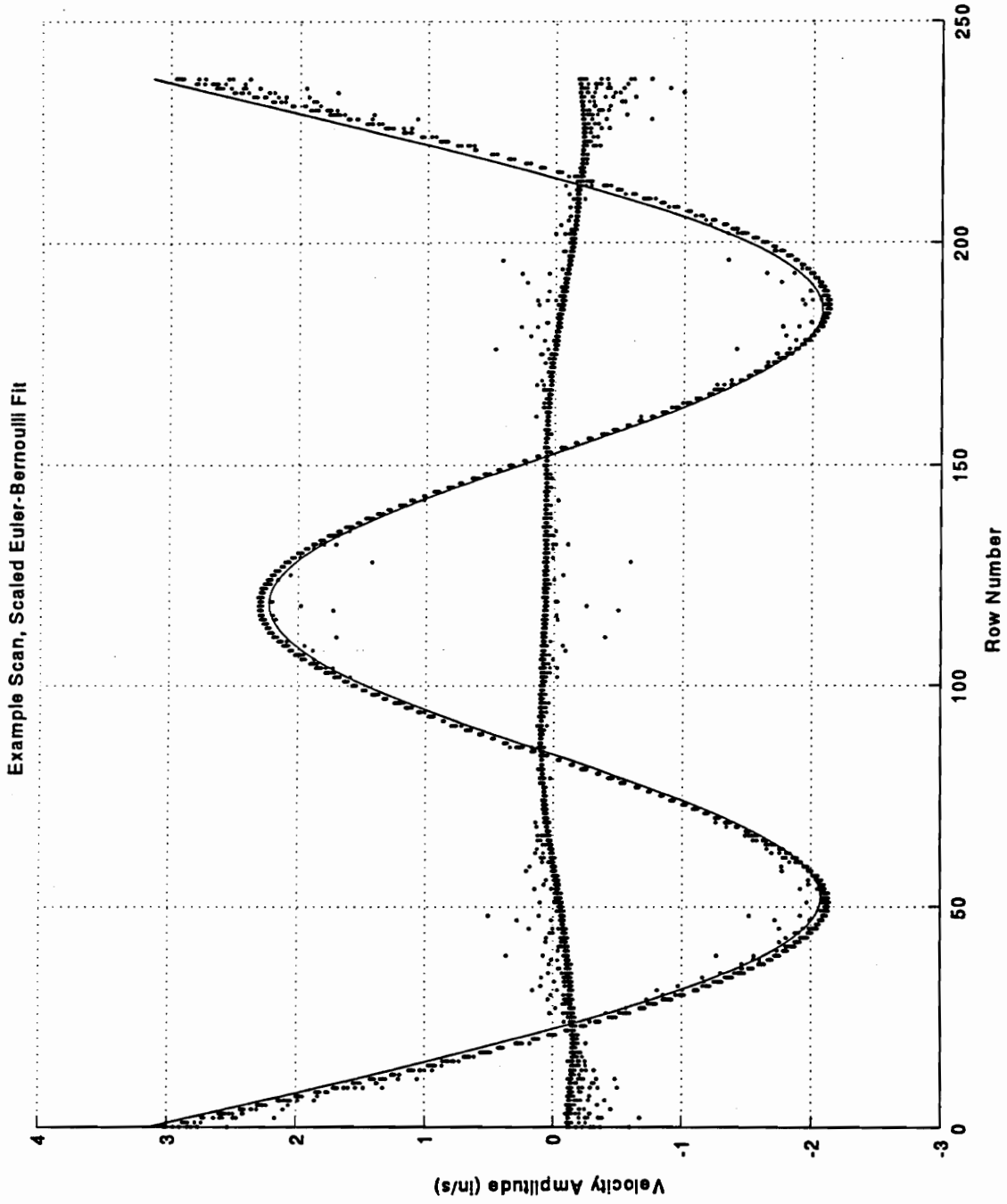


Figure 3.14: Typical 'scan-fit plot' showing the scaled Euler-Bernoulli curve-fit.



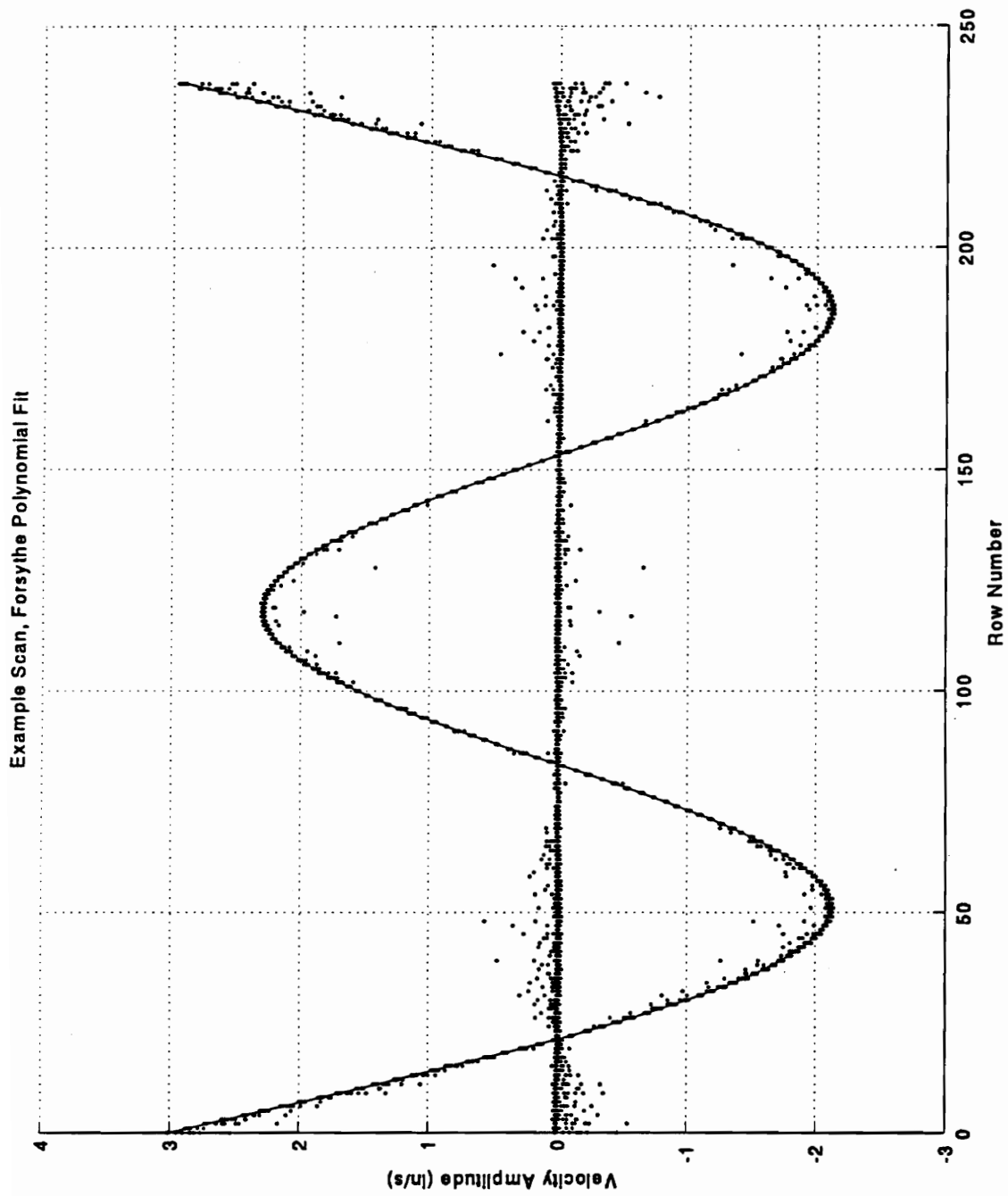


Figure 3.15: Typical 'scan-fit plot' showing the Forsythe polynomial curve-fit.

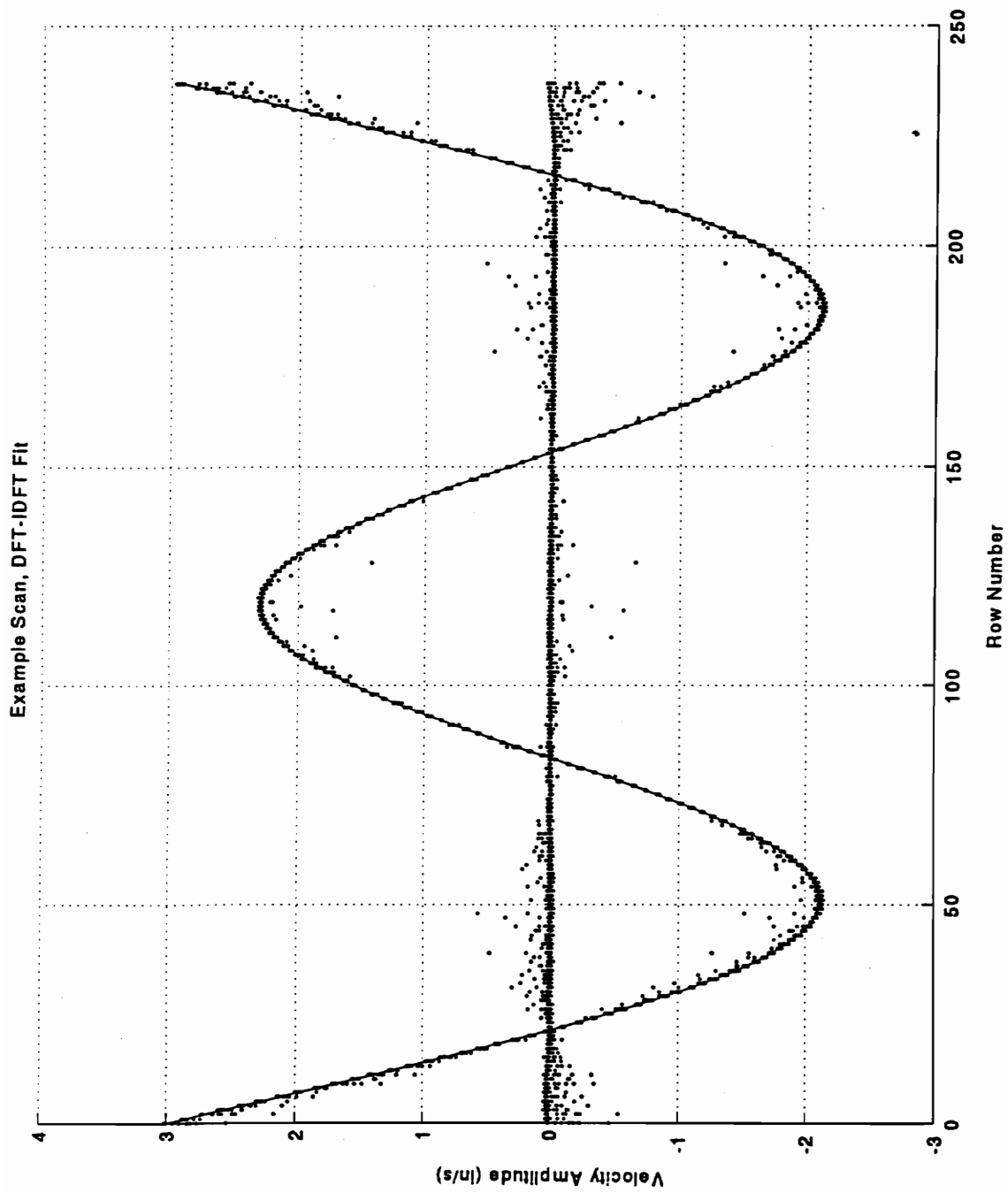


Figure 3.16: Typical 'scan-fit plot' showing the DFT-IDFT curve-fit.

shows that it performed better than the scaled Euler-Bernoulli, and as well as the Forsythe polynomial fit. It has also been written that this technique is preferable to other smoothing methods due to its final analytical description of the results, its close approximation to the structural deflections, and the efficiency of the computing algorithm [48]. It should also be noted, though, that the method used to ensure periodic data (i.e. shearing, mirroring, and flipping) does almost double the amount of data that must be processed by the algorithm. Additionally, the shearing, mirroring, and flipping must be reversed before the curve is returned to the spatial domain. This too adds to the 'cost' of the computing algorithm. Nonetheless the DFT-IDFT seemed to be the appropriate choice for the curve-fitting algorithm.

The validity of the DFT-IDFT method is also based on an assumption of equal data spacing. This requirement is met based on the fact that the scanning angle increment is equal for the entire scan matrix. This assumption has been used previously by Sun and Mitchell [41] among others. The author does note, though, that the linear spacing of the measuring points within the scan matrix are not evenly spaced. The data are all maintained in row number index so that the presentation is consistent with the equal scan angle data acquisition assumption. However, it is noted that the representation of the data and the DFT-IDFT results could be replotted in terms of spatial length along the beam where end points would have greater spacing than the center point. This replotting, though, would not alter the validity of the data.

Another item concerning the DFT-IDFT method should be noted. Section 3.3.3 discussed two parameters which are used to determine the spatial cutoff frequency. For the experiments presented in the next chapter, the percentage value,  $X$ , was chosen as 35%. This was an arbitrary choice, but was made based on Neumann's [45] previous use of this parameter. The second parameter, the number of standard deviations above the mean noise level,  $Y$ , was chosen to be 7. This value was determined using a trial and error method in an attempt to obtain a smooth curve whose residuals did not exhibit any clear harmonic content that needed to be described by the IDFT process. For comparative purposes, these same values were used for each scan matrix. Any concerns that may arise from this will be discussed in Chapter 4.

It is also worthy to note a few items concerning the choice of the median of the row velocity as the representative mid-line velocity for the beam, and the  $DF$  value defined in Section 3.3.4. It should be noted that these values do not address the anticlastic effect described in Beer and Johnson [53]. Therefore, the median row velocity vector and the  $DF$  value are slightly biased with respect to this effect. That is, the 'Deviation Factor' approaches zero as the quality of scan data increases, but it will never reach zero in the presence of the anticlastic effect. A harmonic response analysis of the free-free beam was performed using a computer simulation. Assuming a Poisson's ratio of approximately 0.3, it can be shown that the radius of the anticlastic curvature will be 3.33 times the radius of curvature due to bending. It was found that maximum deflections due to the anticlastic effect were approximately 1.6% of the deflections due to bending. (See Appendix F for

calculations.) Additionally, the row median velocity of the structure will result in a value which, in the areas experiencing the anticlastic effect, will result in residuals above and below the median value. Thus, it can be assumed that the anticlastic effects are minimal compared to the biased laser noise effects under investigation.

Finally, the  $DF$  value represents a simple statistical value by which scan comparisons and conclusions concerning scan quality can be made, but visual inspection of the “scan-fit plots” (such as those shown in Figures 3.9 and 3.12) may give the reader a better feeling for the relative extent and spatial positioning of the biased laser noise effects.

### **3.7 SUMMARY**

The above should give the reader a clear understanding of the general experimental setups, data acquisition, and data analyses procedures used in this thesis. In summary, to examine the effects of the parameters listed in Chapter 1, a general experimental procedure is presented whereby the SLDV system is used to acquire velocity scan matrices from a resonant vibrating free-free steel beam. This scan data is then analyzed and a statistical representation of the relative variation of the scan data from a smoothed representative velocity curve is developed.

The reader should also understand the underlying assumptions made in the experimental setups and experimental procedures. Knowledge of these topics should lay the foundation for the experimental descriptions and results discussed in the next chapter.

## **CHAPTER 4**

### **EXPERIMENTAL DESCRIPTIONS AND RESULTS**

Chapter 3 presented a general experimental procedure and the theory behind the analysis methods presented in this thesis. While most of the experiments follow that procedure, it is most helpful to break up the experiments into separate sections. This study was exploratory in nature. The experiments and results presented in this chapter are progressive. Therefore, dividing up the experiments into sub-experiments may better outline the progression of the experiments performed in this study.

The subsections of this chapter will address each of these sub-experiments individually. The format for each of the sections is the same. First, a short experimental description and the objectives of the sub-experiment will be given. Any pertinent observations that may have occurred during the experiment are then presented. Corresponding results and a short discussion of those results then follow. Conclusions and recommendations based on the sub-experiments individually and as a whole will then be given in Chapter 5.

## **4.1 RANGE OF VELOCITY RESPONSES AS A PERCENTAGE OF FULL-SCALE**

Section 3.1.1 of Chapter 3 discussed the three velocity ranges which can be used with the SLDV system. As mentioned earlier, along with each range there is a specified full-scale velocity capability. These ranges and their corresponding full-scale velocity capabilities are LOW: 0 to  $\pm 0.3937$  in/s (0 to  $\pm 10$  mm/s), MEDIUM: 0 to  $\pm 3.937$  in/s (0 to  $\pm 100$  mm/s), and HIGH: 0 to  $\pm 39.37$  in/s (0 to  $\pm 1000$  mm/s). The general objective of this experiment is to note the spatial distribution of the laser noise and to determine the effect of increasing the excitation forcing amplitude (which will increase the range of velocity responses proportionally) on the corresponding *DF* values defined in Section 3.3.4.

(It should be mentioned that a calibration spot check was performed to verify the accuracy of the calibration factor described in Section 3.3.1. The test indicated that the resultant velocities were well within the accuracy of the accelerometer used to verify their values. These calculations can be found in Appendix G.)

### **4.1.1 EXPERIMENTAL DESCRIPTION**

This experiment was performed using the general experimental setup and data analysis procedure explained in Chapter 3. The experiment was performed on a free-free long slender steel beam. The structure was coated with MAGNAFLUX™ Spotcheck™

Developer<sup>4</sup>, a developer spray which covers the beam with a coat of fine matte white particles and is similar to that suggested by the VPI Sensor Operator's Manual. The beam was excited near its 3rd bending mode and the resonance-dwell technique was employed. The VPI Sensor laser optical unit, utilizing the long-range lens, was placed 133.1 in (3380.7 mm) from the center of the beam, and scan data was taken in the manner discussed in Chapter 3. It should be noted that use of the long-range lens at this distance is within its shortest working distance (see Section 3.1.1) and was used based on its increased light gathering capabilities. This topic will be revisited in Chapter 5.

Excitation forcing amplitudes were chosen in an attempt to characterize the range of velocity responses using the full region plus some overshoot for each velocity range setting. Range of velocity responses were calculated by extracting the maximum velocity response contained in each scan matrix and representing that as a percentage of the full-scale capabilities listed above. It is important to note that at the time of the experiment it was planned that the HIGH velocity range setting would also be examined. It was subsequently found during experimentation that at the particular forcing frequency used, the forcing amplitude levels needed derive adequate signals were beyond the capability of the particular electrodynamic shaker used in the experiments. Therefore, only the LOW and MEDIUM velocity range settings were examined. It should also be noted that the particular values referred to in this thesis as the *excitation forcing amplitudes* were actually the amplitude values taken from the forcing signal generated at HP 3324A

---

<sup>4</sup> MAGNAFLUX™ Spotcheck™ Developer is manufactured by MAGNAFLUX™, Chicago, IL.



Function Generator and do not refer to the force input to the beam as would be measured by the PCB force transducer.

For simplicity the different forcing amplitudes are divided into ‘scan groups’ and are termed L1 through L6 and M1 through M8 for the LOW and MEDIUM velocity settings, respectively. Tables 4.1 and 4.2 show the scan groups and the corresponding maximum velocity responses for each velocity setting. The reader should note that the author will refer to these scan group numbers during subsequent discussions concerning these scans.

**Table 4.1:** Scan groups and corresponding maximum velocity responses for the LOW velocity range.

| <b>LOW Range</b>  |   |
|-------------------|---|
| <b>Scan Group</b> | <b>Range of Velocity Responses<br/>[% Full-Scale<br/>(10 mm/s)]</b> |
| L1                | 15  |
| L2                | 28.5  |
| L3                | 55.5  |
| L4                | 69  |
| L5                | 103.5   |
| L6                | 139.5   |

**Table 4.2:** Scan groups and corresponding velocity responses for the MEDIUM velocity range.

| <b>MEDIUM Range</b> |  |
|---------------------|--|
| <b>Scan Group</b>   | <b>Range of Velocity Responses<br/>[% Full-Scale<br/>(100 mm/s)]</b> |
| M1                  | 15   |
| M2                  | 28.5   |
| M3                  | 54   |
| M4                  | 66   |
| M5                  | 78   |
| M6                  | 99   |
| M7                  | 118.5  |
| M8                  | 135  |

Six velocity scans were taken for each scan group<sup>5</sup> using both the LOW and MEDIUM settings. For each scan group, the laser beam focus knob was adjusted so as to obtain the maximum focus reading possible at a reference point which was chosen as the horizontal and vertical center of the beam. These readings were obtained using the Signal Monitor in the focus position. The SLDV was then used to obtain scan matrices consisting of 13 columns and 238 rows of surface velocity data. The velocity scan data matrices were then saved in ASCII format and transferred so that they could be analyzed using the MATLAB™ code described in Chapter 3 and presented in Appendix B. As mentioned in Chapter 3, it was assumed based on the correct utilization of the resonance-dwell technique that the velocity information was contained in the real portion of the scan matrix. Thus, the subsequent data analysis procedures were performed on the real portion

---

<sup>5</sup> All scan groups contain six scans except L1: 3 scans and M8: 4 scans.

of the scan data matrix. This code then yielded graphical representations of the scan data similar to those presented in the example section of Chapter 3, including two-dimensional representations of the velocity scan matrices, DFT-IDFT fitted curves, and calculations for the  $DF$  values.

## **VELOCITY AND DOPPLER SIGNAL QUALITY**

Also included in the presentation of results are some plots containing information about the observed condition of the velocity and Doppler signals. These plots were taken during the execution of the experiments listed above, and thus the setup is identical. Due to the scan speed of the laser, though, the signals were not captured during actual scanning of the beam. Alternatively, the laser was directed so as to place the illuminating spot on several different sections of the beam. As noted in Chapter 3 and as shown in Figures 3.1 and 3.2, instantaneous monitoring of the Doppler and velocity signals can be obtained via BNC connections on the side of the VPI Sensor laser optical unit. These signals were viewed and acquired on a Tektronix 2214 Digital Storage Oscilloscope. The force signal as measured by the PCB Force transducer was also monitored. Additionally, the full-wave rectified signal from which the EG&G lock-in amplifier (correlator) derives the digitized real portion of the velocity signal was also monitored. This signal will, henceforth, be referred to as the "Correlator Output" signal. Although the transient velocity signal taken from the side of the optical unit also represents the velocity "seen" by the laser, this signal was included because it represents the direct link to the digitized velocity data. In other words as discussed in Chapter 3 the condition of this signal is a

direct indication of the quality of velocity data which would be present in a scan matrix. It should be noted that the oscilloscope plots presented in this section correspond to excitation conditions of the arbitrarily chosen scan group M6.

One of the aims of capturing these signals was to relate their condition at areas which were found to contain the laser noise and those areas which were found to be less prone to the laser noise. Accordingly, oscilloscope plots were acquired at three general areas: the top of the structure, the center of the structure, and near a line of zero response (nodal line).

#### ***4.1.2 EXPERIMENTAL OBSERVATIONS***

An observation was made during the execution of this experiment concerning the focus reading obtained from the VPI Sensor Signal Monitor and the associated Doppler signal amplitudes. It was observed that the maximum focus reading obtained during this experiment was approximately 65 out of 100 units. The average maximum focus readings for most of the scans was approximately 50 units. Correspondingly, as will be demonstrated by the oscilloscope plots presented in the next section, maximum Doppler amplitudes observed during the experiment were approximately 4V pk-pk.

### 4.1.3 EXPERIMENTAL RESULTS

It should be noted that the large number of scans generated in this experiment necessitated that the 'scan-fit plots' for a representative scan for each scan group be placed in the Appendix. It is suggested, though, that the reader examine these plots in order to obtain a sense for the relative noise generated in each scan group. Although the *DF* value does indicate the relative quality of scan data in a scan matrix, these figures are very descriptive in that they explicitly represent the relative quantity and spatial distribution of the laser noise (as it is said: "a picture says a thousand words"). Appendix A.1 contains these figures for a representative scan within each scan group. A statistical summary based on the resultant mean *DF* values is presented in this section.

Table 4.3 shows the mean *DF* values, the sample standard deviations, and the 95% confidence intervals generated from the experimental scans within each scan group listed using the LOW velocity range setting. The 95% confidence intervals are based on the Student t-distribution as described, among others, in [54]. A similar table for the scan groups using the MEDIUM velocity range setting is shown in Table 4.4. The information contained in Tables 4.3 and 4.4 is presented in graphical form in Figures 4.1 and 4.2, respectively.

**Table 4.3:** Statistical summary of the ‘Deviation Factors’ generated for the scan groups using the LOW velocity range setting.

| LOW Range  |   |   |                           |                                   |                                    |
|------------|---|---|---------------------------|-----------------------------------|------------------------------------|
| Scan Group | Maximum Velocity Response (% of Full-Scale) | Mean ‘Deviation Factor’ $\overline{DF}$ | Sample Standard Deviation | 95% Confidence Interval Low Bound | 95% Confidence Interval High Bound |
| L1         | 15  | 4.079E-03                               | 1.058E-03                 | 3.958E-03                         | 4.201E-03                          |
| L2         | 28.5  | 3.409E-03                               | 1.504E-03                 | 3.374E-03                         | 3.535E-03                          |
| L3         | 55.5  | 2.695E-03                               | 1.100E-03                 | 2.651E-03                         | 2.769E-03                          |
| L4         | 69  | 2.099E-03                               | 1.174E-03                 | 2.083E-03                         | 2.176E-03                          |
| L5         | 103.5                                       | 1.203E-03                               | 7.830E-04                 | 1.180E-03                         | 1.234E-03                          |
| L6*        | 139.5                                       | 4.259E-03                               | 2.854E-03                 | 3.490E-03                         | 3.676E-03                          |

**Table 4.4:** Statistical summary of the ‘Deviation Factors’ generated for the scan groups using the MEDIUM velocity range setting.

| MEDIUM Range |   |   |                           |                                   |                                    |
|--------------|---|---|---------------------------|-----------------------------------|------------------------------------|
| Scan Group   | Maximum Velocity Response (% of Full-Scale) | Mean ‘Deviation Factor’ $\overline{DF}$ | Sample Standard Deviation | 95% Confidence Interval Low Bound | 95% Confidence Interval High Bound |
| M1           | 15  | 2.779E-03                               | 1.273E-03                 | 2.750E-03                         | 2.868E-03                          |
| M2           | 28.5  | 1.080E-03                               | 4.512E-04                 | 1.057E-03                         | 1.103E-03                          |
| M3           | 54  | 6.665E-04                               | 3.639E-04                 | 6.655E-04                         | 6.953E-04                          |
| M4           | 66  | 1.130E-03                               | 4.714E-04                 | 1.094E-03                         | 1.143E-03                          |
| M5           | 78  | 1.426E-03                               | 2.368E-04                 | 1.397E-03                         | 1.459E-03                          |
| M6*          | 99  | 2.572E-03                               | 1.607E-03                 | 2.411E-03                         | 2.532E-03                          |
| M7*          | 118.5                                       | 1.936E-03                               | 1.236E-03                 | 1.796E-03                         | 1.881E-03                          |
| M8*          | 135   | 6.834E-03                               | 1.774E-01                 | 5.698E-03                         | 6.102E-03                          |

\* See discussion of results.

### 'Deviation Factor' vs. Maximum Velocity Response (LOW Range)

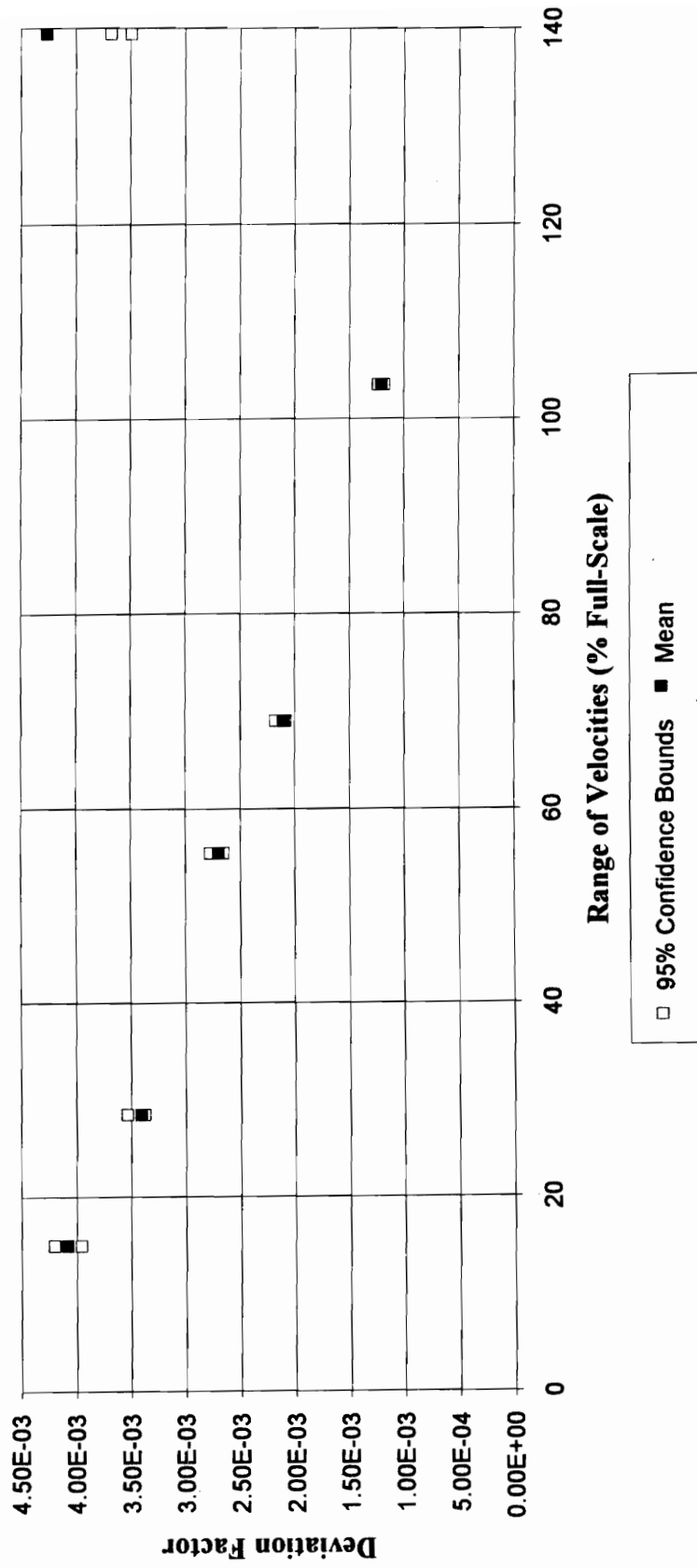


**Figure 4.1:** 'Deviation Factor' mean values and corresponding 95% confidence intervals for LOW velocity range. (MAGNAFLUX™ surface coating).

**'Deviation Factor' vs. Maximum Velocity Response  
(MEDIUM Range)**

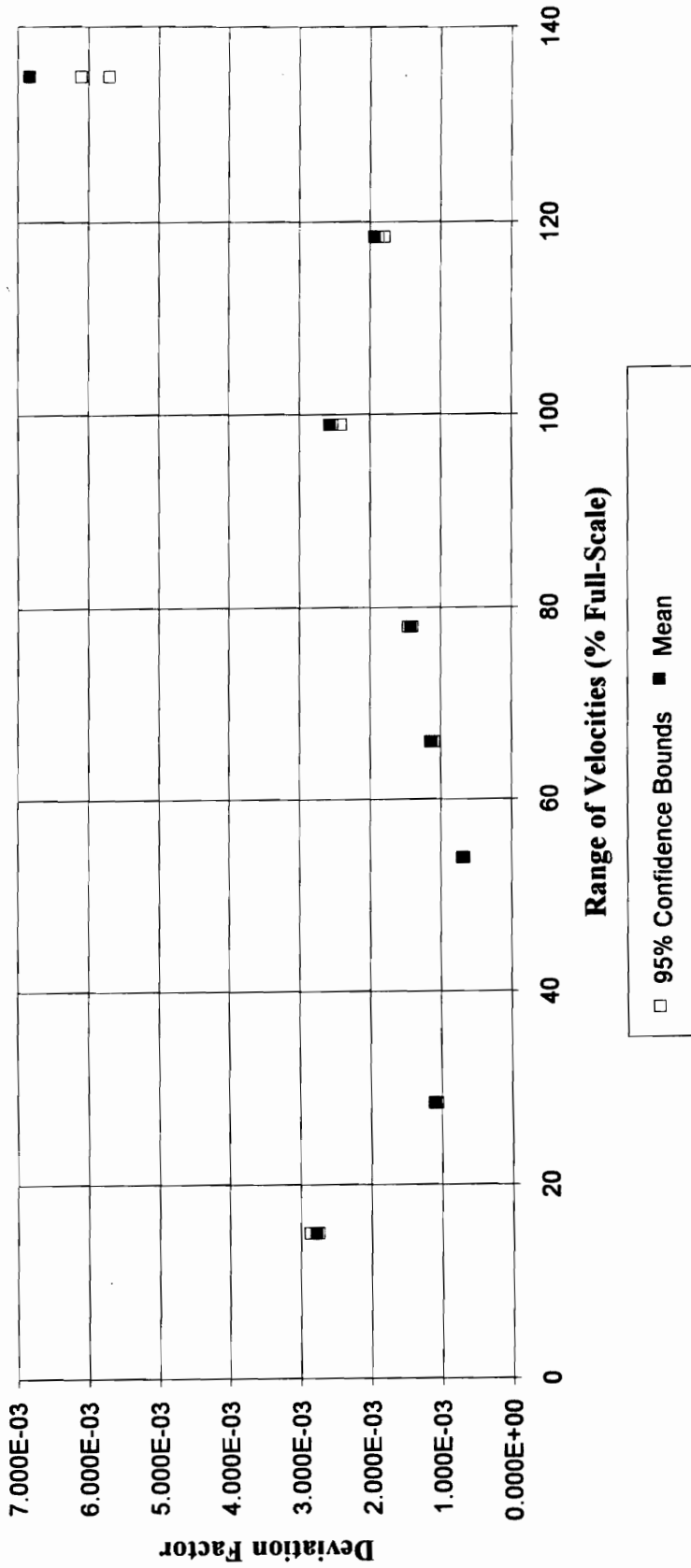


**Figure 4.2:** 'Deviation Factor' mean values and corresponding 95% confidence intervals for MEDIUM velocity range. (MAGNAFLUX™ surface coating).



## VELOCITY AND DOPPLER SIGNAL QUALITY

As mentioned above, the quality of some of the signals available to the SLDV user were also observed and captured via the Tektronix 2214 Digital Storage Oscilloscope. Figure 4.3 shows a representation of a stable Doppler signal and the corresponding velocity, and force signals. The signals are labeled Force, Velocity, Doppler, and Reference Force. Note that the signal labeled Velocity refers to the instantaneous analog velocity signal obtained via the BNC connection on the side of the laser optical unit. This plot was acquired with the laser measuring beam directed at a point near the horizontal center-line of the beam, and is meant to illustrate some characteristics of a point resulting in relatively stable Doppler and velocity signals.

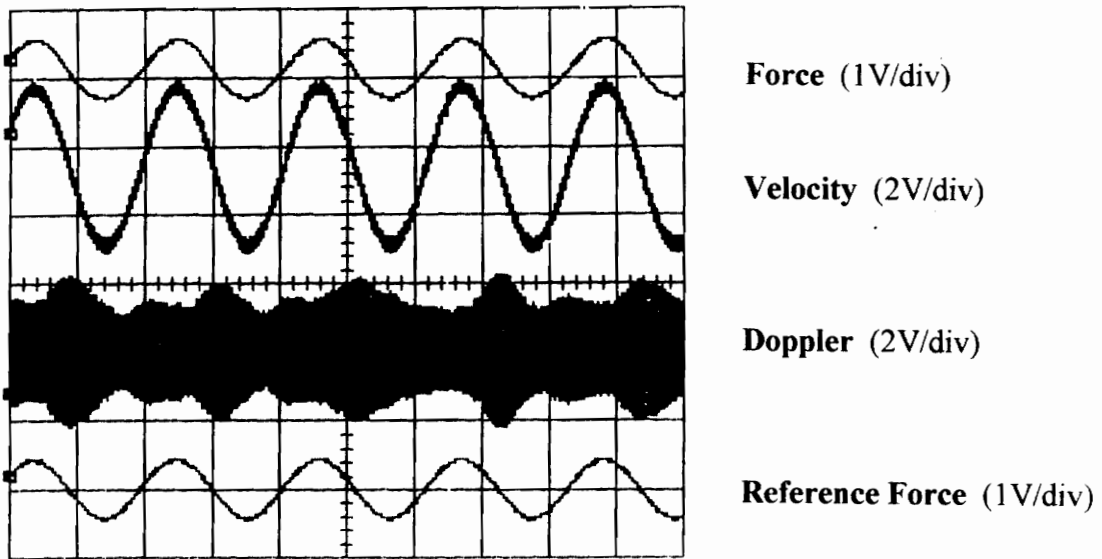
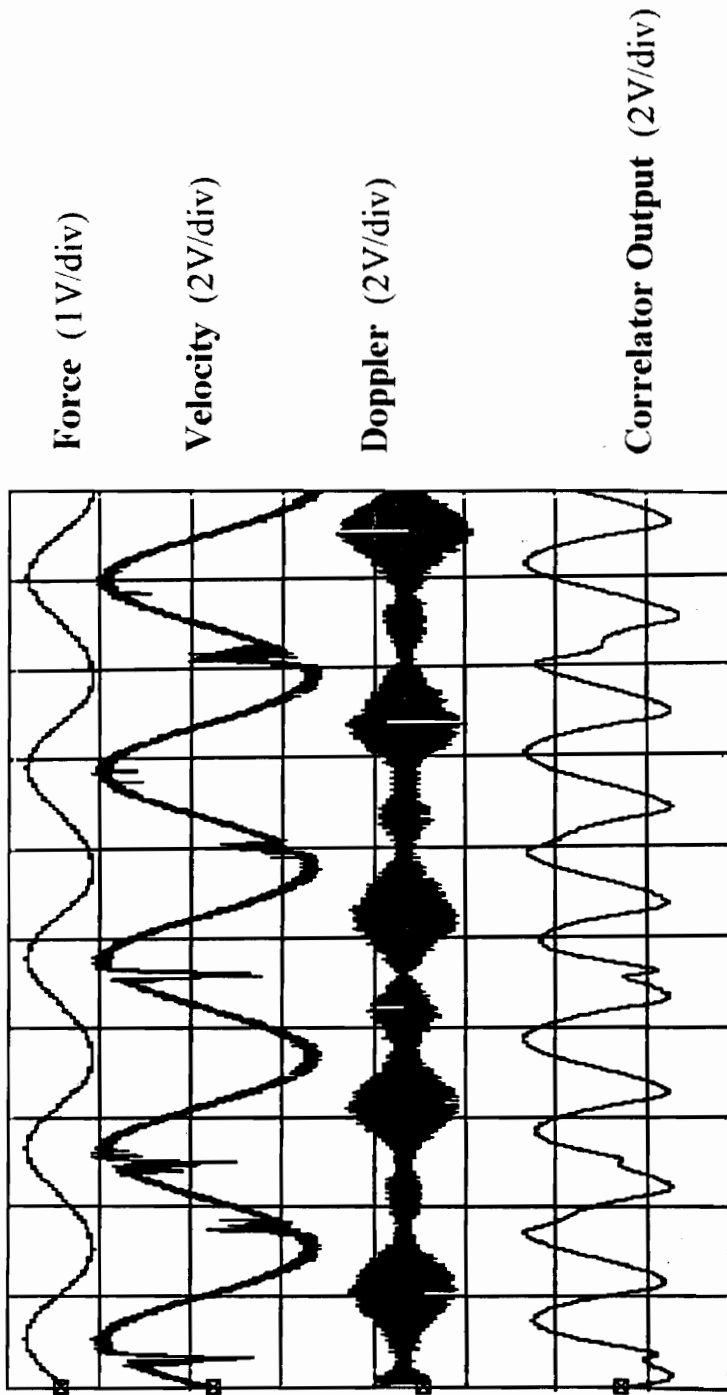


**Figure 4.3:** Oscilloscope plot ( $t = 5 \text{ ms/div}$ ) showing relative stable velocity and Doppler signals (point near center of beam).

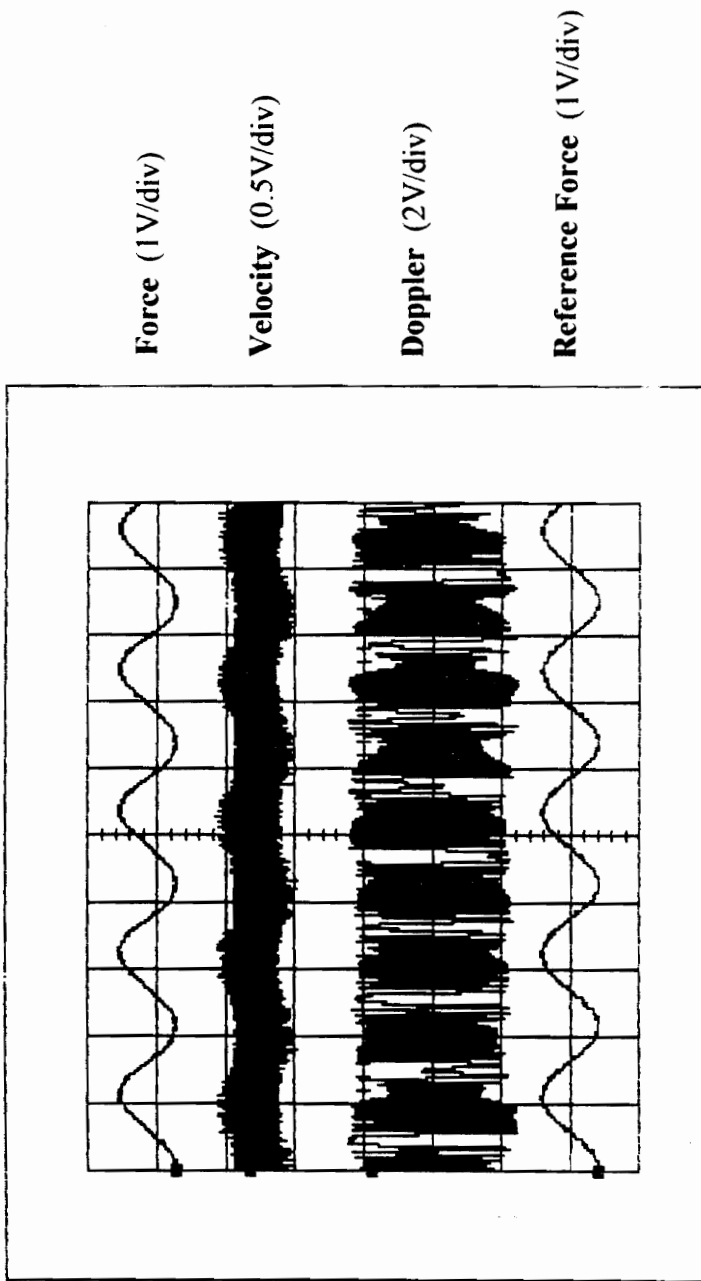
Figure 4.4 shows a similar plot, again acquired with the laser measuring beam directed at another point along the horizontal center-line of the steel beam. Note that in this plot, the signals are labeled Force, Velocity, Doppler, and Correlator Output. The Correlator Output signal refers to the real component of the full-wave rectified signal (as discussed in Section 4.2.1). It should be noted that all subsequent references to Velocity or Correlator Output signals will follow this nomenclature convention. This plot demonstrates the effect of the velocity drop-out on the Correlator Output signal and corresponding Doppler and velocity signals for points near the center-line of the structure.

Figure 4.5 shows an oscilloscope plot taken with the laser measuring beam directed at a point near a line of minimum velocity response. The signal convention presented in this plot is identical to that presented in Figure 4.3. This plot is meant to show some characteristic conditions of Doppler and velocity signals in these areas.

An oscilloscope plot of the Doppler and velocity signals at a point near the top (free-end) of the structure is presented in Figure 4.6. The purpose of this plot is to demonstrate some characteristic Doppler and velocity signals at points near the free-end of the vibrating steel beam. An additional purpose of this plot is to demonstrate the effect of the velocity drop-out on the Correlator Output signal and to demonstrate some characteristic Doppler and velocity signals for points near the free-end of the structure where transverse velocities and in-plane rotations are high simultaneously.



**Figure 4.4:** Oscilloscope plot (5 ms/div) showing velocity drop-out and corresponding Force, Doppler, and Correlator Output signals. (Point near horizontal and vertical center of beam).



**Figure 4.5:** Oscilloscope plot (5 ms/div) showing Velocity, Force, Doppler, and reference Force signals. (Point near line of minimum response).

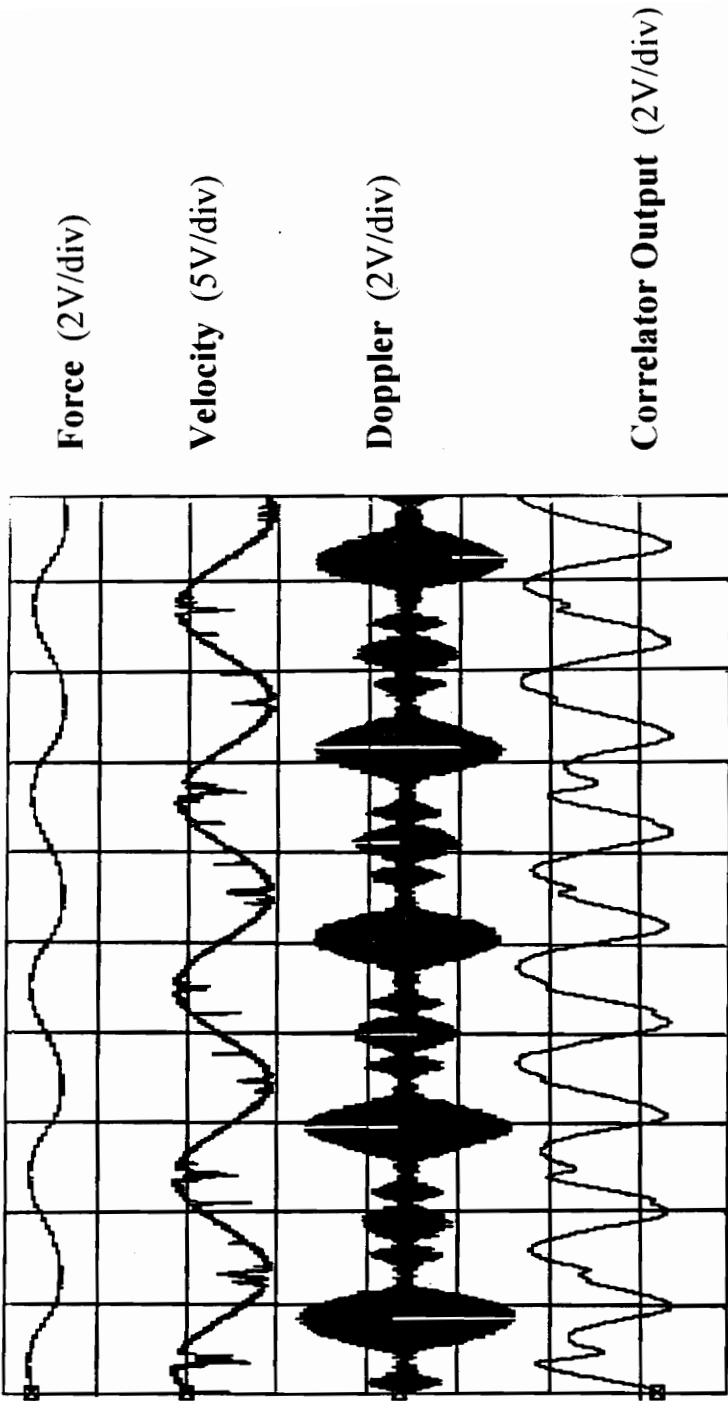


**Figure 4.6:** Oscilloscope plot (5 ms/div) showing velocity drop-out, corresponding Force, Doppler, and Correlator Output signals. (Point near horizontal and vertical center of beam).

#### ***4.1.4 DISCUSSION OF RESULTS***

A review of the individual scan plots in Appendix A.1 demonstrates that the areas of noise do predominately occur at the areas of maximum absolute velocity response. Additionally, it can also be seen that these areas of noise tend to bias the velocity scan data towards the zeros axis. Note that the areas of laser noise within the scans, with the exception of the scans mentioned below, never seem to exceed an “envelope” of data approximately delineated by the median DFT-IDFT fitted-curve. In other words, the velocity data is biased-low by the presence of these areas of noise and, thus, this seems to confirm the definition of biased noise given in Chapter 3. Note that the only exception of this occurs in scan groups L1, L2, M1, and M2 (range of velocity responses of approximately 15% - 30% of full-scale). In these scans it can be seen that some laser noise may occur at absolute velocity levels greater than the DFT-IDFT “envelope”. Although it can also be seen that the bulk of the laser noise still tends to bias the velocity data towards the zero axis.

At first inspection of the scans presented in Appendix A.1 it may seem that the previous assumption of the spatial nature of the velocity drop-outs would require that repeated scans (such as the scans within each scan group) would show identical points of drop-out. It can be seen from the plots within each scan group that although the spatial distribution of the laser noise seems consistent (i.e. occurring at the maximum velocity response areas), identical individual scan points do not consistently show laser noise

effects. A explanation of this could be a result of one or both of the following situations. Previous literature analyzing the operation of the SLDV reported by Li [55] indicates that the non-repeatability of the galvanometer driven mirrors has been observed as high as  $0.053^\circ$ . At best, given the distance from the VPI Sensor to the vibration structure, this translates into 0.123 in (3.12 mm) on the surface of the beam. This is much larger than the size of the theoretical single bright speckle falling on the active area of the detector given in Chapter 3 as approximately 0.04 in (1mm) by 0.04 in (1 mm). Additionally, given the size of this theoretical speckle, it would be hard to believe that during the periodic motion of the vibrating structure the laser measuring beam would illuminate a spot within the specification given by the detector size. Also, given the random nature of the speckle pattern one can argue that minute differences in the laser measuring beam spot position could result in the detector being covered with a dark speckle or a combination of speckles consisting of portions of adjoining speckles. Therefore, one can argue that the assumption of the spatial nature of the velocity drop-outs is still valid.

Another point becomes obvious when viewing the individual scan plots presented in Appendix A.1. Note that although the noise consistently occurs at the areas of maximum velocity response, it does not seem to be consistent with respect to distinct velocity responses. In other words, the occurrence of the laser noise seems to be associated with the position of a particular velocity response with respect to the operating shape. An example to illustrate this point is shown in Figures 4.7 and 4.8. For example in Figure 4.7, note the occurrence of the laser noise at the areas corresponding

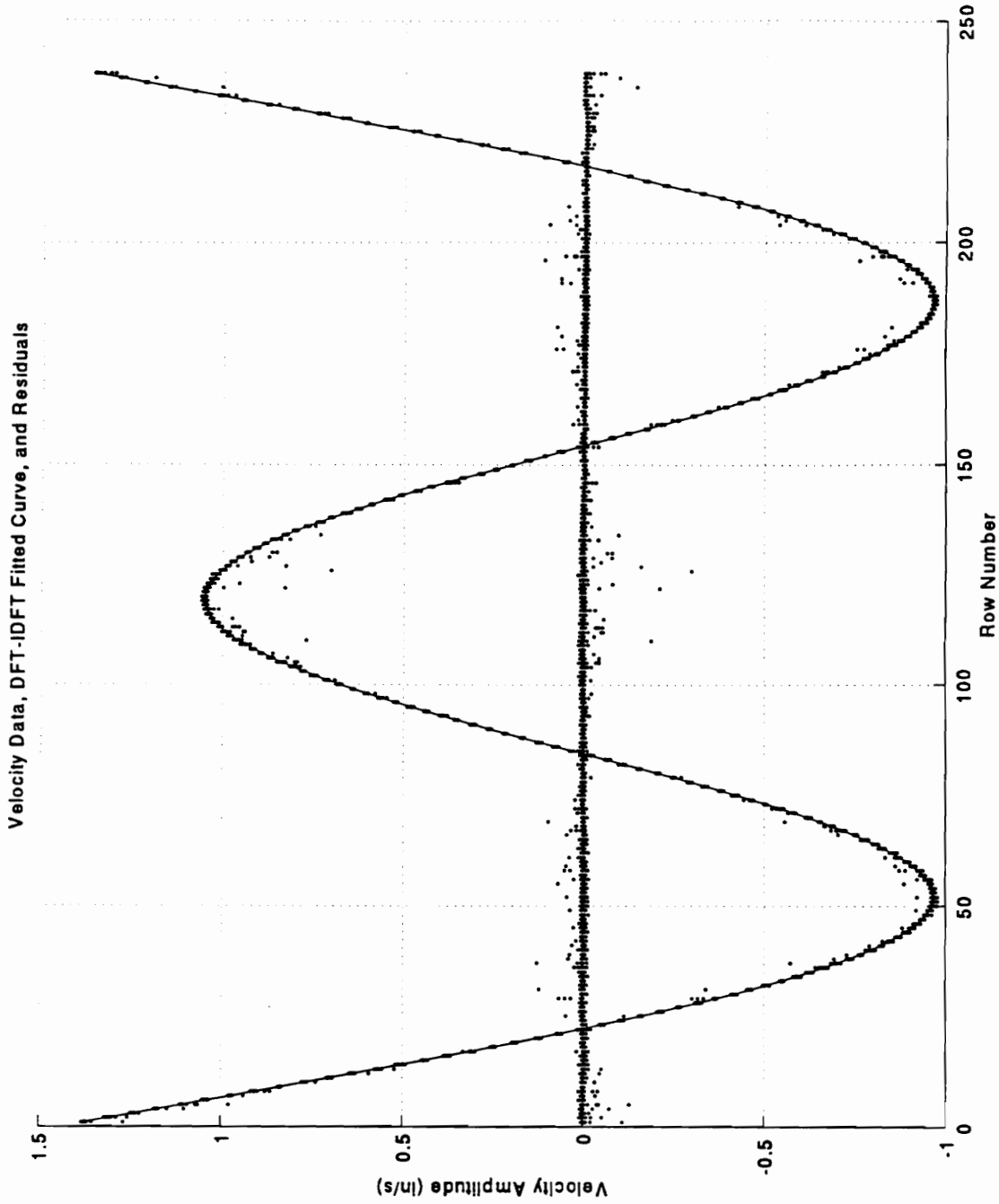


**Figure 4.7:** Example scan-fit plot. Note the noisy areas in the  $\sim 1$  in/sec velocity regions (MEDIUM velocity range setting, MAGNAFLUX™ surface coating).



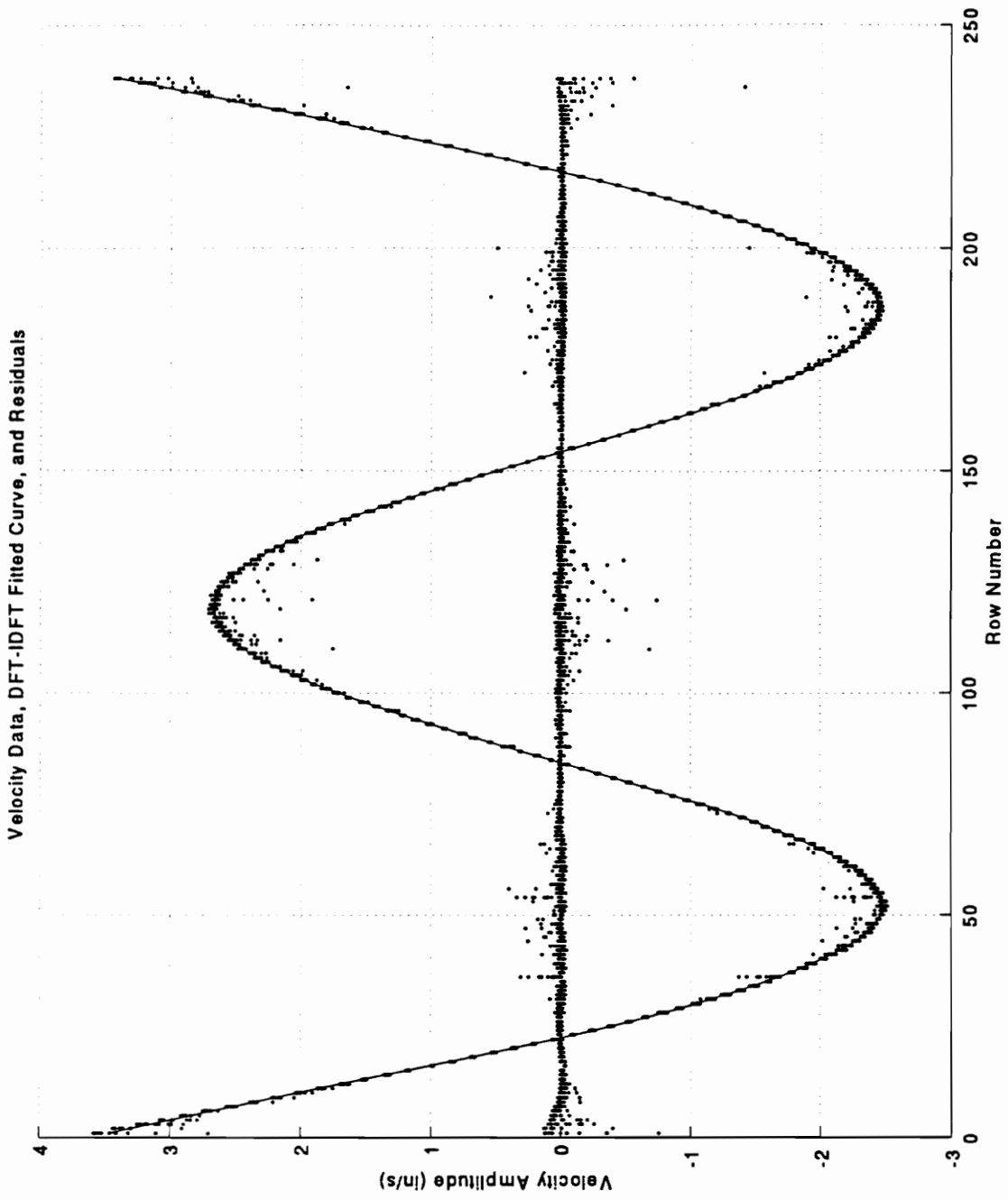


**Figure 4.8:** Example scan-fit plot. Note the lack of noise in the  $\sim 1$  in/sec velocity regions. (MEDIUM velocity range setting, MAGNAFLUX™ surface coating).

to an amplitude of approximately 1 in/s. Now, note the areas on the beam which correspond to a velocity amplitude of 1 in/s in Figure 4.8. There seems to be relatively little noise at this velocity amplitude, but on the other hand there is a relatively large amount of laser noise occurring again at the areas of maximum velocity responses. These representative plots seem to demonstrate that the noise phenomenon, although occurring at the areas of maximum velocity response, seem to be associated with areas which have similar speckle pattern motions. A confounding point is that the area of the beam corresponding to 1 in/s in Figure 4.8 has a high angle of rotation during vibration. This means that gross speckle motion is expected in this region. See Section 2.2 for a discussion of this phenomenon. One wonders if the large scanning of the speckle provides an average speckle pattern that can be decoded by the balanced modulator-demodulator.

In order to further illustrate the above statement, note Figures 4.9, 4.9(a), 4.10, and 4.11. Figure 4.9 shows the relationship between the fraction of absolute velocity response and the corresponding residuals for a typical scan. Note that the residuals seem to increase as the fraction of maximum absolute velocities increase to a certain point (this area corresponds to the maximum velocity response areas not including the free-ends of the structure), but note that residuals then seem to then fall off and rise again as the fraction reaches 1.0 (which corresponds to the free-ends of the structure. The same information can be found in Figure 4.9(a). This figure shows the residuals normalized by the magnitude of the velocity. (Note that the normalized residuals in the areas at, or close to zero velocity are exceptionally large due to division by near-zero terms.)

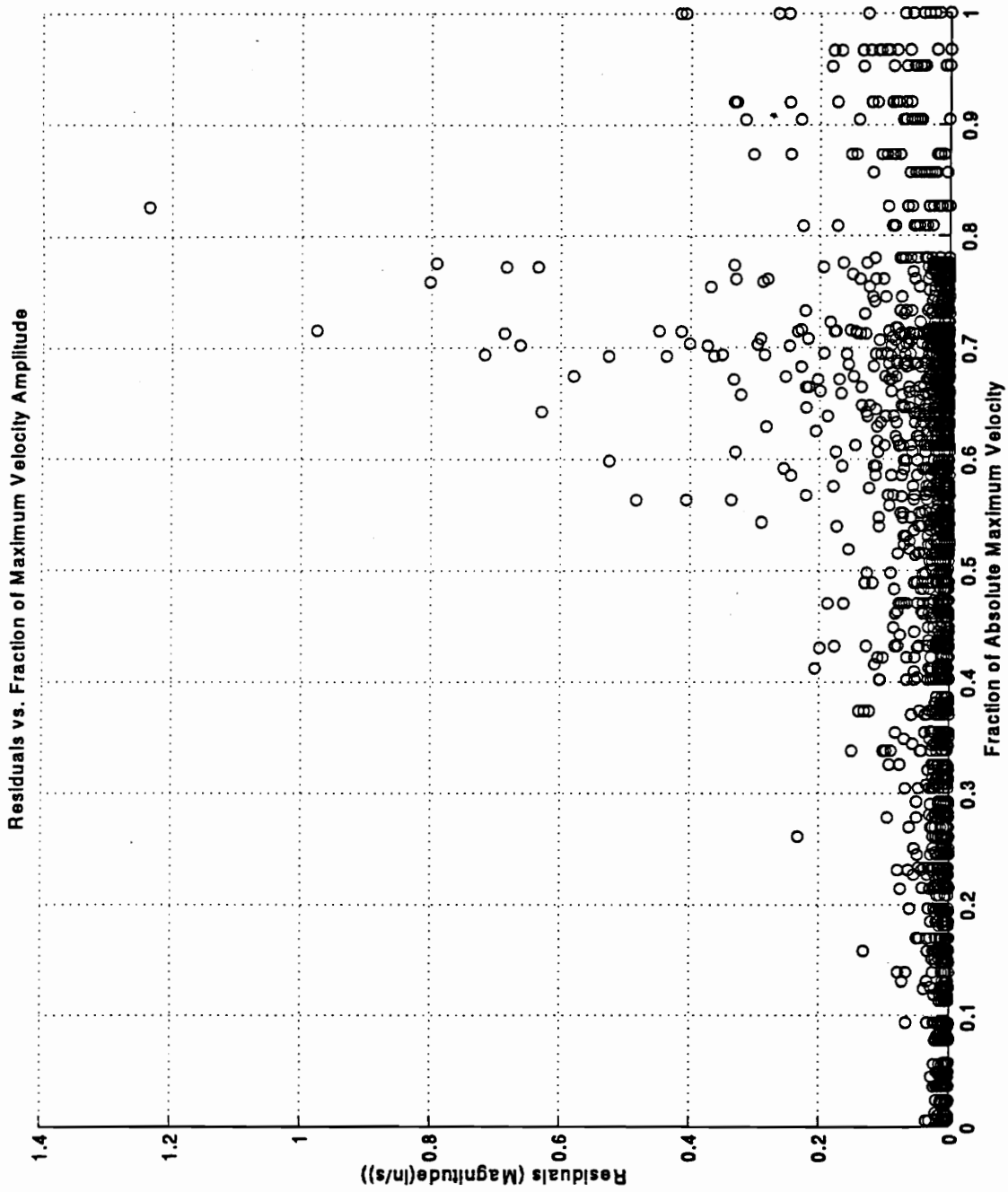


**Figure 4.9:** Magnitude of residuals plotted against fraction of absolute maximum velocity for a typical scan. (MEDIUM velocity range setting, MAGNAFLUX™ surface coating).

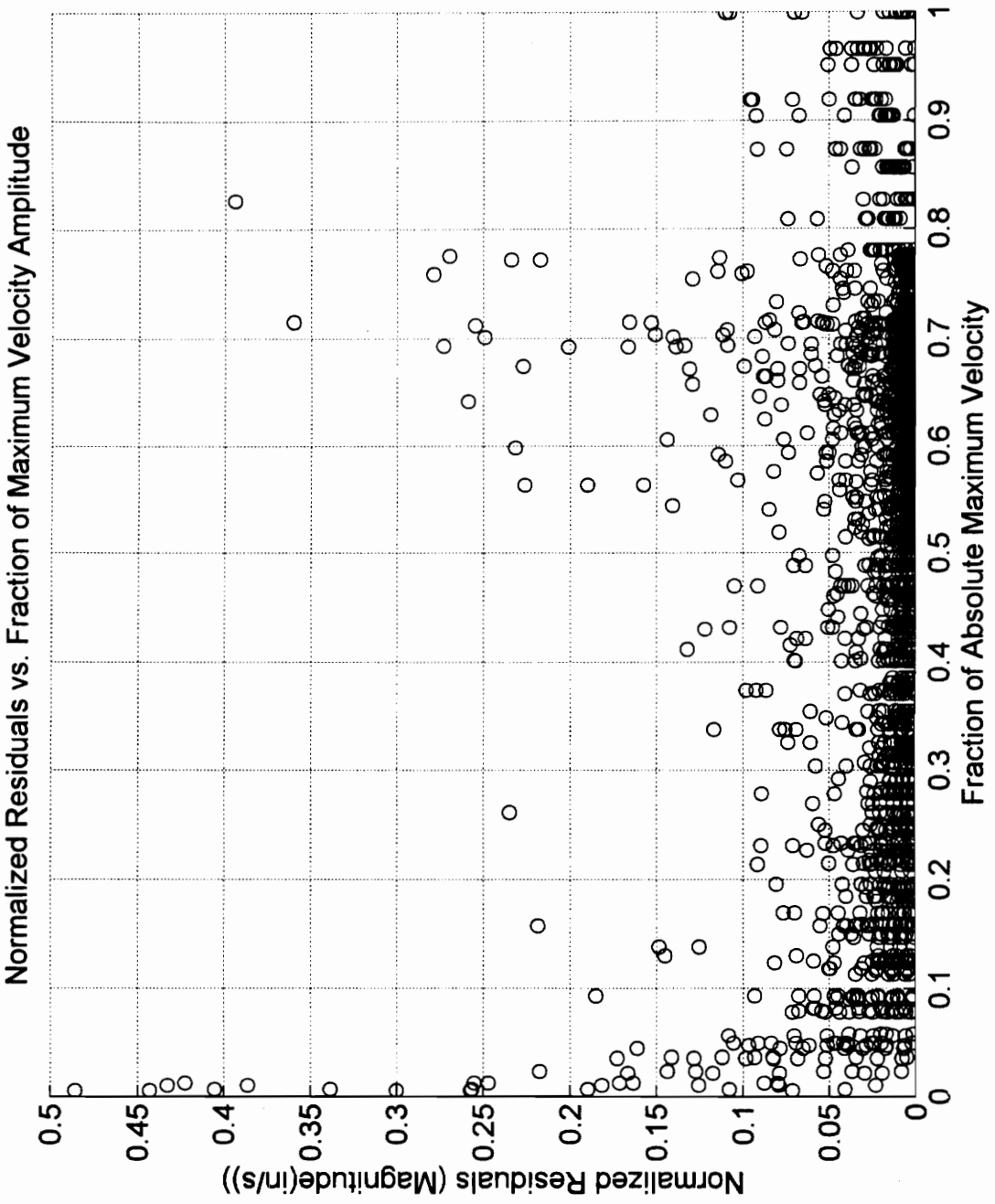


**Figure 4.9(a):** Normalized magnitude of residuals plotted against fraction of absolute maximum velocity for a typical scan. (MEDIUM velocity range setting, MAGNAFLUX™ surface coating).

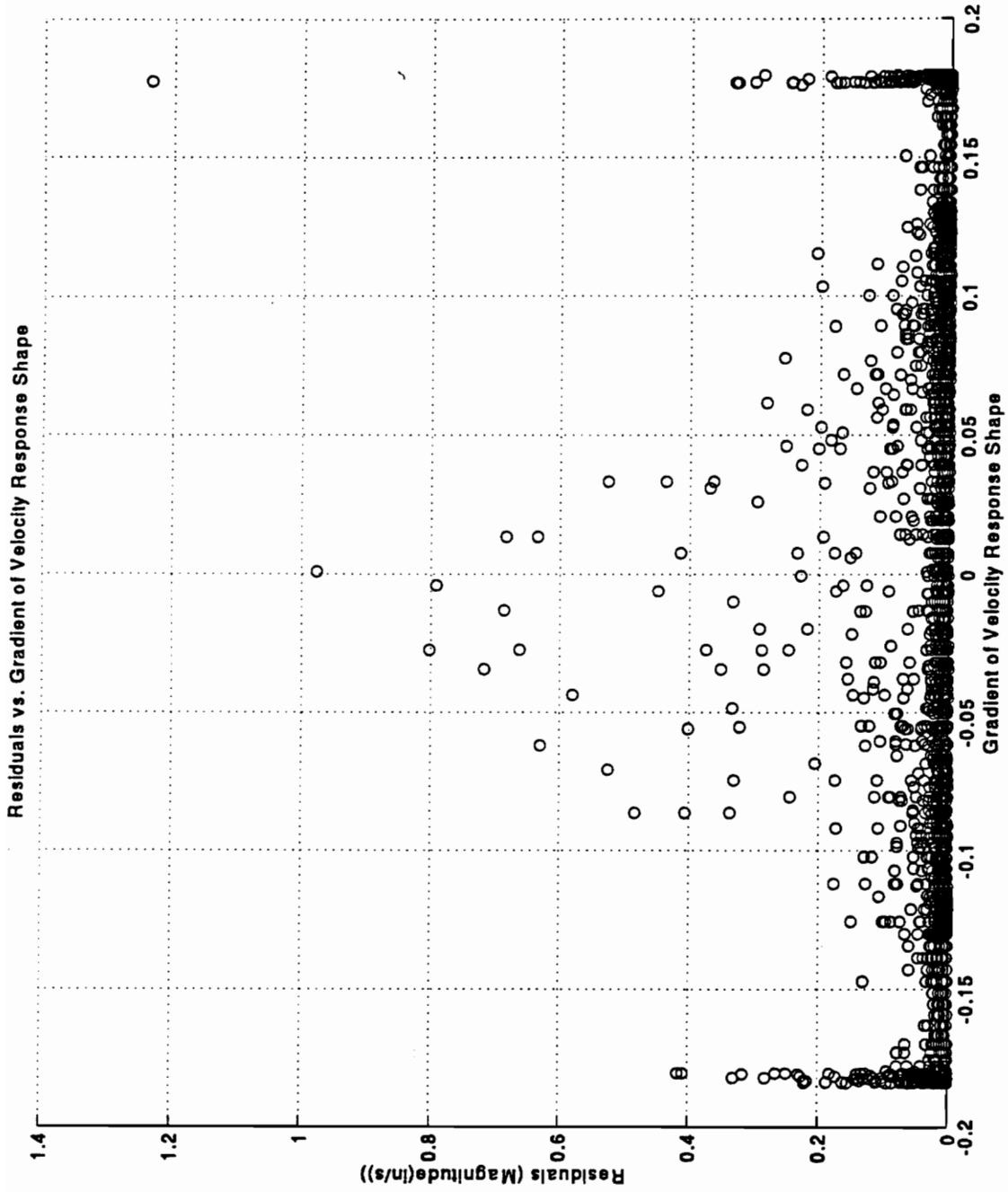


**Figure 4.10:** Magnitude of residuals plotted against gradient of velocity response shape for a typical scan. (MEDIUM velocity range setting, MAGNAFLUX™ surface coating).



**Figure 4.11:** Plot showing magnitude of residuals with respect to fraction of maximum velocity amplitude and gradient of the velocity response shape for a typical scan.

Now note Figure 4.10 which shows the relationship between the gradient of the velocity response shape and the magnitude of the corresponding residuals for the same typical scan. Note that this figure seems to demonstrate that the occurrence of the laser noise increases as the gradient of the response shape approaches zero. Also note the increase of residuals at the largest absolute gradient values. These two areas correspond to the areas of maximum velocity response. In combination, the information contained in these two figures again demonstrates that the occurrence of the residuals (and thus laser noise) seem to correspond to the motion of the beam. More specifically, the areas with less laser noise correspond to areas of the structure which are undergoing large rotations. Areas in which the gradient of the velocity response shape approach zero are more prone to the occurrence of laser noise and correspond to areas of the structure which are undergoing out-of-plane displacements. The free-ends include a combination of the two motions with large rotations and large out-of-plane displacements. The relative sensitivity of the SLDV system to these motions may then explain why the residuals seem to drop off in Figures 4.9 and 4.9(a), in that the large rotation component may be helping to reduce the occurrence of the laser noise in these areas. Figure 4.11 shows a plot combining the information contained in the two previous figures. It should be mentioned that the shape evident in the data is caused by the relationship between the gradient of the response shape and the response amplitude due to the pseudo-harmonic nature of the response shape. What should be noted are the increased residuals for the areas of low gradient - high amplitude and the increased residuals in the areas of high amplitude - high gradient (free-

ends). In total the information suggested by these figures seems to further indicate that the occurrence of the laser noise corresponds to the particular motion of the structure. Portions of the beam with large motions and large rotations have lower residuals than would be expected from their out-of-plane vibration amplitude. These will be further discussed in subsequent experiments.

A review of Tables 4.3 and 4.4 and the corresponding plots given in Figures 4.1 and 4.2 respectively yield a few observations. Specifically the  $DF$  values begin at a larger value and as the range of velocity responses increase they reach a minimum. As the range of velocities increase, the  $DF$  values begin to rise again. Table 4.3 shows that there was an optimal operating range of velocities for the LOW velocity range setting occurring with scan group L5 which corresponds to a range of velocities from zero to 103.5% of full-scale. Table 4.4 shows that there is a similar optimal operating range of velocities for the MEDIUM velocity range setting occurring with scan group M3 which corresponds to a range of velocities of approximately 54% of full-scale. It should be stressed that due to the limitations resulting from the differences between the range of velocities for the scan groups it is difficult to determine the exact location of the optimal operating range of velocities. This is best illustrated in Figures 4.1 and 4.2. Therefore, without further information, a more accurate claim may be that the optimal operating range of velocities for the LOW velocity range falls at a level approximately between 70% and 100% of full-scale and that for the MEDIUM velocity setting falls at a level approximately between 30% and 65% of full-scale. (Note that the given optimal operating range terminates at



100% because the LED velocity Signal Monitor scale available to the user does not include values in excess of 100 units.)

Another point worthy of note concerns the  $DF$  values presented in Table 4.4 and Figure 4.2. A review of the figures in Appendix A.1 corresponding to scan groups M7 and M8 (maximum velocity responses at approximately 120% and 135% respectively) indicates that some of the DFT-IDFT fitted-curves for these scans are corrupted due to an apparent overload of the laser system which severely biases the velocity data low at the ends of the beam. In other words, one can argue that the DFT-IDFT fitted-curves generated for these scans are not representative of the deterministic velocities corresponding to the *true* operating shapes of the vibrating structure. For this reason, it is expected that the true  $DF$  values calculated for scan groups M7 and M8 are greater than those represented in Table 4.4 and Figure 4.2. It is interesting to note that the effect does not seem to be as drastic with the LOW velocity range setting. The scan-fit plots for scan group L6 do not indicate the degree of overloading represented in the plots for scan groups M7 and M8. This may indicate that the LOW velocity range setting is more tolerant to a larger amount of overshoot than the MEDIUM velocity range setting. Nevertheless, with the current Signal Monitor LED configuration it is difficult to determine with any degree of accuracy how much overshoot is involved if the velocities reach the 100 unit graduation.

A final point regarding Figures 4.1 and 4.2 concerns the 95% Confidence Bounds for scan groups L6, M6, M7, and M8. Note that the confidence bounds for these scan

groups do not straddle the mean  $DF$  value. One can theorize that this may be a result of the more severe velocity biasing (as mentioned above) occurring in these scan groups. These excessive 'drop-out' terms may be aggregating such that they violate the underlying assumptions made in the development of the confidence bounds.

## **VELOCITY AND DOPPLER SIGNAL QUALITY**

A review of the oscilloscope plots presented above suggests some interesting characteristics. First, all of the figures seem to confirm that the areas in which the Doppler signal drops below a threshold voltage value do, indeed, result in velocity drop-out. Further observance of the plots displaying the Correlator Output signal confirms the effect of the drop-out on the signal from which the subsequent digitized velocity matrix will result. This seems to confirm that the data points which contain noise, as those described in Section 4.1, are a result of the velocity drop-out resulting from insufficient Doppler signal amplitudes.

Secondly, note that the "stable" Doppler signal shown in Figure 4.3 reveals an amplitude modulation of the signal. Also note the condition of the Doppler signals in Figures 4.4, displaying "unstable" signals corresponding to a measuring point near the horizontal center-line of the steel beam. Before continuing, recall that Chapter 3 described that the SLDV system operates on the assumption that the laser optical unit detector ideally only receives one bright speckle when acquiring data [39]. Now note that the Doppler signal seems to alternate between a large "bulge", a drop-out, a smaller "bulge",

and a drop-out again. It can be argued that the measurement point is slightly off of the vertical and horizontal central position (which is most likely be the case due to the fact that placing the measuring beam on the *exact* center of the beam would be extremely difficult to achieve). Therefore, it is suggested that one cause for the occurrence of this periodic phenomenon may be that the bright speckle (or intensity resulting from a combination of speckles) presumably on the detector is moving slightly off of the detector, changing direction, moving back across the detector, changing direction, and moving once again back across the detector. This could be a result of the anticlastic effect (if the measuring point is slightly off of the vertical center-line) or the bending effect (if the measuring point is slightly off of the horizontal center-line) of the vibrating structure. One can further argue that the points of drop-out may be a result of the random nature of the speckle pattern. At these points the detector may be covered with a completely dark speckle thus driving the Doppler signal amplitudes below the threshold value and in turn resulting in the velocity signal drop-out. The “bright speckle” (or intensity resulting from a combination of speckles) may then cover the detector after which, due to the periodic motion of the beam this process repeats itself as demonstrated in the figure. One can note the potential for the above phenomenon when considering the size of the detector and the extent of motion which may cause such a modulation in the Doppler signal. For example, consider a single bright speckle of approximately 0.0394 in (1 mm) diameter covering the detector and assume that the intensity resulting from this speckle is slightly above the modulator-demodulator threshold. Now assume that the speckle moves so that only half

of the speckle is covering the detector, and that the adjoining speckle is completely dark. This would only require movement of approximately 0.0197 in (0.5 mm). The resulting intensity would be 50% of the that for the entire speckle. Now assume that the speckle begins covering the detector and moves approximately 0.0295 in (0.75 mm). Using the area of the segment of a circle equation, the resulting intensity would be approximately 20% of that for the entire speckle. The above illustrates the potential reduction of speckle intensity due to small motions of the speckle. Furthermore, the above scenario assumes that the intensity distribution within a single speckle is constant, which is most likely not the case. Thus, one can argue that such motions of the speckle may cause the Doppler signal modulations demonstrated in the figure.

One can see from Figure 4.5 the oscilloscope plot taken at a point near a line of zero response, that there are few apparent Doppler modulations similar to those in Figures 4.3 and 4.4. Also note that the Doppler signal amplitude is approximately 4V pk-pk at this point. Based on the inferences developed from this oscilloscope plot, coupled with the spatial distribution of the laser noise noted above, one can then argue that the particular speckle pattern motions produced at similar points seem to produce more “stable” Doppler signal amplitudes.

Figure 4.6, corresponding to measuring points on the top (free-end) of the beam, exhibits a different Doppler signal pattern. Note that Doppler signal seems to alternatively contain one large “burst”, a drop-out, a smaller “burst”, a slightly larger “burst”, a smaller “burst”, and another drop-out. It can be similarly argued that the Doppler signal pattern

shown in this figure is a result of different speckles (or speckle patterns) traveling across the detector in a repeated manner corresponding to the periodic in-plane motion of the vibrating structure. It should be noted that although Figures 4.6 represents signals resulting from the velocity and Doppler signals at the top of the beam, it is assumed these plots are representative of the signals which would occur at both free-ends of the steel beam (i.e. top and bottom ends).

The spatial distribution of the laser noise and the associated oscilloscope plots raises many questions concerning the relationship between the occurrence of the laser noise and the corresponding speckle pattern motions produced. The interesting point being that the occurrence of the laser noise is spatially consistent with respect to the motion of the structure. One can, therefore, theorize that the consistent areas of laser noise are undergoing similar speckle pattern motions. That is to say that the speckle pattern motions at the free ends are presumable similar, that the speckle pattern motions at the minimum response areas are similar, and that the speckle pattern motions at the areas of maximum response are similar to other points of like motion.

Insights into the spatial distribution of the laser noise areas coupled with the observed periodic amplitude modulation of the Doppler plots resulting from the execution of this experiment lead to an investigation into the speckle pattern motions which are “seen” by the detector. This was investigated in the experiment presented in the next section.

## **4.2 SPECKLE PATTERN MOTION EXPERIMENT**

As discussed in Chapter 2, speckle pattern and speckle pattern motion have consistently been mentioned when referring to SLDV velocity data quality and the velocity drop-out effect. It seems, though, that little work has been done concerning observation of the speckle pattern and the speckle pattern motion received at the detector of the SLDV. Consequently, the main objective of this experiment was to observe the differing speckle patterns and speckle pattern motions received at the VPI Sensor detector. Additionally, an attempt to quantify the relative difference in speckle pattern motions observed at separate areas of the vibrating structure were made.

### **4.2.1 EXPERIMENTAL DESCRIPTION**

The setup for this experiment was again similar to those presented above. A signal generator amplitude of 400 mV (taken from the HP 3324A Function Generator) was used to excite the steel beam via the power amplifier and shaker near its 3rd bending mode and in order to remain consistent the resonance-dwell technique was employed. The laser was left in its current position, 133.1 in (3380.7 mm) from the center of the steel beam. In order to observe the speckle pattern received by the detector, a thick white piece of cardboard was placed directly in front of the VPI Sensor laser optical unit. A rectangular hole approximately 1.25 in (31.75 mm) by 1.5 in (38.1 mm) was cut in the cardboard so that the laser beam could pass through without incident throughout the full range of

motion needed for the experiment. Nine points of interest were chosen on the beam: the two free-ends, and the four areas of minimum response and three areas of maximum response in between. The reader should note for the purpose of facilitating a clearer description of the subsequent experiment, the four areas of minimum response will, henceforth, be referred to as *nodes*, and the three areas of maximum response will, henceforth, be referred to as *antinodes*. The position of these points of interest with respect to the steel beam are shown in Figure 4.12. Small circular pieces of 3M Scotchlite™ self-adhesive sheet measuring approximately 0.5 in (12.7 mm) in diameter were cut and placed on the nine areas.

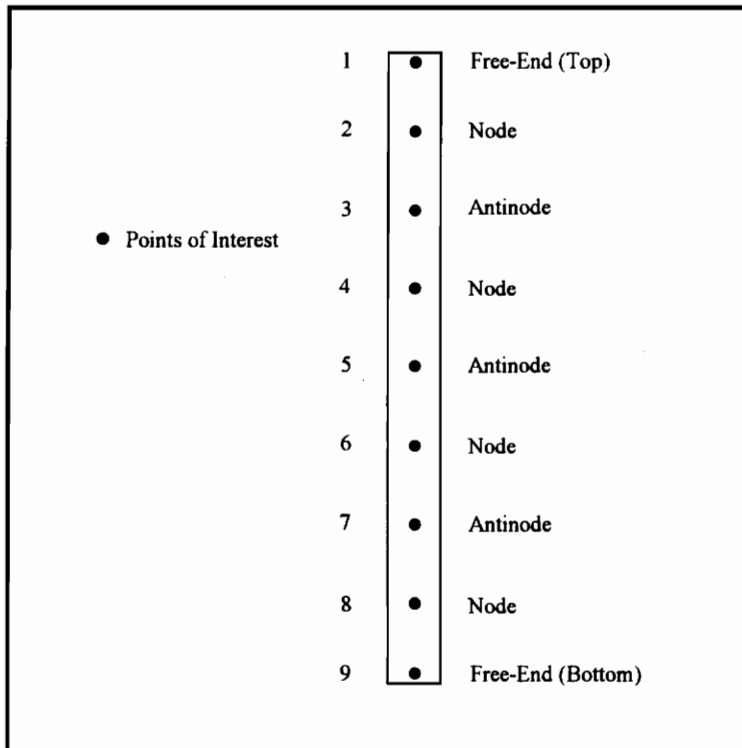


**Figure 4.12:** Steel beam showing nine points of interest for speckle pattern motion experiment.

In order to clearly view the speckle patterns, the experiment was performed at night with the lights in the laboratory turned off. Observations could then be made concerning the relative motion of the speckle pattern at each of the nine points. In an attempt to quantify the motion of the speckle pattern at these points, measurements of speckle size were taken in a static state (beam not vibrating), and a dynamic (beam vibrating) state. In the static state, focus was adjusted to obtain a fine granular speckle pattern. A single speckle was then chosen as a reference and measured with a straightedge which was graduated to 1/100th of an inch. The beam was then returned to its dynamic state, and the same reference speckle (or resulting speckle streak) was measured. This same procedure was carried out for all nine points of interest. A speckle pattern motion gain is introduced which could then be calculated by forming a ratio between the dynamic speckle size (which will be referred to as the ‘speckle motion span’) and the static speckle size (which will be referred to as the ‘typical speckle diameter’). Equation 4.1 shows the relationship for the ‘speckle motion gain’:

$$SG = \frac{s_d}{d_s} \quad (4.1)$$

where  $s_d$  is the speckle motion span and  $d_s$  is the typical speckle diameter. The  $SG$  terms could then be plotted with respect to the nine points in order to graphically represent the relative amount of speckle pattern motion.



#### **4.2.2 EXPERIMENTAL OBSERVATIONS**

There were a few observations made which the author believes important to note. The first observation concerned the dominate direction of the speckle motion observed during the experiment. It was observed that the visible speckle motion (if any was detected) was predominately in the vertical direction with respect to the structure. It should be noted that this observation does not necessarily preclude any small motions in the horizontal direction, it only reports that the observed *dominate* motion was in the vertical direction. Such small “side-to-side” motions were not visible to the naked eye but may have been present.

Another noteworthy point concerns the appearance of the speckle patterns. It was observed that the maximum focus level (as indicated on the side of the optical unit) corresponded to a speckle pattern which contained the largest “granules”, including both bright and dark speckles. Additionally, at the maximum focus level ,the speckle pattern (as viewed on the white cardboard) was relatively blurry. Subsequently, during the execution of this experiment the focus was adjusted to obtain a speckle pattern which was most legible. This meant that the actual focus levels used during the experiment were not maximum. It was assumed, however, that the resultant speckle motion gains were relative and, thus, independent of the focus level.

It was also observed during the execution of this experiment that the Doppler amplitudes and related focus level readings were much higher on the points where the 3M

Scotchlite™ retroreflective tape was used. Typical focus level readings approached 100 units on the Signal Monitor. These levels corresponded to Doppler amplitudes in the neighborhood of 10 V pk-pk.

#### 4.2.3 EXPERIMENTAL RESULTS

The results of the measurements of the speckle patterns for the nine points of interest are summarized in Table 4.5. Also included in the table are the calculated speckle motion gains.

**Table 4.5:** Summary of the speckle pattern motion measurements and speckle gains resulting from the nine points of interest.

| Point # | Position          | Typical Speckle Diameter (in)<br>[mm = x 25.4] | Speckle Motion Span (in)<br>[mm = x 25.4] | Speckle Motion Gain SG |
|---------|-------------------|--|---|------------------------|
| 1       | Free-End (Top)    | 0.04   | 2.50                                      | 62.5                   |
| 2       | Node              | 0.05   | 1.60                                      | 32.0                   |
| 3       | Antinode          | 0.05   | 0.05                                      | 1.0                    |
| 4       | Node              | 0.05   | 0.80                                      | 16.0                   |
| 5       | Antinode          | 0.05   | 0.10                                      | 2.0                    |
| 6       | Node              | 0.05   | 0.80                                      | 16.0                   |
| 7       | Antinode          | 0.05   | 0.07                                      | 1.4                    |
| 8       | Node              | 0.04   | 1.40                                      | 35.0                   |
| 9       | Free-End (Bottom) | 0.05   | 2.20                                      | 44.0                   |

A graphical representation of the speckle motion gain with respect to the position along the beam (point number) is shown in Figure 4.13.

### Speckle Motion Gain vs. Position Along Beam

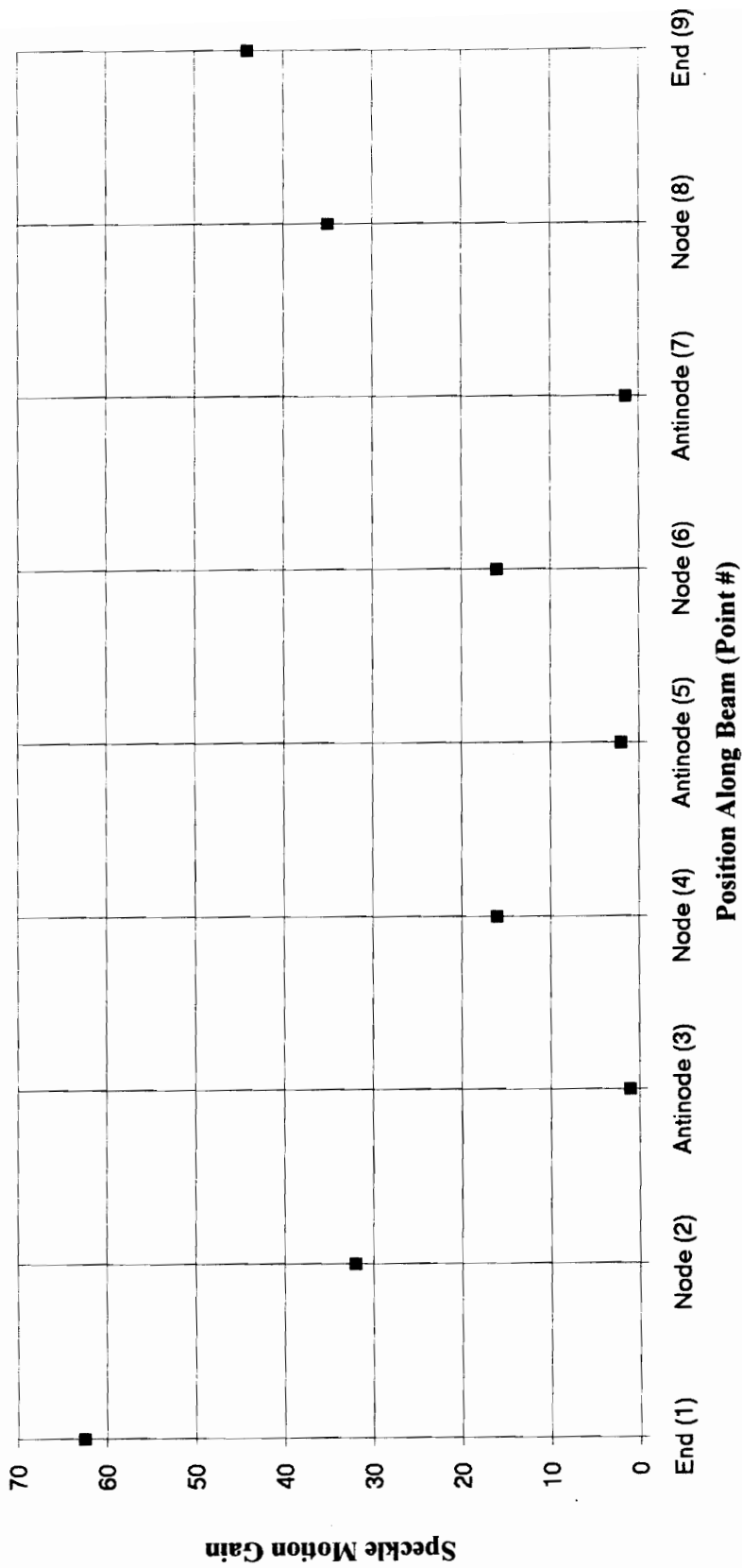


Figure 4.13: Plot showing speckle motion gain with respect to position on steel beam.

#### **4.2.4 DISCUSSION OF RESULTS**

There are several implications resulting from this experiment. First, it can be seen from Figure 4.13 that there was relatively little speckle motion at the antinode areas (Points #3, #5, and #7). In fact, during the experiment it was very difficult to determine whether or not the structure was in a dynamic state when viewing the appearance of the speckle patterns at these points. Note that one possible explanation for a speckle motion gain value of 2 for the antinode at Point #5 could be a result of the laser measuring beam being positioned slightly off of the horizontal center-line of the structure (the theoretical antinode).

Alternatively, it can be seen that the relative speckle motion gain at the nodes and free-ends are much larger. The speckle motion gains at the two nodes closest to the center of the beam (Points # 4 and #6) were approximately an order of magnitude greater than the antinodes. Also note that the speckle motion gains at the nodes corresponding to Points #2 and #8, were approximately 1.5 orders of magnitude greater than the antinodes. Additionally, note that the two free-ends resulted in the largest speckle motion gains. An explanation for the difference in the speckle motion gains resulting between the top free-end (Point #1) and the bottom free-end (Point #9) could be a result of the fact that the electrodynamic shaker placement on the beam corresponds with Point #1.

Previous literature concerning laser noise had hinted that speckle pattern motion across the detector was most likely the cause of such noise. Note that although at the nodal areas there is considerable speckle pattern motion, it was learned in Section 4.1 that the noise is not spatially associated with these areas of minimal response. Additionally, note that at the antinode areas, where the noise was previously found to occur, the visible speckle pattern motion is minimal. A potential explanation in line with the spatial distribution of drop-outs assumption, could be that at the antinode the intensity distribution “picked up” by the detector may be very sensitive to small movements of the theoretical single speckle (or combination of speckles) on the detector. One can further theorize that given the approximate size of the active area of the detector, 0.04 in (1 mm) by 0.04 in (1 mm), a small movement may position a dark speckle (or combination of speckles) resulting in an intensity level below the modulator-demodulator threshold (see Section 4.1.4). It can be further assumed as a result of this experiment, that the detector is not as sensitive with respect to speckle motions resulting from the out-of-plane rotation of the structure such as those motions occurring at the nodal areas. Thus, one can theorize that there may be a time-averaged response to many speckles traveling over the detector which is captured by the detector in these areas.

The speckle pattern motion at the free-ends of the steel beam is complicated by the fact that there are two separate motions involved. Note that the speckle motion span and thus speckle motion gain is a maximum at these areas. In addition, remember that this area was previously shown to be susceptible to the occurrence of laser noise. The two

speckle motions involved at the free-ends consist of the maximum rotation and maximum linear translation of the steel beam. These areas are further puzzling based on the previous theories concerning the association of the occurrence of laser noise and the corresponding speckle pattern motions. In light of that, one can only theorize that the SLDV system is sensitive to the combination of speckle pattern motions created at the free-ends of the structure. Additionally, recalling the results of Section 4.1, one can theorize that the rotation component of the motion may be helping to reduce the extent of the laser noise in these areas, and that without this component, the noise would be more extensive.

It should be noted that although the procedures followed in this experiment provided for a method of viewing the static and dynamic conditions of the speckle patterns resulting from the structure, it is difficult to determine what exactly is happening on the active area of the detector. In other words one can only theorize, based on the information available from this and the preceding experiment (i.e. oscilloscope plots presented above), about the speckle intensity distributions and speckle pattern motions occurring on the active area of the detector.

The visualization of the speckle patterns resulting from this experiment seem to beg several questions concerning the effect of the speckle pattern motion on the observed laser noise. Additionally, the associated observations of the large Doppler signal amplitudes resulting from the use of the 3M Scotchlite™ retroreflective tape necessitated

that an experiment be performed using a complete surface treatment which would result in similar Doppler signal amplitudes. This experiment is presented in the next section.

### **4.3 SURFACE PREPARATION**

The information found and theories developed in the above experiment leads to an investigation into the effect of using the most retroreflective surface available to the author. It was theorized above that the Doppler signals may fall below the modulator-demodulator threshold value resulting from insufficient light intensity reaching the detector at the drop-out points due to the periodic motion of the structure. It is further known that the 3M Scotchlite™ retroreflective surface will approach maximum retroreflectivity. Thus, it was desired to determine if the intensity levels resulting from the use of Scotchlite™ paint would result in Doppler amplitude modulations which would not fall below the detector threshold value and thus ultimately result in better quality scans and lower  $DF$  values.

#### **4.3.1 EXPERIMENTAL DESCRIPTION**

This experiment was performed using the general experimental setup and data analysis procedure explained in Chapter 3. The setup for this experiment was identical to that used in Section 4.1 with the obvious exception of the surface treatment of the structure. In this experiment the beam was painted with a coat of 3M Scotchlite™

retroreflective paint. The author does note that the paint may have altered the structural dynamics of the beam by adding mass and potential surface damping. Thus, an FRF test was again performed on the beam. The FRF diagram from this test can be found in Appendix C. It should be noted that although small changes were noted in the response diagram, based on the objective of determining the increase in scan quality resulting from the use of the paint, the changes were neglected. Again, the beam was excited near its 3rd bending mode and the resonance-dwell technique was employed.

Excitation forcing amplitudes were chosen in an attempt to characterize velocity responses using as much of the full region of the velocity range as possible. Maximum velocity responses were calculated by extracting the maximum velocity response contained in each scan matrix and representing that as a percentage of the full-scale capabilities listed above. It should be noted that only the MEDIUM range of the VPI Sensor was tested, but that any general observations based on the resulting quality of scan would apply to the other levels.

Velocity scans were taken for seven scan groups termed P1 through P7. As above, for each scan group the laser beam focus knob was adjusted so as to obtain the maximum focus reading possible. These readings were obtained using the Signal Monitor in the focus position. The velocity scan data matrices were then saved in ASCII format and transferred so that they could be analyzed using the MATLAB™ code described in Chapter 3 and presented in Appendix B. This code then yielded graphical representations of the scan data similar to those presented in the example section of Chapter 3, including



two-dimensional representations of the velocity scan matrices, DFT-IDFT fitted curves, and calculations for the  $DF$  values.

#### **4.3.2 EXPERIMENTAL OBSERVATIONS**

There were some observations made during the execution of this experiment which may be of note to the reader. The first and most obvious were the focus level readings on the Signal Monitor and corresponding Doppler signal amplitudes. An oscilloscope plot showing the Force, Velocity, Doppler, and Correlator Output signals was acquired during the experiment and will be presented in the following section. It was noted that maximum Focus level readings from the Signal Monitor averaged approximately 90 out of 100 units on the Signal Monitor, and were observed to be very stable as compared to the experiment presented in Section 4.1.

There was another observation made during this experiment which should be noted. It was found during a quick check that the minimum focus reading which could be obtained by severe defocusing of the laser measuring beam was approximately 40 units on the Signal Monitor.

### 4.3.3 EXPERIMENTAL RESULTS

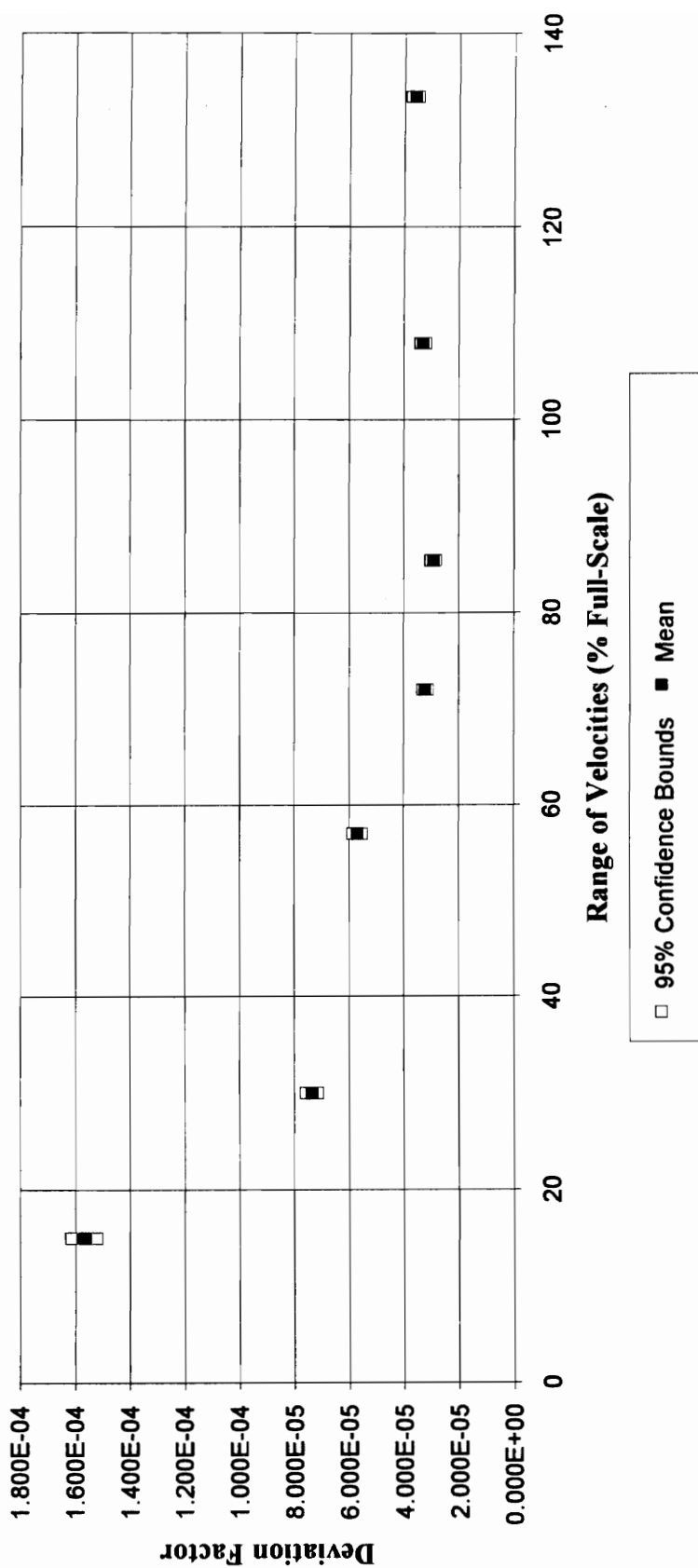
Representative ‘scan-fit plots’ for scans taken from each of the scan groups can be found in Appendix A.2. The resulting mean  $DF$  values, standard deviations and corresponding confidence intervals for scan groups P1 through P7 are summarized in Table 4.6.

**Table 4.6:** Statistical summary of the ‘Deviation Factors’ generated for the retro-reflective painted beam.

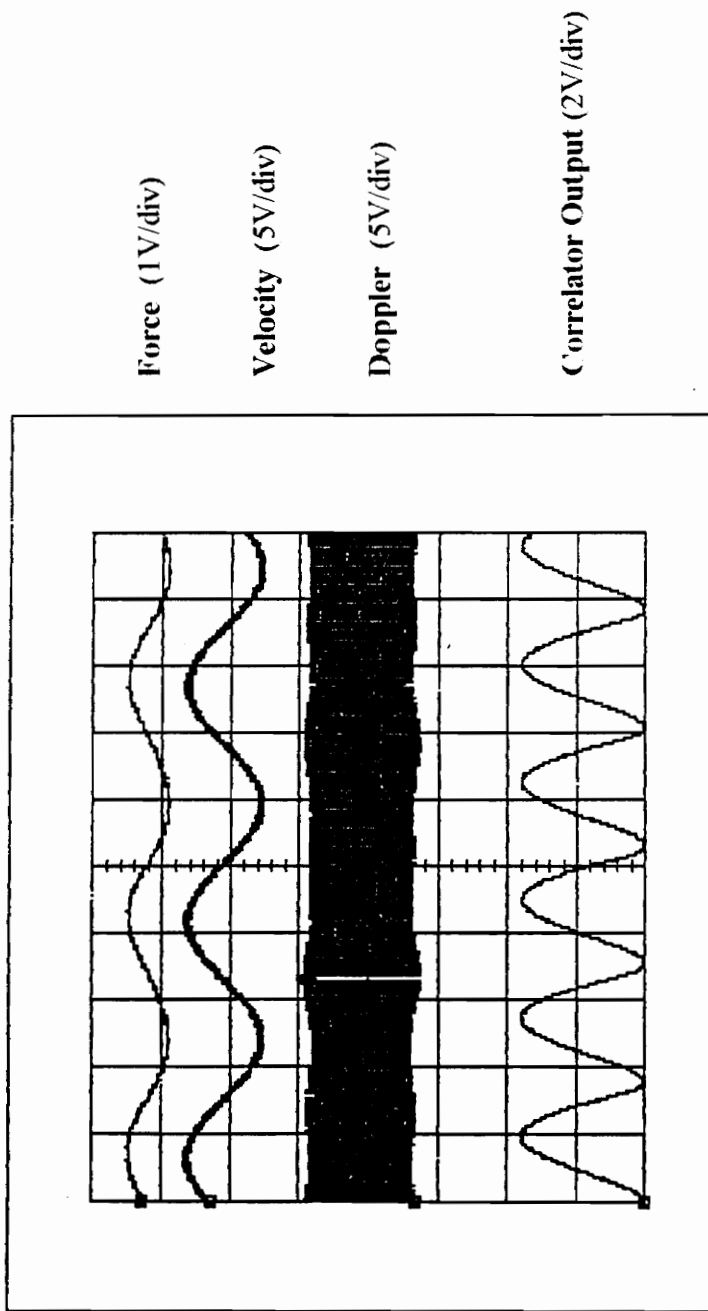
| Scan Group | Range of Velocity Responses (% of Full-Scale) | Mean ‘Deviation Factor’ $\overline{DF}$ | Sample Standard Deviation | 95% Confidence Interval Low Bound | 95% Confidence Interval High Bound |
|------------|---|---|---------------------------|-----------------------------------|------------------------------------|
| P1         | 15  | 1.567E-04                               | 1.316E-05                 | 1.521E-04                         | 1.614E-04                          |
| P2         | 30  | 7.351E-05                               | 5.971E-06                 | 7.124E-05                         | 7.573E-05                          |
| P3         | 57  | 5.689E-05                               | 1.573E-05                 | 5.518E-05                         | 5.873E-05                          |
| P4         | 72  | 3.218E-05                               | 1.208E-06                 | 3.118E-05                         | 3.320E-05                          |
| P5         | 85.5  | 2.925E-05                               | 6.915E-07                 | 2.834E-05                         | 3.018E-05                          |
| P6         | 108   | 3.300E-05                               | 1.020E-06                 | 3.194E-05                         | 3.404E-05                          |
| P7         | 133.5   | 3.604E-05                               | 3.790E-06                 | 3.495E-05                         | 3.724E-05                          |

Figure 4.14 contains the information contained in Table 4.6 in graphical form. Additionally, Figure 4.15 shows an oscilloscope plot taken at a point near the horizontal and vertical center of the structure.

**'Deviation Factor' vs. Maximum Velocity Response  
(Painted Beam - MEDIUM Range)**



**Figure 4.14:** 'Deviation Factor' mean values and corresponding 95% confidence intervals for retroreflective painted steel beam. (MEDIUM velocity range setting).



**Figure 4.15:** Oscilloscope plot showing Force, Velocity, Doppler, and Correlator Output signals for retroreflective painted steel beam. (Point near horizontal and vertical center of beam).

#### **4.3.4 DISCUSSION OF RESULTS**

Inspection of the representative scans for each scan group shows that there is relatively little laser noise in the scans. Note that in the plots in which a laser noise point is present, its spatial occurrence predominately corresponds with the areas of maximum response and is thus consistent with those presented above.

Note in Figure 4.14 that the  $DF$  values seem to level-off at a range of velocities of approximately 70% of full-scale. Also note that the  $DF$  values for the retroreflective painted beam are approximately one to two orders of magnitude lower than corresponding  $DF$  values for the MAGNAFLUX™ treated beam as presented in Section 4.1.

Figure 4.15 shows that the maximum Doppler signal amplitude is approximately 8 V pk-pk. Close inspection of this figure further indicates that there is a modulation of the Doppler signal. An eye-ball estimate shows that this modulation is approximately 1 V 0-pk. This may further endorse the theory concerning the spatial distribution of the drop-outs. It can be theorized that this modulation has the same source as that shown in Figures 4.3 and 4.4 but the intensity of the back-reflected light (and thus Doppler signal amplitude) is at such a large value that the bright speckle on the detector must move almost entirely off of the detector before the resulting detector output falls below the balanced modulator-demodulator threshold value. Thus, it can be further theorized that the general speckle pattern motions resulting from the vibrating structure are consistent

regardless of surface treatment. And furthermore, surfaces which tend to concentrate more of the scattered light into a restricted angle centered along the incident light direction, such as the 3M Scotchlite™, create Doppler signals which are more robust to changes in speckle intensities resulting from the speckle motions generated during the periodic motion of the vibrating structure.

#### **4.4 SUMMARY**

This chapter contains the exploratory progression of experiments which were meant to observe the laser noise and shed some light on its characterization and its possible sources. The experiments presented above included three separate investigations. The first of which analyzed the effect of increasing the range of velocities through full-scale on an author-defined measure of scan quality. The results from these experiments can be summarized as follows:

- Investigations concerning increasing ranges of velocities suggested that there is an optimal operating range of velocities for the SLDV system. For the LOW velocity setting the optimal operating range of velocities was found to be between 70% and 100% of full-scale. For the MEDIUM velocity setting the optimal operating range of velocities was found to be between 30% and 65% of full-scale.

- The areas which were found to contain laser noise exhibited similar Doppler signal amplitude modulations. The laser noise was caused by these modulations in which the Doppler signal dropped below the balanced modulator-demodulator threshold voltage.

The results of this experiment led to an observation of the differing speckle pattern motions corresponding to areas both likely and unlikely to contain laser noise.

- The areas in which laser noise was found to occur, the antinode areas and the free-ends, corresponded with two separate speckle pattern motions which resulted from the different surface motions of the structure. The antinode areas were found to experience very little (if any) speckle pattern motion. These areas were undergoing large out-of-plane motions with minimal rotational components. The free-end areas were experiencing the largest magnitude of speckle pattern motions across the detector. These areas were undergoing a combination of motions resulting from large out-of-plane translations and large rotational components. The areas in which the noise was found to be less likely to occur, the nodal areas, were experiencing speckle pattern motions across the detector. These areas were undergoing small out-of-plane translations and large rotational components of motion. It was further found, in conjunction with the results presented in the first experiment, that the

rotational component of combined motion at the free-ends of the structure was helping to suppress the occurrence of the laser noise.

During the execution of this experiment and based on the Doppler signal modulation theories developed from the first experiment, a study of the effect of a surface treatment which is known to be highly retroreflective (and thus highly intensity-efficient resulting in large Doppler amplitudes) was performed on the quality of the scan data. The results from this experiment can be summarized as follows:

- Treatment of the structure with a highly retroreflective surface resulted in substantial reductions in laser noise and thus resulted in considerable improvements in scan quality. This was due to the relative magnitude of the back-reflected light which resulted in greater intensities and large Doppler signal amplitudes which were robust to amplitude modulations.

As a result of the combination of these experiments, interesting theories and insight into the possible speckle pattern motions and resulting Doppler signal modulations exhibited in the experiments were presented.



## CHAPTER 5

### SUPPLEMENTAL EXPERIMENTS

During the execution of the experiments presented in the previous chapter and per the request of Ometron, Ltd. [7], a set of supplementary experiments were performed to determine the effects of a set of user-controlled parameters on the observed laser noise. Additionally, the objective of these short experiments was to determine if adjustment of these parameters would alleviate the observed laser noise problem. Those parameters again are:

- Output Lens Selection
- Coherence Repeat Distance
- “Slight Defocus” of Laser Measuring Beam

In order to examine these parameters a short set of experiments were performed to investigate each parameter separately. Thus this chapter is divided into three main sections each devoted to an individual parameter. The format for each section is similar, first an experimental description is given, the results are presented, and a discussion of the results follows. The chapter concludes with a summary.

## **5.1 OUTPUT LENS SELECTION**

As mentioned in Chapter 3, there are two output lenses which can be used in the VPI Sensor laser optical unit: a long-range lens and a short-range lens. The VPI Sensor Operator's Manual suggests that the short-range lens be used for measurements up to 197 in (5 m) and the long-range lens is recommended for use beyond 197 in (5 m). Also discussed above was the suggestion that the long-range lens allows for up to four times the light gathering capacity as the short-range lens [41,42]. The main objective of this experiment was to perform a preliminary experiment to determine the effect of using the long-range lens versus the short-range lens.

### **5.1.1 EXPERIMENTAL DESCRIPTION**

The setup for this experiment was identical to that presented in Chapter 3 and used in Section 4.1. The data acquisition procedures were also the same as above. The working distance used in this experiment was the same as before, 133.1 in (3380.7 mm), and the experiment was performed using the MEDIUM velocity range setting. It should be noted that this experiment was performed with some prior speculation as to the importance of the light gathering ability of the lens. Thus, this experimental setup provided for analysis at a working distance which was within the recommended distance for the short-range lens but also within the shortest working distance for the long-range lens, given as 43.3 in (1100 mm) [5]. Consequently execution of the experiment at this

particular working distance could potentially confirm or contradict the importance of the light gathering capability of the lens. The same slender steel beam was used covered with a coat of MAGNAFLUX™ developer. To remain consistent, the steel beam was again excited at its 3rd vibrational mode and the resonance-dwell technique was utilized. The excitation conditions for the scans performed in this experiment were similar to those used in Scan Group M6 (see Section 4.1), and scans were then taken with each lens. For descriptive purposes, the scans taken with the short-range lens will be referred to as the ‘S.R. Lens’ group and the scans taken with the long-range lens will be referred to as the ‘L.R. Lens’ group. The data analyses procedures used in Section 4.1 were also used in this experiment so that mean ‘Deviation Factor’ and standard deviations could be calculated for the two scan groups.

### ***5.1.2 EXPERIMENTAL RESULTS***

Appendix A.3 shows the representative ‘scan-fit plots’ for scans taken from both the L.R. Lens and S. R. Lens scan groups. Table 5.1 shows a statistical summary of the mean ‘Deviation Factors’ and standard deviations for the two scan groups.

**Table 5.1:** Statistical summary of the Deviation Factors generated for the scan groups corresponding to the short-range and the long-range lenses (MAGNAFLUX™ coating, MEDIUM velocity range setting).

| <b>Scan Group</b> | <b>Mean 'Deviation Factor'</b> | <b>Sample Standard Deviation</b> |
|-------------------|--------------------------------|----------------------------------|
| L.R. Lens         | 1.621E-03                      | 1.697E-03                        |
| S.R. Lens         | 7.510E-03                      | 1.852E-03                        |

### **5.1.3 DISCUSSION OF RESULTS**

A review of the representative 'scan-fit plots' given in the Appendix A.3 shows that the spatial distribution of the laser noise is consistent with the previous results. That is the occurrence of the laser noise is predominately at the areas of maximum response. A review of the information presented in Table 5.1 shows that the short-range lens resulted in a mean 'Deviation Factor' approximately 4.6 times larger than that resulting from the long-range lens. The reader should remember that the working distance chosen for this experiment was within the recommended range for the short-range lens. The results presented in this section suggest that the reported increased light gathering capability of the long-range lens does help to reduce the occurrence of the laser noise. The results do not though indicate that the use of either of the lenses will alleviate the laser noise problem. However, it seems advantageous to use the long-range lens whenever possible. It is suggested that the implications from this experiment can be used in conjunction with

the implications from the other experiments to confirm the theories developed concerning the source of the laser noise. These will be discussed in Chapter 6.

## ***5.2 COHERENCE REPEAT DISTANCE***

As mentioned in Chapter 1, the characteristics of the particular Helium-Neon laser used in the VPI Sensor laser optical unit dictate that a set of coherence repeat distances be specified. These were given in Equation (1.1). The VPI Sensor Operator's Manual [5] reports that at these distances the Doppler signal is of optimum amplitude. The manual also reports a set of intermediate (incoherence) repeat distances give in Equation (1.2). These distances are said to result in less optimal Doppler amplitudes. The main objective of this experiment was to perform a preliminary investigation in order to determine the effect of performing velocity scans at a coherent distance and at an intermediate distance, which lies between coherence distances.

### ***5.2.1 EXPERIMENTAL DESCRIPTION***

This experiment was performed using the general experimental setup and data analysis procedures explained in Chapter 3. The setup for this experiment was again identical to that used in Section 4.1. The same structure, with a coat of MAGNAFLUX™ developer, was also used for this experiment. The objective of the experiment was to determine the effect of operation at a coherence repeat distance and at a intermediate

repeat distance as defined in Chapter 1. This objective was met by performing several scans of the vibrating structure at the coherence repeat distance used in the previous experiments, 133.1 in (3380.7 mm) from the structure. The laser was then moved to the closest intermediate repeat distance, 137.2 in (3485 mm) from structure. Both sets of scans were taken using the MEDIUM velocity range setting, and excitation conditions were similar to those used in Scan Group M6 (see Section 4.1). It should be noted that the density of the scan area used in the previous experiments (i.e. scan matrix consisting of 13 columns and 238 rows) was not changed when moving the optical unit to the intermediate working distance. Thus, some rows on the top and bottom of the scan matrix had to be truncated in order to extricate scan points which, at the further distance, were then off of the structure. The resulting scan matrix for the scans taken at the further distance consisted of 13 columns and 232 rows. The calculation of the ‘Deviation Factor’ was adjusted in order to account for this truncation. Thus, it should be noted that the total number of scan points included in the two scanning distances were not consistent.

### ***5.2.2 EXPERIMENTAL RESULTS***

As rendered before, representative ‘scan-fit plots’ for scans taken from both of the scan groups can be found in Appendix A.4 . A statistical summary of two scan groups is presented in Table 5.2.

**Table 5.2:** Statistical summary of the Deviation Factors generated for the scan groups corresponding to a coherence repeat distance and an intermediate distance (MEDIUM velocity setting, MAGNAFLUX™ coating, long-range lens).

| Scan Group        | Working Distance (in) [mm=<br>x 25.4] | Mean 'Deviation Factor' | Sample Standard Deviation |
|-------------------|---------------------------------------|-------------------------|---------------------------|
| D1 (coherent)     | 133.1                                 | 1.740E-03               | 6.144E-05                 |
| D2 (intermediate) | 137.2                                 | 2.576E-04               | 6.694E-05                 |

### 5.2.3 DISCUSSION OF RESULTS

The results of this experiment are interesting. It can be seen in the scan-fit plots presented in Appendix A.4 that the operation of the SLDV at either of the distances continues to indicate laser noise at the areas noted before (at the areas of maximum response). The interesting point becomes apparent when comparing the mean 'Deviation Factors' contained in Table 5.2. The scan group D1 resulted in a mean 'Deviation Factor' of 1.740E-03. The scan group D2 resulted in a mean 'Deviation Factor' of 2.576E-04. It can be seen that the scan group D2, which corresponds to operating the SLDV at an intermediate repeat distance of 137.2 in (3485 mm), resulted in a lower mean 'Deviation Factor', 15% of that from the coherence repeat distance position.

It should be noted that the comparison of the two scan groups must be made with the understanding that the two scan groups do not contain the same number of scan data points. As mentioned before, the spatial distribution of the laser noise seems consistent in

both scan groups. In addition, due to the fact that scans within group D2 were taken with the VPI Sensor laser optical unit further from the vibrating structure it can be shown from the geometry of the scanning angles that the separation of scanning rows are greatest at the free-ends of the structure. Thus, the effect of truncating the scan group is maximum on the concentration of scan rows at the free-ends of the structure which is one of the areas that laser noise had previously been observed to be concentrated. Thus one may argue that the 'Deviation Factors' reported for scan group D2 may be slightly lower for this reason. Thus the reader should be advised of this when evaluating comparisons between the two scan groups. In light of the above, the results of this experiment implore that further investigation be carried out concerning the effect of the coherence versus intermediate repeat distances on the quality of scan data taken with the SLDV. However, it is believed that the small effect of the loss of a few moderately noisy beam end points will not explain the 85% reduction in *DF* values.

### **5.3 "SLIGHT DEFOCUS" OF LASER MEASURING BEAM**

Discussions with Ometron, Ltd. involving the occurrence of the laser noise also concerned the focus level of the VPI Sensor laser optical unit. A suggestion was made concerning the effect of a "slight defocusing" of the laser measuring beam on the observed laser noise. It was theorized by Ometron, Ltd. that a "slight defocusing" of the laser measuring beam may decrease the occurrence of the laser noise. The author has



determined that the source of this theory may be contained in the literature of Drain [9]. In a discussion concerning speckle patterns he postulates that the effect of a changing speckle pattern may be reduced by increasing the illumination spot size. On the other hand, literature presented in Chapter 2 suggested that increasing the illumination spot size may result in operating problems based on the averaging of the intensity over the resultant combination of speckles.

Thus, it is the objective of this experiment to investigate the somewhat disputed remedy of a “slight defocusing” of the laser measuring beam on the occurrence of the observed laser noise. The procedure for this particular experiment is not as cut and dry as one would like. That is, the term “slight defocusing” is a subjective phrase. Yet an attempt was made to quantify the extent of the defocusing. The outcome of this experiment may also add to the confirmations or contradictions of the theories developed in the other experiments presented in this thesis.

### ***5.3.1 EXPERIMENTAL DESCRIPTION***

This experiment was once again performed using the general experimental setup and data analysis procedure explained in Chapter 3. The setup for this experiment was identical to that used in Section 4.1. The VPI Sensor laser optical unit was placed at 133.1 in (3380.7 mm) from the structure. The MEDIUM velocity range setting was used and the excitation conditions were similar to those used in Scan Group M6 (see Section

4.1). To remain consistent, the steel beam again covered with the MAGNAFLUX™ developer was excited at its 3rd vibrational mode and the resonance-dwell technique was utilized. Maximum focus was then achieved by adjusting the focus knob on the side of the optical unit. The reader should note that the horizontal and vertical center of the steel beam was chosen as the reference point at which the focus levels were obtained prior to scanning. Focus levels were noted by using the Signal Monitor on the side of the VPI Sensor laser optical unit in the focus setting. It should be stressed and the author does note that focus readings taken from the Signal Monitor are not a direct indication of the actual *focus* of the laser measuring beam. The focus level readings are also affected by surface preparation of the structure and the working distance. For the purpose of this experiment though it was assumed that the recorded focus level readings were indicative of the level of focus based on the fact that the surface preparation (MAGNAFLUX™ developer) and the working distance (133.1 in [3380.7 mm]) were maintained during the execution of this experiment.

Scans were taken for three separate scan groups. The first scan group corresponded to obtaining a maximum focus level on the signal monitor at the reference point prior to scanning. The other two scan groups corresponded to “slightly defocusing” by rotating the focus knob on either side of maximum focus. It will be assumed that a maximum focus level reading corresponds to placing the focal point of the laser measuring beam on the reference point of the structure. In other words maximum focus will be assumed to mean that the laser measuring beam is at its minimum spot size at the reference

point of the structure. The focus reading on the Signal Monitor at the reference point for this scan group averaged approximately 50 out of 100 units. This scan group will be referred to as REF. An attempt was made to defocus the laser measuring beam at the reference point an equal amount on either side of maximum focus. First the measuring beam was “slightly-defocused” by rotating the focus knob in the counter-clockwise (or left) direction. This scan group will be referred to as DFL, defocus-left. The focus reading on the Signal Monitor for this scan group averaged approximately 40 - 45 out of 100 units. Next, the same defocusing procedure was performed by rotating the focus knob in the clockwise (or right) direction. This scan group will be referred to as DFR, defocus-right. The focus reading on the Signal Monitor for this scan group averaged approximately 40 - 45 out of 100 units.

### ***5.3.2 EXPERIMENTAL RESULTS***

Appendix A.5 shows the representative ‘scan-fit plots’ for scans taken from the three scan groups. Table 5.3 shows a statistical summary of the mean ‘Deviation Factors’ and standard deviations for these scan groups.

**Table 5.3:** Statistical summary of the Deviation Factors generated for the scan groups corresponding to maximum and slight defocus levels (MEDIUM velocity setting, MAGNAFLUX™ coating, long-range lens).

| <b>Scan Group</b> | <b>Slight Defocus Knob Direction</b> | <b>Mean 'Deviation Factor'</b> | <b>Sample Standard Deviation</b> |
|-------------------|--------------------------------------|--------------------------------|----------------------------------|
| REF               | -                                    | 2.065E-03                      | 9.900E-04                        |
| DFL               | Counter-Clockwise                    | 8.428E-03                      | 9.189E-03                        |
| DFR               | Clockwise                            | 1.099E-02                      | 4.200E-03                        |

### **5.3.3 DISCUSSION OF RESULTS**

A review of the representative scans in Appendix A.5 once again show that the spatial distribution of the laser noise is consistent with the results from the previous experiments. That is, the occurrence of the laser noise is predominately at the areas of maximum velocity response. A review of the mean 'Deviation Factors' presented in Table 5.3 show that the REF scan group, which corresponded to obtaining maximum focus at the reference point, resulted in the lowest 'Deviation Factor'. The scan group DFL, which corresponded to a slight defocus of the laser measuring beam by rotating the focus knob counter-clockwise, resulted in a mean 'Deviation Factor' approximately 4 times higher than the REF scan group. The scan group DFR, which corresponded to a slight defocus of the laser measuring beam by rotating the focus knob clockwise, resulted in a mean 'Deviation Factor' approximately 5.3 times higher than the REF scan group. The differences between scan groups DFL and DFR may be explained by the effect on the focal point of the laser beam. The reader should note that defocusing the laser measuring

beam by rotating the focus knob to the left will place the focal point beyond that of maximum focus. Conversely, defocusing the laser measuring beam by rotating the focus knob to the right will place the focal point in front of that of the maximum focus. Thus, one can determine by geometry that placing the focal point beyond the reference point on the structure, as in scan group DFL, will result in the free-ends becoming more in focus. On the other hand placing the focal point in front of the reference point on the structure, as in scan group DFR, will result in the free-ends becoming further out of focus. This may explain the fact that the scan group DFL resulted in better quality scans than those of scan group DFR.

The results of this experiment seem to indicate that obtaining maximum focus is the optimal operating strategy for the SLDV. This was inferred in some of the literature presented in Chapter 2 and more importantly by the assumption of a single bright speckle upon which the SLDV is based. Based on the known change in the speckle pattern when the laser is defocused (i.e. the speckle pattern results in finer granules), one can theorize that a slight defocus will violate this assumption and potentially introduce combinations of speckles which may result in lower resultant intensities. In other words, based on the theories developed from the results of the previous experiments, in its current form a “slight-defocus” of the SLDV laser measuring beam will only exaggerate the laser noise problems caused at points with insufficient Doppler amplitude (and lower focus level readings). A further inference could be that the optimal operation of an SLDV system

would require that *each* scan point be re-focused so as to obtain maximum focus. Unfortunately, this is not an option for the SLDV used in these experiments.

## **5.4 SUMMARY**

This chapter presents three preliminary experiments which were performed at the request of Ometron, Ltd. to determine the effect of three user-controlled parameters on the observed laser noise phenomenon. Output lens selection, working distance, and a “slight defocus” of the laser measuring beam were examined. The results of these experiments can be summarized as follows:

- The increased light gathering capability of long-range lens results in less laser noise and thus the long-range lens should be used whenever possible.
- Operation at intermediate repeat distances may result in more stable Doppler signals and thus less laser noise. Therefore, if the SLDV user notes drop-out problems at a coherence repeat distance the laser should be moved to a intermediate repeat distance.
- Maximum focus of the laser measuring beam results in a more optimal operating condition, especially with less retroreflective surface treatments. Thus a “slight defocus” of the laser measuring beam is not recommended as a remedy for laser noise.

The results from these experiments can then be used in conjunction with the results from the progression of experiments presented in Chapter 4 to generate some theories as the characterization and the possible source of the observed laser noise. These results and some recommendations will be presented in the next chapter.

## CHAPTER 6

### CONCLUSIONS AND RECOMMENDATIONS

This chapter is meant to summarize the research presented in this thesis. In addition some recommendations for changes to the SLDV system, guidelines for optimal use of the SLDV system, and recommendations for future work are presented.

#### 6.1 SUMMARY

The overall objective of the research presented in this thesis was to perform a preliminary investigation regarding the characterization and potential sources of the laser noise phenomenon when using an SLDV system to extract vibration information from dynamic structures. The exploratory and progressive nature of the experiments presented in this thesis manifested itself into three main areas of investigation:

- Range of Velocity Response
- Speckle Pattern Motion
- Surface Preparation



Additionally, a set of supplemental experiments were performed in cooperation with Ometron Ltd. to determine the effect of three user-defined parameters on the observed laser noise. These supplemental experiments included the following:

- Output Lens Selection
- Coherence Repeat Distance
- “Slight Defocus” of Laser Measuring Beam

The results from these experiments produced potential theories regarding the source of the laser noise. Accordingly, the results also produced some suggested steps which can be taken in to minimize occurrence of the laser noise while measuring the dynamic velocity response of a structure.

## **6.2 CONCLUSIONS**

Execution of the progression of experiments presented in this thesis yielded the following conclusions:

- Operation of the SLDV system on the LOW and MEDIUM ranges suggest that there is an optimal operating range of velocities for both velocity settings. Laser noise is minimized using the LOW range by choosing an operating range of velocities which correspond to maximum velocity responses at 70% to 100% of full-scale. Laser noise is minimized using the MEDIUM range by

choosing an operating range of velocities which correspond to maximum velocity responses at 30% to 65% of full-scale.

- The occurrence of the laser noise is dependent on the motion of the vibrating structure and thus the corresponding resultant speckle pattern motion. Areas in which the structure is experiencing large out-of-plane translations and minimal rotations are most susceptible to laser noise. These areas produce minimal speckle pattern motion. Areas in which the structure is experiencing large rotation and small out-of-plane translation are least susceptible to laser noise. These large rotation areas produce increased speckle pattern motion, which manifests itself in a “streaking” of the speckle. Areas in which there exist a combination of motions result in the occurrence of laser noise, but the effect of the noise is somewhat suppressed by rotation component of the motion. These areas produce the largest speckle “streaks”.
- Areas in which laser noise is found to occur possess similar Doppler signal responses. The Doppler signals experience amplitude modulations which include areas which drop below the balanced modulator demodulator threshold voltage. These areas coincide to instances in which there are insufficient light intensities reaching the photodetector.
- Use of a surface which is highly retroreflective, such as 3M’s Scotchlite™ retroreflective tape or liquid, results in substantial reduction of the occurrence

of laser noise. The resultant back-reflected intensity levels are very robust to the speckle pattern motions which were found to produce laser noise with a less retroreflective surface.

Execution of the supplemental experiments presented in this thesis yielded the following conclusions:

- Use of the long-range lens produced considerably less laser noise than the use of the short-range at distance which was conducive to either lens.
- Operation of the SLDV at a distance which was intermediate to the reported coherence repeat distances resulted in a reduction of laser noise.
- A “slight defocusing” of the laser measuring beam does not reduce the occurrence of the laser noise.

### **6.3 RECOMMENDATIONS**

Completion of the experiments contained in this thesis suggested recommendations in the following areas: recommended changes to the SLDV system, recommended guidelines for optimal use of the SLDV system, and recommendations for future work.

### ***6.3.1 RECOMMENDED CHANGES TO THE SLDV SYSTEM***

The important relationship between the Doppler signal amplitude and the occurrence of laser noise was discussed above. Because of this relationship, it is recommended that a simple indicator be added which would represent the Doppler signal amplitude with respect to the modulator-demodulator threshold voltage. This could be accomplished through the use of light which would indicate 'Lock' or 'Unlock of the balanced modulator-demodulator.

It is also suggested that the Signal Monitor on the side of the VPI Sensor be appended so as to include values in excess of 100, possibly up to 125. The LED indicators between 100 and 125 could also be changed to a characteristic color such as red. With the current configuration it is difficult to determine if the SLDV is operating at a level which is at or beyond 100 on the Signal Monitor. The suggested configuration would alleviate this difficulty.

### ***6.3.2 RECOMMENDED GUIDELINES FOR SLDV OPTIMAL USE***

The conclusion of the experiments presented in this thesis suggest the following guidelines to minimize the occurrence of laser noise in measurements taken from a vibrating structure. These guidelines should result in more optimal operation of the SLDV system:

- When possible, treat the surface of the structure with a retroreflective substance (such as 3M's Scotchlite™ retroreflective liquid or tape) this results in maximum back-reflected light intensities and, thus, maximum Doppler signal amplitudes.
- Choose excitation conditions such that the range of velocities occur within 70% to 100% of full-scale for the LOW velocity setting, and 30% to 65% of full-scale for the MEDIUM velocity setting.
- The user should attempt to maximize the stability of the structure *and* the VPI Sensor unit during the execution of the experiment.
- Use the long-range lens whenever possible.
- Achieve maximum focus (and thus maximum Doppler signal amplitudes) during the setup phase and maintain maximum focus during scanning if possible.

### ***6.3.3 RECOMMENDATIONS FOR FUTURE WORK***

The work presented in this thesis generated theories on the possible sources of the laser noise and suggested some methods of minimizing that noise. The results also indicated several areas which should further be investigated. Thus it is suggested that the following areas be considered for further research:

- An investigation should be performed to isolate different speckle pattern motions and attempt to determine their effect of the quality of the scan data taken with the SLDV. This should include isolating speckle pattern motions with resultant motions across the photodetector in both orthogonal orientations. The effect of amplitude on the condition of the speckle pattern should also be included.
- A full investigation should be performed to clarify the effect of the coherence repeat distances and the intermediate repeat distances on the quality of scan data taken with the SLDV system. As above, the effect of these differing operating distances on the condition of the speckle pattern should also be studied.
- An investigation should be carried out to quantify the effects of differing boundary conditions (which result in increased structural stability in the experimental setup) on the observed laser noise.
- An investigation should be performed to determine how the quality of scan data taken with the SLDV system is affected by different operating angles of incidence. For the same structural motions, differing angles of incidence will result in differing speckle pattern motions received by the detector.

## REFERENCES

- [1] Drain, L. E., *The Laser Doppler Technique*, John Wiley & Son Ltd., New York, New York, 1980.
- [2] Sun, F. P., L. D. Mitchell, and J. R. F. Arruda, "Mode Decoupling Considerations in Mode Shape Measurement of a Plate with Monoexcitation and Laser Doppler Vibrometer," *Experimental Techniques*, Vol. 17, No. 4, July/August 1993, pp. 31-37.
- [3] Archibald, M. A., *Parametric Spatial Modal Analysis of Beams*, Doctoral Dissertation, Virginia Polytechnic Institute and State University, Department of Mechanical Engineering, Blacksburg, Virginia, 1994, Committee Chairman: A. L. Wicks.
- [4] Wicks, A. L., K. Kochersberger, and L. D. Mitchell, "Laser Structural Imaging," *Proceedings of the 2nd USAF/NASA Workshop System Identification and Health Monitoring of Precision Space Structures*, California Institute of Technology, Pasadena, California, March 27-29, 1990, pp. 24-42.
- [5] *VPI Sensor Operator's Manual*, Ometron Ltd., London, England, 1987.
- [6] Barker, Andy, Ometron Ltd., London, England, Personal Communication, Virginia Polytechnic Institute and State University, May 25, 1995.
- [7] Barker, Andy, Ometron Ltd., London, England, Personal Communication via Facsimile, June 28, 1994.
- [8] Hecht, J., *Understanding Lasers*, Howard W. Sams & Company, Indianapolis, Indiana, 1988.
- [9] Drain, L. E., *The Laser Doppler Technique*, John Wiley & Sons Ltd., New York, New York, 1980, pp. 220-227.
- [10] Halliwell, N. A., "Laser-Doppler Measurement of Vibrating Surfaces: A Portable Instrument," *Journal of Sound and Vibration*, Vol. 62, No. 2, 1979, pp. 312-315.
- [11] Pickering, C. J. D., N. A. Halliwell, and T. H. Wilmshurst, "The Laser Vibrometer: A Portable Instrument," *Journal of Sound and Vibration*, Vol. 107, No. 3, 1986, pp. 471-485.

- [12] D'Emilia, G., "Evaluation of Measurement Characteristics of a Laser Doppler Vibrometer with Fiber Optic Components," *First International Conference on Vibration Measurements by Laser Techniques: Advances and Applications*, SPIE Vol. 2358, 1994, pp. 240-246.
- [13] Barker, A. J., "Non-contacting Vibration Measurement: Role in Design and Industrial Applications," *Stress and Vibration: Recent Developments in Industrial Measurement and Analysis*, SPIE Vol. 1084, 1989, pp. 293-299.
- [14] Arruda, J. R. F., "Spatial Domain Modal Analysis of Lightly-Damped Structures Using Laser Velocimeters," *Journal of Vibration and Acoustics*, Vol. 115, July 1993, pp. 225-231.
- [15] Miles, R. N., W. Bao, and Y. Xu, "Estimation of Random Bending Strain in a Beam from Discrete Vibration Measurements," *Journal of Sound and Vibration*, Vol. 174, No. 2, 1994, pp. 191-199.
- [16] Trethewey, M. W., H. J. Sommer, and J. A. Cafeo, "A Dual Beam Laser Vibrometer for Measurement of Dynamic Structural Rotations and Displacements," *Journal of Sound and Vibration*, Vol. 164, No. 1, 1993, pp. 67-84.
- [17] E. H. Bokelberg, H. J. Sommer III, and M. W. Trethewey, "A Six-Degree-Of-Freedom Laser Vibrometer, Part I: Theoretical Development," *Journal of Sound and Vibration*, Vol. 178, No. 5, 1994, pp. 643-654.
- [18] E. H. Bokelberg, H. J. Sommer III, and M. W. Trethewey, "A Six-Degree-Of-Freedom Laser Vibrometer, Part II: Experimental Validation," *Journal of Sound and Vibration*, Vol. 178, No. 5, 1994, pp. 655-667.
- [19] Yienger, J., L. D. Mitchell, and R. L. West, "Laser-Based Structural Imaging of an Open and Closed Automobile Door for Noise Control Purposes," *Proceedings of the 11th International Modal Analysis Conference*, Kissimmee, FL, January 31-February 4, 1993, Vol. I, pp. 144-151.
- [20] Abel, J. J., *Three-Dimensional Velocity Extracting Using Laser Doppler Vibrometry*, Masters Thesis, Virginia Polytechnic Institute and State University, Department of Mechanical Engineering, Blacksburg, Virginia, 1993, Committee Chairman: L. D. Mitchell.
- [21] Montgomery, D. E., *Modeling and Visualization of Laser-Based Three-Dimensional Experimental Spatial Dynamic Response*, Doctoral Dissertation, Virginia Polytechnic Institute and State University, Department of Mechanical Engineering, Blacksburg, Virginia, 1994, Committee Chairman: R. L. West.



- [22] Blotter, J. D., and R. L. West, "Experimental Mechanical Intensity in Plates Using a Scanning Laser Doppler Vibrometer," *Proceedings of the 13th International Modal Analysis Conference*, Nashville, Tennessee, February 13-16, 1995, Vol. II, pp. 1185-1191.
- [23] Bruce, R. A., and G. L. Fitzpatrick, "Remote Vibration Measurement of Rough Surfaces by Laser Interferometry," *Applied Optics*, Vol. 14, No. 7, July 1975, pp. 1621-1626.
- [24] Lewin, A., and G. Siegmund, "The Implications of System 'Sensitivity' and 'Resolution' on an Ultrasonic Detecting LDV," *First International Conference on Vibration Measurements by Laser Techniques: Advances and Applications*, SPIE Vol. 2358, 1994, pp. 292-304.
- [25] Barker, Andy, Ometron Ltd., London, England, Personal Communication via Facsimile, July 4, 1995.
- [26] Bream, R. G., B. C. Gasper, B. E. Lloyd, and G. M. Everett, "Applications of Vibration Pattern Imaging to Modal Analysis; A Comparison with Full-Field and Point Measurement Techniques," *Stress and Vibration: Recent Developments in Industrial Measurement and Analysis*, SPIE Vol. 1084, 1989, pp. 279-292.
- [27] Kochersberger, K., L. D. Mitchell, and A. L. Wicks, "Structural Angular Velocity Extraction Using DFT/IDFT Techniques," *Proceedings of the 9th International Modal Analysis Conference*, Vol. I, Florence, Italy, April 14-18, 1991, pp. 657-663.
- [28] Mitchell, L. D., K. Kochersberger, and R. L. West, "Measurement of a One-Dimensional Mobility Using a Laser-Doppler Velocimeter," *Proceedings of The Society of Experimental Mechanics Spring Conference*, Milwaukee, Wisconsin, June 10-13, 1991, pp. 846-853.
- [29] Wagner, J. W., "Optical Detection of Ultrasound," *Physical Acoustics*, Vol. 19, 1990, pp. 201-266.
- [30] Nagy, P. B., and G. Blaho, "Random Speckle Modulation Technique for Laser Interferometry," *Journal of Nondestructive Evaluation*, Vol. 11, No. 1, 1992, pp. 41-49.
- [31] Rothberg, S. J., J. R. Baker, and N. A. Halliwell, "Laser Vibrometry: Pseudo-Vibrations," *Journal of Sound and Vibration*, Vol. 135, No. 3, 1989, pp. 516-522.
- [32] Wilmshurst, T. H., and N. A. Halliwell, "Laser Vibrometer Speckle-Noise Cancellation," *Measurement Science and Technology*, Vol. 4, No. 4, pp. 479-487.
- [33] Dainty, J. C., *Laser Speckle and Related Phenomena*, Springer-Verlag, Berlin, Germany, 1984.

- [34] Hopkins, J. J., and G. H. Tidbury, "A Note on the Interpretation of Laser Speckle Patterns of Vibrating Panels to Yield Information Concerning Mode Shapes," *Optica Acta*, Vol. 24, No. 7, 1977, pp. 773-778.
- [35] Shellabear, M. C., and J. R. Tyrer, "Three Dimensional Analysis of Volume Vibrations by Electronic Speckle Pattern Interferometry," *Stress and Vibration: Recent Developments in Industrial Measurement and Analysis*, SPIE Vol. 1084, 1989, pp. 252-261.
- [36] Slangen, P., L. Berwart, C. de Veuster, J. Golinval, and Y. Lion, "Digital Speckle Pattern Interferometry (DSPI): A Fast Procedure to Detect and Measure Mode Shapes," *First International Conference on Vibration Measurements by Laser Techniques: Advances and Applications*, SPIE Vol. 2358, 1994, pp. 102-110.
- [37] Françon, M., *Laser Speckle and Applications in Optics*, Academic Press, New York, New York, 1979.
- [38] Barker, Andy, Ometron Ltd., London, England, Personal Communication via Facsimile, July 15, 1994.
- [39] Barker, Andy, Ometron Ltd., London, England, Personal Communication, Virginia Polytechnic Institute and State University, May 24, 1995.
- [40] Barker, Andy, Ometron Ltd., London, England, Personal Communication via Facsimile, June 28, 1995.
- [41] Barker, Andy, Ometron Ltd., London, England, Personal Communication via Facsimile, June 28, 1994.
- [42] Dajani, Jamal, Ometron Inc., Sterling, Virginia, Personal Communication, March 20, 1995.
- [43] Maup, James, Statistics Consulting Center Graduate Consultant, Personal Communication, Virginia Polytechnic Institute and State University, Department of Statistics, February 3, 1995, 9:00 a.m.
- [44] West, R. L., C. M. Archibald, and A. L. Wicks, "Spatial Modal Analysis Using Regressive and Autoregressive Techniques," *Proceedings of the 11th International Modal Analysis Conference*, Kissimmee, FL, January 31- February 4, 1993, Vol. II, pp. 1042-1048.
- [45] Neumann, M. L., *A Method for the Spatial Functionalization of the Dynamic Response of a Structure with Structural Stability Considerations*, Masters Thesis, Virginia Polytechnic Institute and State University, Department of Mechanical Engineering, Blacksburg, Virginia, 1993, Committee Chairman: L. D. Mitchell.
- [46] Rao, S. S., *Mechanical Vibrations*, Second Edition, Addison-Wesley Publishing Co., Reading, Massachusetts, 1990.

- [47] Forsythe, G. E., "Generation and Use of Orthogonal Polynomials for Data-Fitting with a Digital Computer," *Journal of the Society for Industrial and Applied Mathematics*, Vol. 5, No. 2, June 1957, pp. 74-88.
- [48] Sun, F. P., and L. D. Mitchell, "Two-Dimensional Velocity Data Smoothing and Structural Angular Velocity Extraction Using a DFT-IDFT Technique," *Proceedings of the Thirteenth Biennial ASME Conference for Mechanical Vibration and Noise*, Miami, Florida, September 22-25, 1991, pp. 303-309.
- [49] Walpole, R. E., and R. H. Myers, *Probability and Statistics for Engineers and Scientists*, Fifth Edition, Macmillan Publishing Company, New York, New York, 1993, pp. 468-469.
- [50] Bendat, J. S., and Piersol, A. G., *Random Data: Analysis and Measurement Procedures*, Second Edition, John Wiley & Sons Ltd., New York, New York, 1986, p.254.
- [51] Bowker, A. H., and G. J. Lieberman, *Engineering Statistics*, Prentice-Hall, Inc., Englewood Cliffs, N.J., 1959, pp. 70-78, 555-557.
- [52] Mitchell, L. D., Randolph Professor of Mechanical Engineering, Virginia Polytechnic Institute and State University, Personal Communication, Virginia Polytechnic Institute and State University, September 25, 1995.
- [53] Beer, F. P., and E. R. Johnston, Jr., *Mechanics of Materials*, Second Edition, McGraw-Hill, Inc., New York, New York, 1992, pp. 194-195.
- [54] Beckwith, T. G., Marangoni, R. D., and Lienhard V, J. H., *Mechanical Measurements*, Fifth Edition, Addison-Wesley Publishing Co., Reading, Massachusetts, 1993, pp. 70-75.
- [55] Li, X. W., *A Precision Laser Scanning System for Experimental Modal Analysis: Its Test and Calibration*, Masters Thesis, Virginia Polytechnic Institute and State University, Department of Mechanical Engineering, Blacksburg, Virginia, 1992, Committee Chairman: L. D. Mitchell.

## **APPENDIX A.1**

### **FIGURES FOR RANGE OF VELOCITIES EXPERIMENT**

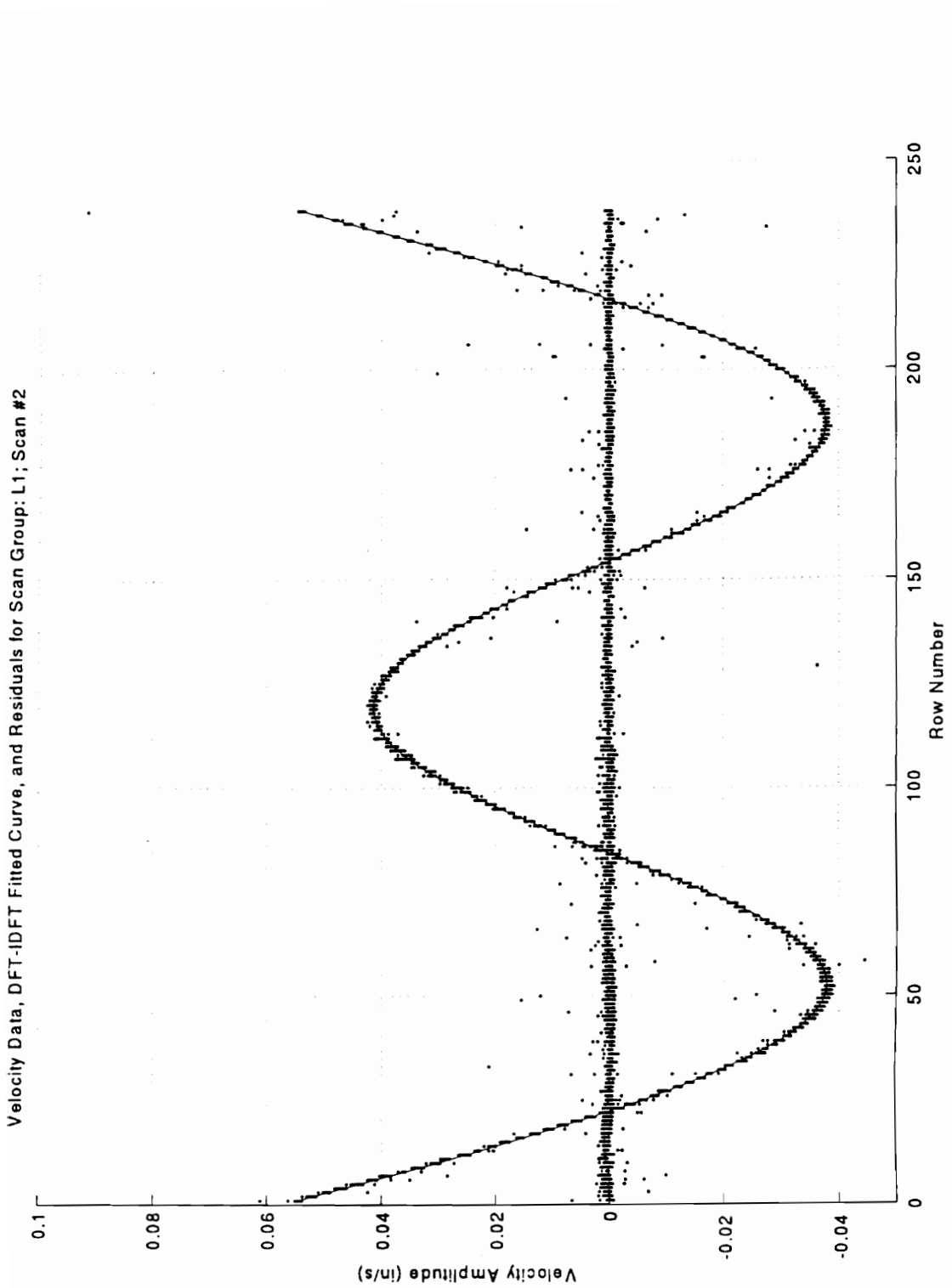


**Figure A.1.1 - Range of Velocity Responses as a Percentage of Full-Scale Experiment: Representative scan-fit plot for Scan Group L1. (LOW velocity range setting, MAGNAFLUX™ coating, Long-Range Lens).**

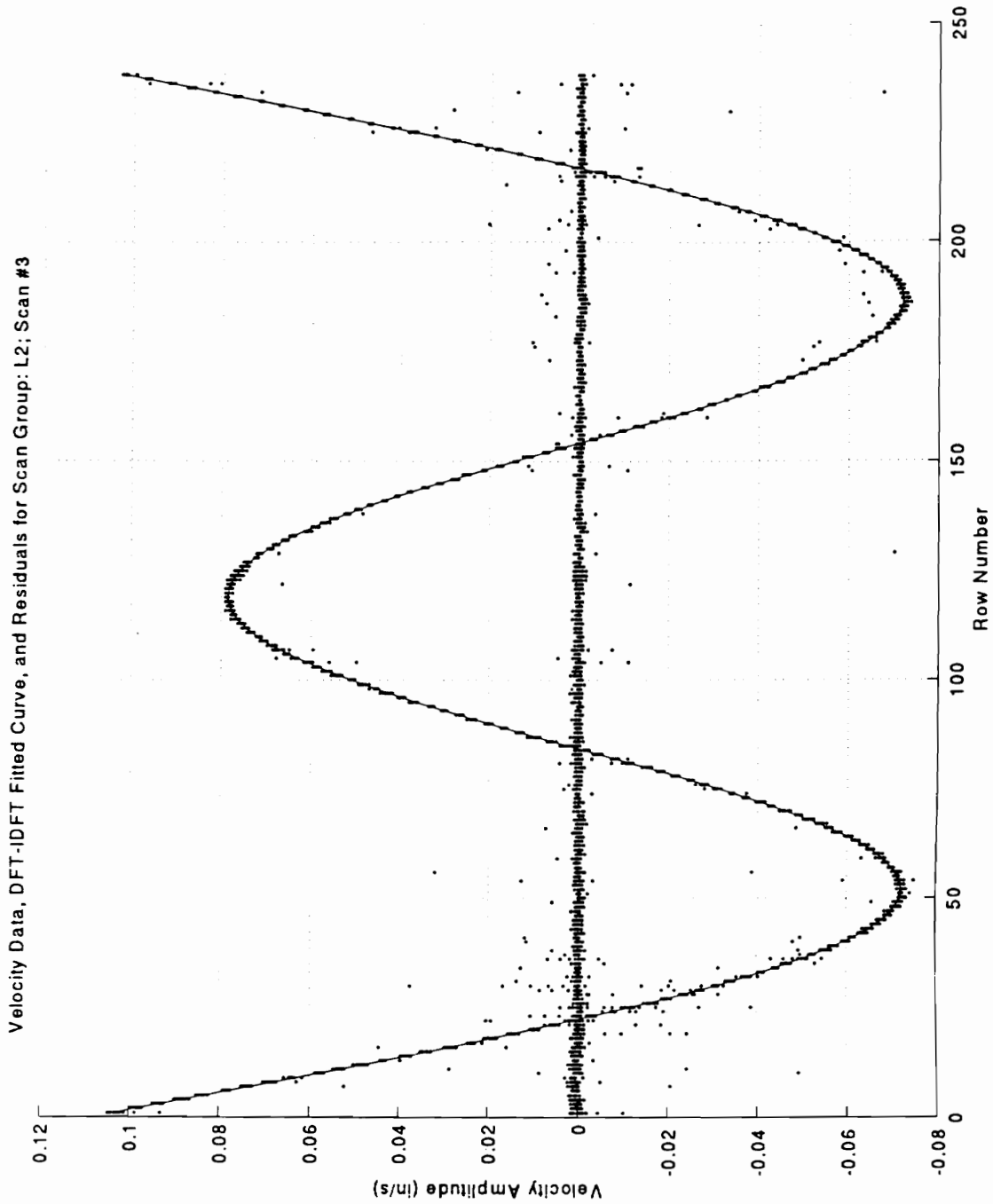


**Figure A.1.2 - Range of Velocity Responses as a Percentage of Full-Scale Experiment: Representative scan-fit plot for Scan Group L2. (LOW velocity range setting, MAGNAFLUX™ coating, Long-Range Lens).**

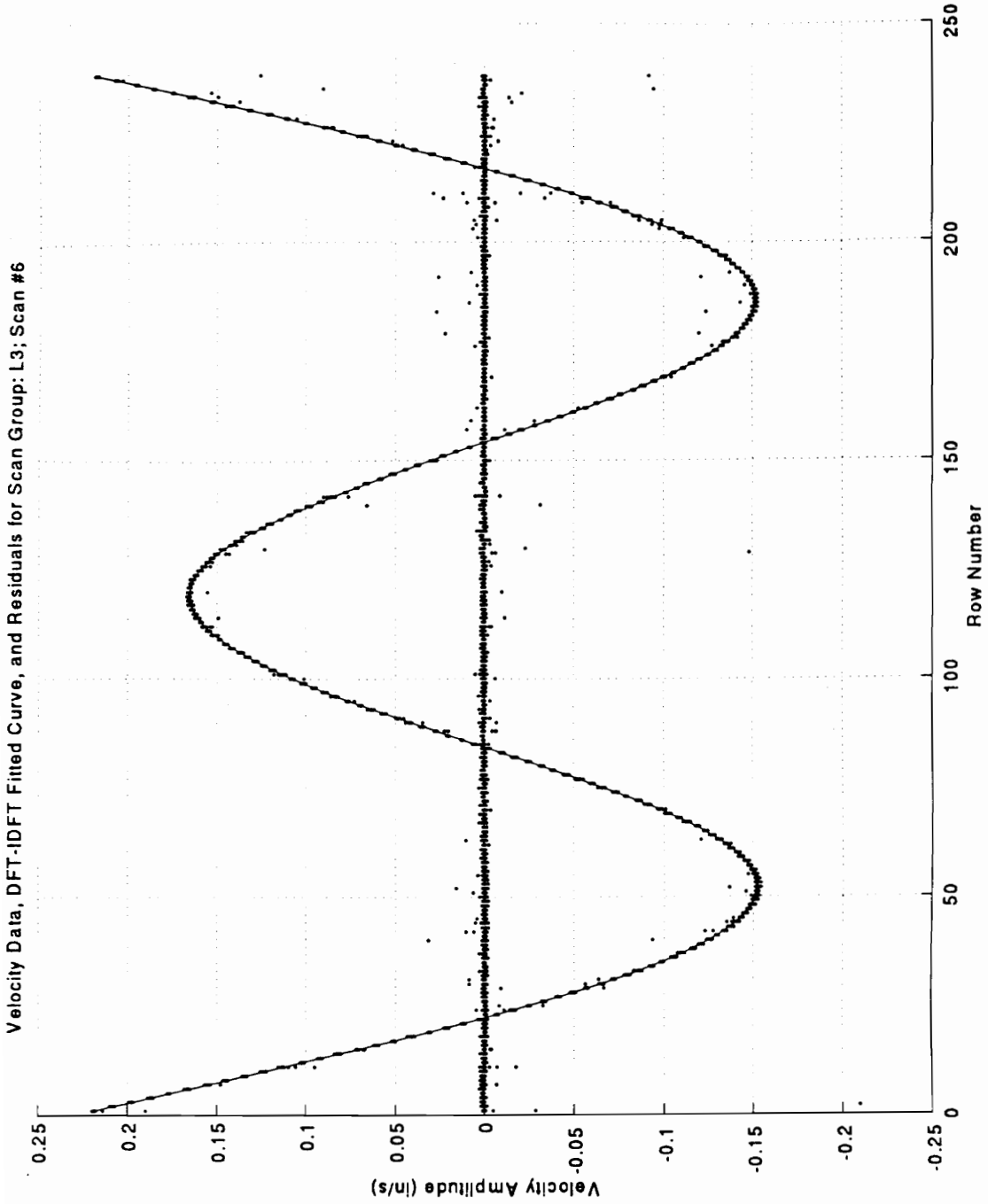


**Figure A.1.3 - Range of Velocity Responses as a Percentage of Full-Scale Experiment: Representative scan-fit plot for Scan Group L3. (LOW velocity range setting, MAGNAFLUX™ coating, Long-Range Lens).**

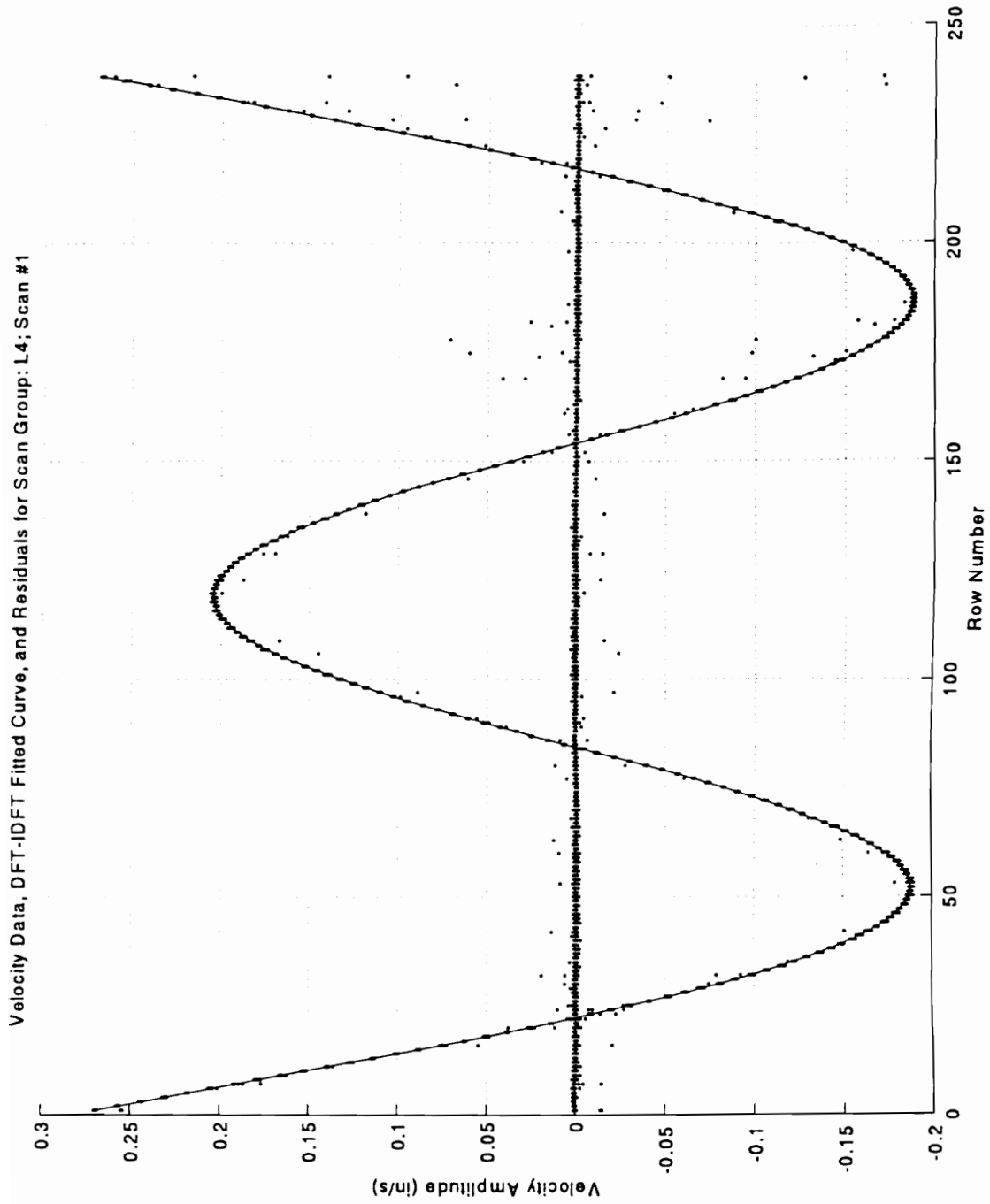


**Figure A.1.4 - Range of Velocity Responses as a Percentage of Full-Scale Experiment: Representative scan-fit plot for Scan Group L4. (LOW velocity range setting, MAGNAFLUX™ coating, Long-Range Lens).**



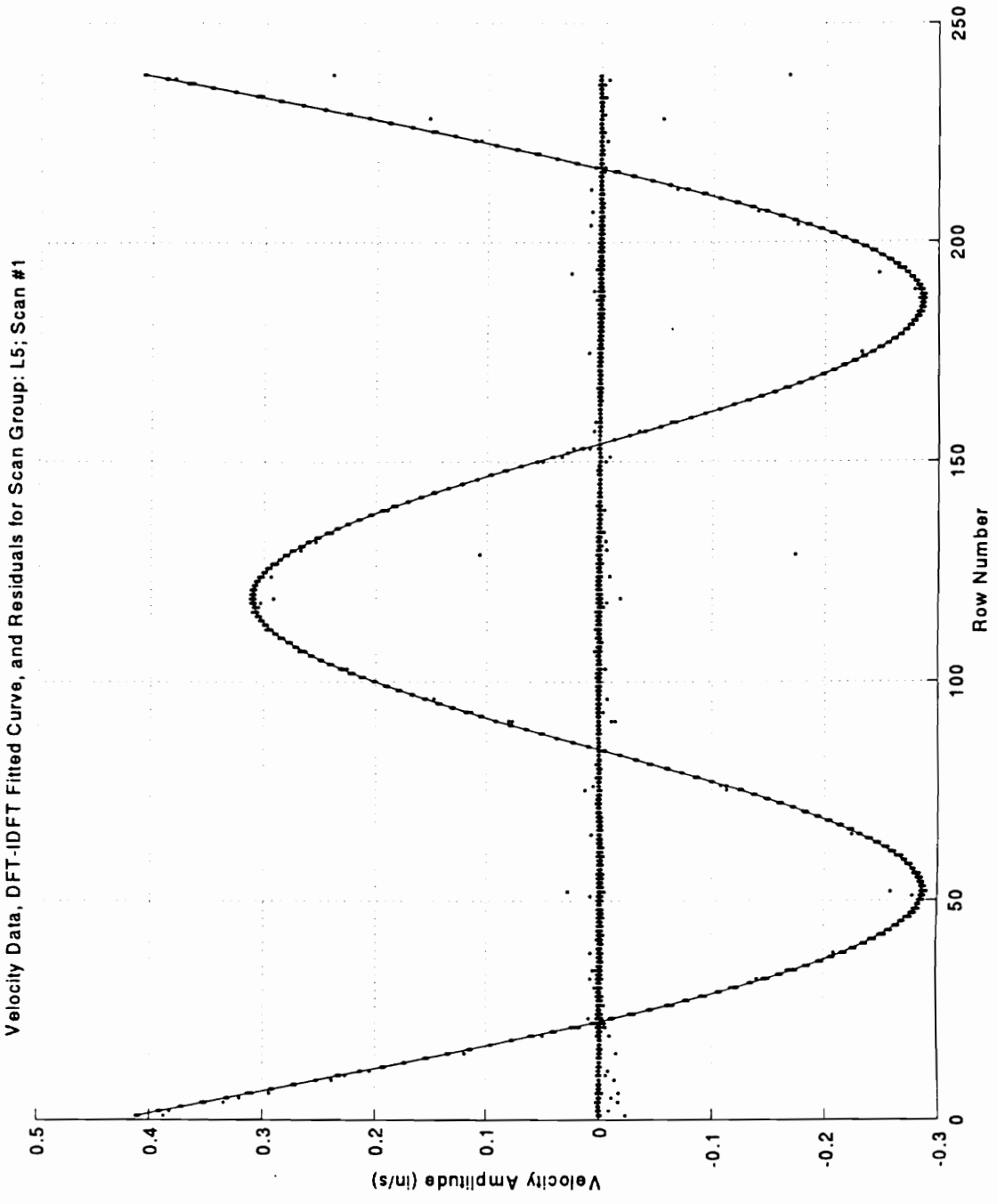


**Figure A.1.5 - Range of Velocity Responses as a Percentage of Full-Scale Experiment: Representative scan-fit plot for Scan Group L5. (LOW velocity range setting, MAGNAFLUX™ coating, Long-Range Lens).**

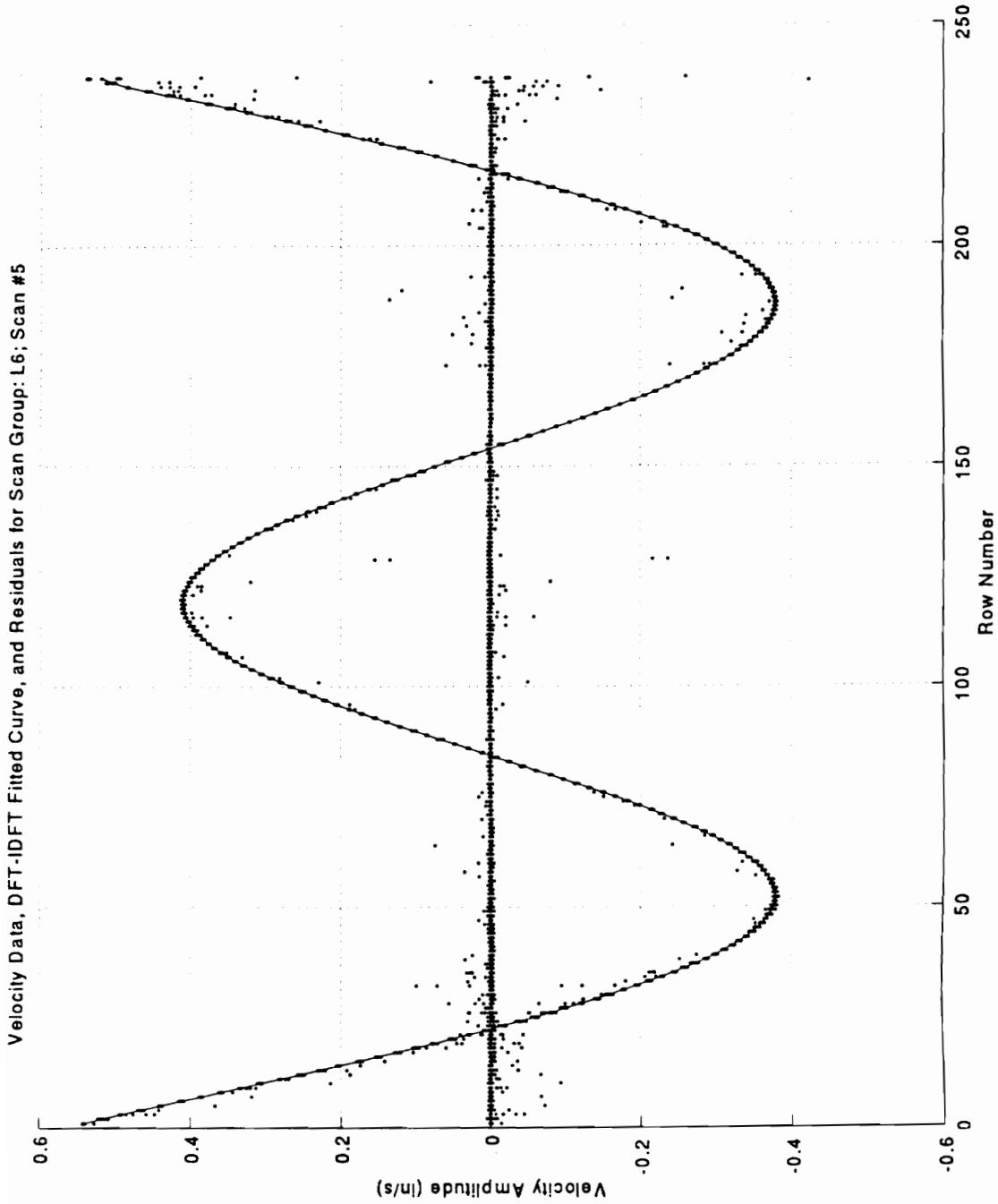


**Figure A.1.6 - Range of Velocity Responses as a Percentage of Full-Scale Experiment: Representative scan-fit plot for Scan Group L6. (LOW velocity range setting, MAGNAFLUX™ coating, Long-Range Lens).**

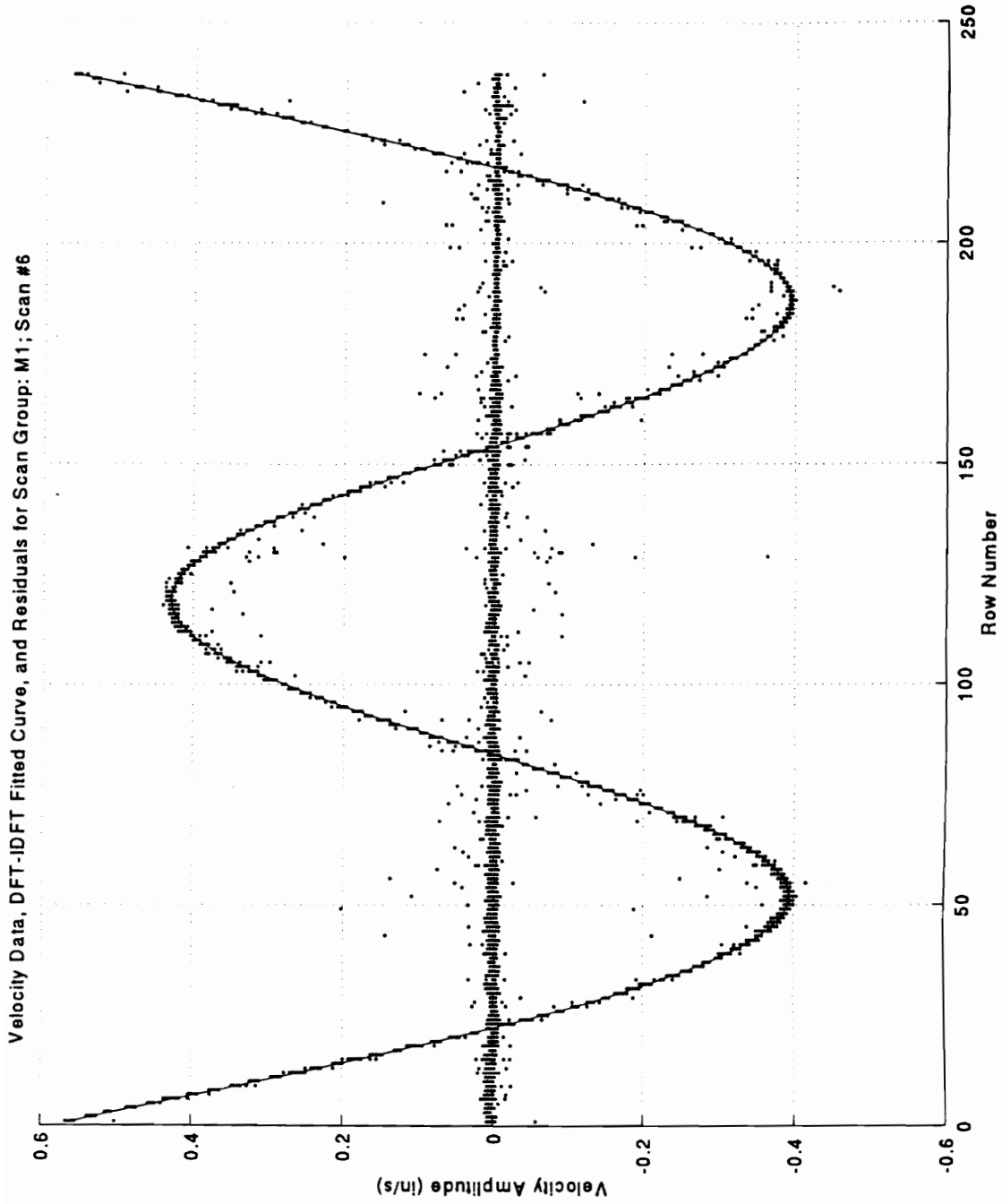


**Figure A.1.7 - Range of Velocity Responses as a Percentage of Full-Scale Experiment: Representative scan-fit plot for Scan Group M1. (MEDIUM velocity range setting, MAGNAFLUX™ coating, Long-Range Lens).**

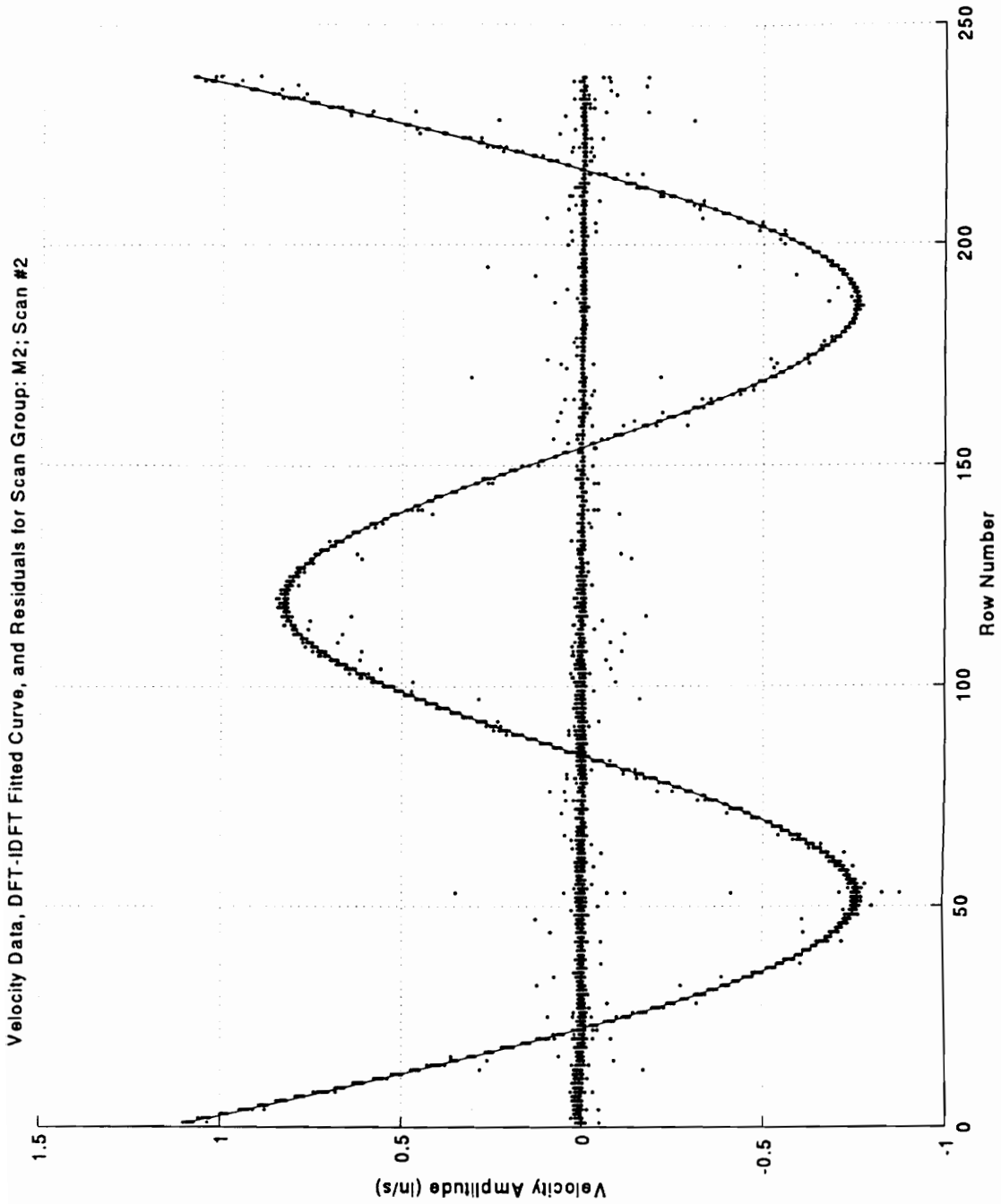


**Figure A.1.8 - Range of Velocity Responses as a Percentage of Full-Scale Experiment: Representative scan-fit plot for Scan Group M2. (MEDIUM velocity range setting, MAGNAFLUX™ coating, Long-Range Lens).**

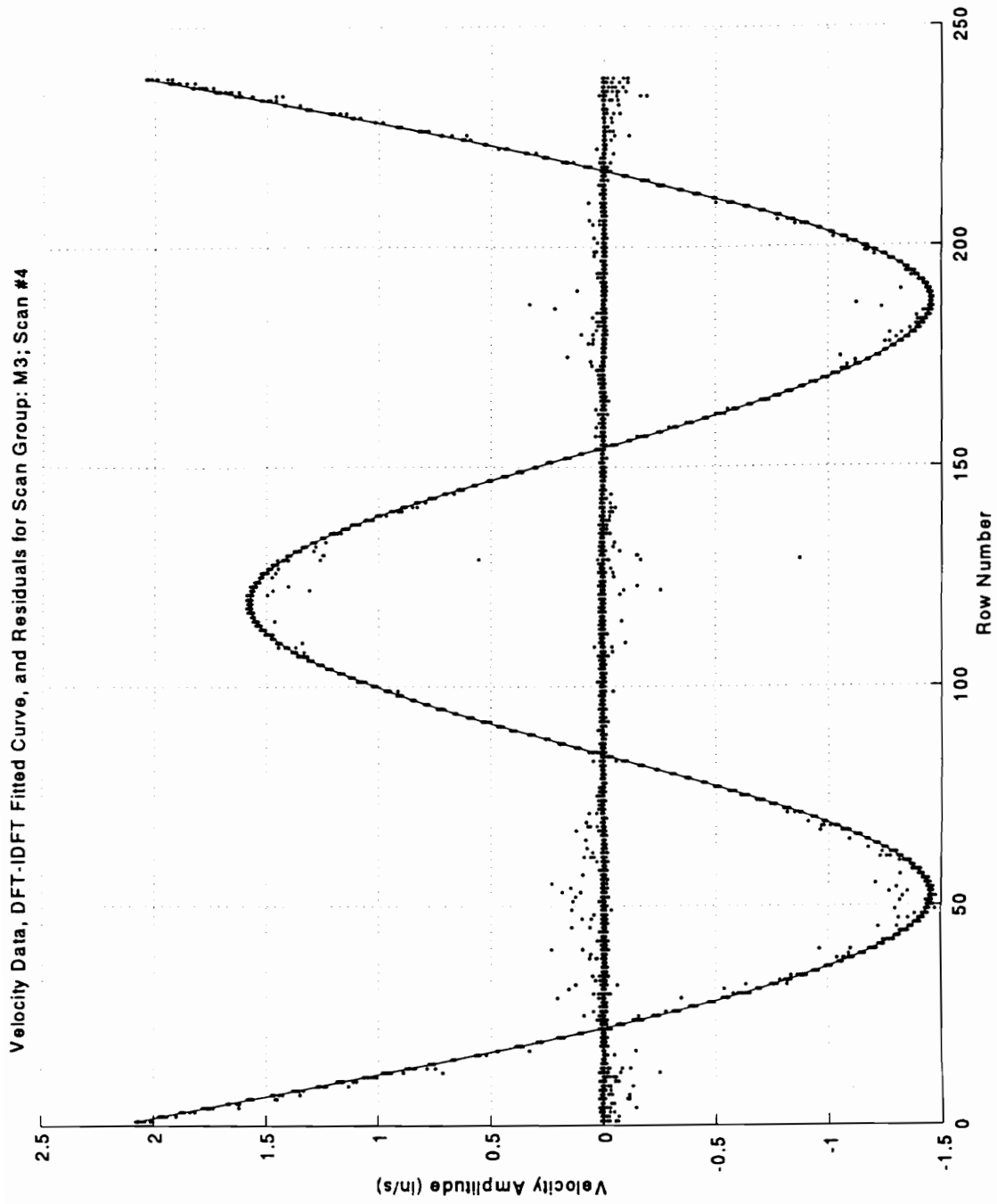
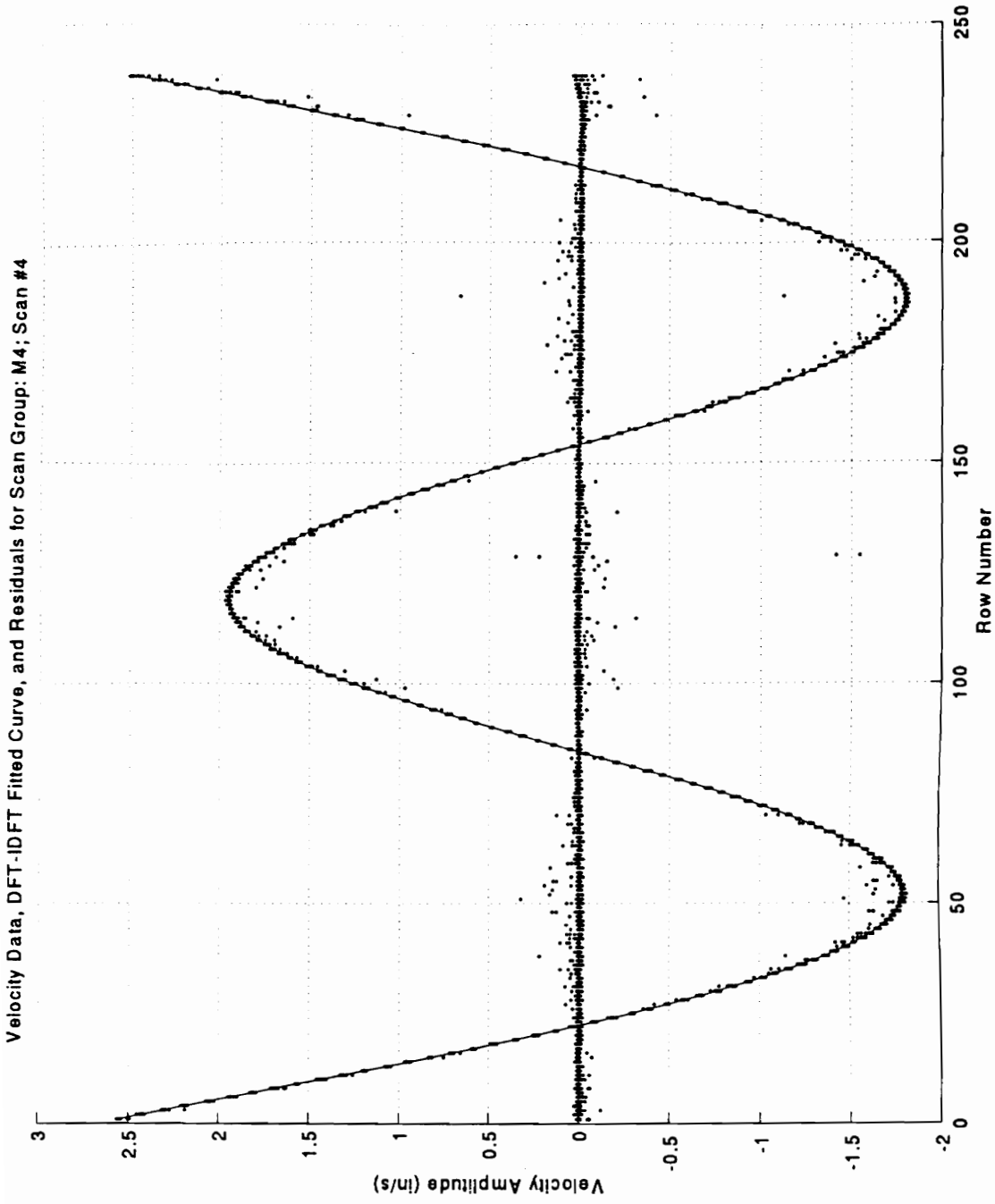


**Figure A.1.9 - Range of Velocity Responses as a Percentage of Full-Scale Experiment: Representative scan-fit plot for Scan Group M3. (MEDIUM velocity range setting, MAGNAFLUX™ coating, Long-Range Lens).**



Velocity Data, DFT-IDFT Fitted Curve, and Residuals for Scan Group: M4; Scan #4

**Figure A.1.10 - Range of Velocity Responses as a Percentage of Full-Scale Experiment: Representative scan-fit plot for Scan Group M4. (MEDIUM velocity range setting, MAGNAFLUX™ coating, Long-Range Lens).**

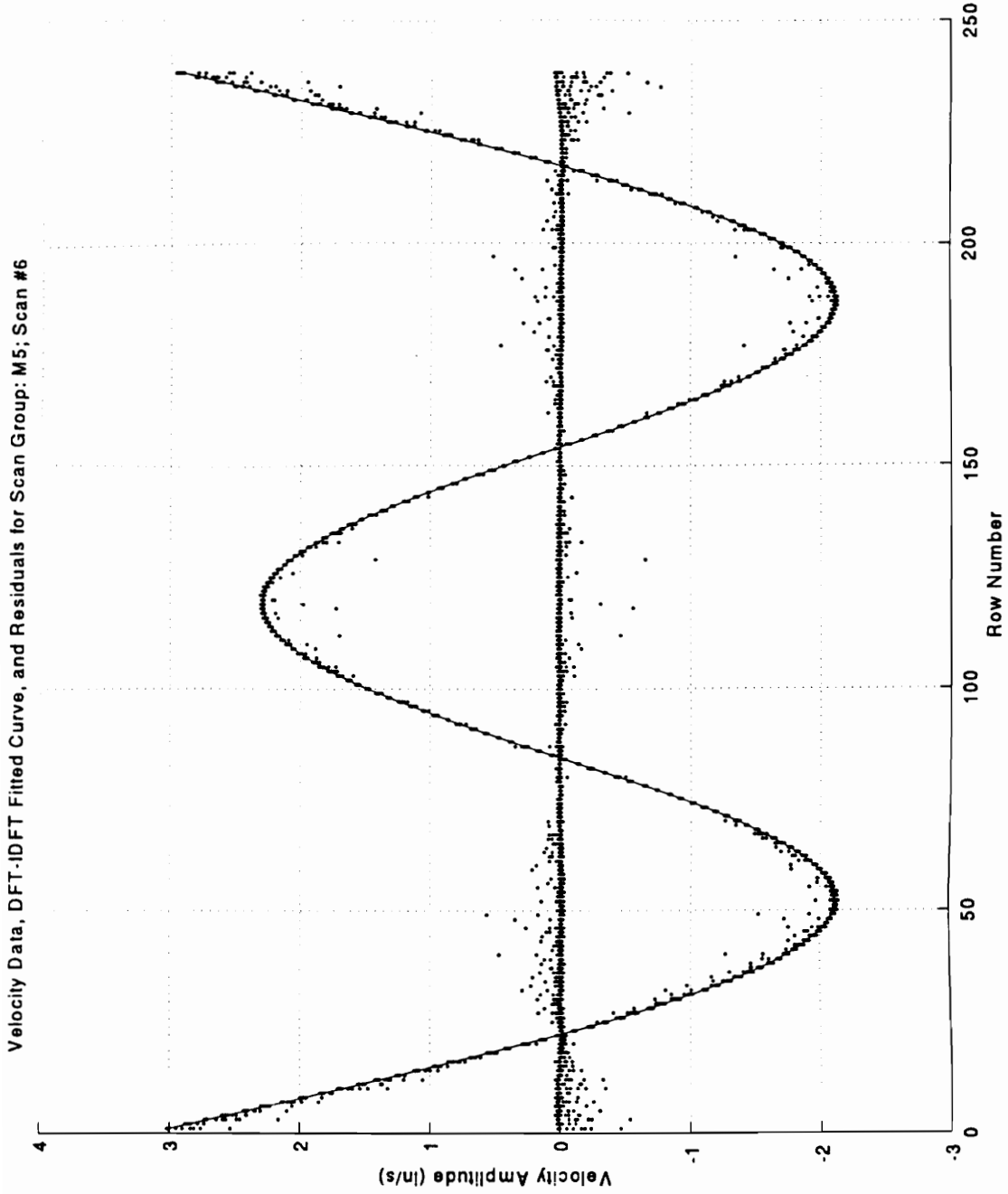


**Figure A.1.11 - Range of Velocity Responses as a Percentage of Full-Scale Experiment: Representative scan-fit plot for Scan Group M5. (MEDIUM velocity range setting, MAGNAFLUX™ coating, Long-Range Lens).**

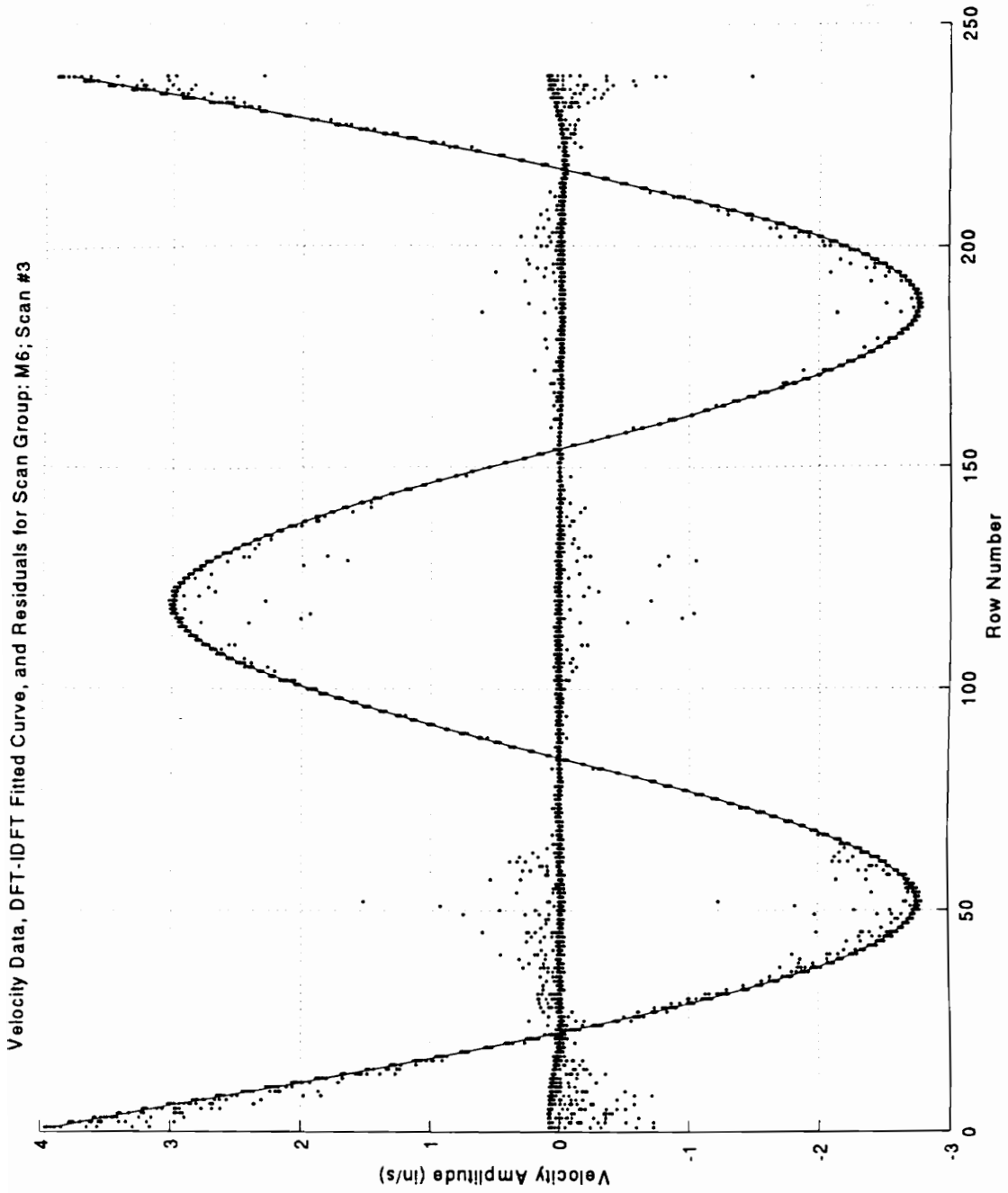
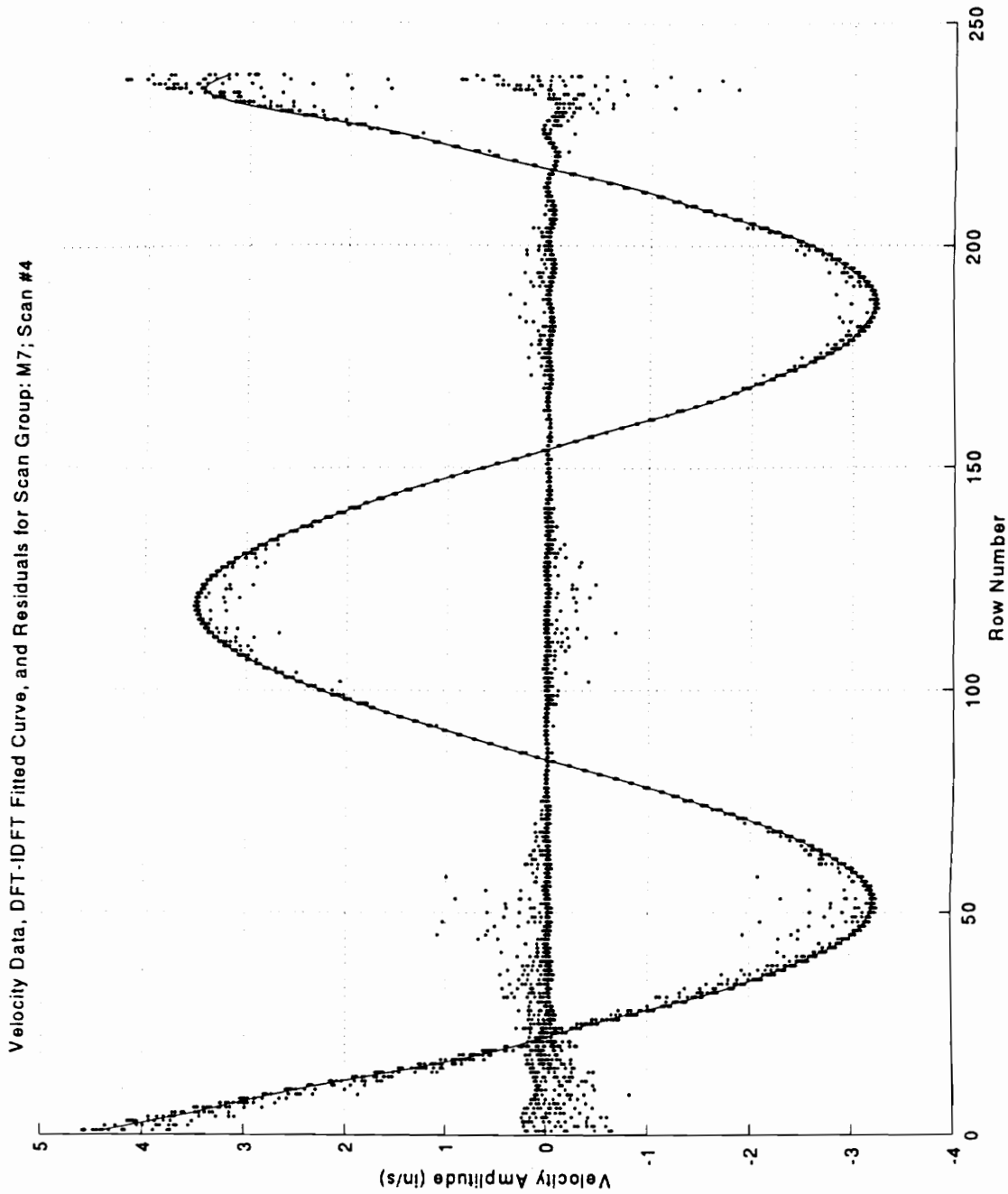


**Figure A.1.12 - Range of Velocity Responses as a Percentage of Full-Scale Experiment: Representative scan-fit plot for Scan Group M6. (MEDIUM velocity range setting, MAGNAFLUX™ coating, Long-Range Lens).**





Velocity Data, DFT-IDFT Fitted Curve, and Residuals for Scan Group: M7; Scan #4

**Figure A.1.13 - Range of Velocity Responses as a Percentage of Full-Scale Experiment: Representative scan-fit plot for Scan Group M7. (MEDIUM velocity range setting, MAGNAFLUX™ coating, Long-Range Lens).**

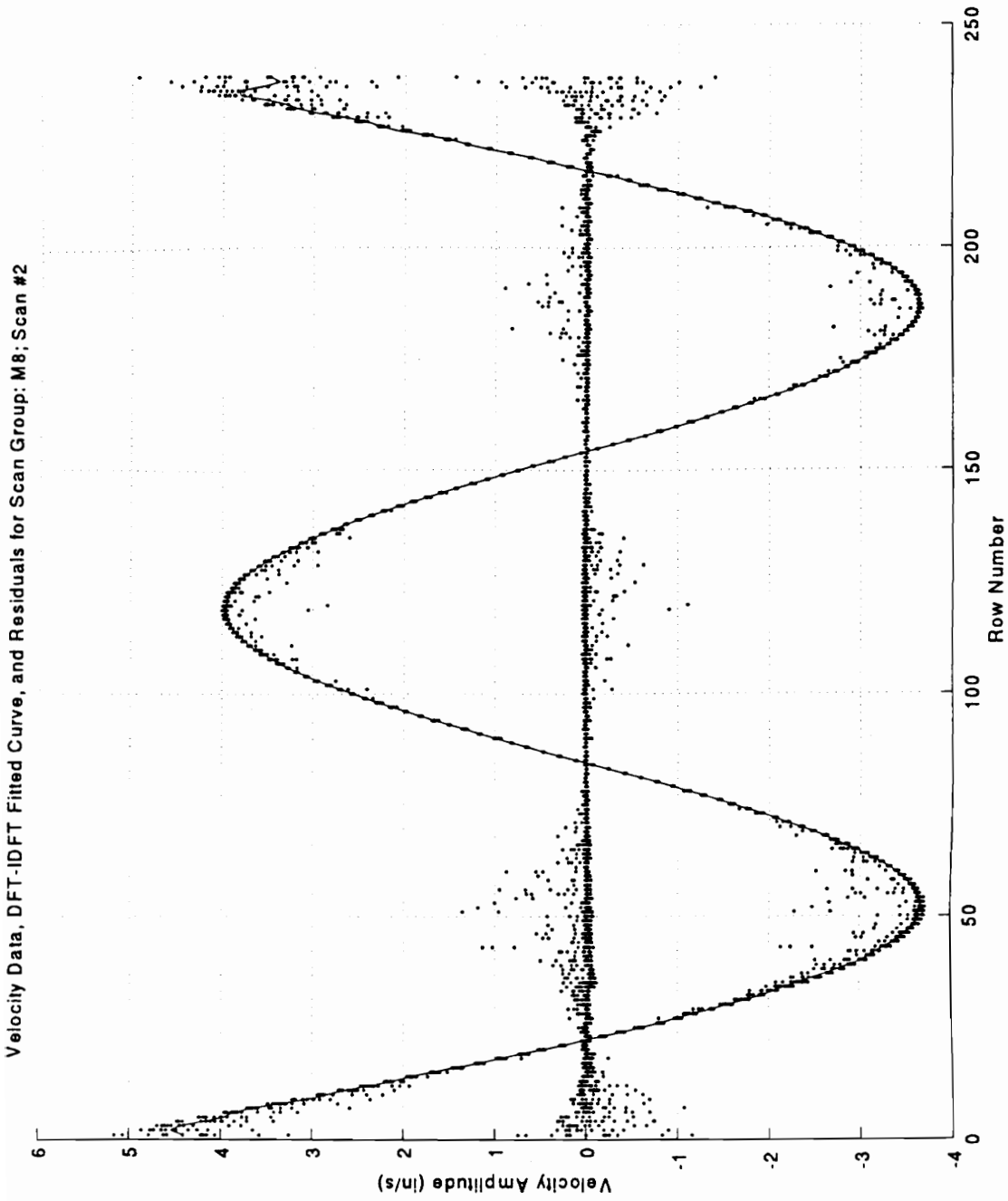
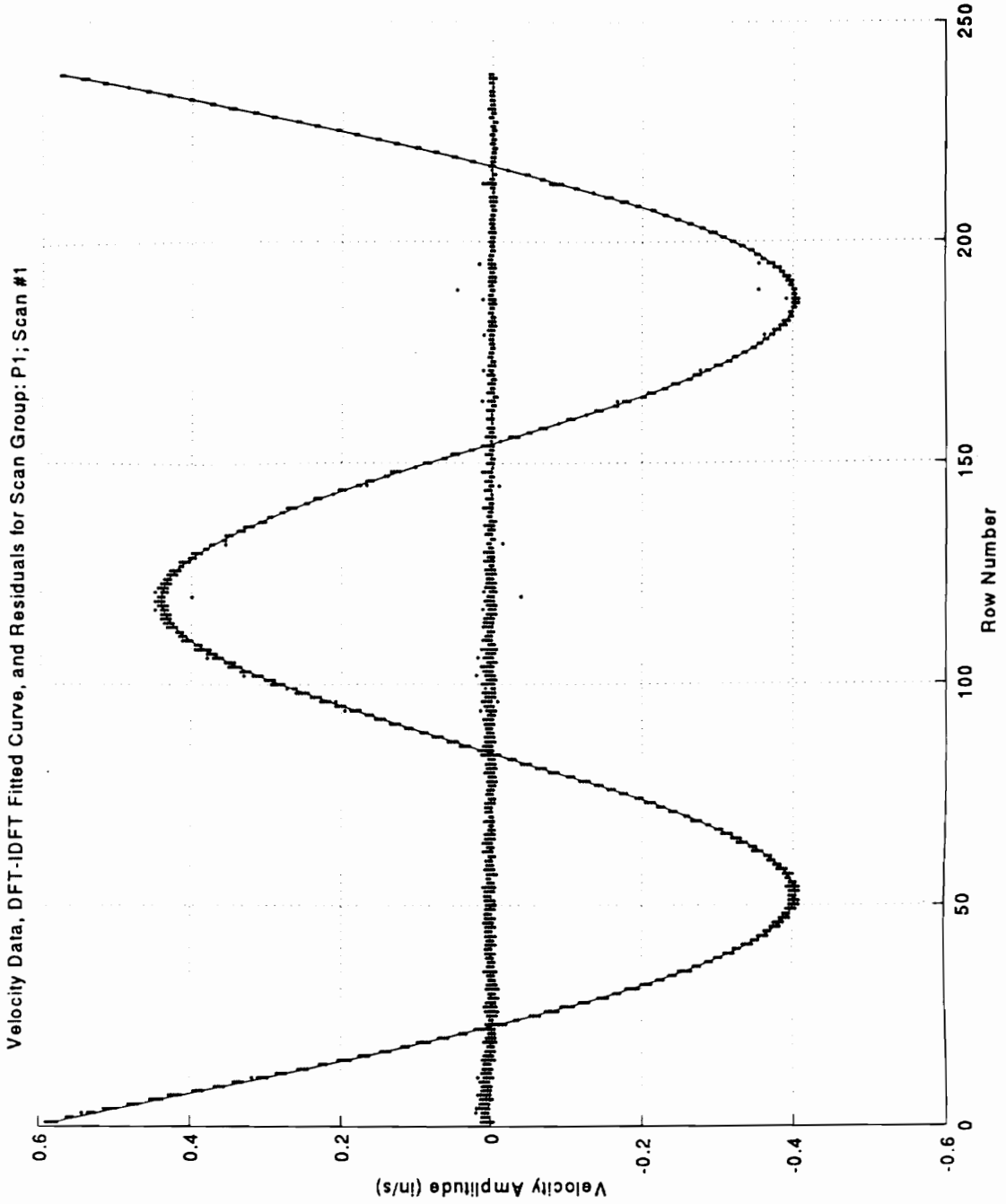


**Figure A.1.14 - Range of Velocity Responses as a Percentage of Full-Scale Experiment: Representative scan-fit plot for Scan Group M8. (MEDIUM velocity range setting, MAGNAFLUX™ coating, Long-Range Lens).**

## **APPENDIX A.2**

# **FIGURES FOR SURFACE PREPARATION EXPERIMENT**



Velocity Data, DFT-IDFT Fitted Curve, and Residuals for Scan Group: P1; Scan #1

**Figure A.2.1 - Surface Preparation Experiment: Representative scan-fit plot for Scan Group P1. (Retroreflective coating, MEDIUM velocity range setting, Long-Range Lens).**

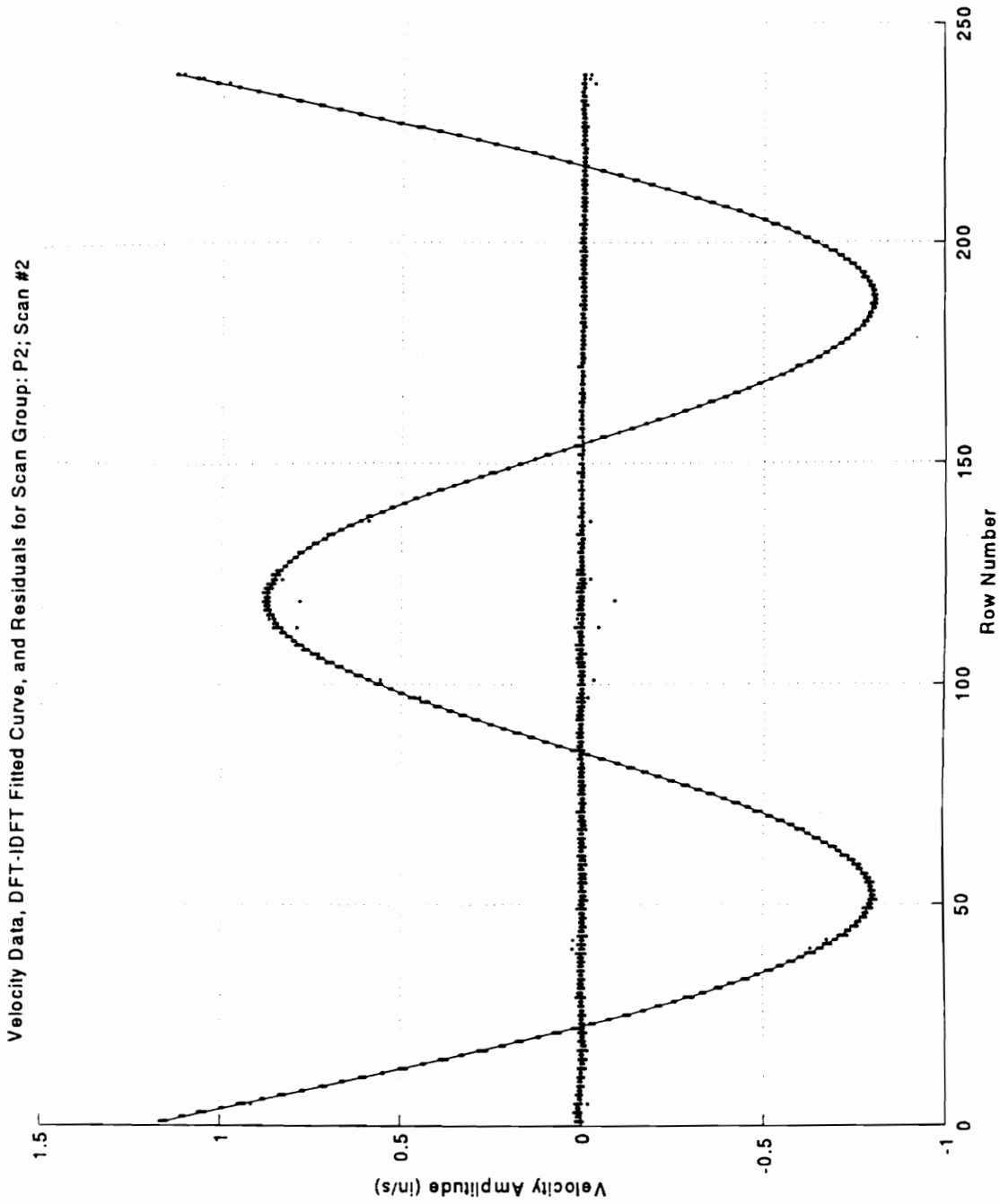


**Figure A.2.2 - Surface Preparation Experiment: Representative scan-fit plot for Scan Group P2. (Retroreflective coating, MEDIUM velocity range setting, Long-Range Lens).**

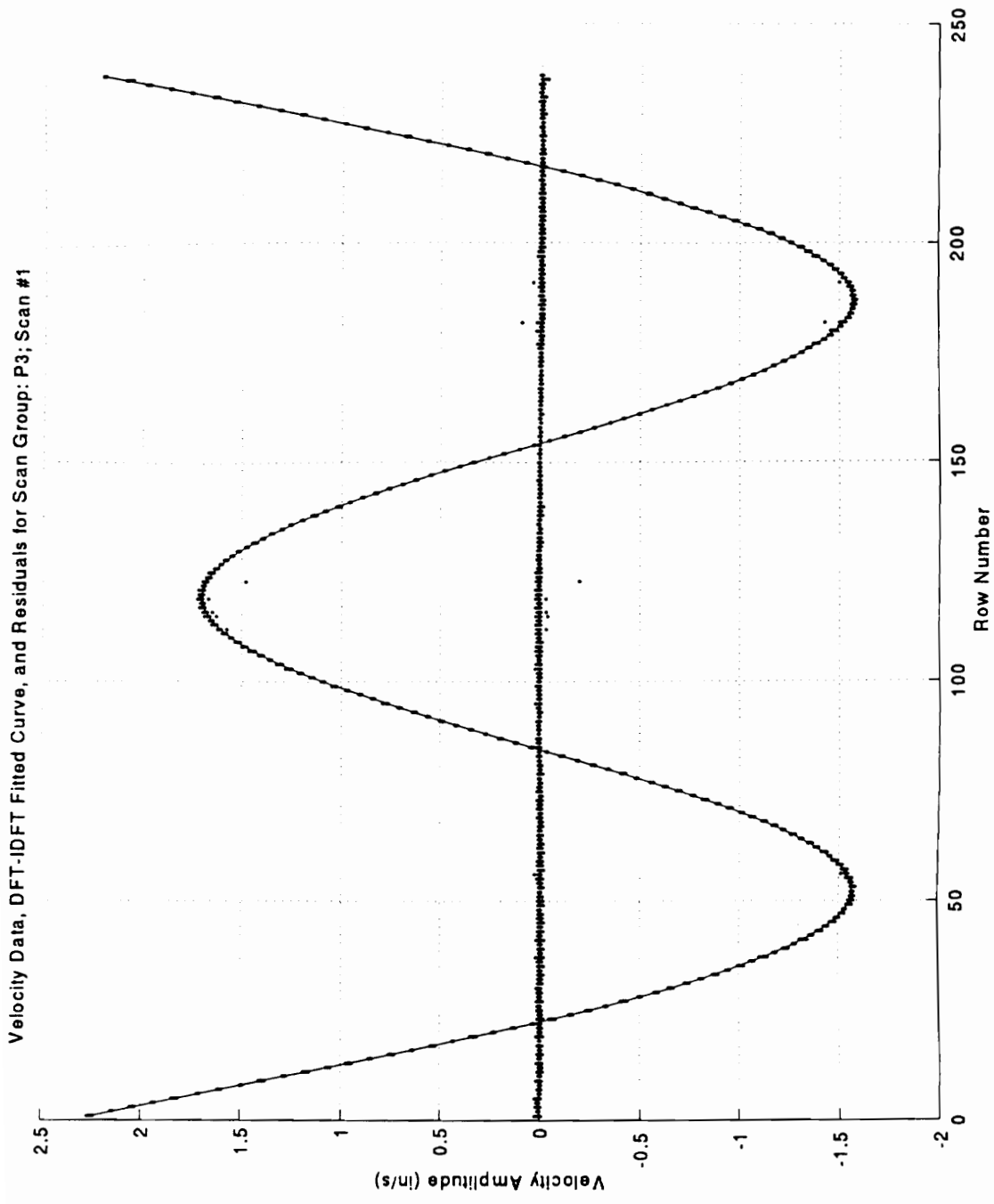
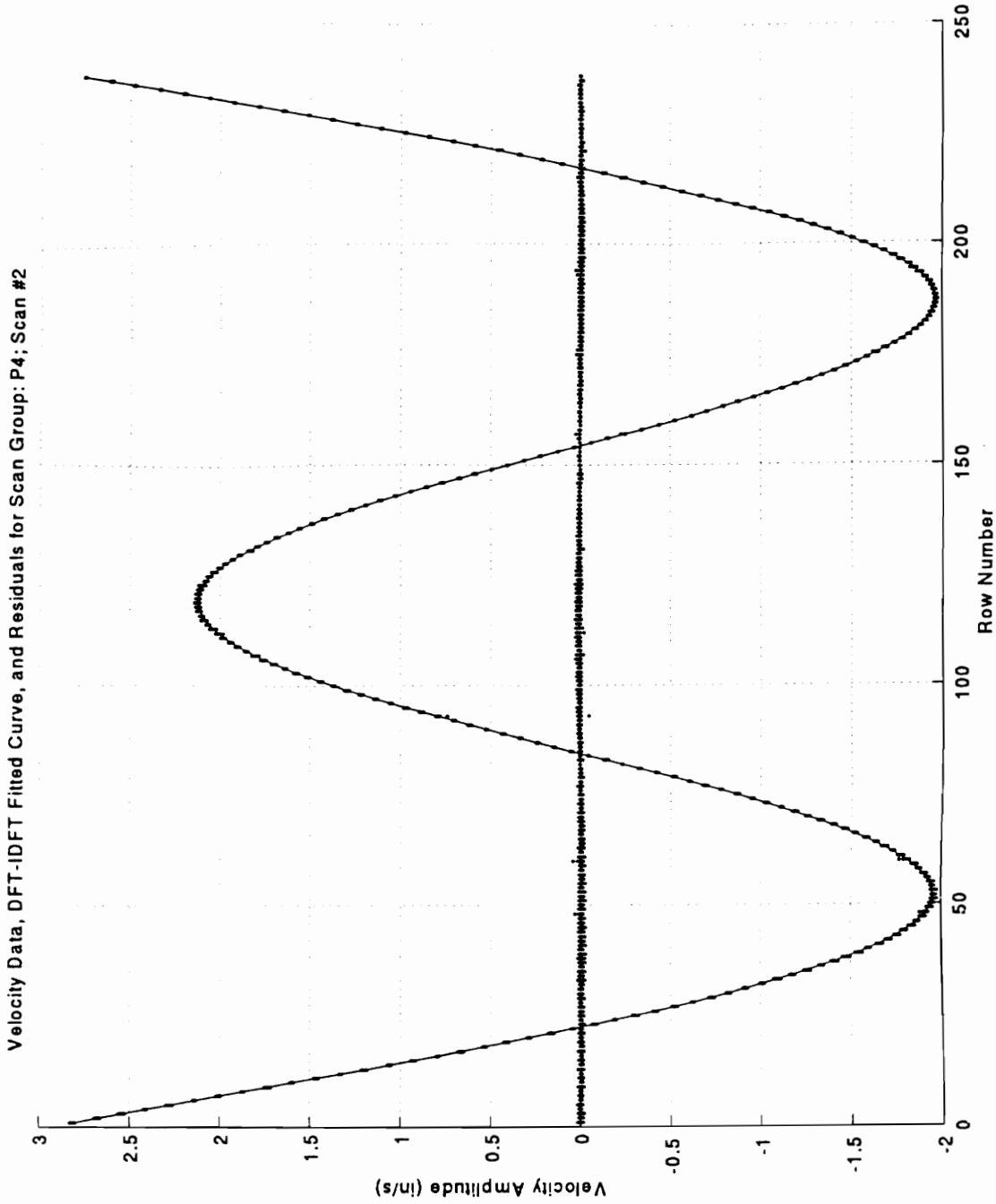


**Figure A.2.3 - Surface Preparation Experiment: Representative scan-fit plot for Scan Group P3. (Retroreflective coating, MEDIUM velocity range setting, Long-Range Lens).**



Velocity Data, DFT-IDFT Fitted Curve, and Residuals for Scan Group: P4; Scan #2

**Figure A.2.4 - Surface Preparation Experiment: Representative scan-fit plot for Scan Group P4. (Retroreflective coating, MEDIUM velocity range setting, Long-Range Lens).**

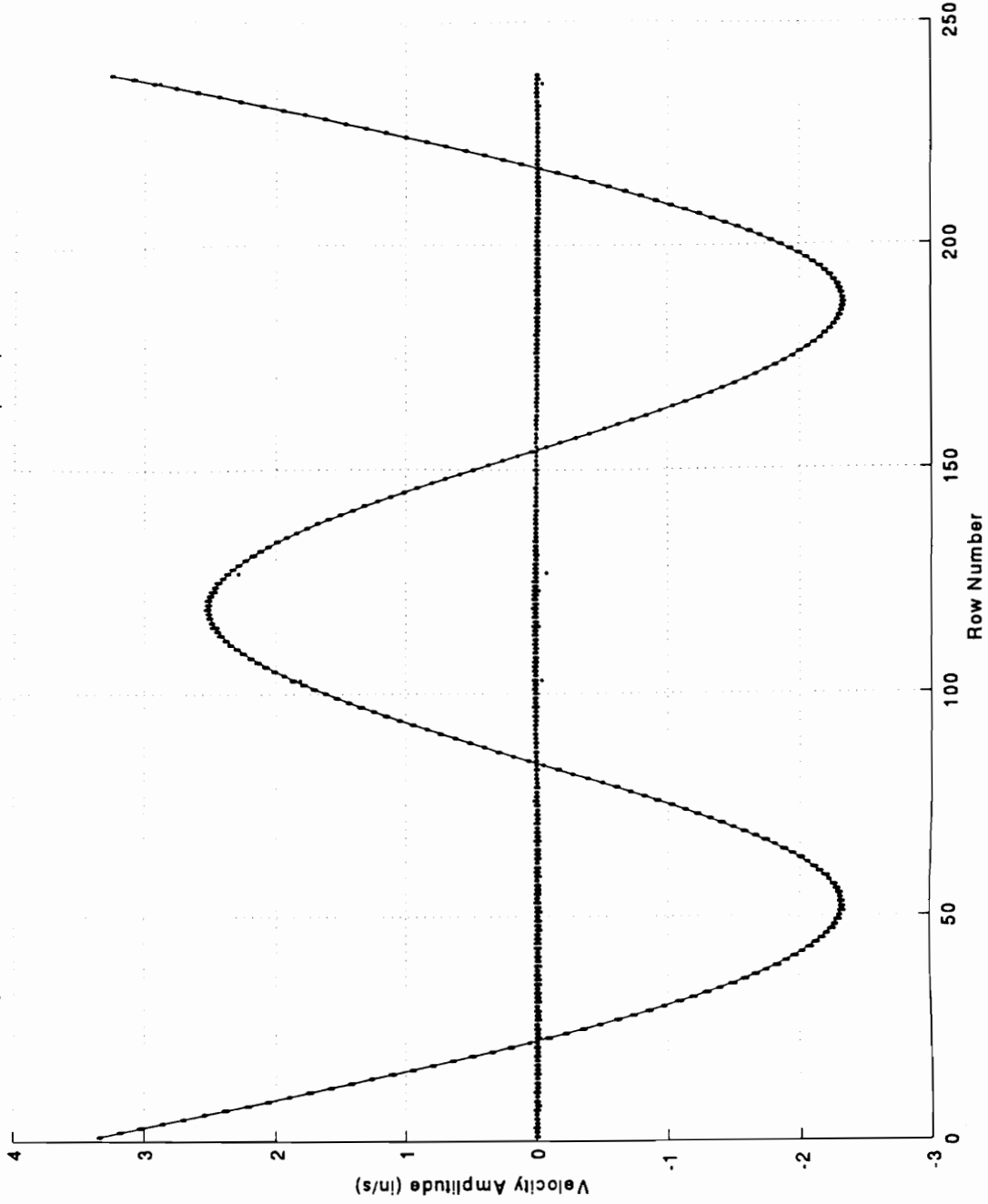
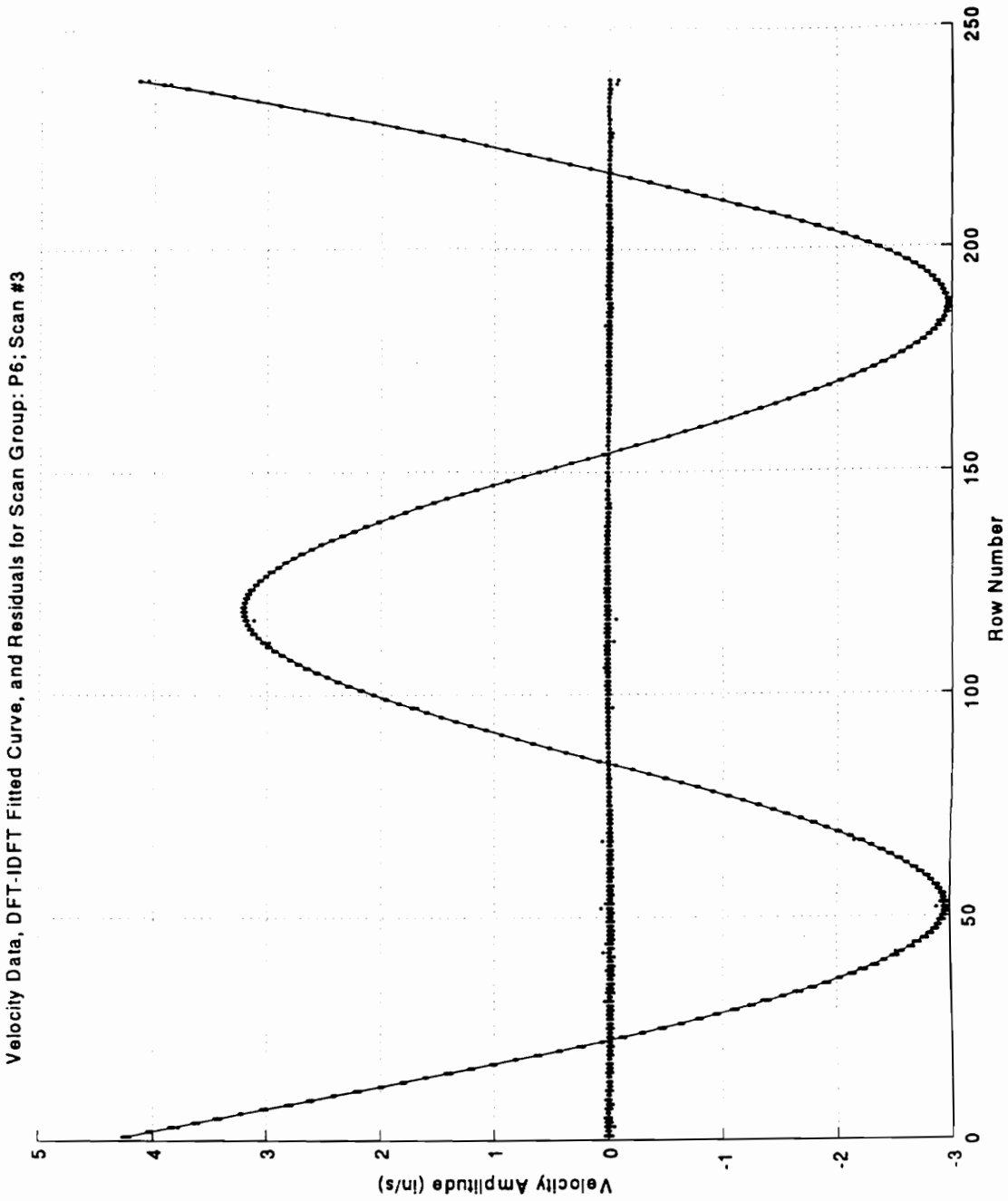


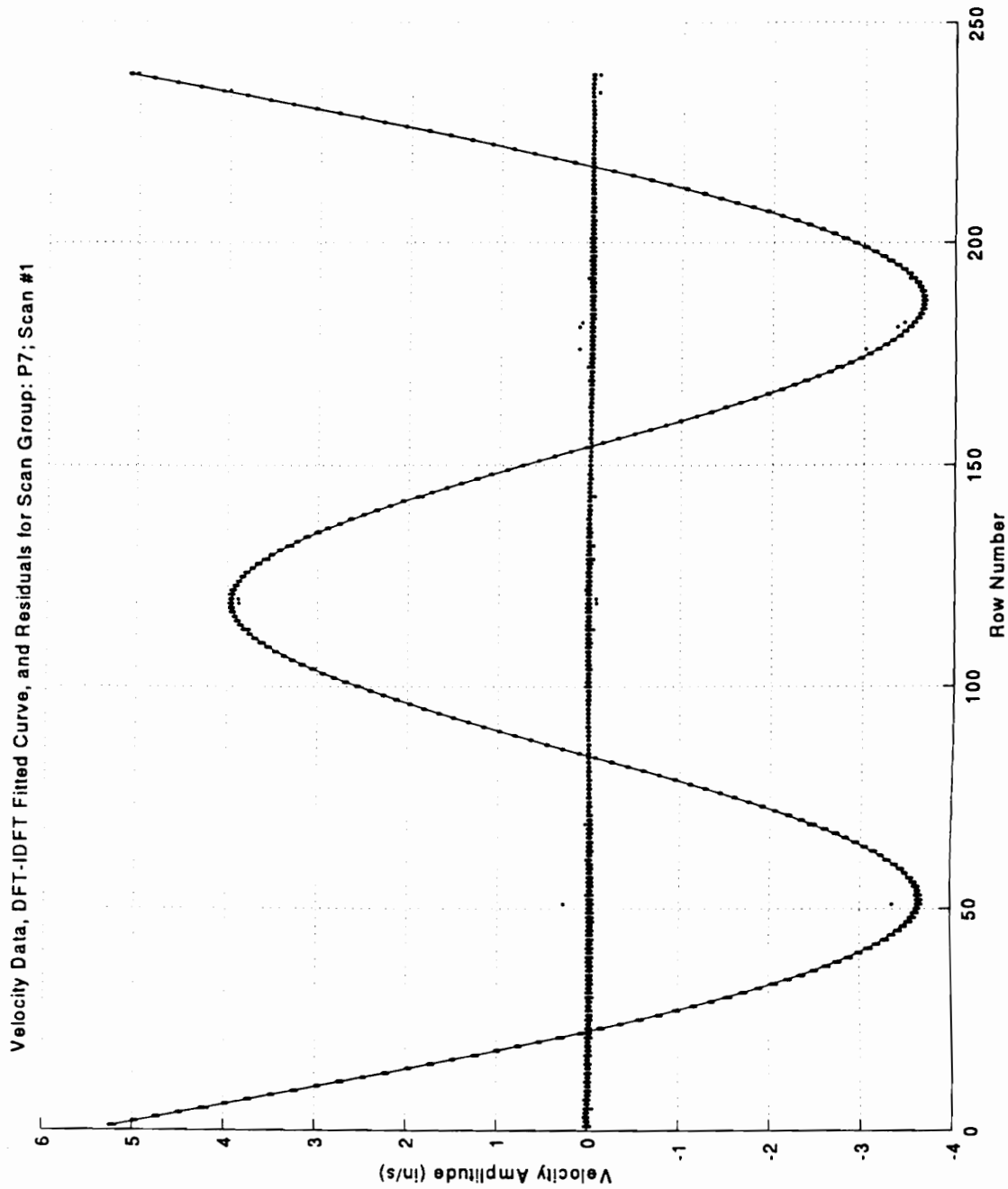
**Figure A.2.5 - Surface Preparation Experiment: Representative scan-fit plot for Scan Group P5. (Retroreflective coating, MEDIUM velocity range setting, Long-Range Lens).**





Velocity Data, DFT-IDFT Fitted Curve, and Residuals for Scan Group: P6; Scan #3

**Figure A.2.6 - Surface Preparation Experiment: Representative scan-fit plot for Scan Group P6. (Retroreflective coating, MEDIUM velocity range setting, Long-Range Lens).**

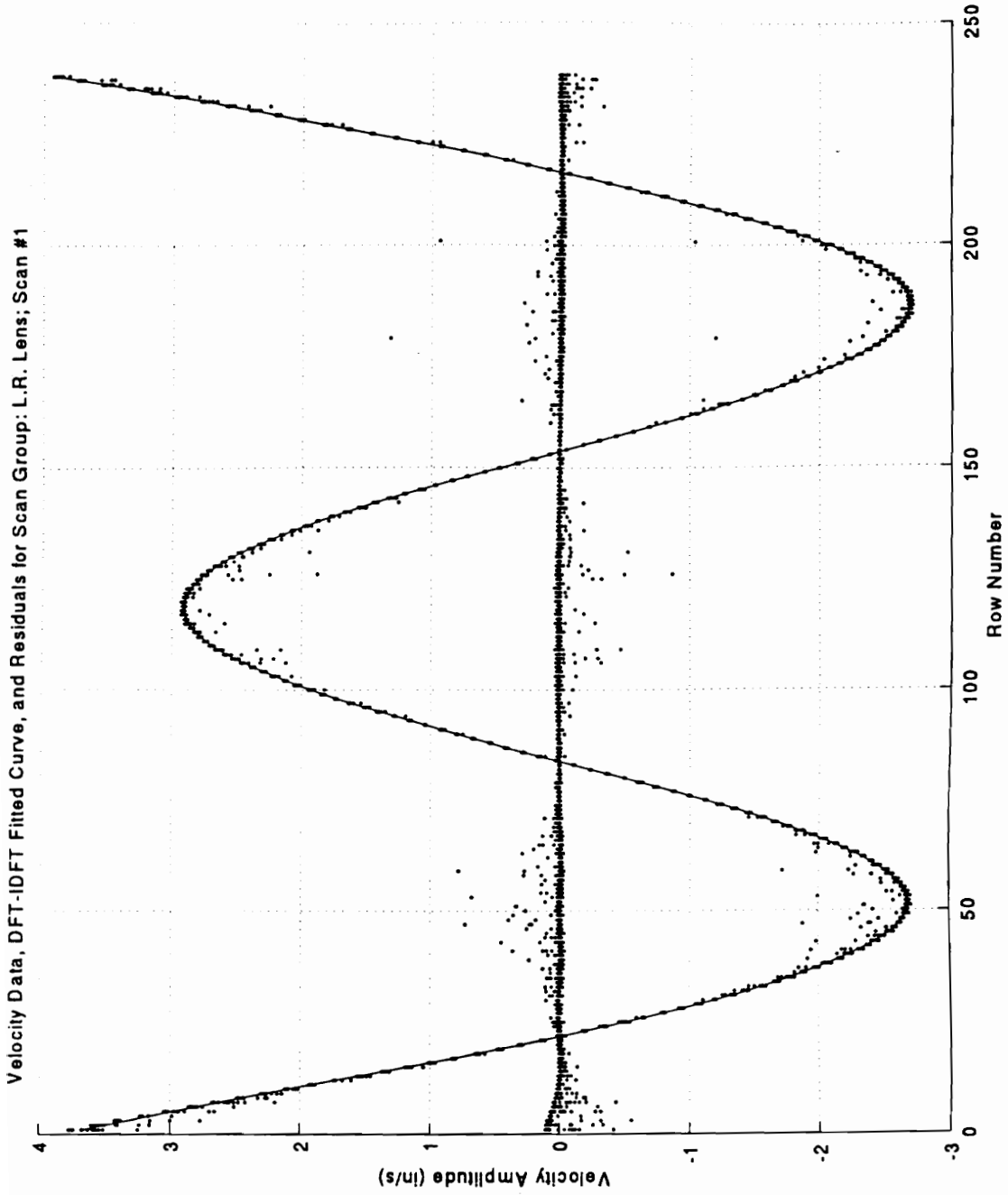


Velocity Data, DFT-IDFT Fitted Curve, and Residuals for Scan Group: P7; Scan #1

**Figure A.2.7 - Surface Preparation Experiment: Representative scan-fit plot for Scan Group P7. (Retroreflective coating, MEDIUM velocity range setting, Long-Range Lens).**

## **APPENDIX A.3**

# **FIGURES FOR OUTPUT LENS SELECTION EXPERIMENT**



Velocity Data, DFT-IDFT Fitted Curve, and Residuals for Scan Group: L.R. Lens; Scan #1

**Figure A.3.1 - Output Lens Selection Experiment: Representative scan-fit plot for Scan Group L. R. Lens. (Long-Range Lens, MAGNAFLUX™ coating, MEDIUM velocity range setting).**

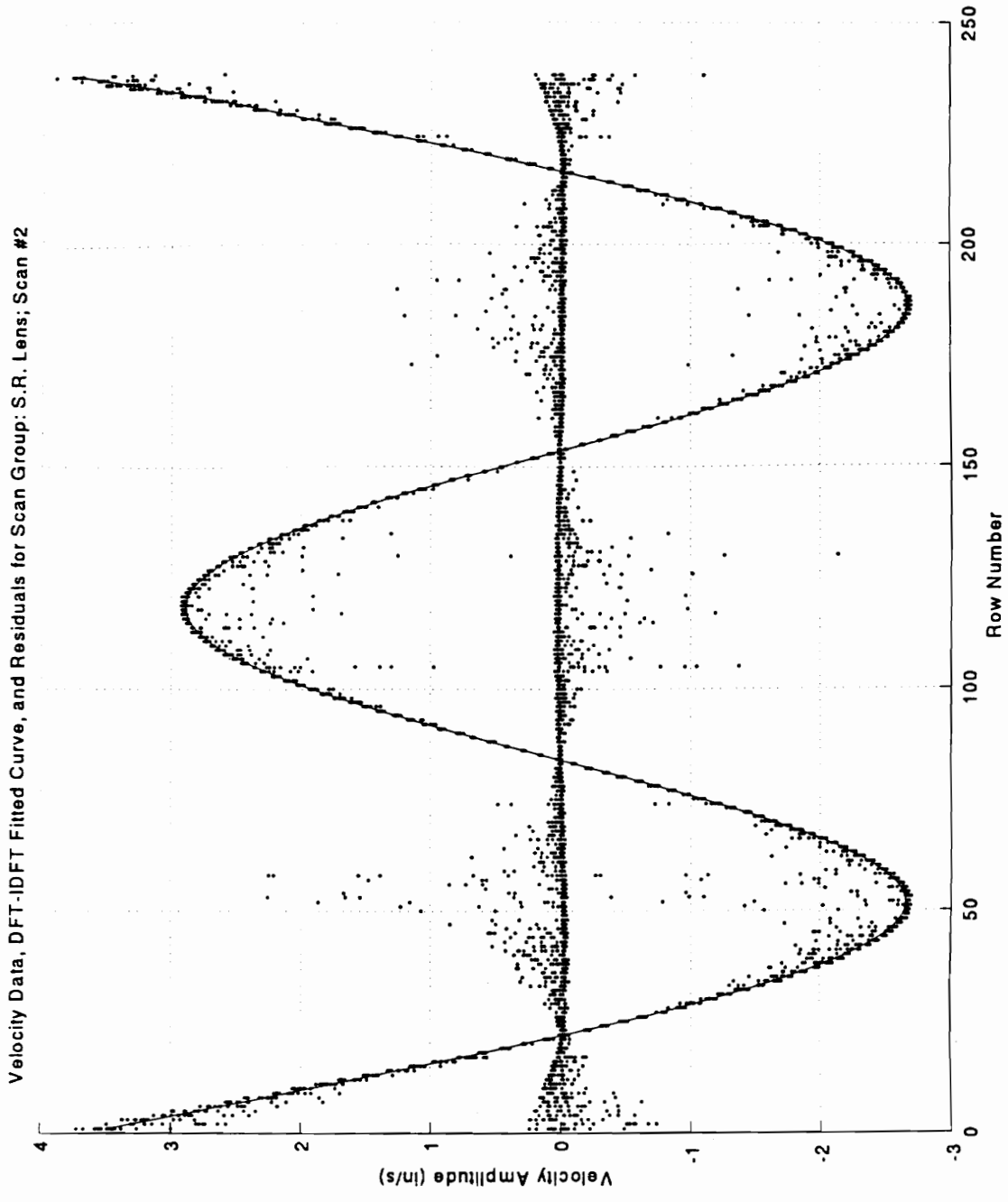


**Figure A.3.2 - Output Lens Selection Experiment: Representative scan-fit plot for Scan Group S. R. Lens. (Short-Range Lens, MAGNAFLUX™ coating, MEDIUM velocity range setting).**

## **APPENDIX A.4**

# **FIGURES FOR COHERENCE REPEAT DISTANCE EXPERIMENT**

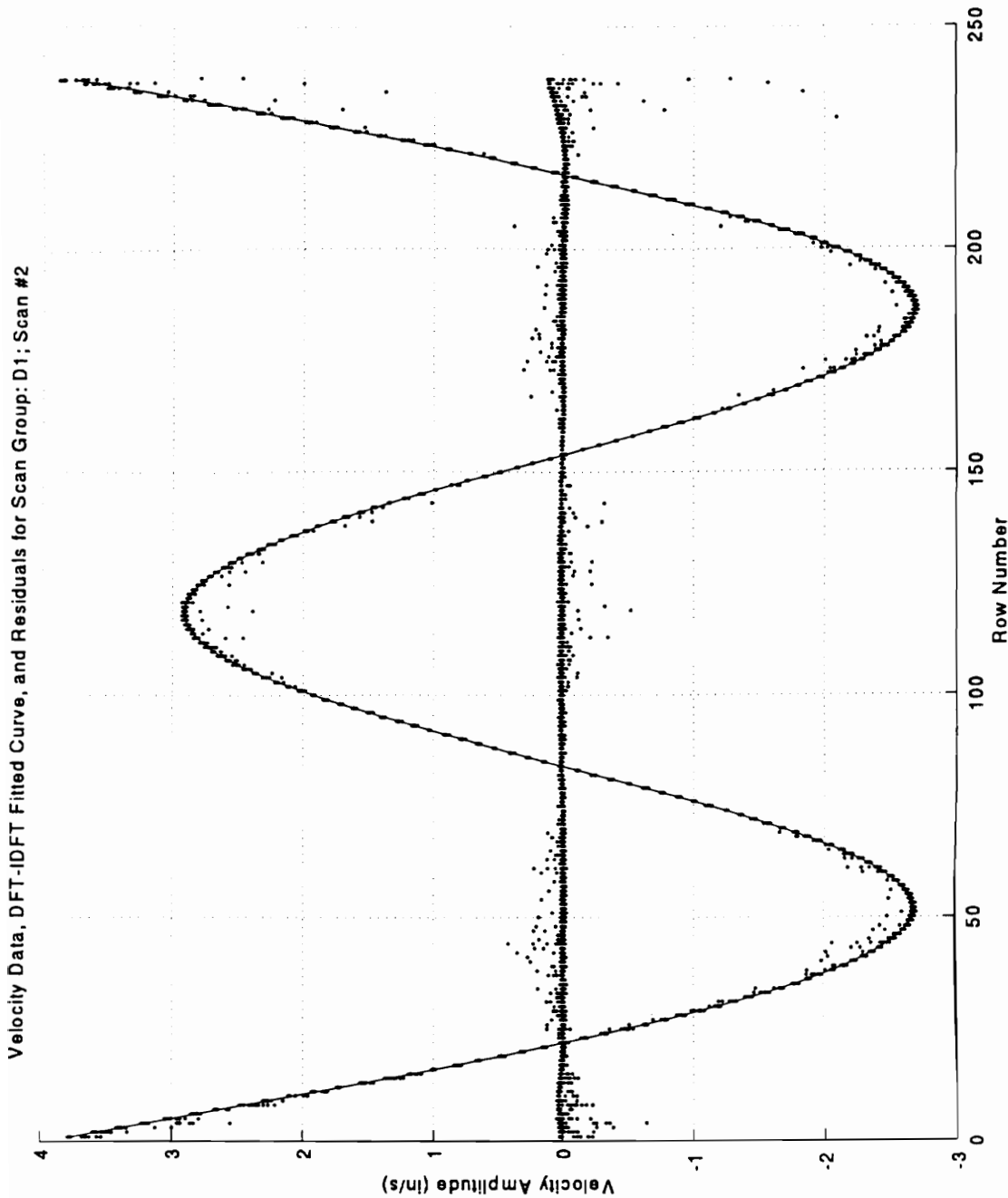


**Figure A.4.1 - Coherence Repeat Distance Experiment: Representative scan-fit plot for Scan Group D1. (133.1 in [3380.7 mm] operating distance, MAGNAFLUX™ coating, MEDIUM velocity range setting, Long-Range Lens).**

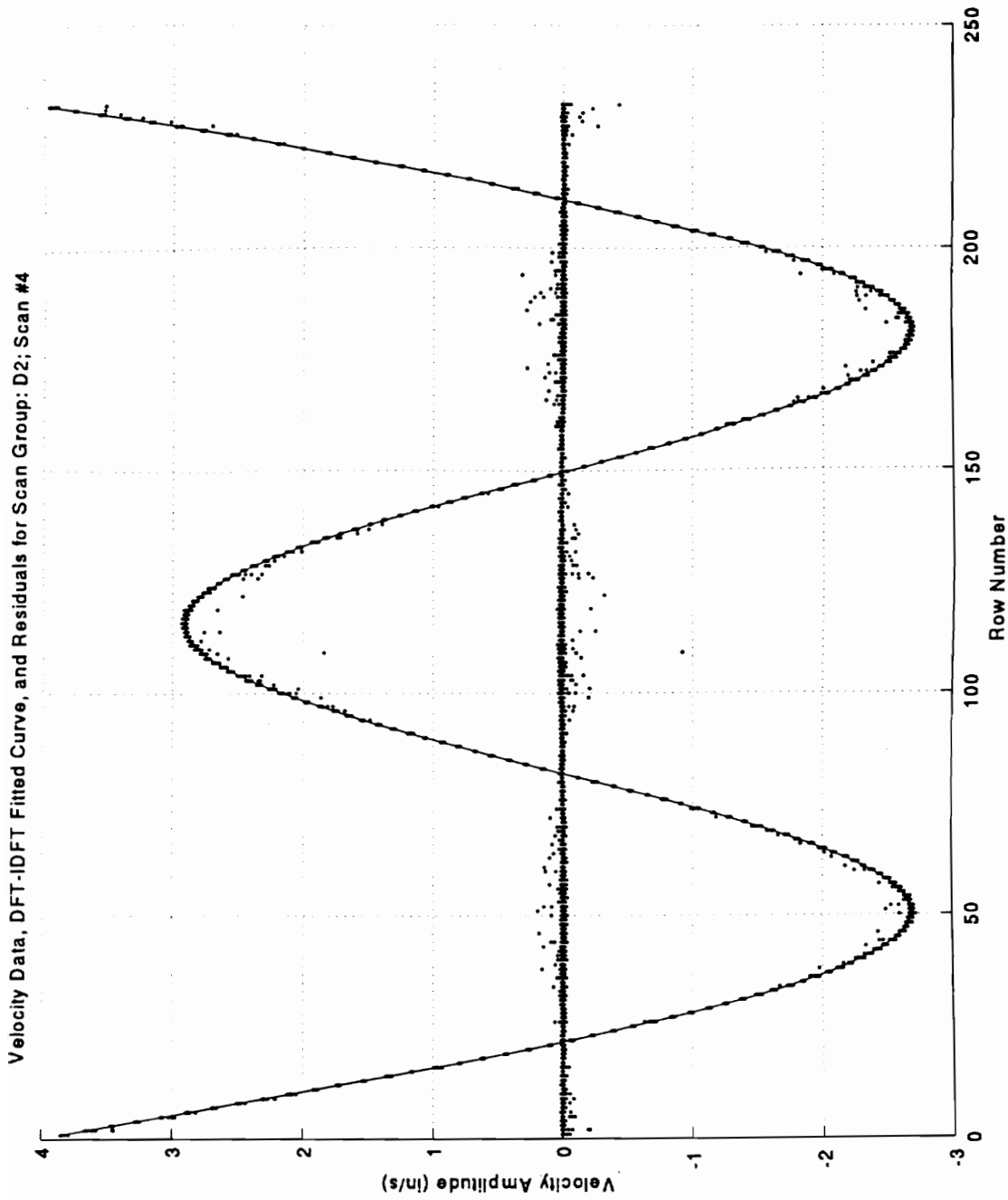


**Figure A.4.2 - Coherence Repeat Distance Experiment: Representative scan-fit plot for Scan Group D2. (137.2 in [3485 mm] operating distance, MAGNAFLUX™ coating, MEDIUM velocity range setting, Long-Range Lens).**



## **APPENDIX A.5**

# **FIGURES FOR “SLIGHT DEFOCUS” EXPERIMENT**

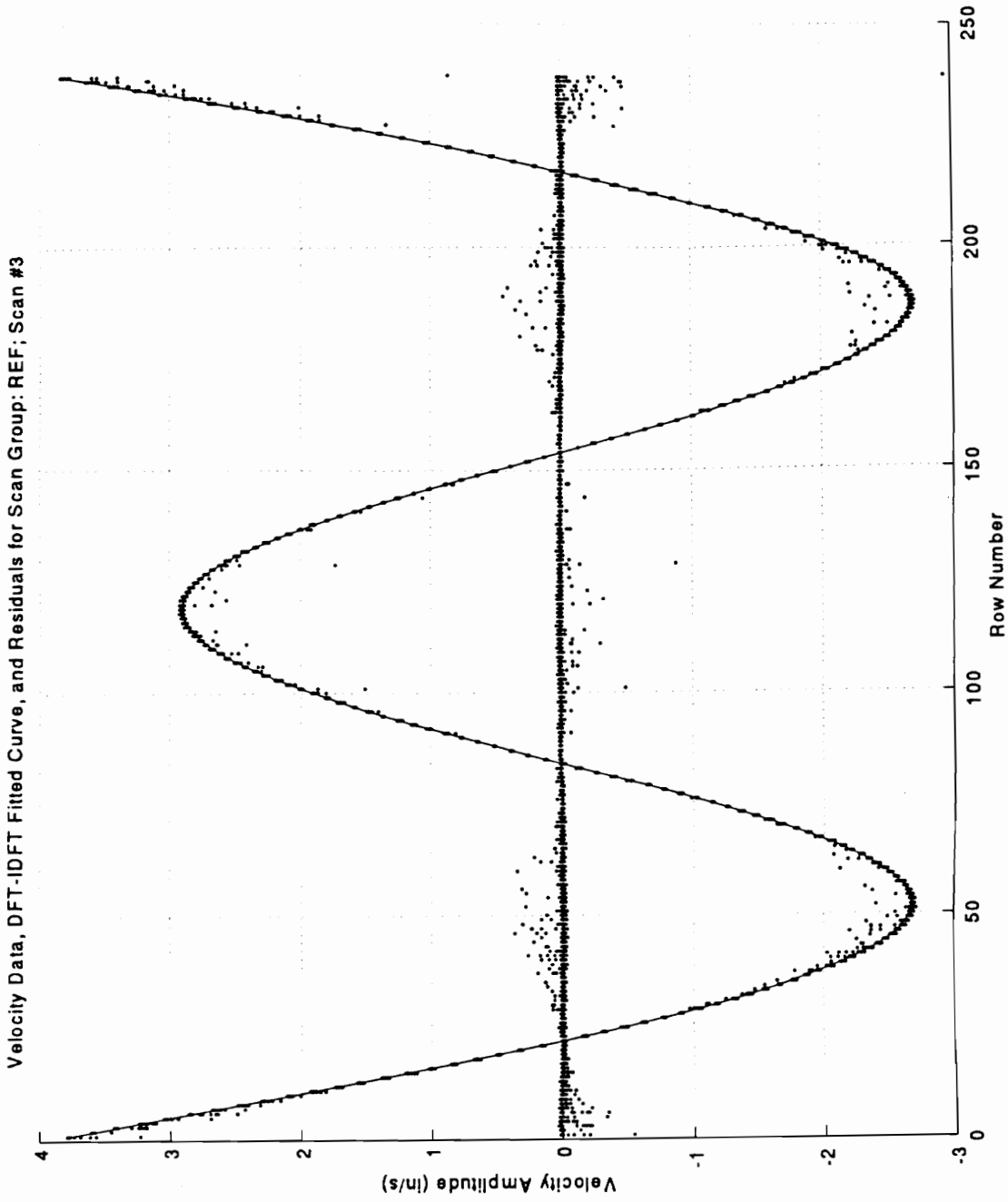


**Figure A.5.1 - "Slight Defocus" of Laser Measuring Beam Experiment: Representative scan-fit plot for Scan Group REF. (Reference scan with maximum focus reading, MAGNAFLUX™ coating, MEDIUM velocity range setting, Long-Range Lens).**

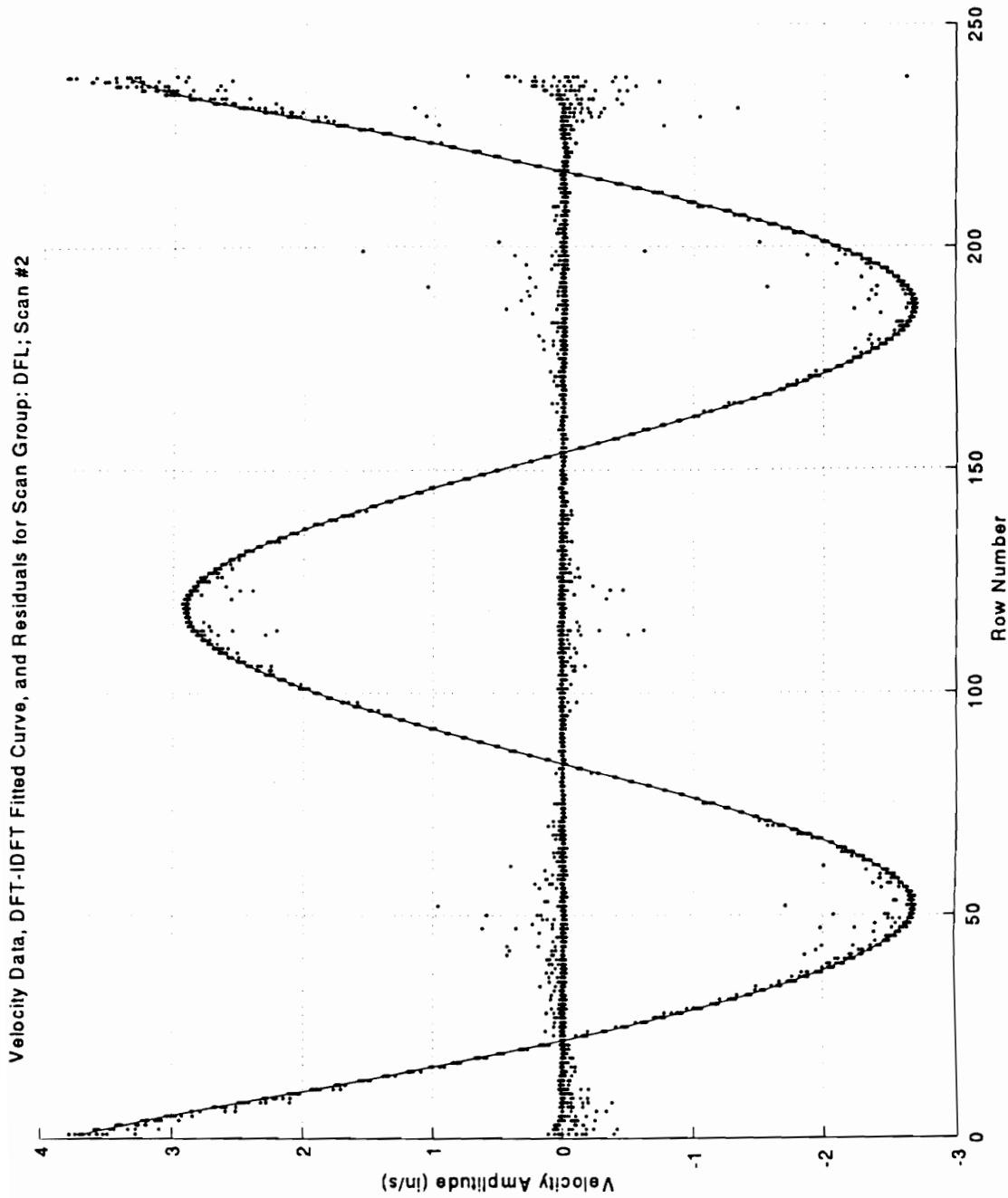


**Figure A.5.2 - "Slight Defocus" of Laser Measuring Beam Experiment: Representative scan-fit plot for Scan Group DFL. ("Slight Defocus" by rotating focus knob counter-clockwise, MAGNAFLUX™ coating, MEDIUM velocity range setting, Long-Range Lens).**

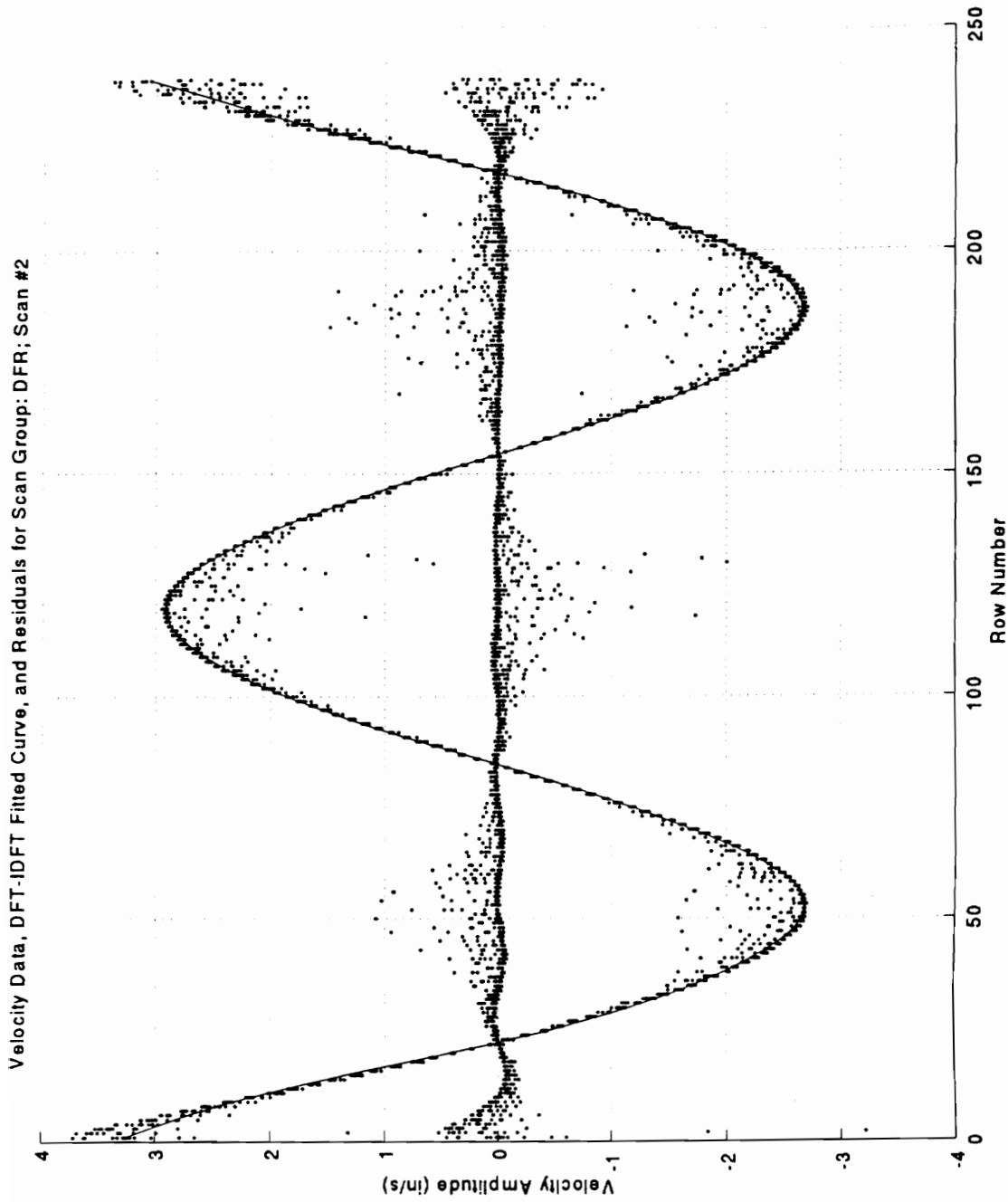


**Figure A.5.3 - "Slight Defocus" of Laser Measuring Beam Experiment: Representative scan-fit plot for Scan Group DFR. ("Slight Defocus" by rotating focus knob clockwise, MAGNAFLUX™ coating, MEDIUM velocity range setting, Long-Range Lens).**

## **APPENDIX B**

# **MATLAB DATA ANALYSIS ALGORITHMS**

```

%%%%%%%%%%%%%%%%%%%%%%%%%%%%%%%%%%%%%%%%%%%%%%%%%%%%%%%%%%%%%%%%%%%%%%%%
#####
#####
##### Program Name: medifinal.m
#####
#####
##### Program to cookie-cut superfluous scan data, separate real and imaginary
##### components, and fit the DFT-IDFT curves for the MEDIUM velocity
##### range setting.
#####
##### Raw Data, Fitted-Curve, and Residuals from the raw data to the fitted cu
##### are also plotted in the "scan-fit plot".
#####
#####
#####
#####
%%%%%%%%%%%%%%%%%%%%%%%%%%%%%%%%%%%%%%%%%%%%%%%%%%%%%%%%%%%%%%%%%%%%%%%%

```

```

clear
format long;

%%% Input the ASCII File Code Name for the Scan

alcode = input('Input File Code For All Column Data Plot: ','s');
alfile = ['FS',alcode,'_ASC'];%%% define data file to load
eval(['load ',alfile]);%%% Load data file

%%% Designate the Number of Standard Deviations Above the Mean for the
%%% DFT-IDFT Filter

nsig = 7;
ssig = int2str(nsig);

%%% Input the Scan Group Code and Scan Number

scancode = input('Input Scan Group Code: ','s');
scannum = input('Input Scan Number: ','s');

eval(['zztemp= ',alfile,',']);
temp=zztemp';

%%% Calculate the Calibration Factor for the MEDIUM Velocity Range Setting

nran=20.0;
npp=1.414;
nun=0.03937;
ng=1.0;
ns=3000;
w = ((1/nran)*npp*nun)/ng;
cv = (ns*w)/2048

%%% Multiply the raw ASCII Data by the Calibration Factor

temp= cv .* temp;

%%% Separate the Real and Imaginary Components, Cookie Cut the Superfluous
%%% Overscan and Orientate the Data

re=temp(:,1:28);
im=temp(:,29:56);
reflp=flipud(re);
imflp=flipud(im);
rcut=(reflp(8:245,8:20));
icut=(imflp(8:245,8:20));
rcutemp=rcut';

%%% Generate a Representative Row Median Velocity Vector

rmedt=median(rcutemp);
rmed=rmedt';
rtempt=[1:238;rmedt];
rfinal=rtempt';
vel=rfinal;

```

**Matlab computer algorithm for curve-fitting the scan matrix, calculating residuals, and generating the "scan-fit" plots.**

```

%%% Calculate the Maximum Velocity as a Percentage of Full-Scale
velmax=max(max(abs(rcut)));
velpercent=(velmax/3.937)*100.0;

x = vel(:,1);   %%%      Data Points (Row Numbers)
y = vel(:,2);   %%%      Velocity at Data Points

percent = 35;   %%%      Percent for DFT
l = 237;
q=[1:238];

%%% Call the DFT-IDFT Subroutine to Calculate the DFT-IDFT Fitted-Curve From th
%%% Vector

wd = beamdft(y, percent, nsig);
dftvar = vari(y,wd)

%%% Call the "Deviation Factor" Subroutine to Calculate the DF Value

[DF,errorsum]=devfac(wd,rcut)
dfstr=num2str(DF);
diary dfcoh.dat;
disp(alfile);
disp(DF);
diary off;
size(rcut)

%%% Plot the Mesh of the Scan Data

figure(1);
mesh(rcut,axis('ij'));
label = ['Real Velocity Components for File Code: ',alcode];
title(label);
xlabel('Column Number')
ylabel('Row Number')

zlabel('Velocity Amplitude (in/s)');

%%% Plot the Scan Data in X-Y Coordinates

figure (2);
hold on;
grid on;
%axis ([0 250 -4 5]);
label=['Velocity Data (All Columns) for File Code: ',alcode];
title(label);
xlabel('Row Number')
ylabel('Velocity Amplitude (in/s)')
for i=1:13
    eval(['C',int2str(i),'= rcut(:,',int2str(i),');']);
    eval(['CC=C',int2str(i),'];']);
    plot(x,CC,'.')
end;
hold off;

%%% Plot the "Scan-Fit Plot" Including the Scan Data, Fitted-Curve, and Residua

figure(3);
hold on;
plot(x,wd,'-')
grid on;
label = ['Velocity Data, DFT-IDFT Fitted Curve, and Residuals for Scan Group: ',
title(label)
xlabel('Row Number')
ylabel('Velocity Amplitude (in/s)')
for i=1:13
    eval(['C',int2str(i),'= rcut(:,',int2str(i),');']);
    eval(['CD=C',int2str(i),'];']);
    plot(x,CD,'.');
    plot(x,CD-wd,'.');
end;
hold off;

```

**Matlab computer algorithm for curve-fitting the scan matrix, calculating residuals, and generating the "scan-fit" plots (cont.).**

```
*** Plot the DFT-IDFT Fitted-Curve  
figure(4);  
plot(x,wd,'-')  
grid on;  
label = ['DFT-IDFT Fitted Curve for File Code: ',alcode];  
  
title(label)  
xlabel('Row Number')  
ylabel('Velocity Amplitude (in/s)')  
  
end;
```

**Matlab computer algorithm for curve-fitting the scan matrix, calculating residuals, and generating the “scan-fit” plots (cont.).**



```

function[fit] = beamdft(data, pct, nsigma)

%%%%%%%%%%%%%%%%%%%%%%%%%%%%%%%%%%%%%%%%%%%%%%%%%%%%%%%%%%%%%%%%%%%%%%%%%%%%%%
%%%
%%%   Program: beamdft.m
%%%
%%%   Subroutine to Perform a DFT-IDFT Curve-Fit on the Representative
%%%   Scan Data Velocity Vector
%%%
%%%%%%%%%%%%%%%%%%%%%%%%%%%%%%%%%%%%%%%%%%%%%%%%%%%%%%%%%%%%%%%%%%%%%%%%%%%%%%
format long;

%%%   Perform the flip and mirror to make the data periodic

T = length(data);
seglen = T-1;
x = 0:seglen;

%%%   Calculate slope of line from first to last point
slope = (data(T)-data(1))/seglen;

%%%   Shear the data
data(:) = data(:)-slope*x(:);

%%%   Flip and mirror
data(T+1:2*T-2) = -data(T-1:-1:2) + 2*data(T);

%%%   Transform to frequency domain
datafrq = fft(data);
lg = 20*log(datafrq);

%%%   Calculate the magnitude
magfrq = abs(datafrq);

%%%   Calculate the mean of the upper end of 'pct' of data
pctbin = round(T* (1.0 - (pct/100)));
binset = magfrq(pctbin:T);
mval = mean(binset)

%%%   Calculate the value 'nsigma' above the mean and
%%%   find the bin containing a value above the 'noise'
noise = nsigma*std(binset) + mval
binset = find(magfrq(1:T) > noise)
setsigto = (magfrq(80)-mval)/std(magfrq(pctbin:T))
if (isempty(binset))
    highbin = 0;
    setsigto = (magfrq(1)-mval)/std(magfrq(pctbin:T));
    disp('Number of standard deviations are too high. ')
    text = ['Try less than ',int2str(round(setsigto))];
    disp(text)
else
    highbin = max(binset)
end

%%%   Calculate the number of spectral lines to retain
ns = highbin - 1

%%%   Filter the frequency data
datafrq(ns+2:2*T-2-ns) = zeros(1,2*T-2*ns-3);

%%%   Inverse transform back to spatial domain
data = ifft(datafrq);

%%%   Discard mirrored upper half
data = real(data(1:T));

%%%   Undo the shear
data(:) = data(:) + slope*x(:);

%%%   Send the fit back
fit = data(1:T);

```

## Matlab subroutine for calculating the DFT-IDFT curve-fit.

```

%*****
%
%      Function to calculate the average variance of fitted data
%      to all columns of the original data
%
%
%      devfac.m
%      R. Flynt Stream
%
%*****

function [DF,errorsum]=devfac(yfit, realmat,sl,alfile)
format long;

%%%%% Zero Out Initial Values

sumd=0;
sum=0;
g=0;
errorsum=0;

%%%%% Loop Scan Rows

for i=1:238
    next=yfit(i);
    nextsq=next^2;

%%%%% Loop Scan Columns

        for j=1:13

                XV=realmat(i,j);
                eval(['dif=XV-yfit(',int2str(i),',:);']);
                difsq=dif^2;
                sum=sum+difsq;
                errorsum=errorsum+dif;
                g=g+1;
        end;

sumd=sumd+nextsq;
end;

k=i;
n=j;

%%%%% Calculate Numerator and Denomenator of DF Value

numer=sum/(n*(k-2*sl));
denom=sumd/k;

%%%%% Calculate DF Value

DF = numer/denom;
errorsum;

end;

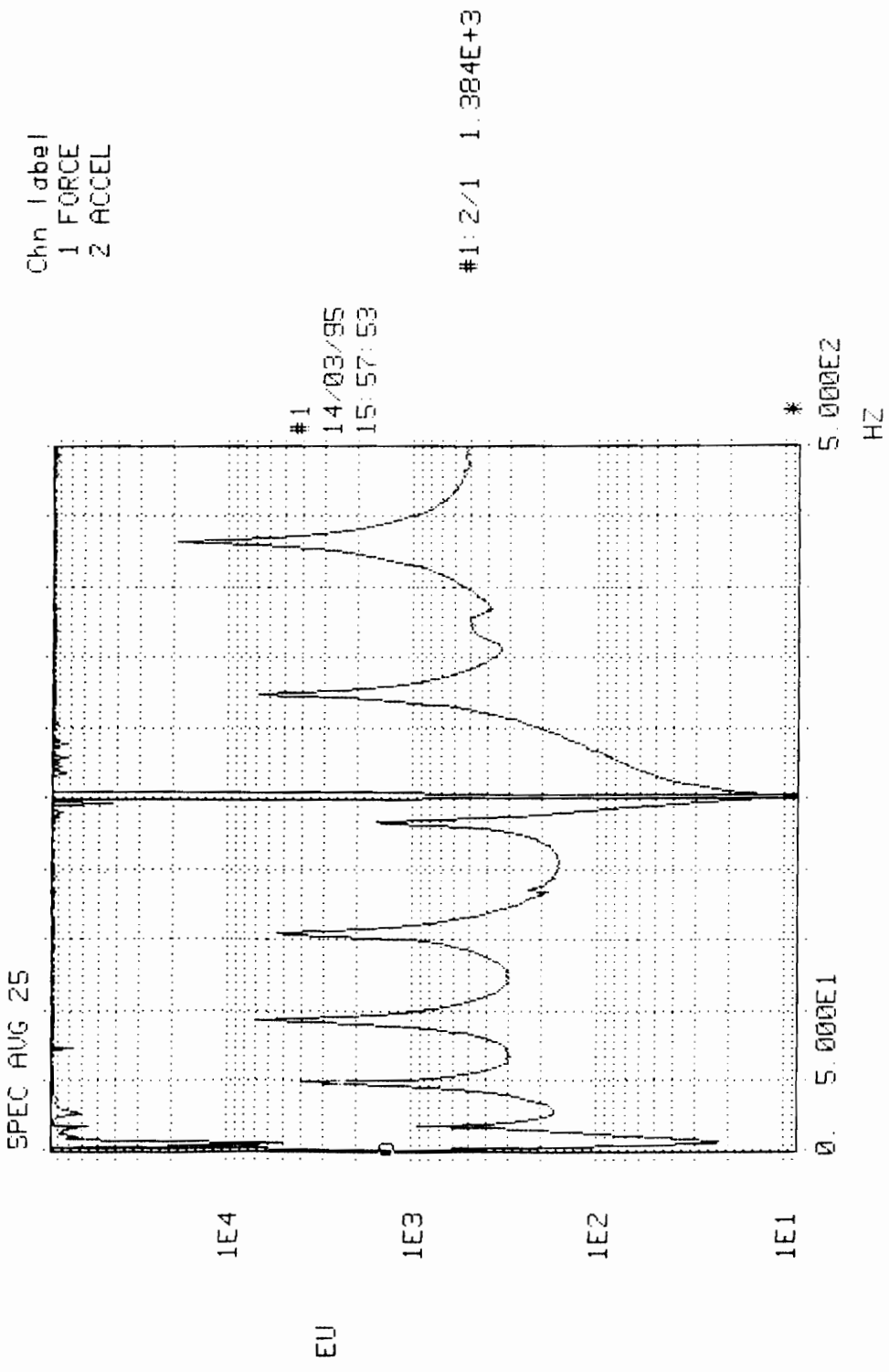
```

## Matlab subroutine for calculating the “Deviation Factors”.

## **APPENDIX C**

# **FREQUENCY RESPONSE FUNCTION (FRF) DIAGRAMS**

6080 MULTICHANNEL FFT ANALYZER



x = 1.250E+0

Figure C.1 - Typical baseband FRF and coherence diagram taken for the steel beam (surface treated with MAGNAFLUX™ coating).

6080 MULTICHANNEL FFT ANALYZER

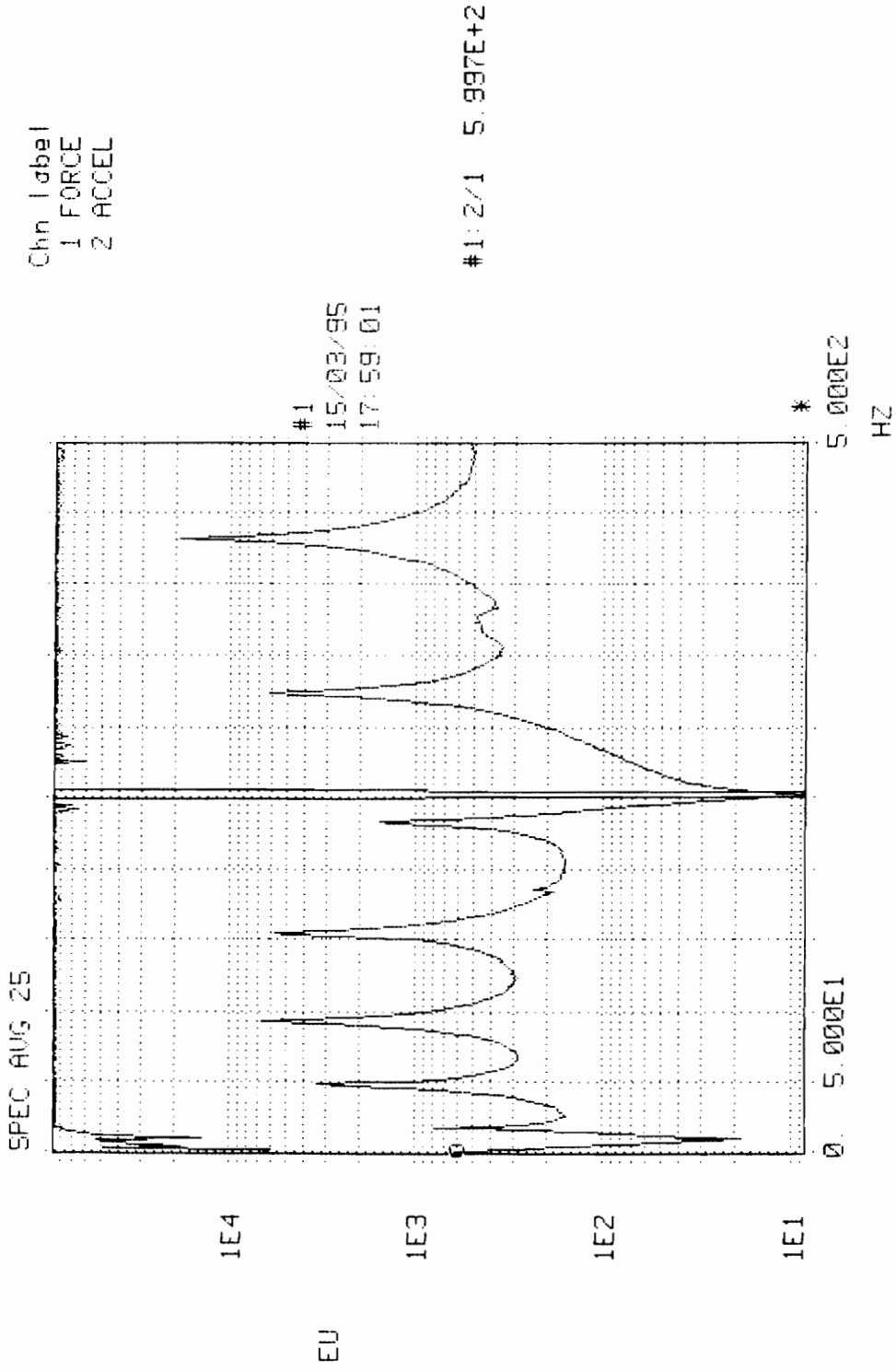
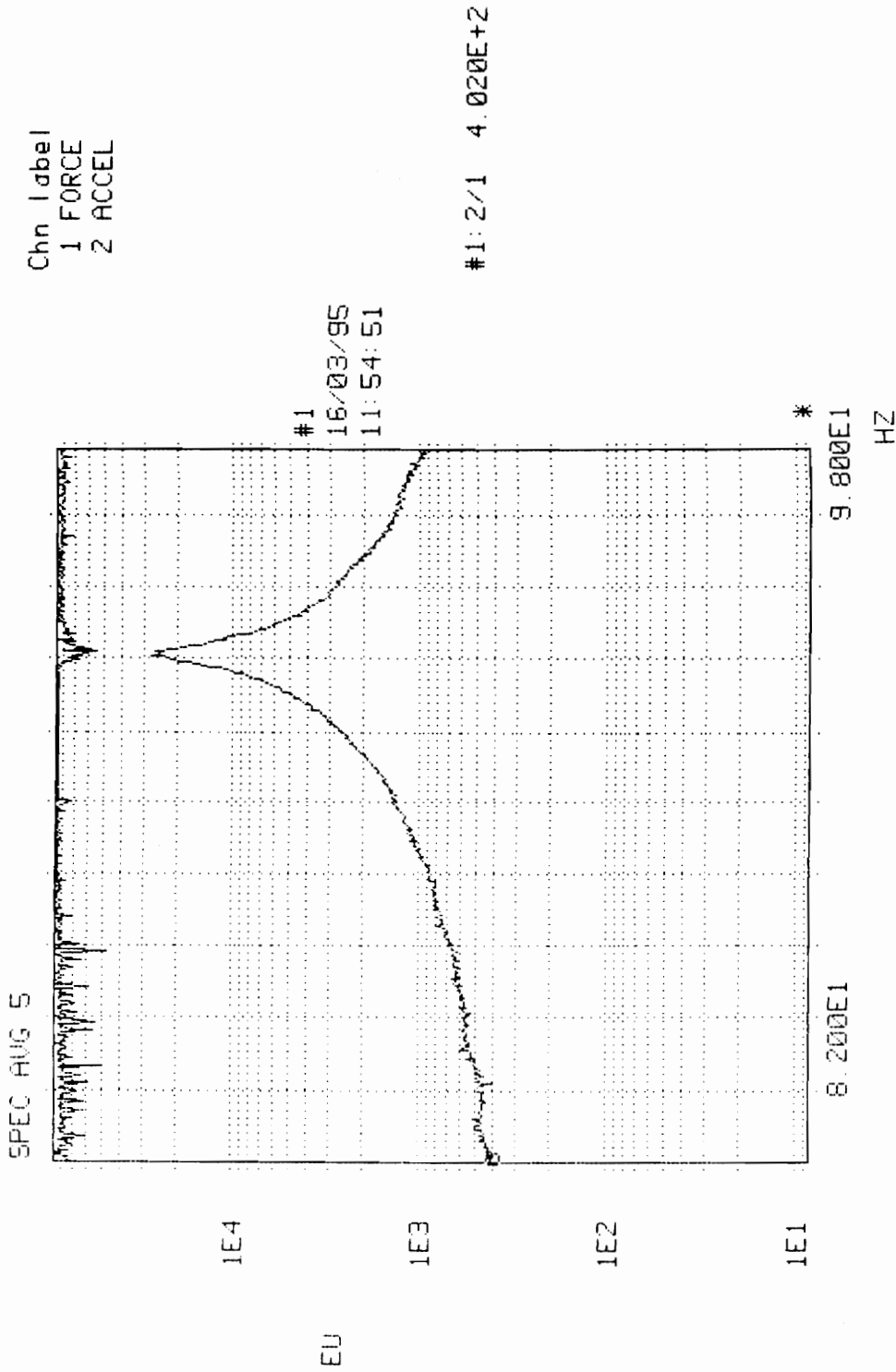


**Figure C.2 -** Typical baseband FRF and coherence diagram taken for the steel beam during the span of the experiments (surface treated with MAGNAFLUX™ coating).

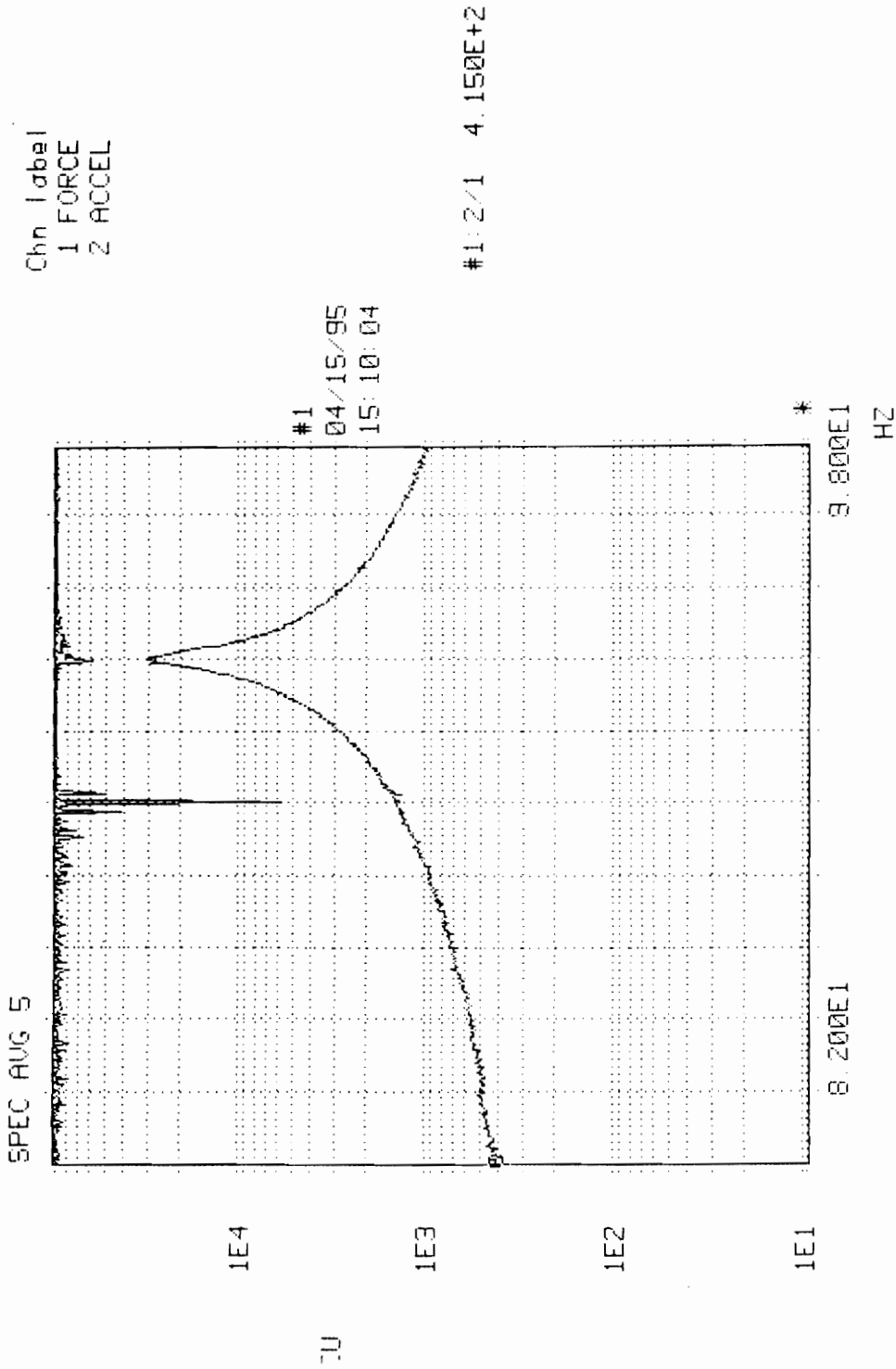
6080 MULTICHANNEL FFT ANALYZER



\* = 8.00391E+1

Figure C.3 - Typical FRF zoom and coherence diagram taken for the steel beam at the peak corresponding the 3<sup>rd</sup> bending mode (surface treated with MAGNAFLUX™ coating).

6080 MULTICHANNEL FFT ANALYZER



x = 8.00391E+1

Figure C.4 - Typical FRF zoom and coherence diagram taken for the steel beam at the peak corresponding to the 3<sup>rd</sup> bending mode. Diagram acquired during the span of the experiments (surface treated with MAGNAFLUX™ coating).

6080 MULTICHANNEL FFT ANALYZER

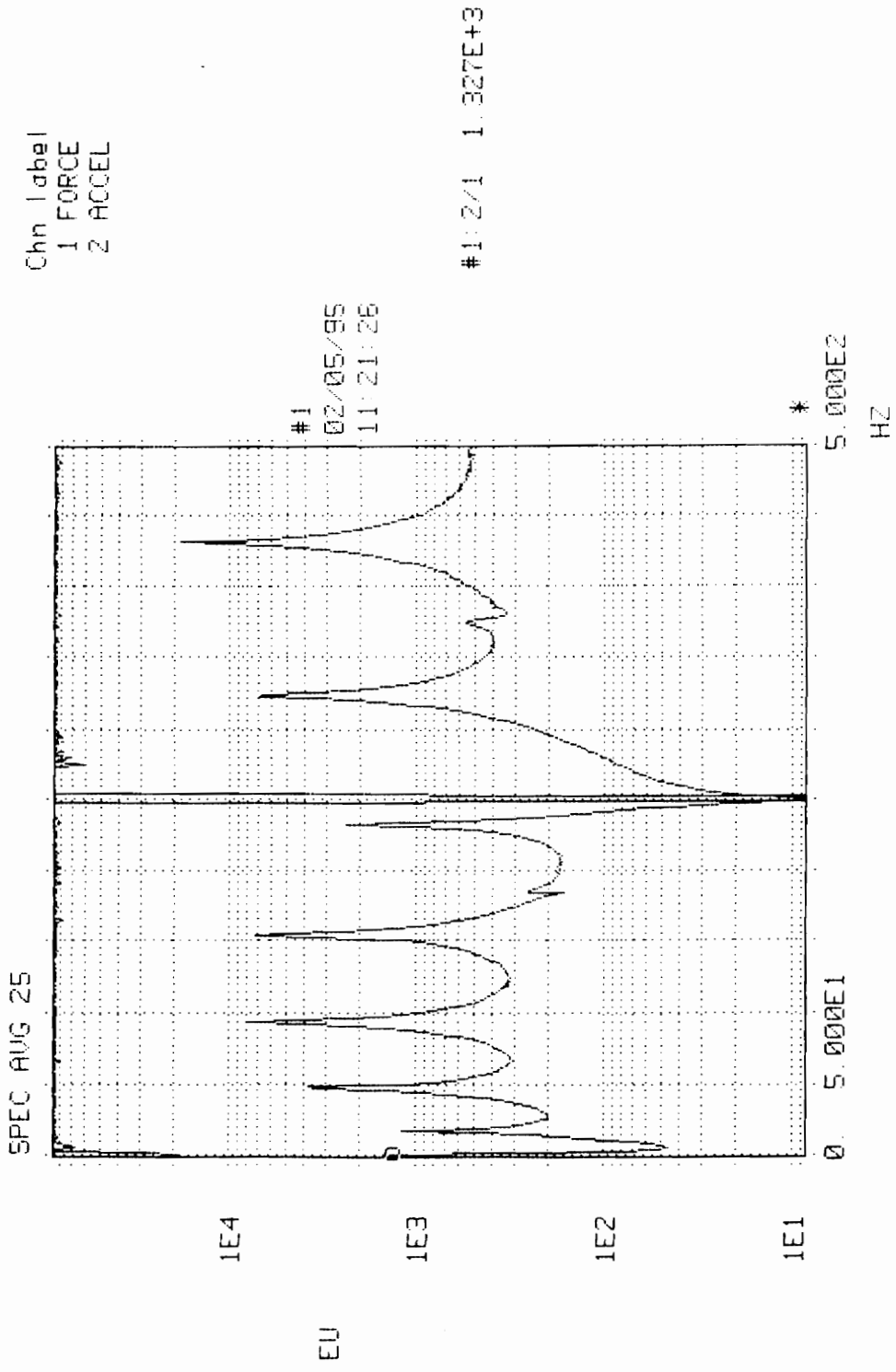
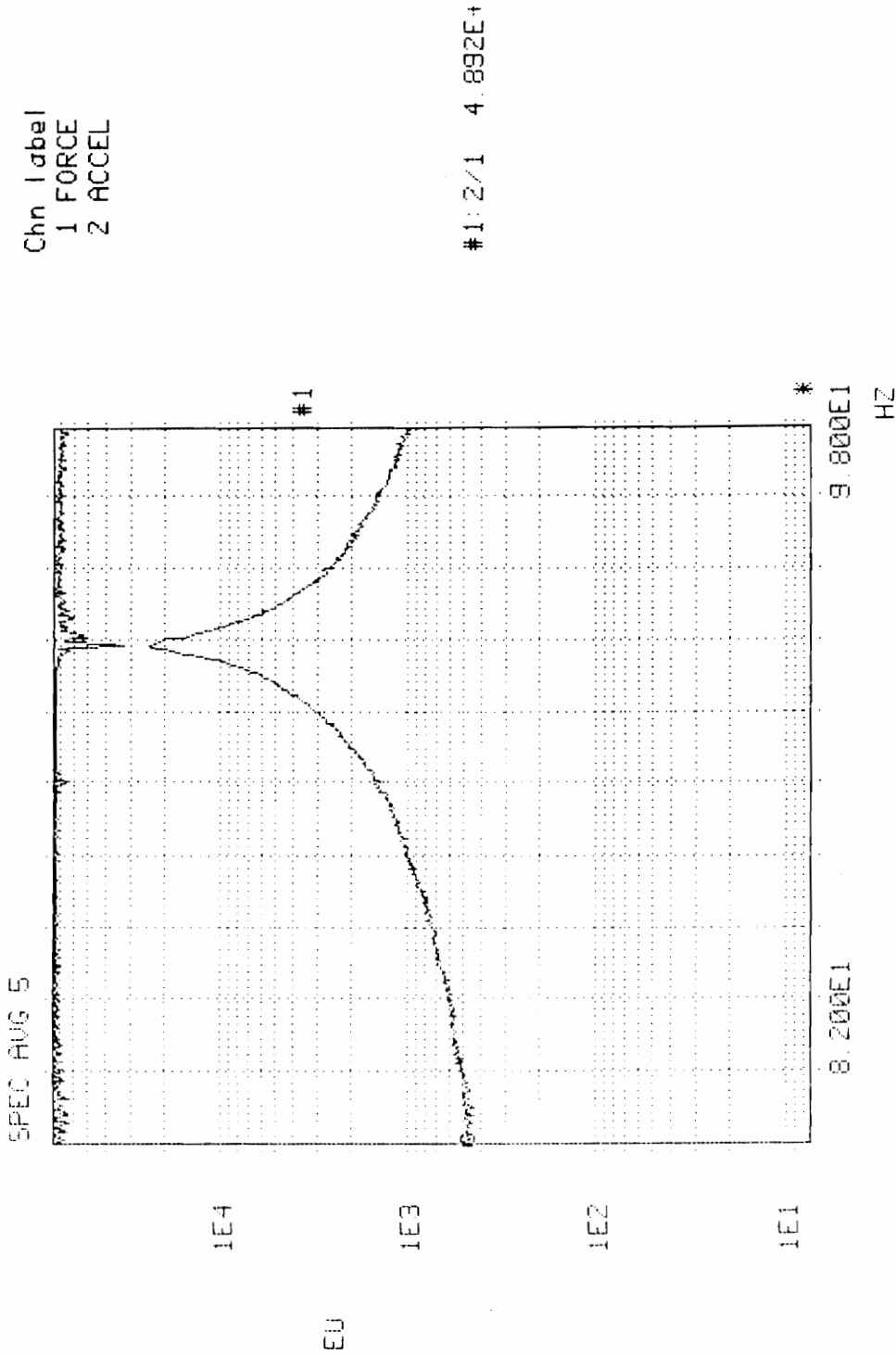


Figure C.5 - Typical baseband FRF and coherence diagram taken for the steel beam (surface treated with 3M Scotchlite™ retroreflective liquid coating).



6080 MULTICHANNEL FFT ANALYZER



\* = 8.00391E+1

**Figure C.6** - Typical FRF and coherence diagram taken for the steel beam at the peak corresponding the 3<sup>rd</sup> bending mode. Diagram acquired during the span of the experiments (surface treated with 3M Scotchlite™ retroreflective coating).

## **APPENDIX D**

### **EXAMPLES OF LASER NOISE OCCURRING AT OTHER EXCITATION FREQUENCIES**

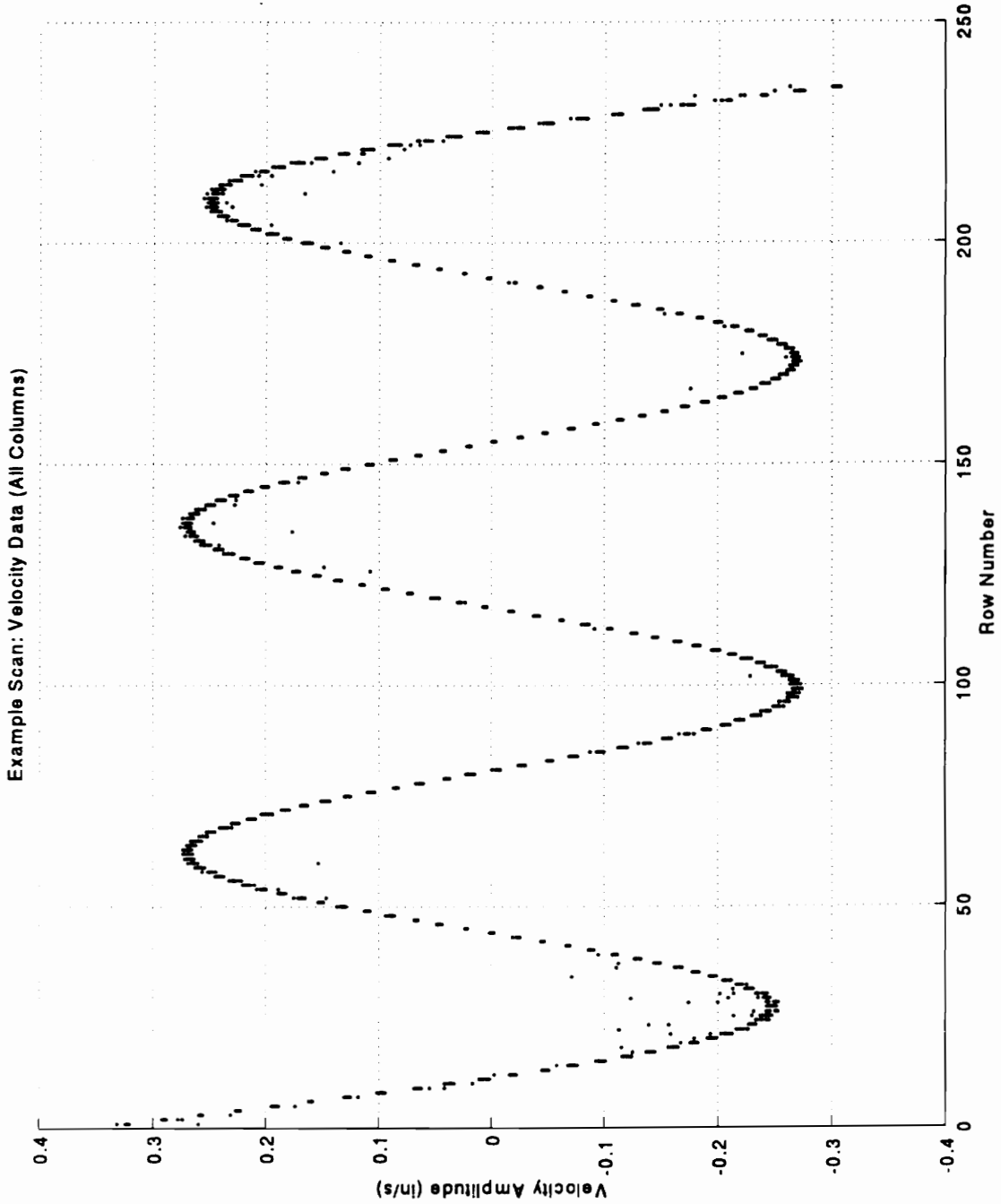


**Figure D.1 -** Example of laser noise occurring at a frequency near the 6<sup>th</sup> bending mode of the steel beam (long-range lens, LOW velocity range setting, MAGNAFLUX™ coating).

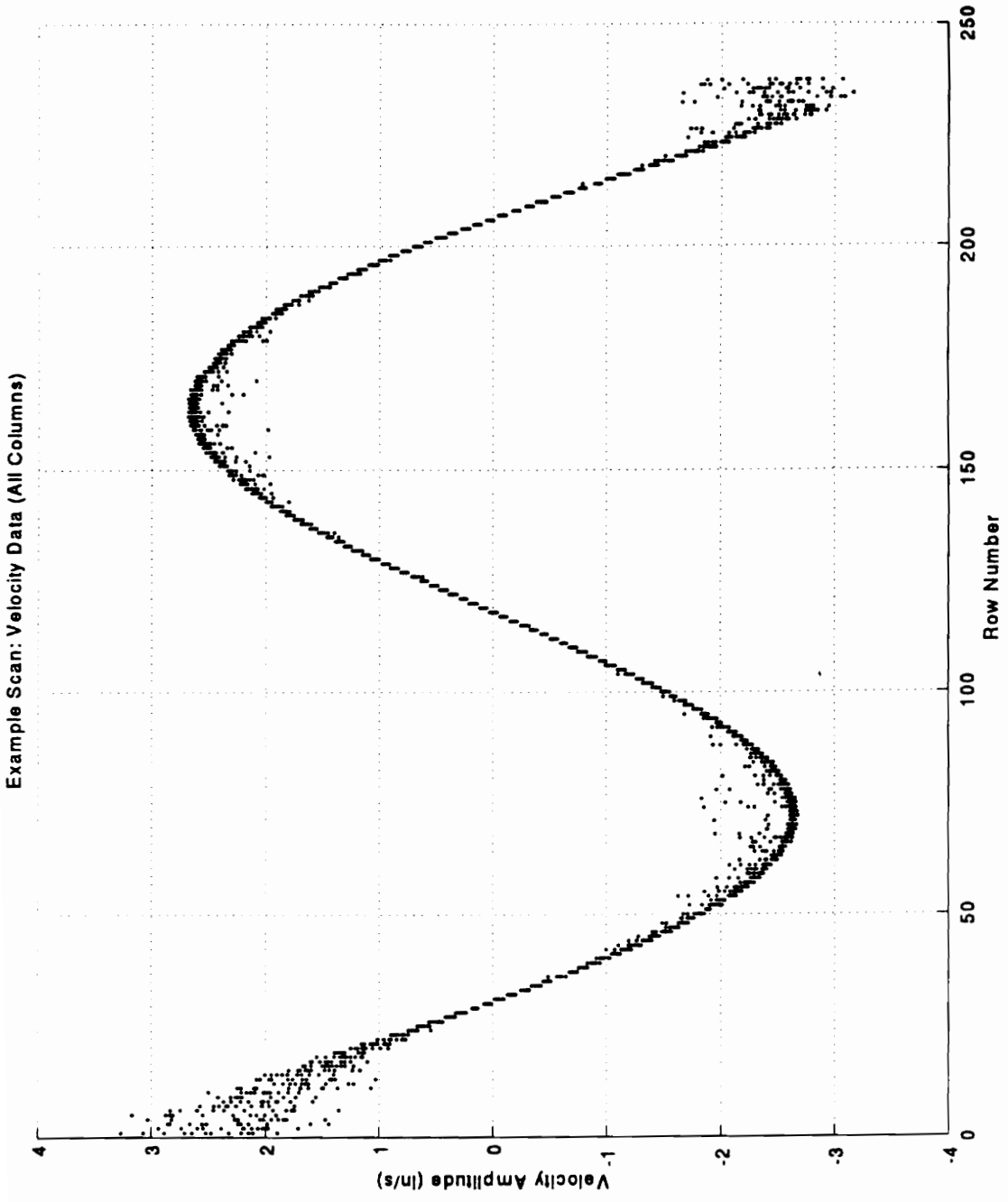
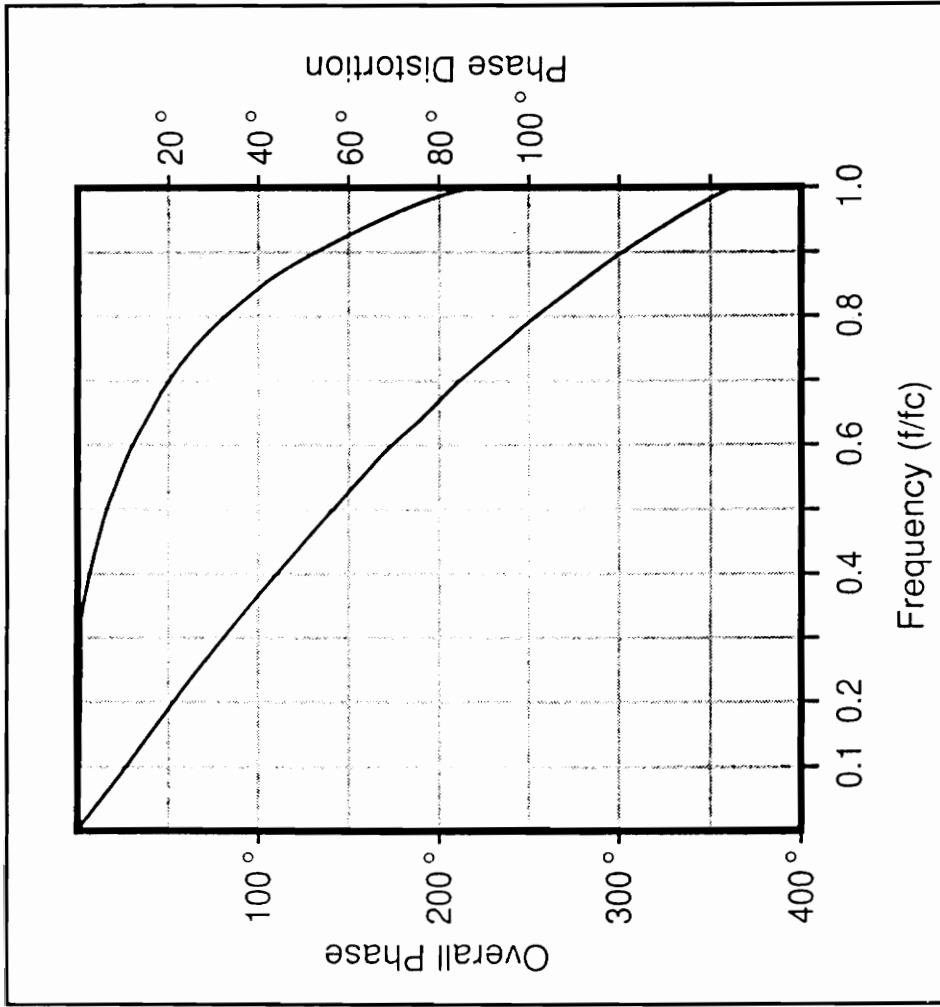


**Figure D.2 -** Example of laser noise occurring at a frequency near the 2<sup>nd</sup> bending mode of the steel beam (long-range lens, MEDIUM velocity range setting, MAGNAFLUX™ coating).

## **APPENDIX E**

# **STANFORD SR640 FILTER PHASE RESPONSE CURVE**



SR640 Phase Response

Figure E.1 - Stanford SR640 low-pass filter phase response curve.

**APPENDIX F**

**ANTICLASTIC CURVATURE**

**CALCULATION**

A study was performed in order to determine the relative extent of the anticlastic curvature on the deflection of the steel beam. The bending of the beam was modeled using BEAM VI (©1992 Department of Mechanical Engineering, Virginia Polytechnic Institute and State University) an analytical computer modeling program.

A unit load was applied using the Forced Dynamic Response function of the program. The moment at the curved section of the beam resulted in  $-2.224 \times 10^2$  in-lb. Now using the relation:

$$\frac{1}{\rho} = \frac{M}{EI} \quad (\text{F.1})$$

where  $\rho$  is the radius of curvature due to bending,  $M$  is the moment, and  $I$  is the moment of inertia;  $\rho$  can be found to be 526.93 in.

Assuming a Poisson's ratio of  $\nu = 0.3$ , and using the definition of the anticlastic effect:

$$\frac{1}{\rho'} = \frac{\nu}{\rho} \quad (\text{F.2})$$

where  $\rho'$  is the radius of curvature due to the anticlastic effect;  $\rho'$  results in 1756.43 in.

Now based on the equation relating the length of an arc,  $s$ , to the radius (in this case  $\rho'$ ) and angle,  $\theta$ :

$$s = \rho'\theta \quad (\text{F.3})$$



one can solve for  $\theta$ . This can then be used to solve for the maximum deflection due to the anticlastic effect,  $\delta_{A-C}$ :

$$\delta_{A-C} = \rho' - \rho' \cos\left(\frac{\theta}{2}\right) \quad (\text{F.4})$$

This deflection,  $\delta_{A-C}$ , results in  $6.405 \times 10^{-4}$  in.

The deflection due to the bending,  $\delta_{Bend}$ , from the BEAM VI model was found to be  $4.07 \times 10^{-2}$  in. Thus the ratio of the deflection due to the anticlastic effect to the deflection due to bending can be calculated, and results in 1.6 %. For the purposes of this thesis, it was determined that this effect is negligible.

**APPENDIX G**

**LASER DOPPLER VIBROMETER**

**CALIBRATION CHECK**

A calibration spot check was performed on the SLDV system by directing the laser measuring beam at the end of a piezoelectric accelerometer mounted at the end of an electrodynamic shaker. With the previous exception, the experimental setup was similar to those presented above. A PCB series 307A accelerometer (S/N 1092) was used for the test. Several checks were performed for both the LOW and MEDIUM velocity range settings. The following represents a typical calibration check.

With the laser set on the MEDIUM velocity range setting, the shaker was set to an excitation frequency of 100 Hz. An arbitrary excitation amplitude was then chosen. The corresponding voltage was then obtained via a digital multimeter. The resultant voltage was 0.3292 V (rms). This voltage can then be converted to g's using the calibration factor of the accelerometer (in this case 0.0982 V/g). The result can then be integrated to obtain the velocity. For this case, the resultant velocity was 74.0 mm/s (0-pk).

This was then checked versus the output from the SLDV system. The system was set with a calibration factor of 1.0 such that the output was in digital bits. In this case the result was 719. Using the calibration factor for the SLDV system (described in Chapter 3) of 0.103564 mm/s (0-pk)/digital bit, the resultant velocity was found to be 74.5 mm/s (0-pk). This velocity is within 0.7% of the velocity obtained from the accelerometer.

Similar results were obtained for the other cases investigated. It was thus found that the calibration factor used in the experiments presented in this thesis were within the

accuracy limits of the instruments used in the calibration check and thus the calibration factor was determined to be valid.

## VITA

Robert Flynt Strean was born on May 17, 1970 to Richard and Beverly Strean in Alexandria, Virginia. Shortly afterwards the family moved to Vienna, Virginia and later to nearby Oakton, Virginia. In June, 1988, Flynt graduated from James Madison High School, and began his studies at Virginia Polytechnic Institute and State University (Virginia Tech) in Blacksburg, Virginia. As he studied towards his Bachelor of Science degree in Mechanical Engineering, Flynt spent two summers as an intern for the Mobil Oil Corporation in the Environmental Engineering department. During his Senior year, Flynt was also involved in the design, fabrication, and competition of the Society of Automotive Engineers sponsored Mini-Baja all terrain vehicle. In May 1993, he graduated cum laude and received his Bachelor of Science Degree in Mechanical Engineering.

Flynt continued his studies in August of 1993 towards a Masters Degree in Mechanical Engineering at Virginia Tech. While completing the graduate requirements, he served an assistantship under Dr. Larry D. Mitchell where he participated in a project designed to develop active-learning based Engineering education methods. In September 1995, he completed the requirements for the Master of Science Degree in Mechanical Engineering. Flynt currently resides in Lexington, Kentucky and is employed as a Product Development Engineer for Lexmark International.

